eman ta zabal zazu

Universidad del País Vasco
Euskal Herriko Unibertsitatea

FACULTY
OF SCIENCE
AND TECHNOLOGY
UNIVERSITY
OF THE BASQUE
COUNTRY

Ultrafast Dynamics in Isolated Molecules, Molecular Clusters and Solutions:

Filling the Gap between the Gas- and Condensed-Phases

Doctoral Thesis

Iker Lamas Frejo

Supervisors:

Asier Longarte Aldama

Raúl Montero Santos

Department of Physical Chemistry
University of the Basque Country
Leioa, 2021

Iker Lamas was recipient of a predoctoral fellowship from the University of the Basque Country. This research was supported by the Ministry of Economy and Competitiveness-FEDER (CTQ2015-68148-C2-1-P and PGC2018-098561-B-C21) and the Basque Government (PIBA18-11 and IT1162-19). Technical and human support provided by SGIker is also gratefully acknowledged.

“Satisfaction of one’s curiosity is one of the greatest sources of happiness in life.”

Linus Pauling

A la abuela Nacha.

Acknowledgements

This thesis would not have been possible without the support of many people that have contributed to this work throughout these four years.

First and foremost, I would like to wholeheartedly express my gratitude to my two thesis supervisors, Asier Longarte and Raúl Montero. Thank you for the patience, the time, the constant help and the wise advice. You both have always challenged me to perform my best and encouraged me in my darkest moments. I have been incredibly fortunate of having such scientific mentors.

I am also deeply indebted to the rest of Spectroscopy Group, past and present, for your assistance and camaraderie over the last years. Individually, I thank Montse Vallejo for her willingness to solve my doubts at the very beginning of my thesis, but also for her closeness. To Roberto Fernandez, thanks for sharing your love for rock music and sci-fi movies. You have always made me feel very comfortable in the group. Especial thanks must go to Jone Garate and Lucía Martín, for listening to me, for the useful discussions and for making the time we have spent together in the office or during coffee/lunch breaks so interesting and enjoyable. I am also extremely grateful to Imanol Usabiaga and Camilla Calabrese for the frank conversations and the invaluable tips not only for my professional career, but also for my personal life. To Ander Camiruaga, thanks for your help and good advice in the lab and for all the brainstorming sessions during these years. Many thanks also to Aran Insausti and Elena Rita Alonso for their daily support and for solving my many naïve questions. I am also thankful to Iciar Uriarte and Otger Crehuet for their kindness and disposition to help me. To the new PhD students of the group, Maider Parra, Juan Jose Gutiérrez and Fernando Torres, thank you for your positivity and good vibes; they have been essential for the write-up. I would like to further acknowledge the support of the senior members of the group, especially Jose Andrés Fernández, Fran Basterretxea and Carolina Redondo.

Thanks must also go to our collaborators on the different projects. Prof. Dave Townsend from Heriot-Watt University, for the helpful discussion regarding transient absorption and for making possible my short-term visit in his research group, although we finally conducted a virtual collaboration because of the pandemic. Prof. Lluís Blancafort from Universitat de Girona, who performed the computational calculations for azaindoles in

the gas-phase. Dr. Virginia Martínez Martínez, who dedicated a significant amount of her time to the steady-state study of azaindoles in solution. Prof. Diego Sampedro from Universidad de la Rioja, who synthesized the MAA analogues and conducted the complementary theoretical study.

Outside the work, there have been many friends who have supported me and I must mention. My collegemates Aitana, Aitor and Israel because this long way started with you. Marta, since we met by chance in Salamanca during my first congress you have become an indispensable person in my life. Yours is the credit for not only helping me put things into perspective, but for the inspiration you have given me. You are the best. My *kuadrilla*: Aritz, Arkaitz, Eduardo, Iker, Etxe, Perez, Iñigo, Ismael, Javier, Jon, Andonegi, Equiza, Aitor, Gonzalo, Leto, Mario, Fran… Guys, you always kept me laughing and provided your moral support throughout this challenging time, I am incredibly blessed to have such amazing friends. Especial thanks to those who always had time for one more pint on our sacred temples [K, A, G and L]. Nagore, thank you for the unforgettable shared moments and laughs, but in particular for cheering me up when I was worried. Thanks for being there in good and bad times; this would have been much harder without your limitless support.

Last but certainly not least, I would like to thank my family for their unconditional love and support over the years, most outstandingly my mother whose strength and resilience has been fundamental for everything I have achieved.

Contents

List of Publications

This doctoral thesis is based on the following publications:

1 *Influence of the solvent polarity on the photophysics of azaindoles*

I. Lamas, R. Montero, V. Martínez-Martínez and A. Longarte

In preparation.

2 *Excited state dynamics of pyrrole-containing clusters*

I. Lamas, R. Montero and A. Longarte

In preparation.

3 *An nπ* gated decay mediates excited state lifetimes of isolated azaindoles*

I. Lamas, R. Montero, V. Martínez-Martínez, A. Longarte and L. Blancafort

Physical Chemistry Chemical Physics, 2020, 22(33), 18639-18645.

4 *Photophysical characterization of new and efficient synthetic sunscreens*

R. Losantos, I. Lamas, R. Montero, A. Longarte and D. Sampedro

Physical Chemistry Chemical Physics, 2019, 21(21), 11376-11384.

5 *Excited state dynamics of aniline homoclusters*

R. Montero, I. Lamas, I. León, J.A. Fernández and A. Longarte

Physical Chemistry Chemical Physics, 2019, 21(6), 3098-3105.

Apart from the above-mentioned articles, during the period of the thesis the following publications have also been produced:

6 *Tracking electronic and vibrational coherent relaxation through conical intersection by sub-20 fs UV pulses*

A. Peralta, I. Lamas, M. Sánchez-Albaneda, C. Méndez, A. Longarte and R. Montero

To be submitted to Physical Chemistry Chemical Physics.

7 *Exploring the influence of intermolecular interactions in the prebiotic chemistry using laser spectroscopy and calculations*

A. Camiruaga, I. Usabiaga, C. Calabrese, I. Lamas, F. Basterretxea and J.A. Fernández

To be submitted to Chemistry ─ A European Journal.

8 *Dynamics of pyrroles excited to the 3s/πσ* state*

I. Lamas, A. Longarte, A. Peralta, G. Muga, D. Townsend and R. Montero

The Journal of Physical Chemistry A, 2019, 123, 42, 8982-8993.

9 *Singlet fission mediated photophysics of BODIY dimers*

R. Montero, V. Martínez-Martínez, A. Longarte, N. Epelde-Elezcano, E. Palao, I. Lamas, H. Manzano, A.R. Agarrabeitia, I. López, M.J. Ortiz, I. García-Moreno

The Journal of Physical Chemistry Letters, 2018, 9, 3, 641-646.

List of Abbreviations and Acronyms

2ω	Second Harmonic
3ω	Third Harmonic
4ω	Four Harmonic
Abs	Absorption
ACN	Acetonitrile
AI	Azaindole
An	Aniline
as	Attosecond (10^{-18} s)
BBO	β-Barium Borate
BSSE	Basis Set Superposition Error
C153	Coumarine 153
CAS	Coherent Artifact Signal
CASPT2	Complete Active Space Second-Order Perturbation Theory
CASSCF	Complete Active Space Self-Consistent Field
CC	Cross-Correlation
CCD	Charge-Coupled Device
CH	Cyclohexane
CI	Conical Intersection
CPA	Chirped Pulse Amplifier
CT	Charge Transfer
CTTS	Charge-Transfer-to-Solvent
DAS	Decay-Associated Spectrum
DC	Direct Current
DFT	Density Functional Theory
DCM	Dichloromethane
ESA	Excited State Absoption
ESPT	Excited State Proton Transfer
Fl	Fluorescence
fs	Femtosecond (10^{-15} s)
FuC	Fluorescence Up-Conversion
FWHM	Full Width at Half Maximum

GDD	Group Delay Dispersion
GRENOUILLE	Grating-Eliminated No-Nonsense Observation of Ultrafast Incident Laser Light E-Fields
GSB	Ground State Bleach
GVD	Group Velocity Dispersion
GVM	Group Velocity Mismatch
IC	Internal Conversion
IET	Intermolecular Energy Transfer
IR	Infrared
IRC	Intrinsic Reaction Coordinate
ISC	Intersystem Crossing
IVR	Intramolecular Vibrational Redistribution
LIIC	Linear Interpolation in Internal Coordinates
m/z	Mass-to-Charge Ratio
MAA	Mycosporine-Like Amino Acid
MCP	Micro-Channel Plate
MeOH	Methanol
MEP	Minimum Energy Path
MP2	Second-Order Møller–Plesset Perturbation Theory
MS-CASPT2	Multi-State Complete Active Space Second-Order Perturbation Theory
ND	Neutral Density
NMPy	N-methylpyrrole
ns	Nanosecond (10^{-9} s)
OD	Optical Density
OPA	Optical Parametric Amplifier
OPO	Optical Parametric Oscillator
PCET	Proton Coupled Electron Transfer
PCM	Polarizable Continuum Model
PEC	Potential Energy Cut
Ph	Phosphorescence
PMT	Photomultiplier
ps	Picosecond (10^{-12} s)

Py	Pyrrole
R2PI	Resonant Two-Photon Ionization
REMPI	Resonance Enhanced Multi-Photon Ionization
s	Second
SE	Stimulated Emission
SFG	Sum-Frequency Generation
SHG	Second Harmonic Generation
SOC	Spin-Orbit Coupling
SSA	Single-Shot Second Order Autocorrelator
TA	Transient Absorption
TD-DFT	Time-Dependent Density Functional Theory
TOF	Time-of-Flight
TR-ID	Time-Resolved Ion Dip
TR-IY	Time-Resolved Ion Yield
TS	Transition Structure
UV	Ultraviolet
VEE	Vertical Excitation Energy
VET	Vibrational Energy Transfer
Vis	Visible
WLC	White Light Continuum
µs	Microsecond (10^{-6} s)

1. INTRODUCTION

1.1. Ultrafast Molecular Dynamics

Spectroscopy is the field that studies the interaction between light and matter and it has become an indispensable tool for understanding both the structure and the dynamics of molecular systems. Whereas the former is related with the characterization of the main interactions that rule the atomic arrangement leading to stable molecules, the latter studies the transformation of the system over time, trying to unravel the mechanisms of a variety of photochemical and photophysical events such as inter- and intra-molecular interactions, electronic energy transfer pathways among excited states or chemical reactivity. These interactions are described in terms of quantum mechanics, which is the theoretical subject that permits to explain and predict the experimental results through semi-classical treatments.

The basis of molecular dynamics were formed in the 19th century when Arrhenius, in 1889, expressed the influence of temperature in the chemical reaction rate constant in terms of the activation energy and the pre-exponential factor.[1] In the 20th century, several contributions where made not only on the theoretical framework, but also on the experimental observations: On the one hand, in 1913 Bohr modelled the hydrogen atom[2] and in 1926 Schrödinger developed quantum mechanics after De Broglie and Heisenberg proposed the dual particle-wave nature[3] and the uncertainly principle,[4] respectively. Furthermore, Eyring and Polanyi, in 1931, developed a semi-empirical method, based on the Heither-London theory, for constructing the potential energy surface of a three-atom reaction.[5] Later, Eyring and Evans, and Polanyi, independently, developed the Transition State theory.[6] On the other hand, in 1949 Norrish, Eigen and Porter implemented methods for studying fast reactions and short-lived intermediates of a few microseconds ($1\ \mu s = 10^{-6}$ s), particularly by the flash photolysis technique.[7-8] However, the real-time observation of nuclear and electronic motion required ultrafast techniques with better time-resolution.

After the first laser sources were constructed in the early 1960s, laser pulses with shorter duration became available, enabling the research of faster dynamics.[9] In 1974 the first laser producing femtosecond ($1\ fs = 10^{-15}$ s) pulses was created,[10] which constituted a revolutionary step in the field of molecular dynamics since the reorganization of chemical bonds occurs on the fs time-scale. In this sense, Ahmed Zewail was the pioneer on tracking the dynamics of several molecular systems, from simple diatomic and triatomic molecules such as ICN,[11-12] NaI[13-15] or I_2[16-17] to more complex and larger systems,[18-26] by pump-probe techniques and therefore laying the foundations of *Femtochemistry*, for which was awarded with the Nobel Prize in 1999.[27] More recently, laser pulses of attosecond (1 as = 10^{-18} s) duration have been achieved by high harmonic generation process, which permits to monitor the dynamics of electrons.[28-31]

Grounding on these tools, the work presented in this thesis focuses primarily on applying fs time-resolved pump-probe techniques to investigate the relaxation dynamics of molecules with biological interest in the isolated- and condensed-phases. In the following sections an overview of the fundamental principles and concepts of the studied molecular dynamics, together with a brief description of the pursued goals is provided.

1.1.1. Wavepacket Dynamics

The photodynamical behavior of a molecule can be described through wavepackets. The fs laser pulses exhibit a wide spectral width due to its short duration, which is a consequence of the uncertainly principle.[4, 32] This relationship between time and energy implies a broad energy profile for a fs laser pulse that is able to prepare a range of vibrational levels when electronic photoexcitation occurs and thus a vibrational wavepacket, $\Psi(x,t)$, is formed. Therefore, a wavepacket is the linear superposition of several molecular states, which mathematically can be expressed as follows:[33-35]

$$\Psi(x,t) = \sum_{n=1}^{\infty} a_n \psi_n(x,t) = \sum_{n=1}^{\infty} a_n \exp\left(-i\left[\frac{E_n t}{\hbar} + \phi_n\right]\right)\psi_n(x) \qquad (1.1)$$

where ψ_n is the time-independent eigenstate of the Hamiltonian with a specific energy (E_n), amplitude (a_n) and time-dependent phase (φ_n). Following photoexcitation the wavepacket may freely evolve across the corresponding potential energy surface, reflecting a decrease in the amplitude due to the electronic coupling between states and the population transfer to a lower energy states. The pump-probe technique permits to track the temporal evolution of the wavepacket by projecting it to a final state at different time-delays.

1.1.2. Pump-Probe Methods

Pump-probe method forms the basis of the different time-resolved spectroscopic techniques.[27] Since the optoelectronic detectors are not capable of reaching sufficient time-resolutions, ultrashort laser pulses are employed to initiate (synchronously for an ensemble of molecules) and monitor the evolution of processes that occur on subpicosecond (1 ps = 10^{-12} s) time-scale. Figure 1.1 illustrates the general concept of the pump-probe technique in terms of wavepacket dynamics.[36] The method consist on a first pump laser pulse exciting the system to a particular electronic excited state and therefore initiating a photodynamical process, in which the created wavepacket starts to evolve on the potential energy surface. Subsequently, a probe pulse interrogates the system at several time-delays (Δt) making possible to observe the changes on the photophysical and photochemical behavior of the system by monitoring the detected signal with respect to the time-delay between the pump and probe pulses.

In this context, attending to the observable that is detected as pump-probe signal, different fs time-resolved techniques can be distinguished. For example, in the isolated-phase experiments, charged fragments of molecules or free electrons can be detected,[37-44] while in the condensed-phase the change in the absorbance or the emission of the sample after photoexcitation can be measured.[45-47] The fundamentals of the spectroscopic methods employed in this thesis are introduced in the following chapter.

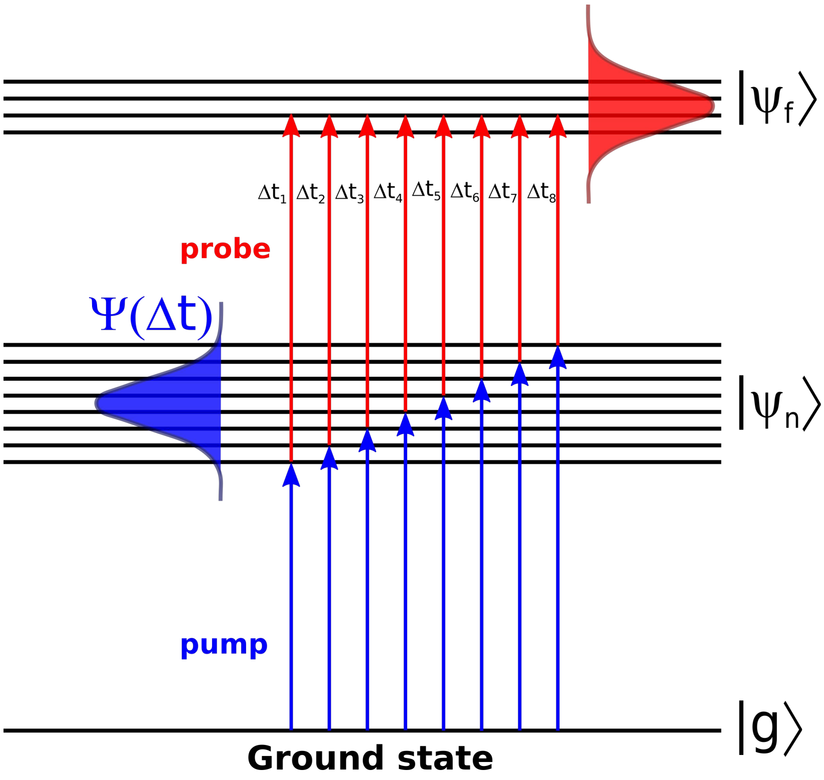

Figure 1.1. *The pump-probe method: The pump pulse creates a wavepacket from the ground state at $t = 0$. Then, the wavepacket is projected onto a specific final state by the probe pulse at different time-delays (Δt), enabling the detection of the molecular event. Figure adapted from reference* 36.

1.1.3. Born-Oppenheimer Approximation

The classical manner to model the dynamics of wavepackets is by employing the Born-Oppenheimer approximation.[48-49] Since the electrons are three orders of magnitude lighter than nuclei ($m_{proton}/m_{electron} \approx 1836$), it can be assumed that the movement of electrons is instantaneous with respect to the time-scale of nuclear motion. Thus, it is possible to separate the electronic and nuclear motions.

The wavefunctions and energies of any molecular system can be described by solving the Schrödinger equation:[50-51]

$$\hat{H}\psi(r,R) = E\psi(r,R) \tag{1.2}$$

where ψ is the wavefuction of the molecule that is a function of both the electron (r) and nuclear (R) coordinates and E is the total energy. The Hamiltonian operator is represented by $\hat{H}$, which is the sum of kinetic and potential energies of the system, as shown in Equation 1.3.

$$\hat{H} = \hat{T}_e + \hat{T}_n + \hat{V}_{en} + \hat{V}_{ee} + \hat{V}_{nn} \tag{1.3}$$

Here, $\hat{T}_e$ and $\hat{T}_n$ are the kinetic energies for the electrons and nuclei, respectively, whereas $\hat{V}_{ee}$ and $\hat{V}_{nn}$ account for the potential energies from the coulombic repulsion between the electrons and between the nuclei, in that order; $\hat{V}_{en}$ represents the potential energy of the electron-nuclei coulombic attraction. It should be noted that other terms such as the spin-orbit coupling (SOC) have been neglected in Equation 1.3 for simplicity.

Since the Born-Oppenheimer approximation separates the nuclear and electronic motion, the total molecular wavefunction can be expressed by:[50-51]

$$\psi(r,R) = \psi_e(r,R)\psi_n(R) \tag{1.4}$$

where ψ_e and ψ_n are the electronic and nuclear components of the molecular wavefuction, respectively. This factorization assumes that the electronic and nuclear terms are decoupled and therefore it is possible to solve the Schrödinger equation for each term, being the total energy of the molecule the sum of the energy corresponding to the nuclear (E_n) and the electronic (E_e) wavefunctions, as shown in Equation 1.5.

$$E = E_n + E_e \tag{1.5}$$

It should be noted that the nuclear wavefunction can be further factorized into vibrational (ψ_v) and rotational (ψ_r) components by means of the rigid rotor approximation:[52]

$$\psi_n(R,\theta,\phi) = \psi_v(R)\psi_r(\theta,\phi) \tag{1.6}$$

Considering this, the electronic Schrödinger equation can be written as:[50-51]

$$\hat{H}_e\psi_e = E_e\psi_e \tag{1.7}$$

where

$$\hat{H}_e = \hat{T}_e + \hat{V}_{en} + \hat{V}_{ee} \tag{1.8}$$

due to the fact that for fixed nuclei $\hat{T}_n$ is zero, and $\hat{V}_{nn}$ is constant.

As $\hat{V}_{en}$ depends on nuclear coordinates, so do ψ_e and E_e, but they can be considered parametric variables because it is assumed that nuclear coordinates are stationary.

On the other hand, the movement of nuclei is described by the nuclear Schrödinger equation, which is given by:[50-51]

$$\hat{H}_n\psi_n = E_n\psi_n \tag{1.9}$$

where

$$\hat{H}_n = \hat{T}_n + \hat{V}_{nn} + E_e \tag{1.10}$$

Consequently, this adiabatic approximation makes possible the construction of a potential energy surface by repeatedly calculating the electronic energy contribution using the electronic Schrödinger equation for the different nuclear configurations. Nonetheless, for polyatomic molecules it is complex to predict the potential energy surfaces because of the many degrees of freedom that exist in a system with a large number of atoms (N). Indeed, in a nonlinear polyatomic molecule $3N$ - 6 coordinates ($3N$ - 5 for linear molecules) are necessary to construct the potential energy surface. For this reason, typically a one-dimensional curve along a specific coordinate, the so-called potential energy cut (PEC), is calculated in order to shed light on the evolution of excited state dynamics and guide the interpretation of time-resolved experiments. The PECs can be empirically constructed by employing potential energy functions, being the Morse potential the preferred function.[53]

1.1.4. Franck-Condon Principle

The Franck-Condon principle explains the intensity distribution of vibrational transitions in the absorption or emission processes.[54-56] The intensity of a transition depends on the population of vibrational levels and is proportional to the square of the transition dipole moment (μ_{if}):[50, 57]

$$I \propto \left|\mu_{if}\right|^2 \tag{1.11}$$

where, the transition dipole moment can be expressed as follows when the Born-Oppenheimer approximation is considered:

$$\mu_{i\to f} = \int \psi_{fe}^{*}\hat{\mu}_e \psi_{ie} d\tau_e \int \psi_{fn}^{*}\psi_{in} d\tau_n \tag{1.12}$$

Here, ψ_i is the wavefunction of the initial state, ψ_f^* represents the complex conjugate of the wavefunction of the final state and $\hat{\mu}_e$ is the electric dipole moment operator. The subscripts *e* and *n* indicate the electronic and nuclear components, respectively.

Thus, the different terms of Equation 1.12 define the selection rules that govern which transitions are allowed, and which are forbidden. Moreover, a transition is formally allowed if all the terms are non-zero. The first integral defines the electronic selection rules, which are derived from the symmetry properties of the electronic states. Actually, an electronic transition occurs if the product between the irreducible representations of the initial state (Γ_i), transition dipole moment (Γ_μ) and final sate (Γ_f) contains the totally symmetric representation of the pertinent point group of the molecule (*A*), as shown in Equation 1.13.[50, 57]

$$\Gamma_i \otimes \Gamma_\mu \otimes \Gamma_f \supseteq A \tag{1.13}$$

Consequently, the electronic selection rule states that transitions between orbitals of the same character are allowed. For example, transitions such as π* ← n or σ* ← π are said to be optically dark, which means that these transitions are very weak, with a low oscillator strength ($f << 1$), and therefore formally forbidden. Contrarily, π* ← π transitions are optically bright ($f \sim 1$). Additionally, for formally allowed transitions the total electron spin multiplicity must remain the same ($\Delta S = 0$) according to the spin selection rule. Therefore, singlet – triplet transitions are formally forbidden unless there is an atom with a high nuclear charge that enables an intense SOC.[50, 57]

The second term in Equation 1.12 is the vibrational overlap integral whose square value is termed the Franck-Condon factor (*S*):[52, 57]

$$\left|S(\upsilon_f, \upsilon_i)\right|^2 = \left|\int \psi_{fn}^{*}\psi_{in} d\tau_n\right|^2 \tag{1.14}$$

According to the Franck-Condon principle, since the electronic transition takes place instantaneously, before any nuclear rearrangement, the most likely vibronic transition occurs to the excited state whose wavefuction has the greatest overlap with the initial state, which is also called Franck-Condon state or vertical transition. Indeed, Figure 1.2

illustrates how, during an electronic transition, the different topologies between the potential energy surfaces of the initial and final electronic states influence the vertical transition. If the potentials of the initial and final electronic states exhibit similar equilibrium nuclear arrangements, the vertical excitation occurs from the $\upsilon = 0$ of the initial electronic state to the $\upsilon' = 0$ of the final electronic excited state, as shown in Figure 1.2a. However, when the minimum energy geometry of the excited state differs from that of the initial state, the preferred transition leads to the population of higher lying vibrational states, as in the case of Figure 1.2b.

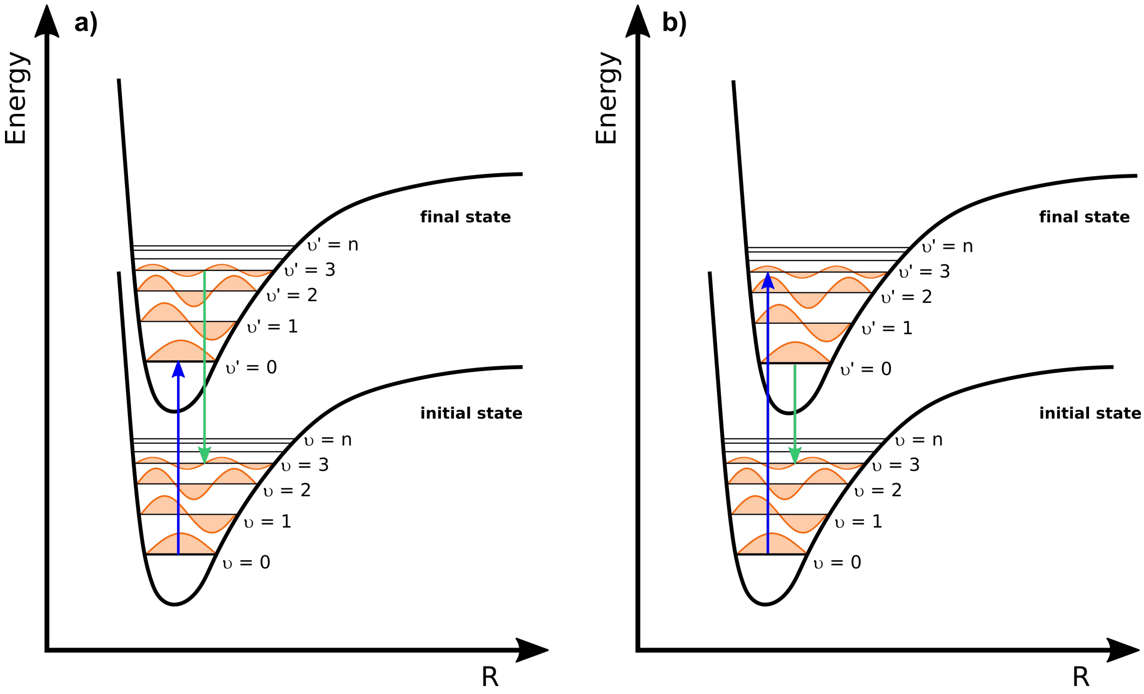

Figure 1.2. *The Franck-Condon principle: The blue arrow represents the vertical excitation from the initial electronic state to the vibrational level of the final excited state with the greatest overlap with the initial state. If the potential energy curves are aligned (a) the most intense absorption corresponds to the* $\upsilon = 0 \rightarrow \upsilon' = 0$ *transition. However, if the potentials are displaced (b), the vertical excitation may preferentially occur to a higher lying vibrational state, which in this case is the* $\upsilon = 0 \rightarrow \upsilon' = 3$ *transition. Similarly, the green arrow denotes the vertical emission.*

1.1.5. Conical Intersections

As already mentioned, the Born-Oppenheimer approximation considers that the electronic and nuclear motions are decoupled, however in some cases this adiabatic approximation breaks down, leading to the appearance of nonadiabatic processes, which exhibit a strong coupling between nuclei and electrons.[58-60] Conical intersections (CIs) are indeed a perfect example of these phenomena. When two or more electronic states become degenerate, the CI is the point of crossing on the potential energy surfaces between the states. It should be noted that a CI is actually an n - 2 dimensional seam, where n is the number of degrees of freedom of the system. This space, in which degeneracy is preserved, is also known as hyperline because it can be seen as an infinite number of connected points.[61-65] Consequently, since in polyatomic systems there are $n = 3N - 6$ nuclear coordinates a $3N - 8$ dimensional subspace is necessary for the formation of a point of degeneracy. Nevertheless, in some cases, a $3N - 8$ dimensional subspace cannot be constructed and therefore an avoided crossing is formed instead of a CI, for example in diatomic systems.

The dimensional subspace where the point of degeneracy is located is termed the branching space (also referred as g-h space) and defines the space in which the degeneracy is lifted. This plane is orthogonal to the n - 2 dimensional seam of CIs. Figure 1.3a depicts a CI in a two dimensional subspace, where the topography of the point of degeneracy can be envisaged as a double-cone shape. Here, g and h are the gradient difference and the derivative coupling vectors, respectively. Whereas the h vector accounts for the strength of the nonadiabatic coupling between the two states, which is inversely proportional to the energy gap between the two electronic states, the g vector represents the steep gradient leading to the point of crossing.[62] Alternatively, the branching vectors can be expressed in terms of normal modes, allowing passage through the intersection region to be interpreted using a vibrational basis.[65] In light of the vibronic-coupling theory, the population transfer between electronic states is achieved through specific vibrational modes: the tuning (g) and coupling (h) modes.[62, 66-67] The former tune the energy gap of two electronic states, while the latter modulate the interstate electronic-vibronic coupling. In this sense, symmetry selection rules play a key role in the identification of the dominant tuning and coupling coordinates and therefore in the characterization of a CI.[62, 66-67]

Although the concept of the CI was defined in the 1930s,[68-70] its relevance in the photochemistry and photophysics of molecular systems was realized at the end of the 1980s with the development of *ab initio* calculations that permitted to compute the potential energy surface and localize the CIs.[61, 71-79] Nowadays, it is widely accepted that many photoinduced phenomena are mediated by the presence of CIs. In this regard, over the past few decades, several studies have established that different CIs govern the photodynamics of aromatic biomolecules,[62, 80-82] enabling the nonradiative population transfer through the coupling of the optically bright $\pi\pi^*$ states with dark states, such as $n\pi^*$ or $\pi\sigma^*$ states, and/or the ground state. These nonradiative transitions occur in sub-ps time-scales, but depends severely on the topology of the implicated potential energy surfaces.

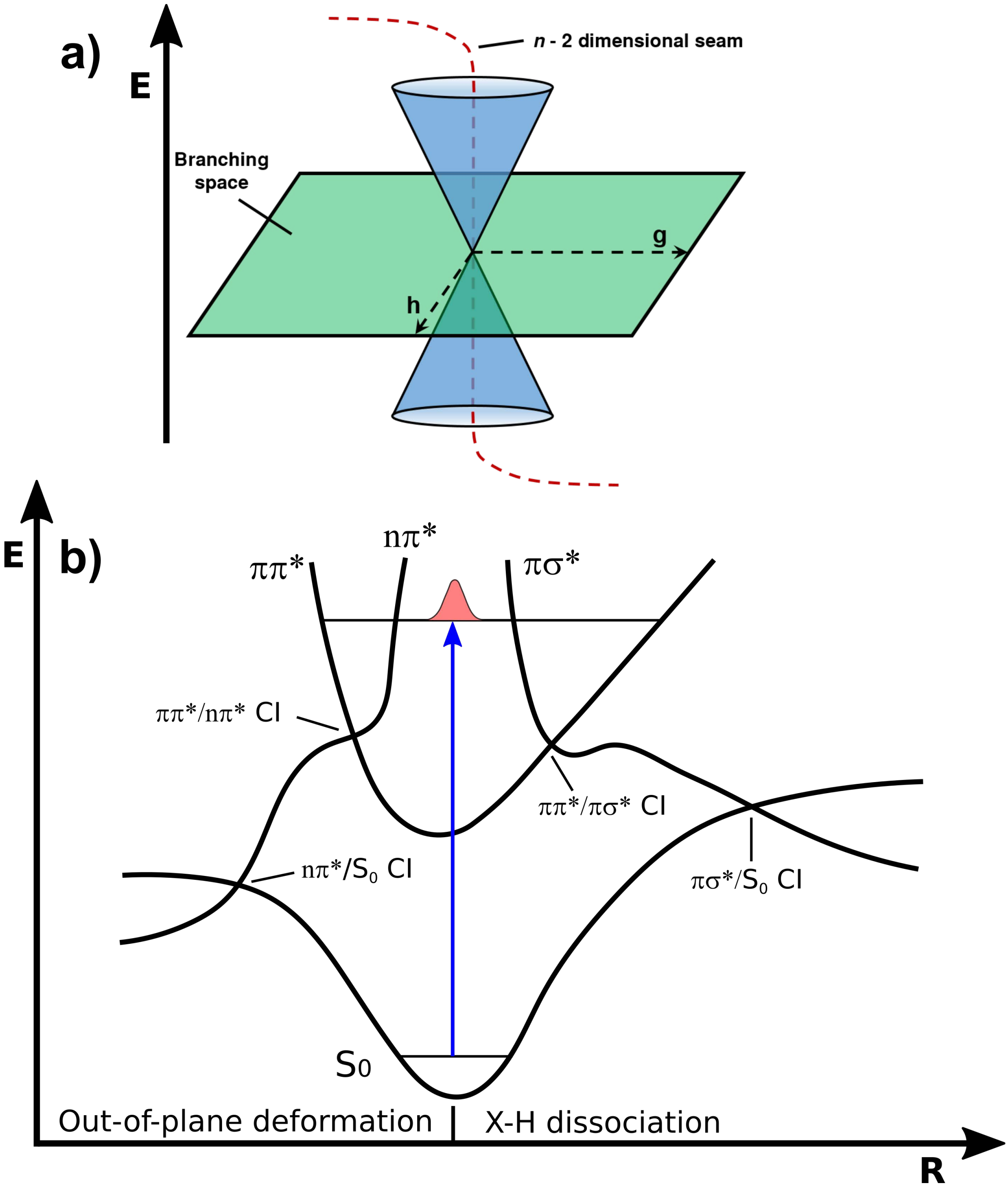

Figure 1.3. *Representation of a conical intersection between two electronic states of same spin multiplicity (a). Cartoon of common conical intersections that can be found in a heteroaromatic molecule (b).*

1.2. Molecular Relaxation Pathways

Following electronic excitation, the system possesses excess energy that needs to dissipate and therefore returns to the ground state by different relaxation mechanisms. The Jablonski diagram[83] in Figure 1.4 summarizes the different decay pathways, which can be categorized into two main groups: Nonradiative and radiative decays. In this section, an overview of the different decay pathways is provided.

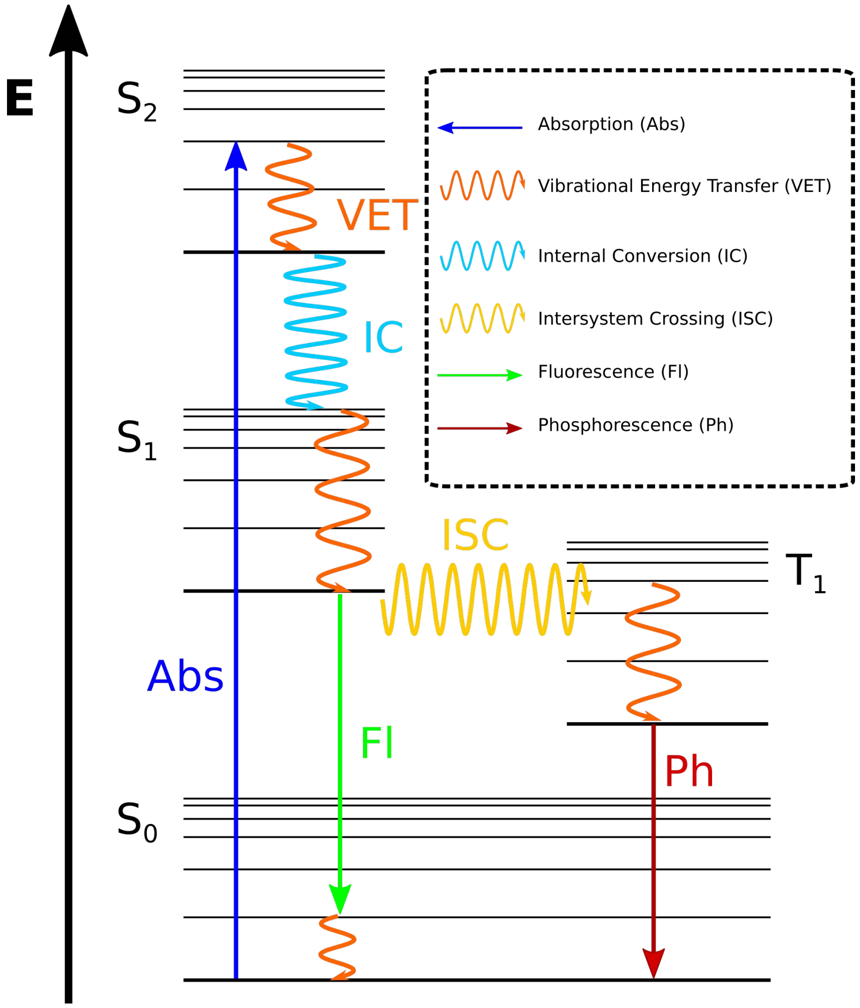

Figure 1.4. *Simplified Jablonski diagram presenting the possible nonradiative and radiative relaxation processes a molecule can undergo after photoexcitation. See the main text for further details.*

1.2.1. Nonradiative Decays

In nonradiative decay pathways, the excited molecule is able to dissipate the energy excess without emitting radiation. There are several nonradiative mechanisms and generally, these relaxation processes take place on the fs – ps time-scale.

1.2.1.1. Vibrational Energy Transfer

Vibrational energy transfer (VET) is a relaxation mechanism that consist on the relaxation from highly energetic vibrational modes to lower modes, within a particular electronic excited state. The nature of this process is different for isolated molecules or in solution. In the gas-phase, since the system conserves the energy, intramolecular vibrational redistribution (IVR) occurs, which implies the vibrational energy transfer across the vibrational modes along a particular reaction coordinate of the molecule. The probability of the transition can be modelled by Fermi's golden rule:[52, 57]

$$k_{NR} = \frac{2\pi}{\hbar} J_{if}^{2} \rho(E_f) \tag{1.15}$$

where k_{NR} is the rate of the transition, which is proportional to the strength of the coupling between states, J_{if}, and to the density of states at the final state energy, $\rho(E_f)$. Thus, IVR is more efficient in large molecules because of their numerous vibrational modes.

On the other hand, in the condensed-phase, the excess energy can also be dissipated as heat to the surrounding solvent molecules, that act as a bath, enabling the cooling of the excited state, and consequently the mechanism is termed intermolecular energy transfer (IET).[84]

1.2.1.2. Internal Conversion

Internal conversion (IC) is a nonradiative population and energy transfer between two electronic states of the same spin multiplicity. The IC mechanism is based on the nonadiabatic coupling of the vibrational modes between an excited state and an energetically lower electronic state, which generally is mediated by a CI.[52] However, nonradiative transitions between two electronic states can also occur in the absence of a CI. The correct coupling between two electronic states depends on symmetric considerations derived from group theory. Indeed, electronic transitions occur through promoting modes, which make possible that the product between the irreducible representations of the initial and final states contains the totally symmetric representation of the pertinent point group of the molecule.[85] The probability for IC is dependent on the energy gap (ΔE) between the electronic states and increases when the energy between the excited states is very low.[86] Therefore, the maximum probability of the transition is when the states become degenerated ($\Delta E = 0$), which accounts for CIs or avoided crossings.

1.2.1.3. Intersystem Crossing

Intersystem crossing (ISC) is a nonradiative transition between two electronic states of different spin multiplicity (for example $S_n \rightarrow T_n$). This process is formally forbidden, however attending to El-Sayed's rule, ISC is a competitive relaxation pathway especially when the energy gap (ΔE) between the singlet and triplet states is small and SOC is high.[87] Indeed, SOC is favored in transitions between states of different symmetry *e.g.* S_1 ($^1n\pi^*$) → T_2 ($^3\pi\pi^*$) ISC. The lifetime of ISC is usually longer than IC, being typically in the time-scale of nanoseconds, although ultrafast ISC has also been reported.[88-90]

1.2.1.4. Photodissociation

In some cases, the relaxation pathway leads to fragmentation of the molecule. This process occurs when the excess energy provided to the molecule upon excitation permits the population of a dissociative electronic state and therefore promotes bond fission, or alternatively, when it exceeds the binding energy of a bound state. A dissociative state has repulsive character along a specific bond coordinate. For example, many heteroaromatic molecules have $\pi\sigma^*$ excited states, which result from the promotion of an electron in a π orbital to a σ^* orbital that possess significant 3s Rydberg character in the Franck-Condon region, but increases its anti-bonding σ^* valence character upon X–H (X = O, N, *etc.*) bond extension. Although these repulsive states are in general optically dark states with low oscillator strength, they can be populated directly after photoexcitation by vibronic coupling to near bright excited states, or indirectly by the conversion from a previously populated state; for example, by the coupling mediated through a CI to a bright $\pi\pi^*$ state.[91-93] In the case of 3s/$\pi\sigma^*$ states, due to the dissociative character that the $\pi\sigma^*$ states acquire upon increasing the X–H distance, they can lead to H atom detachment and ultrafast IC to the ground state *via* a $\pi\sigma^*/S_0$ CI, as shown in Figure 1.3b. The barrier that arises from the Rydberg/valence $\pi\sigma^*$ states is what finally defines the time-scale of the process.

1.2.1.5. Tunneling

All the relaxation pathways described above were explained using the classical view that neglected the quantum tunneling. In the classical description, when the population encounters an energy barrier along the potential energy surface and there is not enough energy to surmount it, the relaxation pathway is inaccessible. However, the tunneling effect allows for a wavepacket passing through the barrier without possessing the required energy because the probability of finding a molecule on the other side of the barrier is non-zero. The rate of tunneling depends exponentially on both the mass of the tunneling specie and the size of the barrier.[52] Consequently, short tunneling lifetimes are only observed for light particles such as electrons or protons, through small barriers.

1.2.2. Radiative Decays

In radiative pathways, the relaxation to the ground state from an electronic excited state implies the emission of a photon. There are two main radiative mechanisms: fluorescence (Fl) and phosphorescence (Ph), which usually occur on longer time-scales than nonradiative mechanisms. While the former takes place on the nanosecond-microsecond time-scale, the latter may exhibit lifetimes of up to several seconds.

1.2.2.1. Fluorescence

In fluorescence, the radiative transition occurs between two electronic states with same spin multiplicity. In general, fluorescence take place after thermal relaxation (VET) of the excited state, which results on a redshift in the emission spectrum with respect to the absorption spectrum because the energy of the emission is less than the energy absorbed by the molecule. This phenomenon is known as the Stokes shift and can be further promoted by other mechanisms such as solvent effect, excited state reactions or complex formations.[47]

1.2.2.2. Phosphorescence

When the emission process is between states of different spin multiplicity, the radiative pathway is termed phosphorescence. For example, this transition occurs after the triplet manifold is populated through ISC prior to its radiative decay to the ground state. Since the $T_n \rightarrow S_0$ transition is forbidden, the lifetime of the process is several orders of magnitude slower than fluorescence ($\tau_{Ph} > 10^{-3}$ s).[47, 52]

1.3. Photostability

The origin of life on Earth remains unknown and is one of the major challenges for the scientific community. The most extended hypothesis implies a chemical evolution process, where a few prebiotic biomolecules were selected as precursors of the actual nucleobases and life building blocks, as shown in Figure 1.5. In the early-biotic ages, the ultraviolet (UV) radiation levels on Earth’s surface were much higher than the present ones, because the ozone layer was not formed yet and therefore it is suggested that the prebiotic precursors were aromatic molecules able to resist under intense UV irradiation conditions.[94-97] Consequently, these molecules were required to be photostable, which is the capability to dissipate efficiently the absorbed excess energy to the surroundings in the form of heat (vibrational energy) and without detriment to their integrity. In principle, it is thought that this could be achieved through nonradiative relaxation pathways because their short excited state lifetimes, in contrast to the long-lived radiative decays, prevent molecules from photochemical reactions leading to the eventual formation of harmful photoproducts.[98-99]

In the last twenty years, several experimental and computational research groups have been studying the photophysical properties of nucleobases and their derivatives, observing that these molecules generally show very low fluorescence quantum yields and ultrashort excited state lifetimes, which can be linked to the accessibility to efficient nonradiative relaxation pathways. Indeed, the main deactivation mechanism in nucleobases occurs through ultrafast IC to the ground state.[98, 100]

For the canonical pyrimidines, part of the population undergoes ultrafast IC to the ground state through a $\pi\pi^*/S_0$ CI, which can be accessed by motion along a deformation coordinate that involves the $C_5{=}C_6$ bond. The remaining population decays to an $n\pi^*$ state before completing IC to the ground state or decaying to the lowest triplet state through ISC.[98, 100-105] For the purine nucleobases, adenine and guanine, the main relaxation channel implies a $\pi\pi^*/S_0$ CI involving out-of-plane motion (ring puckering) along the C_2-N_3 bond.[98, 100-106] However, the topology of the excited states potential energy surfaces, which ultimately depends on the molecular structure,[107] determines the accessibility to the CIs responsible of the photophysical behavior of the molecules and thus, their photostability. This seems to explain why the photodynamics between some nucleobases and their derivatives or even their tautomers differ so much.[100-101, 105, 108-109]

Aiming to understand the role that photoexcitation has played in the choice of some specific molecules to sustain life, the bottom-up approach has emerged as a valid tool to unravel not only the key structural factors that control the rapid deactivation of these molecules, but also to improve our knowledge on more complex and biologically relevant systems. Since large molecules exhibit a higher number of electronic and nuclear coordinates, the interpretation of the experimental results is obviously more difficult. For this reason, it is preferable to start studying the photophysics of simple chromophores, and then systematically increase the complexity of the systems, including additional substituents and/or the interaction with solvent molecules.

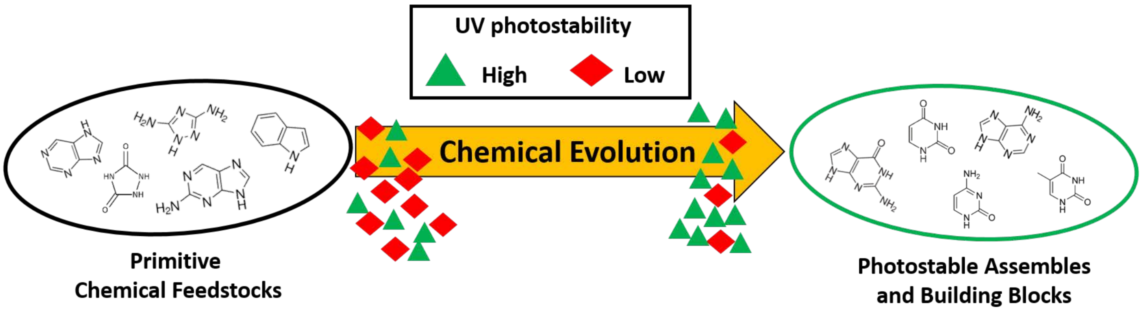

Figure 1.5. *Cartoon of chemical evolution: The canonical nucleobases (structures in green circle) were preceded by alternative UV photostable aromatic molecules.*

1.4. Photoprotection

Overexposure to UV radiation has been demonstrated to have severe effects on different biomolecules, leading to changes in the molecular structure and promoting the formation of free radicals, which in the case of humans can be translated in health problems such as erythema, DNA mutation and skin cancers (carcinomas and melanomas).[110-114] In order to reduce these damaging effects, humans, among other forms of life, have developed photoprotective mechanisms driven by UV absorbing molecules termed melanins. These pigments with high photostability can be further divided into eumelanin, pheomelanin and neuromelanin. While the latter is only found in the brain, eumelanin and pheomelanin are in the human skin and thus are the main photoprotectors against UV radiation. Nonetheless, the photoprotection level of each person is regulated by melanogenesis, which is a gene response that adapts the production of melanin according to the UV exposure. Since melanogenesis is not an instant process, it may take 3-5 days for producing extra melanin, photodamage can occur if the skin is insufficiently protected. Furthermore, recently has been reported that eumelanins are potentially phototoxic after long-term exposure to UV-A radiation.[115]

For this reason, there has been a growing interest on artificial sunscreens, particularly on those synthetic compounds able to mimic the photophysical behavior of natural UV filters. In commercial sunscreens, two categories can be distinguished attending to the UV active components: physical blockers and chemical absorbers. The former group are in general inorganic nanoparticles, typically of titanium dioxide (TiO_2) or zinc oxide (ZnO) that scatter the UV radiation, whereas the latter are photostable molecules with high absorption rates along the UV-A/UV-B region that are capable of relaxing back to the ground state through nonradiative pathways. In order to ensure an efficient photoprotection across the entire UV-A/UV-B region, different organic filters are mixed on a commercial sunscreen, together with other important ingredients that control the texture, ease of application, color, odour or water resistance.[113]

However, the photostability and safety of commercial sunscreens has been subject of debate, since some works revealed the photoallergic potential of some UV filters such as benzophenone derivatives.[116] Moreover, recent time-resolved experiments have showed the formation of long-lived photoproducts due to photoisomerization processes for some sinapate and cinnamates derivatives.[112-114] Consequently, in an effort to unravel the photophysical mechanisms that control the photodynamics of these molecules and having the future generation of UV filters in sighs, further research on appropriate structural modifications and on the role of the solvent is required for the development of novel efficient sunscreens.

1.5. Objectives

The main aim of the present thesis is to understand the photophysical and photochemical relaxation pathways available in biologically relevant molecules and to evaluate how the modulations introduced by structural changes and/or intermolecular interactions influence their photochemistry/photophysics. The molecular systems investigated present aromatic chromophores that can be efficiently photoexcited along intense $\pi\pi^*$ transitions, providing them the ability to absorb radiation in the near UV region. For these systems, Nature has selected specific deactivation channels according to their roles in the machinery in life. In this scenario, pushing forward the boundaries of knowledge on the photodynamical behavior of chromophoric biomolecules is essential to understand their functions and perhaps their origin, making possible at the same time, the rational design of synthetic systems capable of mimicking their properties.

The first motifs studied were azaindoles, which are considered structural precursors of purine bases. Identifying the crucial role of structural factors and the surrounding environment on the relaxation mechanisms of this family is a key step to understand how life evolution selected adenine and guanine as canonical DNA bases.

Secondly, in order to address the influence of the intermolecular interactions that chromophores establish with solvent and/or other chromophoric molecules, two type of model systems were investigated in this thesis: multi-chromophore molecular clusters containing simple aromatic chromophores such as pyrroles or anilines, and the pyrrole-water aggregate. The goal in the former systems is to understand how the electronic excitation and relaxation works in species where several chromophoric units are present, while in the latter the research is focused on obtaining detailed information on the role that solvent molecules play in the photodyanamics of pyrrole.

Finally, the photodynamical behavior of synthetic UV sunscreening agents was studied in the context of a collaboration with a group from the field of synthetic organic chemistry. Understanding how these kind of molecules are able to release the absorbed energy in a non-detrimental way sheds light on evaluating their photoprotective capability.

1.6. Thesis Overview

The remaining parts of the present thesis are organized in the following way:

Chapter 2 explains the details of the different experimental setups employed to conduct the gas- and condensed-phase measurements presented in the ensuing chapters. Chapter 3 explores the ultrafast photodynamics of a set of azaindole structural isomers in the isolated-phase. Then, Chapter 4 increases the complexity of the system by studying the photophysical behavior of azaindoles in solution and compares the differences observed with respect to the gas-phase experiments. Chapter 5 provides an understanding of ion-dip methodology and shows the dynamical signature of particular size pyrrole-containing clusters. In this sense, the photophysical behavior of homo- and heteroclusters between pyrrole and N-methylpyrrole molecules have been investigated. Additionally, the effect of the inclusion of a water molecule on the photodynamics of isolated pyrrole has also been studied. Chapter 6 presents the results and conclusions for the research conducted to unravel the excited state dynamics of aniline homoclusters. Chapter 7 focuses on the nonradiative deactivation of a family of synthetic sunscreens in order to elucidate its potential photoprotective behavior. Finally, Chapter 8 presents the overall conclusions from the studies presented in this thesis and a brief outlook for future works.

1.7. References

1. Laidler, K. J., The development of the Arrhenius equation. *Journal of chemical Education* **1984,** *61* (6), 494.

2. Bohr, N., I. On the constitution of atoms and molecules. *The London, Edinburgh, and Dublin Philosophical Magazine and Journal of Science* **1913,** *26* (151), 1-25.

3. MacKinnon, E., De Broglie's thesis: A critical retrospective. *American Journal of Physics* **1976,** *44* (11), 1047-1055.

4. Heisenberg, W., Über den anschaulichen Inhalt der quantentheoretischen Kinematik und Mechanik. *Zeitschrift für Physik* **1927,** *43* (3), 172-198.

5. Eyring, H.; Polanyi, M., On Simple Gas Reactions. *Zeitschrift für Physikalische Chemie* **2013,** *227* (11), 1221-1246.

6. Laidler, K. J.; King, M. C., Development of transition-state theory. *The Journal of Physical Chemistry* **1983,** *87* (15), 2657-2664.

7. Norrish, R. G. W.; Porter, G., Chemical Reactions Produced by Very High Light Intensities. *Nature* **1949,** *164* (4172), 658-658.

8. Porter, G.; Norrish, R. G. W., Flash photolysis and spectroscopy. A new method for the study of free radical reactions. *Proceedings of the Royal Society of London. Series A. Mathematical and Physical Sciences* **1950,** *200* (1061), 284-300.

9. Maiman, T. H., Stimulated Optical Radiation in Ruby. *Nature* **1960,** *187* (4736), 493-494.

10. Shank, C. V.; Ippen, E. P., Subpicosecond kilowatt pulses from a mode-locked cw dye laser. *Applied Physics Letters* **1974,** *24* (8), 373-375.

11. Scherer, N. F.; Knee, J. L.; Smith, D. D.; Zewail, A. H., Femtosecond Photofragment Spectroscopy: The Reaction ICN → CN + I. *The Journal of Physical Chemistry* **1985,** *89* (24), 5141-5143.

12. Dantus, M.; Rosker, M. J.; Zewail, A. H., Femtosecond real-time probing of reactions. II. The dissociation reaction of ICN. *The Journal of Chemical Physics* **1988,** *89* (10), 6128-6140.

13. Rosker, M. J.; Rose, T. S.; Zewail, A. H., Femtosecond real-time dynamics of photofragment-trapping resonances on dissociative potential energy surfaces. *Chemical Physics Letters* **1988,** *146* (3), 175-179.

14. Rose, T. S.; Rosker, M. J.; Zewail, A. H., Femtosecond real-time probing of reactions. IV. The reactions of alkali halides. *The Journal of Chemical Physics* **1989,** *91* (12), 7415-7436.

15. Cong, P.; Roberts, G.; Herek, J. L.; Mohktari, A.; Zewail, A. H., Femtosecond Real-Time Probing of Reactions. 18. Experimental and Theoretical Mapping of Trajectories and Potentials in the NaI Dissociation Reaction. *The Journal of Physical Chemistry* **1996,** *100* (19), 7832-7848.

16. Yan, Y.; Whitnell, R. M.; Wilson, K. R.; Zewail, A. H., Femtosecond chemical dynamics in solution. Wavepacket evolution and caging of I2. *Chemical Physics Letters* **1992,** *193* (5), 402-412.

17. Lienau, C.; Zewail, A. H., Solvation Ultrafast Dynamics of Reactions. 11. Dissociation and Caging Dynamics in the Gas-to-Liquid Transition Region. *The Journal of Physical Chemistry* **1996,** *100* (48), 18629-18649.

18. Dantus, M.; Bowman, R. M.; Gruebele, M.; Zewail, A. H., Femtosecond real-time probing of reactions. V. The reaction of IHgI. *The Journal of Chemical Physics* **1989,** *91* (12), 7437-7450.

19. Mokhtari, A.; Cong, P.; Herek, J. L.; Zewail, A. H., Direct femtosecond mapping of trajectories in a chemical reaction. *Nature* **1990,** *348* (6298), 225-227.

20. Sims, I. R.; Gruebele, M.; Potter, E. D.; Zewail, A. H., Femtosecond real-time probing of reactions. VIII. The bimolecular reaction Br+I2. *The Journal of Chemical Physics* **1992,** *97* (6), 4127-4148.

21. Herek, J. L.; Pedersen, S.; Bañares, L.; Zewail, A. H., Femtosecond real-time probing of reactions. IX. Hydrogen-atom transfer. *The Journal of Chemical Physics* **1992,** *97* (12), 9046-9061.

22. Janssen, M. H. M.; Dantus, M.; Guo, H.; Zewail, A. H., Femtosecond reaction dynamics of Rydberg states. Methyl iodide. *Chemical Physics Letters* **1993,** *214* (3), 281-289.

23. Cheng, P. Y.; Zhong, D.; Zewail, A. H., Transition states of charge-transfer reactions: Femtosecond dynamics and the concept of harpooning in the bimolecular reaction of benzene with iodine. *The Journal of Chemical Physics* **1995,** *103* (12), 5153-5156.

24. Baskin, J. S.; Bañares, L.; Pedersen, S.; Zewail, A. H., Femtosecond Real-Time Probing of Reactions. 20. Dynamics of Twisting, Alignment, and IVR in the trans-Stilbene Isomerization Reaction. *The Journal of Physical Chemistry* **1996,** *100* (29), 11920-11933.

25. Motzkus, M.; Pedersen, S.; Zewail, A. H., Femtosecond Real-Time Probing of Reactions. 19. Nonlinear (DFWM) Techniques for Probing Transition States of Uni- and Bimolecular Reactions. *The Journal of Physical Chemistry* **1996,** *100* (14), 5620-5633.

26. Diau, E. W.-G.; Feyter, S. D.; Zewail, A. H., Direct observation of the femtosecond nonradiative dynamics of azulene in a molecular beam: The anomalous behavior in the isolated molecule. *The Journal of Chemical Physics* **1999,** *110* (20), 9785-9788.

27. Zewail, A. H., Femtochemistry: Atomic-Scale Dynamics of the Chemical Bond. *The Journal of Physical Chemistry A* **2000,** *104* (24), 5660-5694.

28. L'Huillier, A.; Balcou, P., High-order harmonic generation in rare gases with a 1-ps 1053-nm laser. *Physical Review Letters* **1993,** *70* (6), 774-777.

29. Christov, I. P.; Murnane, M. M.; Kapteyn, H. C., High-Harmonic Generation of Attosecond Pulses in the ``Single-Cycle" Regime. *Physical Review Letters* **1997,** *78* (7), 1251-1254.

30. Paul, P. M.; Toma, E. S.; Breger, P.; Mullot, G.; Augé, F.; Balcou, P.; Muller, H. G.; Agostini, P., Observation of a Train of Attosecond Pulses from High Harmonic Generation. *Science* **2001,** *292* (5522), 1689.

31. Hentschel, M.; Kienberger, R.; Spielmann, C.; Reider, G. A.; Milosevic, N.; Brabec, T.; Corkum, P.; Heinzmann, U.; Drescher, M.; Krausz, F., Attosecond metrology. *Nature* **2001,** *414* (6863), 509-513.

32. Rulliere, C., *Femtosecond laser pulses*. Springer: 2005.

33. Heller, E. J., Time dependent variational approach to semiclassical dynamics. *The Journal of*

Chemical Physics **1976,** *64* (1), 63-73.

34. Abramczyk, H., *Introduction to laser spectroscopy*. Elsevier: 2005.

35. Wu, G.; Hockett, P.; Stolow, A., Time-resolved photoelectron spectroscopy: from wavepackets to observables. *Physical Chemistry Chemical Physics* **2011,** *13* (41), 18447-18467.

36. Stolow, A., Femtosecond Time-Resolved Photoelectron Spectroscopy of Polyatomic Molecules. *Annual Review of Physical Chemistry* **2003,** *54* (1), 89-119.

37. Antonov, V. S.; Knyazev, I. N.; Letokhov, V. S.; Matiuk, V. M.; Movshev, V. G.; Potapov, V. K., Stepwise laser photoionization of molecules in a mass spectrometer: a new method for probing and detection of polyatomic molecules. *Optics Letters* **1978,** *3* (2), 37-39.

38. Rosker, M. J.; Dantus, M.; Zewail, A. H., Femtosecond real-time probing of reactions. I. The technique. *The Journal of Chemical Physics* **1988,** *89* (10), 6113-6127.

39. Eppink, A. T. J. B.; Parker, D. H., Velocity map imaging of ions and electrons using electrostatic lenses: Application in photoelectron and photofragment ion imaging of molecular oxygen. *Review of Scientific Instruments* **1997,** *68* (9), 3477-3484.

40. Reid, K. L., Photoelectron Angular Distributions. *Annual Review of Physical Chemistry* **2003,** *54* (1), 397-424.

41. Roberts, G. M.; Nixon, J. L.; Lecointre, J.; Wrede, E.; Verlet, J. R. R., Toward real-time charged-particle image reconstruction using polar onion-peeling. *Review of Scientific Instruments* **2009,** *80* (5), 053104.

42. Suits, A. G.; Continetti, R. E., Imaging in Chemical Dynamics: The State of the Art. In *Imaging in Chemical Dynamics*, American Chemical Society: 2000; Vol. 770, pp 1-18.

43. Stolow, A.; Bragg, A. E.; Neumark, D. M., Femtosecond Time-Resolved Photoelectron Spectroscopy. *Chemical Reviews* **2004,** *104* (4), 1719-1758.

44. Seel, M.; Domcke, W., Model studies on femtosecond time-resolved ionization spectroscopy of excited-state vibrational dynamics and vibronic coupling. *Chemical Physics* **1991,** *151* (1), 59-72.

45. Beechem, J. M.; Brand, L., Time-Resolved Fluorescence of Protein. *Annual Review of Biochemistry* **1985,** *54* (1), 43-71.

46. Shah, J., Ultrafast luminescence spectroscopy using sum frequency generation. *IEEE Journal of Quantum Electronics* **1988,** *24* (2), 276-288.

47. Lakowicz, J. R., *Principles of fluorescence spectroscopy*. Springer science & business media: 2013.

48. Born, M.; Oppenheimer, R., Zur Quantentheorie der Molekeln. *Annalen der Physik* **1927,** *389* (20), 457-484.

49. Eckart, C., The Kinetic Energy of Polyatomic Molecules. *Physical Review* **1934,** *46* (5), 383-387.

50. Hollas, J. M., *Modern spectroscopy*. 4th ed. ed.; J. Wiley: Chichester ;, 2004.

51. Levine, I. N., *Quantum chemistry*. 7th ed. ed.; Pearson: [Boston], 2014.

52. Atkins, P. W.; Paula, J. d., *Atkins' Physical Chemistry*. 9th ed. ed.; Oxford University Press: Oxford, 2010.

53. Murrell, J. N., *Molecular potential energy functions*. J. Wiley: Chichester [West Sussex]; New York, 1984.

54. Franck, J.; Dymond, E., Elementary processes of photochemical reactions. *Transactions of the Faraday Society* **1926,** *21* (February), 536-542.

55. Condon, E., A Theory of Intensity Distribution in Band Systems. *Physical Review* **1926,** *28* (6), 1182-1201.

56. Condon, E. U., Nuclear Motions Associated with Electron Transitions in Diatomic Molecules. *Physical Review* **1928,** *32* (6), 858-872.

57. Requena Rodríguez, A.; Zúñiga Román, J., *Espectroscopía*. Pearson Educación: Madrid, 2003.

58. Garraway, B. M.; Suominen, K. A., Wave-packet dynamics: new physics and chemistry in femto-time. *Reports on Progress in Physics* **1995,** *58* (4), 365-419.

59. Worth, G. A.; Cederbaum, L. S., Beyond Born-Oppenheimer: Molecular Dynamics Through a Conical Intersection. *Annual Review of Physical Chemistry* **2004,** *55* (1), 127-158.

60. Jasper, A. W.; Zhu, C.; Nangia, S.; Truhlar, D. G., Introductory lecture: Nonadiabatic effects in chemical dynamics. *Faraday Discussions* **2004,** *127* (0), 1-22.

61. Yarkony, D. R., Conical Intersections: The New Conventional Wisdom. *The Journal of Physical Chemistry A* **2001,** *105* (26), 6277-6293.

62. Domcke, W.; Yarkony, D.; Köppel, H., *Conical intersections: electronic structure, dynamics & spectroscopy*. World Scientific: 2004; Vol. 15.

63. Matsika, S.; Krause, P., Nonadiabatic Events and Conical Intersections. *Annual Review of Physical Chemistry* **2011,** *62* (1), 621-643.

64. Domcke, W.; Yarkony, D. R., Role of Conical Intersections in Molecular Spectroscopy and Photoinduced Chemical Dynamics. *Annual Review of Physical Chemistry* **2012,** *63* (1), 325-352.

65. Schuurman, M. S.; Stolow, A., Dynamics at Conical Intersections. *Annual Review of Physical Chemistry* **2018,** *69* (1), 427-450.

66. Köppel, H.; Domcke, W.; Cederbaum, L. S., Multimode molecular dynamics beyond the Born-Oppenheimer approximation. *Advances in chemical physics* **1984,** *57*, 59-246.

67. Domcke, W.; Stock, G., Theory of Ultrafast Nonadiabatic Excited-State Processes and their Spectroscopic Detection in Real Time. In *Advances in Chemical Physics*, 1997; pp 1-169.

68. Hund, F., Zur deutung der molekelspektren. I. *Zeitschrift für Physik* **1927,** *40* (10), 742-764.

69. von Neuman, J.; Wigner, E., Uber merkwürdige diskrete Eigenwerte. Uber das Verhalten von Eigenwerten bei adiabatischen Prozessen. *Physikalische Zeitschrift* **1929,** *30*, 467.

70. Teller, E., The Crossing of Potential Surfaces. *The Journal of Physical Chemistry* **1937,** *41* (1), 109-116.

71. Koga, N.; Morokuma, K., Determination of the lowest energy point on the crossing seam between two potential surfaces using the energy gradient. *Chemical Physics Letters* **1985,** *119* (5), 371-374.

72. Bonačić-Koutecký, V.; Koutecký, J.; Michl, J., Neutral and Charged Biradicals, Zwitterions, Funnels in S1, and Proton Translocation: Their Role in Photochemistry, Photophysics, and Vision. *Angewandte Chemie International Edition in English* **1987,** *26* (3), 170-189.

73. Yarkony, D. R., Diabolical conical intersections. *Reviews of Modern Physics* **1996,** *68* (4), 985-1013.

74. Yarkony, D. R., Conical Intersections: Diabolical and Often Misunderstood. *Accounts of Chemical Research* **1998,** *31* (8), 511-518.

75. Farazdel, A.; Dupuis, M., On the determination of the minimum on the crossing seam of two potential energy surfaces. *Journal of Computational Chemistry* **1991,** *12* (2), 276-282.

76. Atchity, G. J.; Xantheas, S. S.; Ruedenberg, K., Potential energy surfaces near intersections. *The Journal of Chemical Physics* **1991,** *95* (3), 1862-1876.

77. Bernardi, F.; Olivucci, M.; Robb, M. A., Potential energy surface crossings in organic photochemistry. *Chemical Society Reviews* **1996,** *25* (5), 321-328.

78. Zilberg, S.; Haas, Y., Molecular Photochemistry: A General Method for Localizing Conical Intersections Using the Phase-Change Rule. *Chemistry – A European Journal* **1999,** *5* (6), 1755-1765.

79. Levine, B. G.; Coe, J. D.; Martínez, T. J., Optimizing Conical Intersections without Derivative Coupling Vectors: Application to Multistate Multireference Second-Order Perturbation Theory (MS-CASPT2). *The Journal of Physical Chemistry B* **2008,** *112* (2), 405-413.

80. Robb, M. A.; Garavelli, M.; Olivucci, M.; Bernardi, F., A Computational Strategy for Organic Photochemistry. In *Reviews in Computational Chemistry*, 2000; pp 87-146.

81. Olivucci, M., *Computational photochemistry*. Elsevier: 2005.

82. Improta, R.; Santoro, F.; Blancafort, L., Quantum Mechanical Studies on the Photophysics and the Photochemistry of Nucleic Acids and Nucleobases. *Chemical Reviews* **2016,** *116* (6), 3540-3593.

83. Jablonski, A., Efficiency of Anti-Stokes Fluorescence in Dyes. *Nature* **1933,** *131* (3319), 839-840.

84. Rosspeintner, A.; Lang, B.; Vauthey, E., Ultrafast Photochemistry in Liquids. *Annual Review of Physical Chemistry* **2013,** *64* (1), 247-271.

85. Kuhlman, T. S.; Sauer, S. P. A.; Sølling, T. I.; Møller, K. B., Symmetry, vibrational energy redistribution and vibronic coupling: The internal conversion processes of cycloketones. *The Journal of Chemical Physics* **2012,** *137* (22), 22A522.

86. Englman, R.; Jortner, J., The energy gap law for radiationless transitions in large molecules. *Molecular Physics* **1970,** *18* (2), 145-164.

87. El-Sayed, M. A., Spin—Orbit Coupling and the Radiationless Processes in Nitrogen Heterocyclics. *The Journal of Chemical Physics* **1963,** *38* (12), 2834-2838.

88. Minns, R. S.; Parker, D. S. N.; Penfold, T. J.; Worth, G. A.; Fielding, H. H., Competing ultrafast intersystem crossing and internal conversion in the “channel 3” region of benzene. *Physical Chemistry Chemical Physics* **2010,** *12* (48), 15607-15615.

89. Zobel, J. P.; Nogueira, J. J.; González, L., Mechanism of Ultrafast Intersystem Crossing in 2-Nitronaphthalene. *Chemistry – A European Journal* **2018,** *24* (20), 5379-5387.

90. Mewes, L.; Ingle, R. A.; Megow, S.; Böhnke, H.; Baranoff, E.; Temps, F.; Chergui, M., Ultrafast Intersystem Crossing and Structural Dynamics of [Pt(ppy)(μ-tBu2pz)]2. *Inorganic Chemistry* **2020,** *59* (20), 14643-14653.

91. Paterson, M. J.; Townsend, D., Rydberg-to-valence evolution in excited state molecular dynamics. *International Reviews in Physical Chemistry* **2020,** *39* (4), 517-567.

92. Ashfold, M. N. R.; King, G. A.; Murdock, D.; Nix, M. G. D.; Oliver, T. A. A.; Sage, A. G., πσ* excited states in molecular photochemistry. *Physical Chemistry Chemical Physics* **2010,** *12* (6), 1218-1238.

93. Roberts, G. M.; Stavros, V. G., The role of πσ* states in the photochemistry of heteroaromatic biomolecules and their subunits: insights from gas-phase femtosecond spectroscopy. *Chemical Science* **2014,** *5* (5), 1698-1722.

94. Sagan, C., Ultraviolet selection pressure on the earliest organisms. *Journal of Theoretical Biology* **1973,** *39* (1), 195-200.

95. Joyce, G. F., RNA evolution and the origins of life. *Nature* **1989,** *338* (6212), 217-224.

96. Beckstead, A. A.; Zhang, Y.; de Vries, M. S.; Kohler, B., Life in the light: nucleic acid photoproperties as a legacy of chemical evolution. *Physical Chemistry Chemical Physics* **2016,** *18* (35), 24228-24238.

97. Rios, A. C.; Tor, Y., On the Origin of the Canonical Nucleobases: An Assessment of Selection Pressures across Chemical and Early Biological Evolution. *Israel Journal of Chemistry* **2013,** *53* (6-7), 469-483.

98. Middleton, C. T.; Harpe, K. d. L.; Su, C.; Law, Y. K.; Crespo-Hernández, C. E.; Kohler, B., DNA Excited-State Dynamics: From Single Bases to the Double Helix. *Annual Review of Physical Chemistry* **2009,** *60* (1), 217-239.

99. Gustavsson, T.; Improta, R.; Markovitsi, D., DNA/RNA: Building Blocks of Life Under UV Irradiation. *The Journal of Physical Chemistry Letters* **2010,** *1* (13), 2025-2030.

100. Barbatti, M.; Borin, A. C.; Ullrich, S., Photoinduced Phenomena in Nucleic Acids I: Nucleobases in the Gas Phase and in Solvents. Springer: Cham, 2015.

101. Crespo-Hernández, C. E.; Cohen, B.; Hare, P. M.; Kohler, B., Ultrafast Excited-State Dynamics in Nucleic Acids. *Chemical Reviews* **2004,** *104* (4), 1977-2020.

102. Saigusa, H., Excited-state dynamics of isolated nucleic acid bases and their clusters. *Journal of Photochemistry and Photobiology C: Photochemistry Reviews* **2006,** *7* (4), 197-210.

103. Shukla, M. K.; Leszczynski, J., Electronic Spectra, Excited State Structures and Interactions of Nucleic Acid Bases and Base Assemblies: A Review. *Journal of Biomolecular Structure and Dynamics* **2007,** *25* (1), 93-118.

104. Barbatti, M.; Aquino, A. J. A.; Szymczak, J. J.; Nachtigallová, D.; Hobza, P.; Lischka, H., Relaxation mechanisms of UV-photoexcited DNA and RNA nucleobases. *Proceedings of the National Academy of Sciences* **2010,** *107* (50), 21453.

105. Kleinermanns, K.; Nachtigallová, D.; de Vries, M. S., Excited state dynamics of DNA bases. *International Reviews in Physical Chemistry* **2013,** *32* (2), 308-342.

106. Marchetti, B.; Karsili, T. N. V.; Ashfold, M. N. R.; Domcke, W., A 'bottom up', ab initio computational approach to understanding fundamental photophysical processes in nitrogen containing heterocycles, DNA bases and base pairs. *Physical Chemistry Chemical Physics* **2016,** *18* (30), 20007-20027.

107. Otterstedt, J. E. A., Photostability and molecular structure. *The Journal of Chemical Physics* **1973,** *58* (12), 5716-5725.

108. Kobayashi, T.; Kuramochi, H.; Harada, Y.; Suzuki, T.; Ichimura, T., Intersystem Crossing to Excited Triplet State of Aza Analogues of Nucleic Acid Bases in Acetonitrile. *The Journal of Physical Chemistry A* **2009,** *113* (44), 12088-12093.

109. Crespo-Hernández, C. E.; Martínez-Fernández, L.; Rauer, C.; Reichardt, C.; Mai, S.; Pollum, M.; Marquetand, P.; González, L.; Corral, I., Electronic and Structural Elements That Regulate the Excited-State Dynamics in Purine Nucleobase Derivatives. *Journal of the American Chemical Society* **2015,** *137* (13), 4368-4381.

110. Sinha, R. P.; Häder, D.-P., UV-induced DNA damage and repair: a review. *Photochemical & Photobiological Sciences* **2002,** *1* (4), 225-236.

111. Dahle, J.; Kvam, E., Induction of Delayed Mutations and Chromosomal Instability in Fibroblasts after UVA-, UVB-, and X-Radiation. *Cancer Research* **2003,** *63* (7), 1464.

112. Rodrigues, N. D. N.; Staniforth, M.; Stavros, V. G., Photophysics of sunscreen molecules in the gas phase: a stepwise approach towards understanding and developing next-generation sunscreens. *Proceedings of the Royal Society A: Mathematical, Physical and Engineering Sciences* **2016,** *472* (2195), 20160677.

113. Baker, L. A.; Marchetti, B.; Karsili, T. N.; Stavros, V. G.; Ashfold, M. N., Photoprotection: extending lessons learned from studying natural sunscreens to the design of artificial sunscreen constituents. *Chemical Society Reviews* **2017,** *46* (12), 3770-3791.

114. Abiola, T. T.; Whittock, A. L.; Stavros, V. G., Unravelling the Photoprotective Mechanisms of Nature-Inspired Ultraviolet Filters Using Ultrafast Spectroscopy. *Molecules* **2020,** *25* (17), 3945.

115. Premi, S.; Wallisch, S.; Mano, C. M.; Weiner, A. B.; Bacchiocchi, A.; Wakamatsu, K.; Bechara, E. J. H.; Halaban, R.; Douki, T.; Brash, D. E., Chemiexcitation of melanin derivatives induces DNA photoproducts long after UV exposure. *Science* **2015,** *347* (6224), 842.

116. Heurung, A. R.; Raju, S. I.; Warshaw, E. M., Benzophenones. *Dermatitis* **2014,** *25* (1), 3-10.

2. EXPERIMENTAL SETUP AND METHODOLOGY

2.1. Introduction

In this chapter, a detailed description of the different time-resolved experimental setups and computational methodologies employed is given. All experiments described in this manuscript were performed using the laser system and experimental setups shown in Figure 2.1. Isolated-phase experiments were carried out by time-resolved ion yield (TR-IY) spectroscopy, whereas the ultrafast dynamics of condensed-phase samples was tracked by transient absorption (TA) spectroscopy and fluorescence up-conversion (FuC) techniques. In addition, aiming to fill the gap between the gas-phase and the intrinsically complex condensed-phase, the photophysical behavior of molecular complexes has been studied by the time-resolved ion dip (TR-ID) method. This technique overcomes fragmentation issues and permits to track the ultrafast dynamics and also collect infrared (IR) spectra of size-selected molecular aggregates by combining high-resolution ns tunable sources and high intensity fs pulses. Regarding theoretical modelling, different kinetic approaches are employed for data simulation, while *ab initio* methods are used to predict the electronic structure and main nonradiative decay pathways. Further experimental and computational details related to each specific experiment are given in Chapters 3-7.

2.2. Femtosecond Laser Source

The ultrashort light pulses are generated by a commercial Ti:sapphire oscillator-regenerative amplifier laser system (Coherent Mantis – Coherent Legend Elite). The oscillator is pumped by a 532 nm 5 W frequency-doubled, continuous wave optically pumped semiconductor laser (Coherent OPS), producing a pulse train consisting of ~15 fs pulses centered at 800 nm, with a bandwidth of 55 nm measured at full width at half maximum (FWHM). The repetition rate of the pulses is 80 MHz, with a power of ~450 mW (~6 nJ per pulse).

Since the fs pulses generated by the oscillator are not intense enough for our experiments, the oscillator feeds its output into the Legend Elite CPA (chirped pulse amplifier) regenerative amplifier. The seeded pulses are amplified in a second Ti:sapphire cavity, which is pumped by a 527 nm 20 W frequency-doubled Nd:YLF laser (Coherent Evolution-30). After the amplification stage, the regenerative amplifier delivers a 1 kHz train of pulses centered at 800 nm, with a bandwidth of 30 nm (FWHM) and energies up to 3.5 mJ. The Fourier transform limited pulse duration of this fundamental beam is approximately 35 fs. The temporal and amplitude-phase characterization of the fundamental beam is conducted by using a single-shot second order autocorrelator[1] (SSA) and a GRENOUILLE[2] device, respectively.

The 800 nm fundamental beam is split into several branches in order to seed the multiple beam lines required for the experiments. A first beam splitter produces two beams, with energies of 1.5 mJ and 2 mJ, to pump two optical parametric amplifiers (OPA).[3-4] The transmitted 1.5 mJ beam is directed into the OPA1 (Coherent TOPAS-C) that is able to generate wavelengths in the range of 235-5000 nm. The reflected 2 mJ beam is further split into two beams: the first pumps a second OPA2 (Coherent OPerA Solo) tunable in the 300-2600 nm region, which is used as variable wavelength pump source for both isolated-phase and condensed-phase experiments. The remaining radiation (~1 mJ) is used to generate the second (2ω = 400 nm), third (3ω = 267 nm) or fourth harmonics (4ω = 200 nm), depending on the experiment requirements. Indeed, two different sets of β-barium borate (BaB_2O_4, BBO) crystals located in the isolated-phase (TR-IY and TR-ID) and condensed-phase (TA and FuC) setups can be used. For the 2ω, a type I BBO crystal ($\theta = 29^o$) is used in the second harmonic generation (SHG) process. For the 3ω, the 400 nm beam is combined with the residual 800 nm fundamental on a type I BBO crystal ($\theta = 39^o$) where sum-frequency generation (SFG) occurs. The 4ω is produced by SFG between the 267 nm and the residual 800 nm on a type I BBO crystal ($\theta = 63.7^o$).[3, 5-6] The spectral characterization of the beams is done by a fiber optic spectrometer (Ocean Optics HR2000) that operates in the 200-1100 nm range. Finally, the dispersion of the UV pulses is compensated using a CaF_2 prism compressor.

A portion of the fundamental beam (~500 nJ) is reserved to be used as probe, when required, in the different setups. For the isolated-phase experiments, the fundamental is sent into a delay line (APE ScanDelay), which controls the pump-probe delay for TR-IY and TR-ID setups. In the condensed-phase experiments, the fundamental is sent into a delay stage (Thorlabs ODL220-FS), which controls the temporal overlap between the pump and probe pulses for TA experiments; the same beam is then employed to seed the generation of the white light continuum (WLC) probe pulse. Furthermore, previously to the TA setup the same fundamental beam can be employed for FuC experiments.

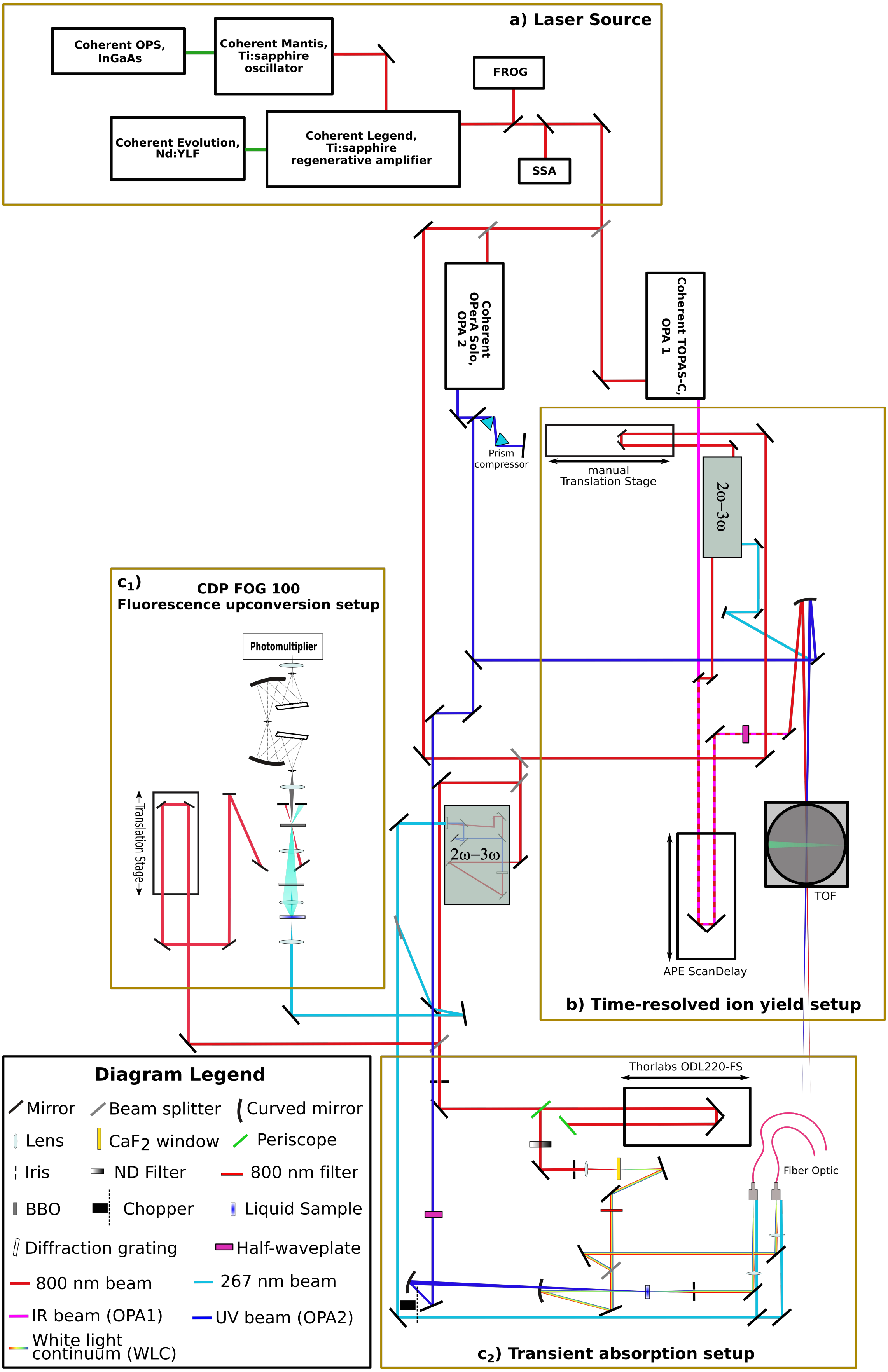

Figure 2.1. *General scheme of the laser system (a) and the experimental setups employed for time-resolved experiments in the isolated (b) and condensed-phases (c$_{1-2}$).*

2.3. Isolated-Phase Experiments

2.3.1. Time-Resolved Ion Yield Spectroscopy

In this gas-phase pump-probe technique, firstly, the molecule of interest is prepared into a selected electronic excited state by a pump pulse, and then, the evolution of the system is tracked by ionization with an ionizing probe pulse.[7-11] By measuring the amount of ions formed as a function of the time delay (Δt) between the pump and probe pulses, the relaxation dynamics of the initially prepared electronic excited state can be monitored (see Figure 2.2). The use of a time-of-flight (TOF) spectrometer allows us to selectively track the dynamics of the parent molecule and the formed fragment species, which are separated in different channels attending to their mass-to-charge (*m/z*) ratio.

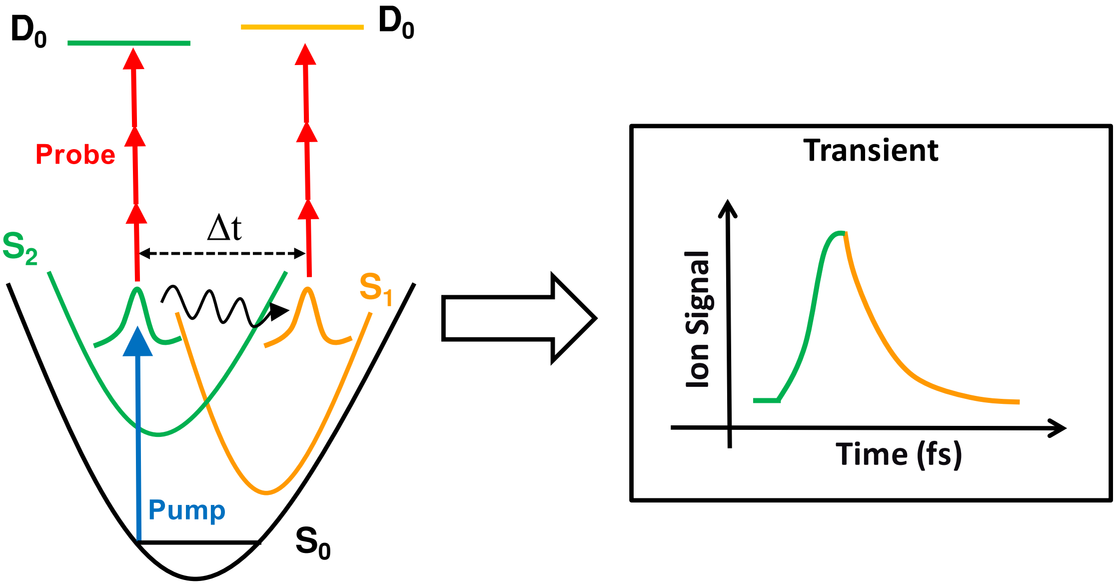

Figure 2.2. *Diagram of TR-IY spectroscopy.*

Since the methods to generate molecular clusters offer a limited control over the size distribution, time-resolved measurements able to extract the dynamics of specific size clusters are required. Moreover, the fragmentation process that these weakly bound species undergo notably complicates the identification of the different species contributing to each mass channel. In order to avoid this difficulty time-resolved ion dip (TR-ID) method is applied, which is a variant of TR-IY that combines the fs pump-probe scheme with an IR ns laser. Further details related to this technique are given in section 2.3.3.

2.3.2. TR-IY Setup

2.3.2.1. Mass Spectrometer

The system is a modified Wiley-McLaren[12] TOF mass spectrometer with the following parts:

a) Source chamber

The vapor samples are introduced in the form of a supersonic jet[13-15] generated by a solenoid pulsed valve (Parker General Valve Series 9), which fires at 100 Hz in a pre-chamber coupled to the mass spectrometer. Before entering the ionization region, the coldest part of the beam is selected by a 0.8 mm skimmer located 2 cm away from the 0.51 mm nozzle. Depending on the experiment, Ar or He at a pressure of 0.5-2 bar are used as carrier gases. Typically, the samples under study are solids or liquids with low vapor pressure, and consequently it is often required to increase the temperature to obtain a useful amount of gaseous sample. For that purpose, the temperature can be increased using a heating tape (JP Selecta 3031715) attached along the pipe that connects the sample reservoir and the pulsed valve, which is controlled by a digital benchtop temperature controller (Philips KS40). By doing so, condensation process in the nozzle is avoided. Experimental conditions such as pulsed valve duration, carrier gas pressure, sample temperature and laser-valve delay can be carefully set to maximize the signal of interest and avoid contributions of undesirable species.

b) Ionization region

The ionization region is constituted by three charged plates: a repeller, an extractor and a grounded accelerator. A schematic representation is depicted in Figure 2.3. The ions are generated due to the interaction of the laser with the molecular beam in the region between the repeller and extractor, which are 12.7 cm apart and operate at potentials about 4.3 and 3.75 kV, respectively. The formed ions are directed to the next region, where they are accelerated between the extractor and the ground plates. Both the laser and the molecular beam are oriented orthogonal to the TOF tube, directing ions upwards to the detector. The laser enters the chamber, perpendicularly to the molecular beam, through 3 mm thick fused silica windows. The ionization region and the TOF are evacuated by two turbomolecular pumps: the first one below the interaction chamber (Alcatel PTM 5900, 400 Ls^{-1} N_2) and the second one close to the detector (Leybold Turbovac TW 250 S, 230

Ls^{-1} N_2). The turbomolecular pumps are connected to a rotatory pump (Leybold TRIVAC D 25 B, 71.4 Ls^{-1}) to achieve a primary vacuum of $2\cdot10^{-3}$ mbar. Typically, a pressure about 10^{-7} mbar is reached in the ionization region, which increases up to ~$5\cdot10^{-5}$ mbar when the molecular beam is operated.

c) TOF tube and detector

The accelerated ions acquire velocities proportional to the square root of their *m/z* ratio enabling an effective separation of the different ions along its length (86.5 cm). Consequently, it is possible to estimate the arrival time of specific ions according to the expression:

$$t_i = t_{ref}\sqrt{\frac{m_i}{m_{ref}}} \tag{2.1}$$

where t_{ref} is the arrival time of a reference molecule with m_{ref} mass.

Along the TOF tube, four ionic lenses (two for x-axis and two for y-axis) are located perpendicular to the flight axis (z). Their potentials can be varied in order to correct the transverse components of the ion velocity. The mass-resolution of the mass spectrometer can be determined by:

$$R_t = \frac{t}{2\Delta t} = \frac{m}{2\Delta m} \tag{2.2}$$

where t is the time-of-flight corresponding to the m mass, and Δt is the FWHM of the signal.

The detector consists of two microchannel plate arrays (MCPs, 18 mm diameter) in a chevron (v-stack) arrangement, whose output current is collected by a digital oscilloscope (Tektronix TDS 2024/Agilent technologies DSO7054B). Up to three ion signals of interest can be integrated simultaneously by three Boxcars (Stanford SR250). After digitalization by an A/D converter (National Instruments PCI-6221), the signals are stored in a personal computer for analysis. For a typical transient, about $5\cdot10^{4}$ – $3\cdot10^{5}$ experimental points (ion signal as a function of pump-probe delay) are collected by a custom-made LabVIEW (National Instruments) virtual instrument.

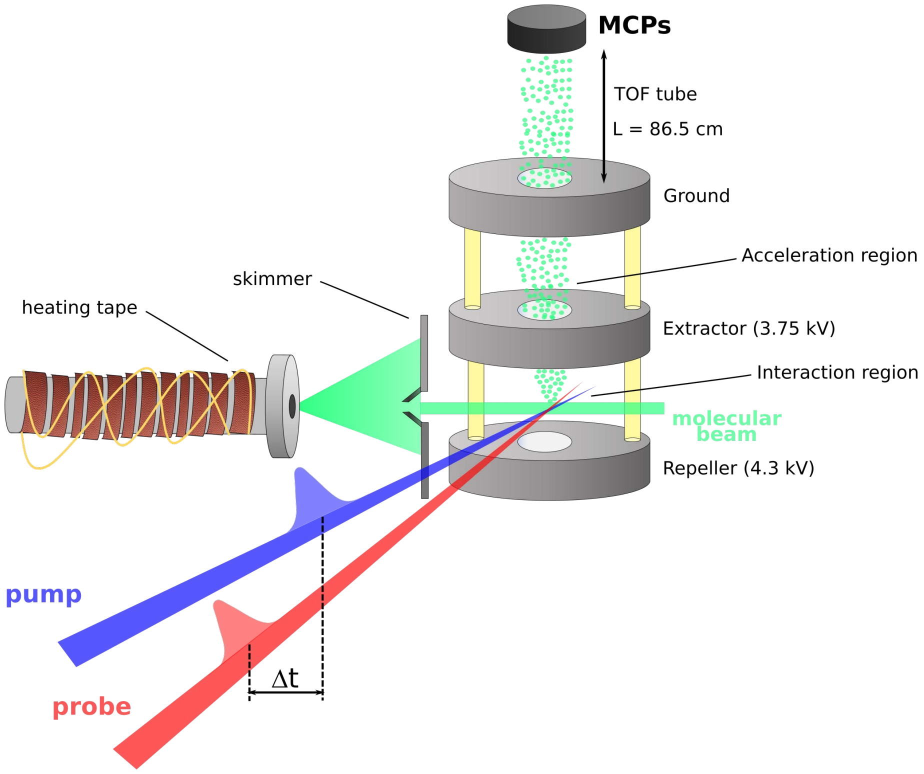

Figure 2.3. *Schematic representation of the TR-IY experimental apparatus.*

2.3.2.2. Delay Line

Pump-probe delay is controlled by a silver coated retroreflector mounted on a motorized continuous displacement delay line (APE ScanDelay 150), allowing a maximum temporal delay of 150 ps (2.25 cm) with a precision of 5 fs. The delay is periodically controlled by a fast scanning shaker at frequencies in the range of 0.2-1 Hz.

2.3.2.3. Optics

In this section an overview of the different beam lines for isolated-phase experiments is given. As described previously in Figure 2.1, laser pulses from either the OPA2 or the harmonic generation setup can be used as pump for TR-IY measurements. Analogously, the fundamental 800 nm or laser pulses from the OPA1 can be employed as probe. The relative polarization between the pump and probe pulses is controlled by a rotary half-waveplate (λ/2, 800 nm) and it is typically set at magic angle (54.7º) to eliminate rotational alignment effects.[16-18] The pump and probe beams are spatially overlapped in the ionization region. For that purpose, the beams are focused with an angle of 2º (near copropagation) into the vacuum chamber using a concave spherical aluminum mirror. The focusing conditions are different depending the experimental requirements. Indeed, when 800 nm probe is needed a mirror with focal length of 600 mm is employed for pump and probe beams. However, for longer probe wavelengths from OPA1 a focal length of 300 mm is used. Actually, large numerical apertures are preferable when high photon densities are required for the multiphoton ionization step. The intensity of the pump and probe beams is precisely adjusted by variable neutral density (ND) filters. Typically, the pump and probe beam intensities are estimated to be around 10^9 and 10^{12} Wcm^{-2}, respectively.

2.3.2.4. Synchronization

Although the repetition rate of the laser system output is 1 kHz, the pumping capacity of the vacuum system limits the valve firing at 100 Hz, which is the final repetition rate of the experiments. The synchronization of the laser, pulsed valve and detection is achieved by a digital delay generator (Standford DG535).

2.3.2.5. Data Fitting and Analysis

In order to extract the dynamical information, the recorded time-dependent data are treated by using a rate equation kinetic model. For this purpose, the multi-exponential molecular response function is convoluted with the pump-probe cross-correlation (CC) function. More detailed information regarding the modelling of ion transient signals is given in section 2.5.1.

2.3.3. Time-Resolved Ion Dip Spectroscopy

One of the main drawbacks of TR-IY spectroscopy, when apply to molecular aggregates, resides in the difficulty to track the dynamics of size-selective ions due to the fragmentation during the ionization probing process. Because of this undesirable effect, the dynamical signature of the target molecular complex can be sent to lower mass channels. Analogously, the mass channel of interest may have contributions from larger species. Consequently, these intricate fragmentation pattern turn the interpretation of the temporal evolution of a particular mass channel into a hard or even impossible task.[19] Aiming to overcome these difficulties, the TR-ID technique permits disentangling the transient signal belonging to a particular size cluster, by associating it to a characteristic IR absorption of the targeted complex. The foundations of the technique, which builds upon frequency-resolved double resonance techniques[20-22] and combines nanosecond and femtosecond pulses to gain time and frequency resolution, is graphically explained in Figure 2.4: initially, a ns IR laser pulse, tuned into a vibrational transition of the cluster of interest, interacts with the supersonic expansion at a fixed time prior to the fs pump-probe pulses that will prepare and track the excited state dynamics.[23] In close analogy to the IR ion-dip methods,[21-22] the absorption of the IR radiation fragments the targeted cluster due to the fact that the deposited energy exceeds the intermolecular binding energy, which will cause a dip (or an enhancement) of the ion current in the corresponding mass channel. Therefore, by examining the changes induced by the IR beam in the appropriate mass channel, it is possible to extract not only the dynamics but also the IR signature of the species contributing to a particular mass channel. The IR-dip spectrum is acquired by scanning the IR source, while integrating the IR_{on}-IR_{off} ion signal resulting from the fs pump-probe pulses overlapped at a given relative time-delay (typically, Δt = 0 fs). On the other hand, the TR-ID transients, which permit tracking the temporal evolution of the species absorbing at specific IR wavelengths, are recorded by collecting the IR_{on}-IR_{off} signal as a function of the pump-probe delay, with the IR fixed on a chosen vibration.

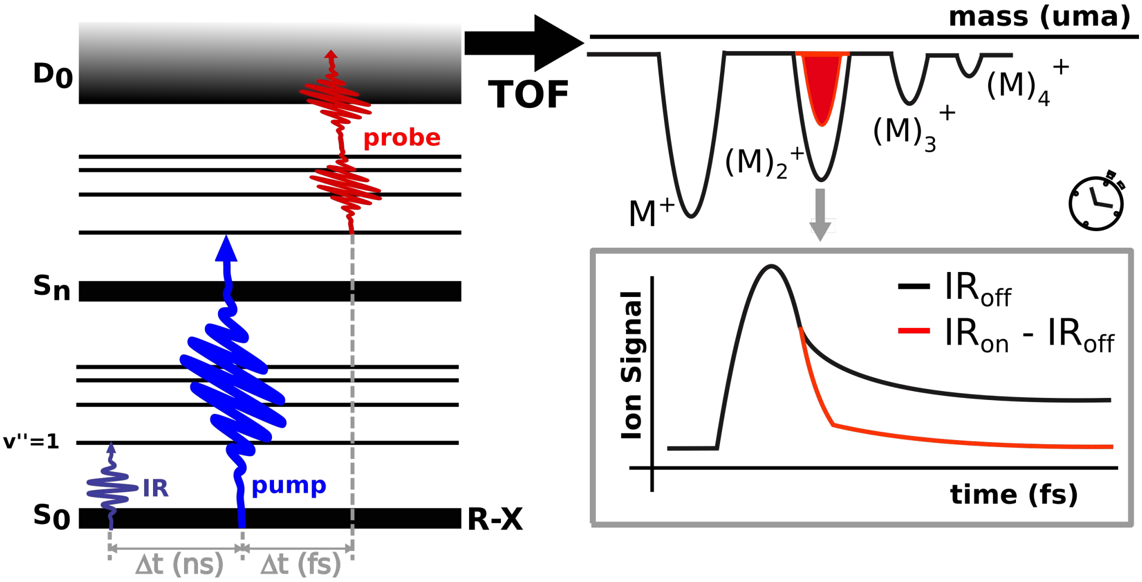

Figure 2.4. *Schematic of the TR-ID method applied to track the relaxation dynamics of size selected molecular aggregates, adapted from reference 23.*

2.3.4. TR-ID Setup

In the TR-ID experiments, the same basic setup described above for the TR-IY experiments, including fs laser system, optics, pulsed valve, mass spectrometer and delay line, is employed. In addition, a commercial optical parametric oscillator (OPO)/OPA system (Laser Vision) with 10 cm^{-1} bandwidth, pumped by a Nd:YAG (Continuum Surelite) is employed to produce ns IR pulses in the 2500-4000 cm^{-1} range, with an energy of ~10 mJ per pulse. About 0.5 mJ of the ns IR is focused by a 100 cm lens and spatially overlapped with the fs pump and probe beams at the interaction region of the mass-spectrometer, as shown in Figure 2.5. The ns IR is fired 100 ns in advance, which ensures enough time for the fragmentation processes to take place. For the TR-ID transients the fs pump-probe delay is varied by the APE ScanDelay continuous displacement delay line. To synchronize the fs and ns sources with the pulsed valve, two properly delayed triggers at 20 and 10 Hz that fire the valve and the ns IR laser, respectively, are produced using a delay generator (Standford SR535) triggered by the 1 kHz regenerative amplifier reference output. Consequently, the final sampling rate of the experiments is limited to 10 Hz. The $\mathrm{IR_{on}}$ and $\mathrm{IR_{off}}$ signals of up to three mass channels are simultaneously integrated by Standford SR250 Boxcars and stored in a personal computer. Data acquisition and analysis procedures are analogous to those described for TR-IY experiments.

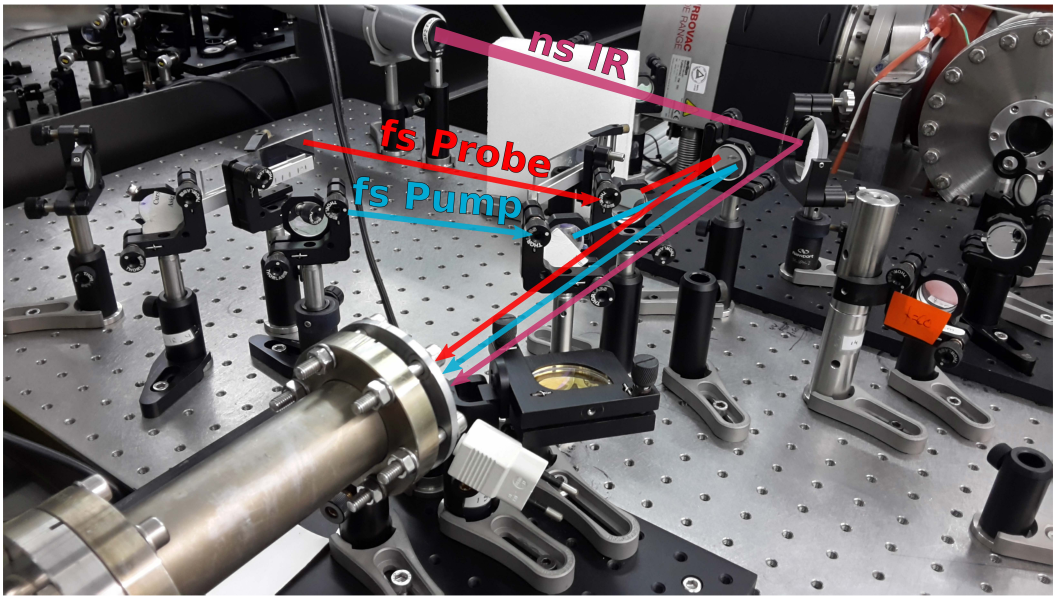

Figure 2.5. *Image of the configuration employed in the TR-ID setup to introduce the laser beams in the mass spectrometer.*

2.4. Condensed-Phase Experiments

2.4.1. Transient Absorption Spectroscopy

Transient absorption (TA) spectroscopy is a pump-probe technique to unravel the photophysical and photochemical events following excitation of dilute solutions. For this experiment, a first UV/Visible (Vis) pump pulse prepares the molecule into a selected electronic excited state. Then, at a variable time-delay (Δt) a probe pulse, which is spatially overlapped with the pump, is sent to a spectrometer after interacting with the sample. Consequently, the recorded variation of probe pulse intensity with the time-delay makes possible to monitor the evolution of the sample. Nevertheless, in contrast with the isolated-phase techniques, in TA experiments a broadband probe pulse is used, which consist of a white light continuum (WLC) generated in a nonlinear medium such as a sapphire, water or CaF_2.[24-26] Therefore, the absorption of different probe wavelengths are tracked simultaneously, permitting the acquisition of a time-resolved UV/Vis absorption spectrum of the states prepared by the pump.

In TA experiments, the transient signal is given by the differential optical density (ΔOD) of the sample as a function of the pump-probe delay time. The sample ΔOD can be expressed according to: [27-28]

$$\Delta OD(\lambda_{pr},\Delta t) = -\log\left(\frac{I_{pu}(\lambda_{pr},\Delta t)}{I_0(\lambda_{pr})}\right) \tag{2.3}$$

where I_0 and I_{pu} are the transmitted probe light through the unpumped sample and after excitation, respectively (see Figure 2.6).

Generally, the recorded TA spectrum is the product of four different contributions that have an effect on the ΔOD, as shown in Figure 2.7: the ground state bleach (GSB), the stimulated emission (SE), the excited state absorption (ESA) and the photoproduct absorption. [24, 29]

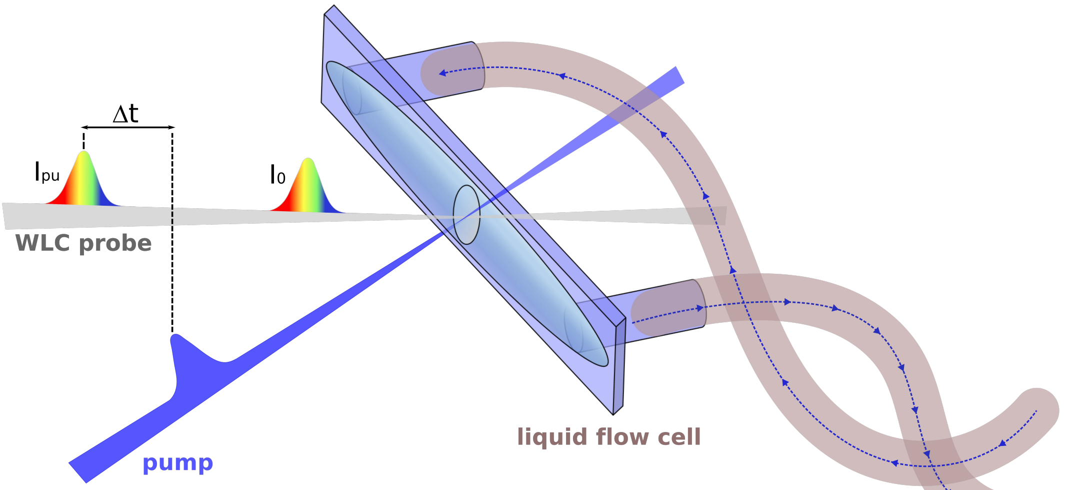

Figure 2.6. *Schematic representation of the pump-probe sequence in TA experiments. The probe pulse interacts alternatively with the unpumped and excited sample, which is constantly recirculating in a liquid flow cell.*

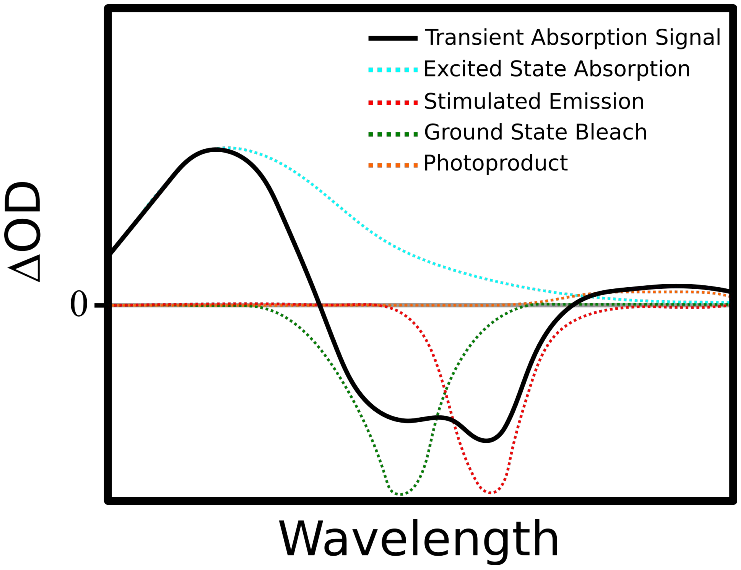

Figure 2.7. *Schematic of the principal contributions to the TA spectrum, adapted from reference 24.*

2.4.1.1. Ground State Bleach

The GSB is a contribution that appears as a negative signal (ΔOD < 0) in the region of the ground state absorption spectrum. After excitation, the population of the ground state decreases and consequently, since this fraction of molecules do not contribute, the ground state absorption is reduced. This means that upon excitation more probe light is transmitted through the sample ($I_{pu} > I_0$). The temporal evolution of the GSB tell us about the relaxation pathways of the photoexcited molecule back to the ground state.

2.4.1.2. Stimulated Emission

SE is a process that only occurs when a probe photon induces emission of an additional photon from an electronically excited state of the molecule. This results in an increase on the probe light intensity, which means a negative signal in the TA spectrum. In general terms, this contribution is observed in the region that corresponds to the fluorescent emission spectrum of the molecule.

2.4.1.3. Excited State Absorption

Upon excitation, the probe can induce optically active transitions from the prepared excited states of the molecule to higher excited states. The absorption of probe light by the exited state reduces the intensity of the light transmitted through the sample ($I_{pu} < I_0$), which means a positive signal (ΔOD > 0) in the TA spectrum in the region of the ESA.

2.4.1.4. Photoproduct Absorption

During the relaxation of the prepared excited state, the sample molecule can reach dissociative states that result in transient or long-living fragmentation products. The absorption of the probe by these species yields, in general, additional positive contributions across the TA spectrum. Depending on the nature of the electronic state involved in the fragmentation process, the absorption of neutral photoproducts, radicals or charged species such as radical cations or solvated electrons can be observed in the TA spectrum.

2.4.2. TA Setup

In this section, the main elements of the TA setup, which has been decisively improved during this thesis, are shown and described. As already anticipated, this setup has been used for many of the condensed-phase experiments reported here (Chapters 4 and 7). In Figure 2.8, a general scheme of the experimental setup can be found.

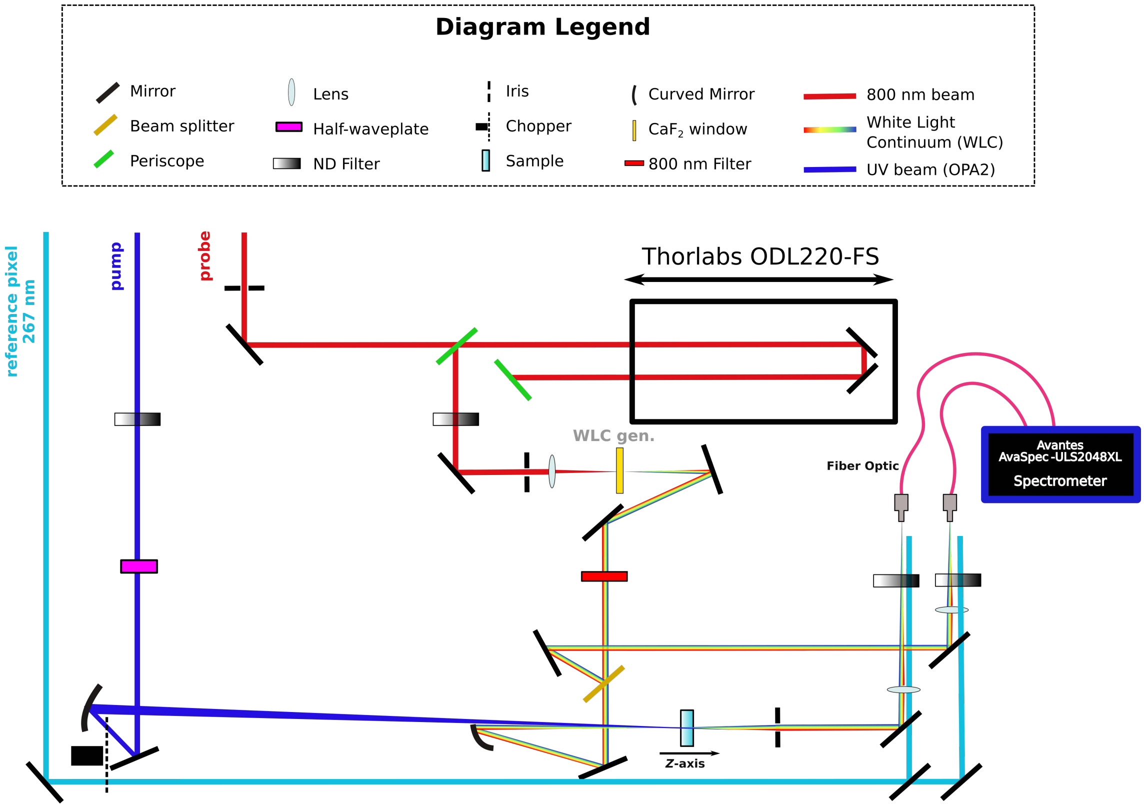

Figure 2.8. A schematic of the TA setup.

2.4.2.1. Pump Pulses

As it was explained in section 2.2, our experimental setup has two different methods to generate the pump pulses from the fundamental 800 nm beam, for vacuum and condensed-phase experiments. The first one uses the OPA2, which is capable of generating radiation in the 235-5000 nm range. The second method relies in the harmonic generation process that provides the 400, 267 or 200 nm wavelengths when required. These pump beams share most of the optical path and are focused on the sample by a spherical mirror with focal length of 500 mm. In order to record the intensity of the transmitted probe continuum through the sample with and without the presence of the pump, a synchronized optical chopper running at 100 Hz blocks alternatively bursts of ten excitation pulses. The energy of the pump pulses is controlled by using variable ND filters, whereas the relative polarization between the pump and probe pulses is set by employing a Berek's variable waveplate. Typically, pump energies in the range of 0.2 – 2 μJ are employed and the relative polarization of the pump-probe beams is fixed at magic angle (54.7º) configuration to avoid rotational dephasing effects.

2.4.2.2. Probe Pulse

As described in section 2.2, about 500 nJ of the fundamental are employed to seed the generation of the WLC probe pulse. The process is schematically illustrated in Figure 2.8. Firstly, the 800 nm fundamental is sent to a linear translation stage (Thorlabs ODL220-FS), which permits to adjust the probe beam pathway with 0.3 μm precision (~1 fs) and allows a maximum delay of ~1.5 ns (22 cm). During this thesis, the maximum delay of the translation stage has been increased up to ~2.5 ns by adding a second pass through the delay line. To achieve this, a second pair of mirrors on the motorized delay stage and two periscope assemblies have been implemented. Then, about 1 μJ of the fundamental beam is focused into a 2 mm thick CaF_2 (<001>) window for the WLC generation. To assure a stable white light generation the power density and focusing conditions are carefully adjusted by an iris with an aperture of ~4 mm, a variable ND filter and a $f = 100$ mm fused silica lens. Although CaF_2 permits obtaining a stable broadband probe from 350 to 750 nm (see Figure 2.9), it has a major drawback: the damage threshold of the material is very close to the threshold for WLC generation.[30] With the aim of minimizing permanent damage and extending its lifespan, the CaF_2 window is mounted on a 3-axis translation stage. The focal position of the window (z-axis) is controlled by a manual micrometric actuator, while two motorized direct current (DC) servo actuators (Thorlabs Z825) continuously translate the window in perpendicular directions (x and y-axes) to assure a periodic refreshing of the irradiated section. The generated white light is then collimated ($f = 100$ mm) and split before being focused ($f = 250$ mm) into the sample with a spot radii of ~65 μm by spherical aluminum mirrors. A small fraction (40%) of the WLC beam, which is used as reference beam to significantly improve signal-to-noise ratio, is directly sent to the spectrometer fiber by means of a $f = 150$ mm lens. It is worth mentioning that the residual 800 nm radiation (~1 μJ) that is not converted to white light has to be removed to avoid the interaction with the sample and the saturation of the spectrometer. For this purpose, most of the remaining 800 nm fundamental is filtered by a highly reflective (750-850 nm) dielectric mirror (Altechna).

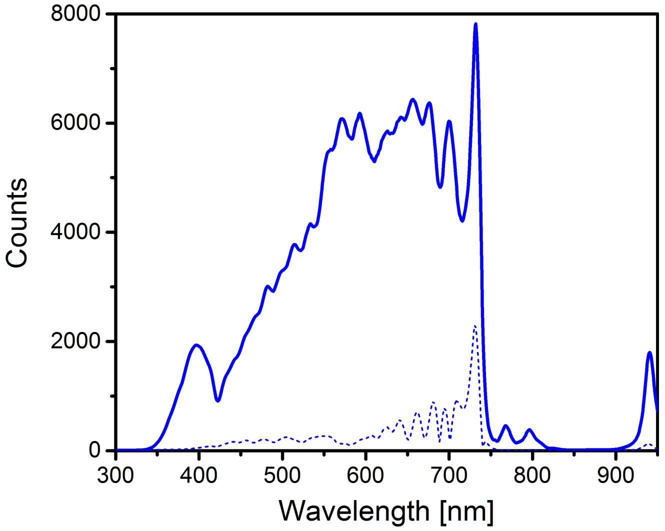

Figure 2.9. *Spectrum of the WLC (solid line) together with its standard deviation (dash line). The lack of counts in the 750-900 nm range is due to the filtering of the 800 nm.*

2.4.2.3. Liquid Samples

Choosing the appropriate liquid target is of great importance for TA measurements. One of the key factors is the thickness (optical path) of the sample film, not only because affects to the required sample concentration, but also due to its direct influence on the temporal resolution of the experiment. When the pump and probe laser pulses pass through the sample, they undergo group velocity dispersion (GVD), which accounts for the dependence between the speed of light and wavelength in a medium. Actually, when a pulse propagates through a transparent medium with normal dispersion, it undergoes a phase distortion inducing an increase of its temporal duration and a frequency chirp, because not all the frequencies travel though the medium at the same speed. Since the index of refraction for the blue light is higher than that for the red light, the red wavelengths travel faster than the blue wavelengths.[31] Additionally, the group velocity mismatch (GVM) between the pump and probe pulses contributes significantly to the degradation of time resolution. This effect, which depends directly on the optical path, is almost negligible when the excitation and probe wavelengths are degenerated but becomes the dominant contribution when the energy difference between pulses increases. Therefore, in order to reduce the velocity mismatch and GVD, an appropriate solution would be reaching a compromise value between the temporal resolution, which is inversely proportional to the thickness, and the signal-to-noise ratio. Further details regarding the impact of these effects on the temporal resolution are provided in section 2.4.2.7.

In our TA setup, multiple liquid targets are employed depending on the conditions of the sample solution under study. Typically, a flow cell (Starna Scientific UTWA2) that minimizes the optical path through the fused silica windows and the sample (0.2 mm) is used. The sample is pumped to the cell from a glass reservoir (50 cm^3) – through silicone tubing (Tygon S3 E-3603) – by a centrifugal (RS PRO M400-S) or a magnetic drive pump (Pittman 9413E269). A minimum flow speed of 500 cm^{3}min^{-1} is required to ensure that the sample is refreshed for every pump pulse. A manual micrometric actuator permits controlling the focal position of the flow cell (z-axis), whereas two motorized DC servo actuators (Thorlabs Z825) continuously translate the cell in perpendicular directions (x and y-axes). Nonetheless, in some cases photoexcitation with UV pulses results in the formation of photoproducts on the surface of the windows that cannot be removed by circulating the sample solution. To overcome this issue, a homemade gravity-driven thin liquid film flow system is employed.

2.4.2.4. Detection

After being focused and passed through the sample, the probe continuum, together with a portion of the excitation beam, is focused by a 100 mm lens onto an optical fiber connected to a spectrometer (Avantes AvaSpec-ULS2048XL). In order to reduce the scattering light that reaches the detector, the pump beam is blocked with an iris. As mentioned in section 2.4.2.1, the generated WLC is split to create a reference WLC beam, which, after following an alternative path avoiding the sample, is also focused by a 120 mm lens onto an optical fiber connected to the second channel of the spectrometer. It is worth to remark that both WLC beams pass through variable ND filters to avoid the saturation of the detector at certain wavelengths. Figure 2.10 compares the baseline reflecting sensitivity between this dual channel configuration, using a reference WLC beam, and the single channel configuration by collecting a TA spectrum of pure methanol following 267 nm excitation at negative time-delays ($\Delta t = -1$ ps), where the signal should be zero for all probe wavelengths. The dual channel configuration ensures an enhancement on the signal-to-noise ratio, which permits to reach sensitivities in the order of 0.1 mΔOD.

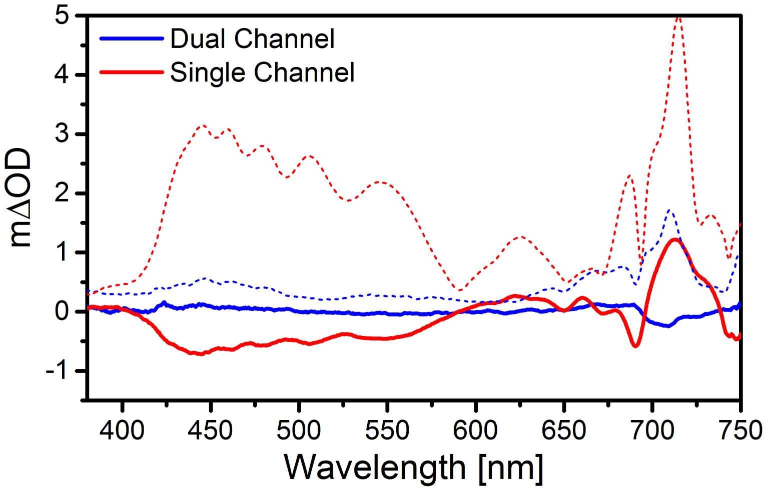

Figure 2.10. *Comparison of the baseline of the TA setup when a reference WLC is used (blue solid line) or single channel configuration is employed (red solid line). The dash lines correspond to the standard deviation of each configuration. See text for details.*

2.4.2.5. Synchronization and Data Acquisition

The data collection and processing is carried out by a homemade LabVIEW (National Instruments) software, which uses the collected spectra with and without pump to calculate the corresponding TA spectrum according to the expression:

$$\Delta OD(\lambda_{pr},\Delta t)=\log\left(\frac{I_0(\lambda_{pr})-I_0^{ref}(\lambda_{pr})}{I_{pu}(\lambda_{pr},\Delta t)-I_{pu}^{ref}(\lambda_{pr},\Delta t)}\right) \tag{2.4}$$

where I_0 is the transmitted probe continuum intensity passing through the unpumped sample, I_{pu} is the intensity of the transmitted probe passing through the excited sample, I_0^{ref} is the intensity of the reference probe without the excitation and I_{pu}^{ref} the intensity of the reference WLC when the sample is excited.

The repetition rate of TA measurements is limited by the 3.5 ms data transfer speed from the spectrometer to the personal computer. Consequently, it is essential to reach a compromise between delivering and integration times in order to obtain a good signal-to-noise ratio. For this reason, the spectrometer integrates the probe spectrum during 6 ms temporal windows, with the excitation alternatively on and off *via* an optical chopper running at 100 Hz. A Standford SR535 delay generator is used to achieve the synchronization of the laser, chopper and spectrometer. The excitation narrowband signal is also recorded to detect the presence of the excitation and to correct from intensity fluctuations.

2.4.2.6. Analysis

To extract the temporal and spectral information from the collected data, the processing involves the following steps:

a) Chirp and baseline correction

Firstly, the TA spectra have to be aligned in time to correct the broadband pulse chirp by using the coherent artifact signal (CAS, see section 2.4.2.7 for further information) as a zero delay time reference ($\Delta t = 0$).[28, 32-34] This chirp causes that the spectral components of the WLC reach the sample at different times. Figure 2.11a shows the raw TA spectrum of methanol excited at 267 nm. As it can be seen, the temporal overlap of a certain component of the WLC probe with the pump pulse results in a wavelength dependent CAS, whose central position travels along a ~2 ps temporal window for wavelengths between 350 and 700 nm. To obtain the corrected TA spectrum, a fourth order polynomial function is employed to fit the CAS position at different wavelengths. Finally, the time-axis is corrected by applying the correction function resulted from the fitting, as shown in Figure 2.11b. As the scattering of the pump pulse and eventually the spontaneous emission from the sample are also coupled to the spectrometer, the baseline is also corrected by subtracting a spectrum collected at negative time delays ($\Delta t < 0$), taking advantage of the fact that these contributions are independent from the pump-probe delay.[35]

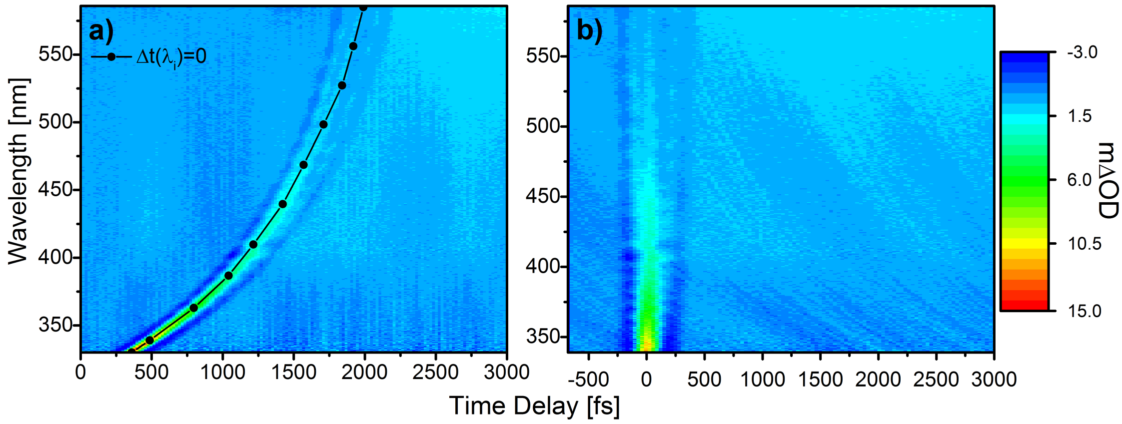

Figure 2.11. *TA spectrum of methanol after excitation at 267 nm without (a) and with chirp correction (b). The spectrum shows the CAS of methanol, which is used to establish the zero delay time and to measure the instrument response function.*

b) Data modelling

Analogously to gas-phase measurements, the transients at single selected probe wavelengths are modelled by the convolution of a multi-exponential molecular response with the CC function of the laser pulses. This is carried out by a dedicated LabVIEW software. Additionally, it is also possible to use a global fitting procedure, which allows us to extract the wavelength dependent pre-exponential factors, $A_i(\lambda_{pr})$, that permit to a single set of temporal components, τ_i, to reproduce the TA spectrum, the so-called decay associated spectrum (DAS). Additional details about the TA data modelling are given in section 2.5.

2.4.2.7. Temporal Resolution

The temporal resolution of TA setup is affected by several factors such as pump and probe pulse durations, geometry of both beams at the interaction region, and the velocity mismatch and the GVD at the sample.[31, 36-38] The temporal resolution can be easily determined by measuring the CC of the pump and probe pulses from the width of the CAS observed in a pure solvent in the full spectral range of the probe broadband.[28, 32] The coherent artifact is mainly produced due to the cross-phase modulation effect, which accounts for the spectral modifications within the probe upon pump-induced temporal changes of the refractive index, although two-photon absorption and stimulated Raman amplification can also contribute to the CAS.[39-40] This phenomenon for WLC probe pulses with nonlinear spectral phase has been theoretically described by several groups[26, 32, 39, 41-42] and consequently the CAS has been fitted, as shown in Figure 2.12, with the following expression:[26]

$$\Delta OD_{CAS} = \sin(f_1 t + f_2 t^2 + \varphi) A \exp\left(\frac{t^2}{\omega^2}\right) \tag{2.5}$$

where f_1, f_2 and φ are adjustable parameters, whereas ω is the FWHM of the instrumental response. It is worth to note that the width of the artifact increases for longer probe wavelengths due to the group velocity mismatch between the pump and the probe, resulting on a loss of temporal resolution, as shown in Figure 2.11a.

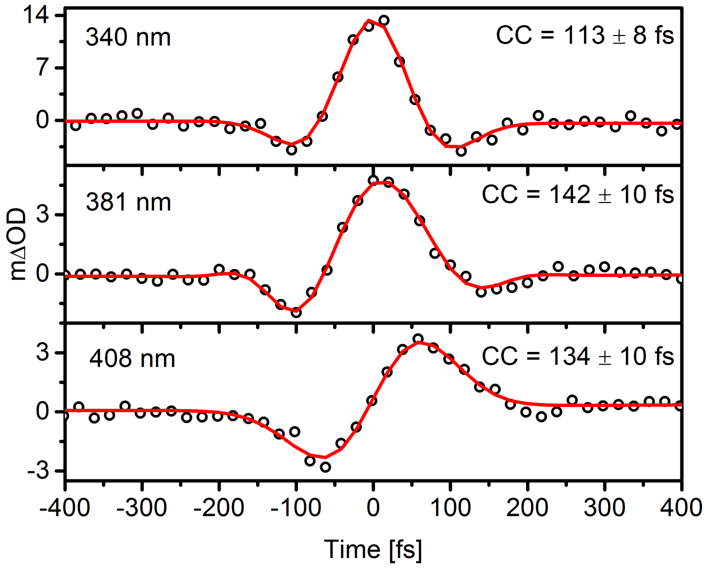

Figure 2.12. *CAS of methanol after excitation with 267 nm at different probe wavelengths used to measure the CC function for TA experiments.*

Excitation geometry is another key factor that affects directly the temporal resolution. The angle between pump and probe beams and their diameter influence the width of the CAS. Indeed, the CC function of pump and probe pulses is given by:[38]

$$R(\tau) = \iiint \int_{-\infty}^{\infty} I_{pu}(t,x,y,z) I_{pr}(t-\tau,x,y,z) \partial t \partial x \partial y \partial z \qquad (2.6)$$

where I_{pu} and I_{pr} is the intensity of pump and probe beams, respectively, and τ is the time delay between both pulses.

Figure 2.13 shows the beam geometries in the excitation region, where L is the thickness of the sample, D and d denote de diameter of pump and probe beam, respectively, and θ is the angle between both pulses. Assuming that pulses have a Gaussian temporal profile and spatial distribution, the pulse intensities can be expressed by:[38]

$$I_{pu}(t,x,y,z) = I_{pu}^{0}(z) \exp\left(-\frac{4\ln 2}{\tau_{pu}^{2}} \left[t - x\frac{\cos\theta}{\upsilon_{pu}} + y\frac{\sin\theta}{\upsilon_{pu}} \right]^{2} \right) \exp\left(-\frac{4\ln 2}{D^{2}} [x\sin\theta + y\cos\theta]^{2} \right) \qquad (2.7)$$

$$I_{pr}(t-\tau,x,y,z) = I_{pr}^{0}(z) \exp\left(-\frac{4\ln 2}{\tau_{pr}^{2}} \left[t - \tau - \frac{x}{\upsilon_{pr}} \right]^{2} \right) \exp\left(-\frac{4\ln 2}{d^{2}} y^{2} \right) \qquad (2.8)$$

where τ_{pu} and τ_{pu} are the temporal widths and υ_{pu} and υ_{pr} the group velocity of pump and probe, respectively.

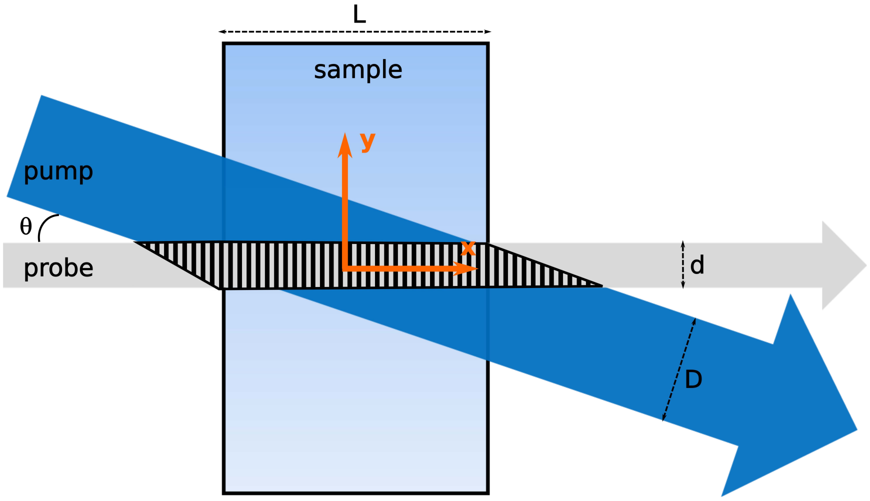

Figure 2.13. *Schematic diagram of the pump-probe interaction geometry, adapted from reference 38.*

Consequently, for 100 fs pulses and probe diameters of 200 μm, an angle (θ) greater than 5° results in a significant broadening of the CC function. Nevertheless, for shorter pulses this critical angle can be even smaller. Furthermore, if the probe beam diameter is smaller than that of the pump one ($D > d$) the change of the latter does not affect the temporal resolution. On the contrary, a subtle increase in the probe beam diameter implies a great loss of resolution. For this reason, in our experimental setup both pulses intersect with an angle of 2°, while typically spot radii of 130 and 65 μm are employed at the interaction region for the excitation and probe beams, in that order. The diameters of both beams can be characterized at the interaction region after sending them to a charge-coupled device (CCD) camera by using a flip mirror (see Figure 2.14). This procedure is very useful to achieve a proper spatial overlap of the beams.

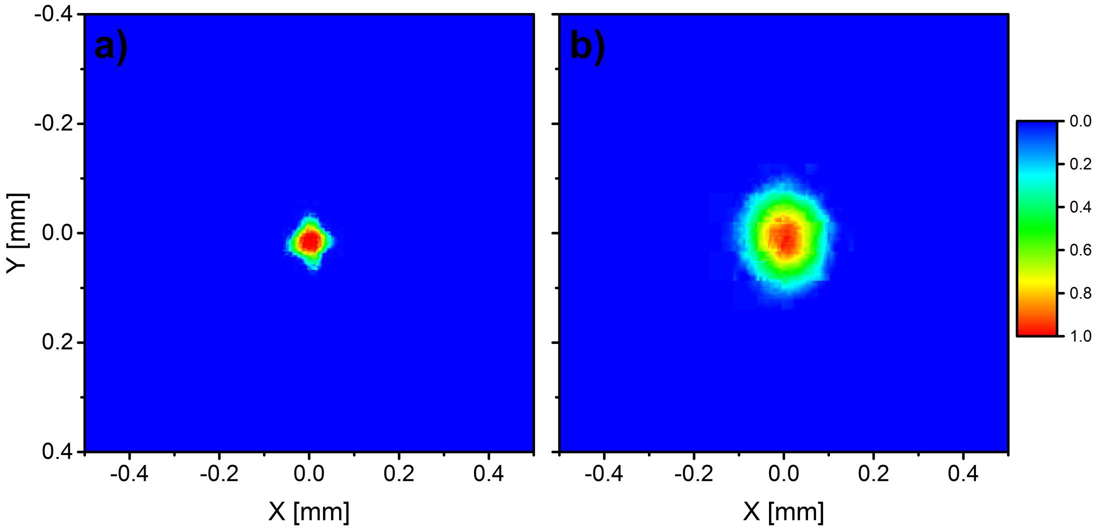

Figure 2.14. *Probe (a) and pump (b) pictures taken by CCD camera at interaction region.*

The temporal resolution is also affected by another factor: the group delay dispersion (GDD), which expresses the difference between transit times of the pump and probe pulses traveling a distance (L) through a medium (GDD = GVD · L).[43] However, it can be neglected if the sample cell is relatively thin or the difference between pump and probe wavelengths is small enough. Therefore, the theoretical temporal resolution can be defined as the sum of all the effects explained and is given by:

$$R = \tau_{pulse} + \Delta\tau_{GVM} + \Delta\tau_{geom} + \Delta\tau_{GDD} \tag{2.9}$$

In this sense, the experimentally determined CC function is a good approximation if it is compared with the theoretical resolution for a pulse of 60 fs at different probe wavelengths, as shown in Figure 2.15.

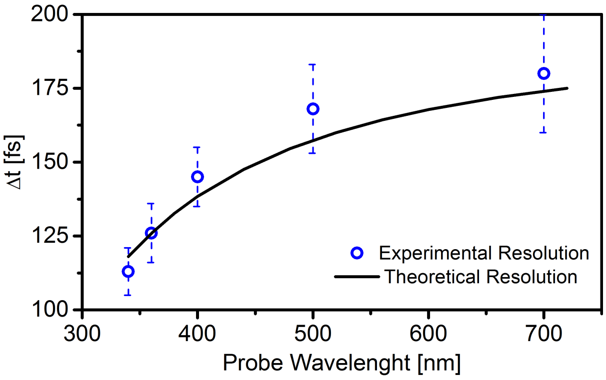

Figure 2.15. *Comparison between the experimental and theoretical resolution.*

2.4.3. Fluorescence Up-Conversion

The fluorescence up-conversion (FuC) technique is a powerful tool, complementary to TA spectroscopy, for investigating ultrafast processes in solution such as solvation dynamics, relaxation of excited states and vibrational cooling.[44-47] In a FuC experiment, the target molecule is prepared into an excited state and then its fluorescent emission is resolved in time with fs resolution. To do so the emission signal (ω_{fl}) is mixed with a gate fs pulse (ω_g) in a non-linear crystal to generate the sum-frequency of both beams ($\omega_{SF} = \omega_{fl} + \omega_g$). Therefore, by varying the delay of the gate pulse respect to the excitation pulse, it is possible to slice in time the emission process.

2.4.4. FuC Setup

Figure 2.16 shows the setup we use for time-resolved fluorescence experiments. The system is based on a commercial kit (CDP FOG 100), which has been modified to allow the introduction of an external pump beam from the OPA2. In this way, the excitation can be tuned in the 200-800 nm interval. The pump beam is focused by a lens (*f* = 60 mm) on a rotatory cuvette of 0.3 mm path that contains the solution under study. The sample emission is collected by an *f* = 60 mm lens and focused by a second one with *f* = 150 mm, on a 0.2 mm thick BBO crystal, where it interacts with the 800 nm gate beam to generate the up-converted signal by type-I phase matching. The latter is detected by a photomultiplier (PMT) coupled to a monochromator (CDP 220D), whose signal is integrated by a boxcar (CDP 2021A). It is important to note that specific cut-off filters are employed to filter the remaining excitation light. The temporal overlap between the excitation and gate beams is controlled by a retroreflector mounted on a motorized delay stage allowing a maximum delay of ~2 ns with a precision of 1.5 fs. The angle of the nonlinear crystal is optimized for the emission wavelength of choice, which is selected by the monochromator. For a typical measurement, 5 to 10 delay scans containing 1500 laser shots at each delay position are accumulated. Temporal resolutions around 150-250 fs are reached at the studied excitation and emission wavelengths.

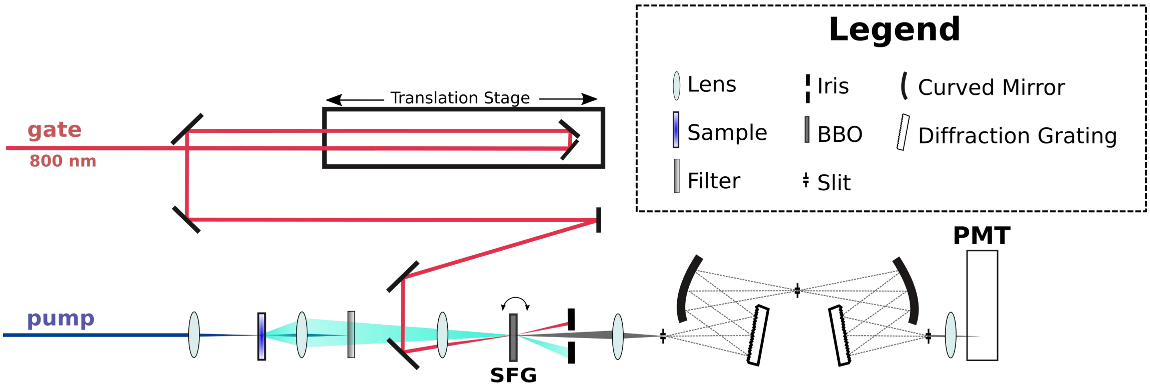

Figure 2.16. *Schematic diagram of the time-resolved fluorescence up-conversion setup.*

2.5. Computational Methodologies

2.5.1. Signal Modelling

In order to extract the dynamical information contained in the recorded transients, different analysis methods are used depending on the type of experiments. In isolated-phase and FuC experiments we collect one-dimensional transients (*signal vs.* Δt) since the measurements are carried out at single probe wavelength. However, in TA spectroscopy the data are two-dimensional because the temporal evolution is simultaneously registered at all the wavelengths of the WLC and consequently, it is possible to model them by global fitting method. Additional information of each specific case will be given in the next chapters.

2.5.1.1. Single Wavelength Transients

The transients at fixed probe wavelengths are modelled by the following convolution function:[48]

$$S(\lambda_{pr},t)=\int_{-\infty}^{+\infty}M(\lambda_{pr},t-t')R(\lambda_{pr},t')dt' \tag{2.10}$$

where

$$M(t)=\sum_{i=1}^{n}a_i e^{-t/\tau_i} \tag{2.11}$$

is a multi-exponential molecular response, being a_i the amplitude (a positive amplitude represents a decay while a negative indicates a rise), τ_i the time constants of the exponentials, and $R(\lambda,t)$ the CC function of the laser pulses, which typically is a Gaussian. In this method, each probe wavelength is fitted individually and consequently the value of τ_i and a_i is different for every wavelength.

In isolated-phase experiments, in order to derive the CC function and to establish the zero delay time ($\Delta t = 0$), the nonresonant ionization signal of ethylene (C_2H_4) or xenon is acquired simultaneously to the ion of interest. Depending on the pump-probe wavelengths, values in the 70-120 fs (FWHM) range are typically measured, as shown in Figure 2.17a. In condensed-phase experiments, different approaches are used according to the technique employed. In TA experiments, as it was previously described in section 2.4.2.7, the CC function and the zero delay time at the different spectral wavelengths is derived from the CAS acquired from a pure solvent-only measurement, as shown in Figure 2.12. Typically, values between 120 and 190 fs were obtained for the CC in the 350-700 nm probe range. In FuC technique, the temporal resolution is generally determined by measuring the Raman response from the solvent.[49] However, in our setup it is not possible to address this characterization when excitation wavelengths below 275 nm are employed because the sum-frequency of the Raman signal would be beyond the detection limit of the monochromator, which is 220 nm. In this case, the CC function is derived from a measurement of the rise-time in the blue region of the fluorescence from a long-lived molecule such as coumarine 153 in the solvent of interest (see Figure 2.17b), which has been demonstrated to be an acceptable estimation.[50]

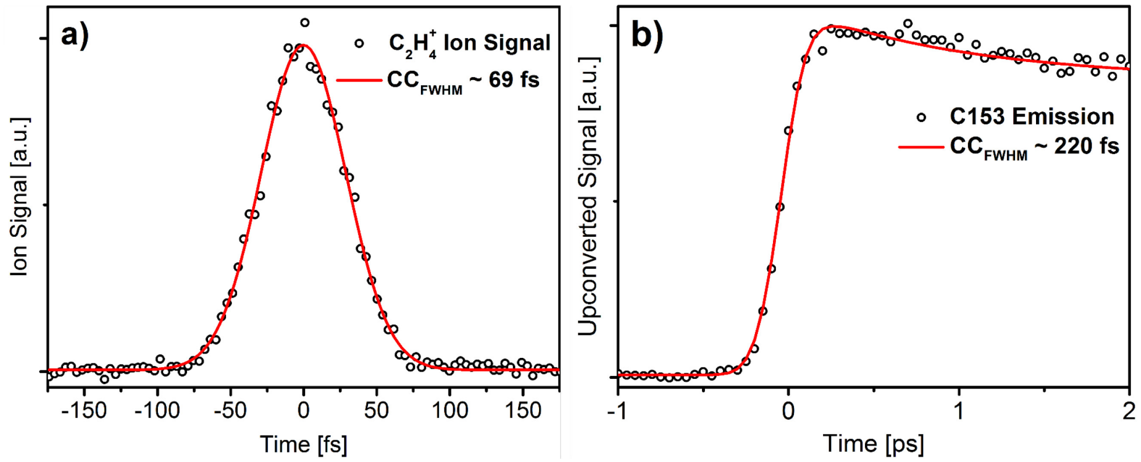

Figure 2.17. *Examples of CC functions derived for TR-IY (a) and FuC (b) setups: a) The ethylene⁺ 1+4' nonresonant ionization signal, registered with 260 nm excitation and 800 nm probe, is used as zero delay time reference and fits with a Gaussian of ~69 fs (FWHM). b) The rise-time of coumarine 153 in dichloromethane at 495 nm emission wavelength after 267 nm excitation fits with a Gaussian with width of ~220 fs (FWHM).*

2.5.1.2. Time- and Frequency-Resolved Data

Since TA experiments yield two-dimensional data sets, where one independent dimension is given by the probe wavelength and the other one by the pump-probe time delay, it is possible to obtain a qualitative perspective of the dynamical processes in play by modelling all the probe wavelengths simultaneously. For this purpose, a global fitting procedure[35, 51-53] is employed, for which it is assumed that time and wavelength dependence of the data are separable and therefore all the transients are fitted to a sum of *n* exponential functions convoluted with a Gaussian CC function:

$$S(\lambda_{pr},t)=\sum_{i}^{n} A_i(\lambda_{pr})e^{-t/\tau_i}\otimes R(\lambda_{pr},t') \tag{2.12}$$

where $A_i(\lambda_{pr})$ is the decay-associated spectrum (DAS) for the corresponding *i*th exponential function with lifetime τ_i. Since all the probe wavelengths are modelled at once, common τ_i lifetimes are iterated for every probe wavelength, while the value of $A_i(\lambda_{pr})$ varies for each wavelength. In our experiments the global lifetime analysis is carried out in two steps by using a custom LabVIEW virtual instrument: Firstly, the lifetime of *n* exponential components is extracted for a set of fixed probe wavelengths. Then, the pre-exponential factors of those common lifetimes are obtained for all the probe wavelengths, enabling us to plot the DAS (A_i *vs.* λ_{pr}), which makes possible a clear visualization of the different spectral contributions, especially when they are spectrally overlapped. In general, three exponential are sufficient to model the collected data at the entire probe window.

2.5.2. *Ab initio* Calculations

A brief overview of the computational methods employed to predict the involved electronic states and, in some cases, the minimum energy pathways (MEPs) is given here. Firstly, in the experiments presented in this thesis the ground state geometries are mainly optimized with density functional theory (DFT) using the Coulomb attenuated model Becke-3rd parameter, Lee-Yang-Parr (CAM-B3LYP)[54] functional with the Pople type 6-311++G(d,p)[55-56] basis and Grimme's Dispersion with Becke-Johnson damping (GD3BJ).[57-58] However, in some cases the M06-2X[59] or Perdew-Burke-Ernzerhof parameter-free (PBE0)[60] functionals are also employed. Furthermore, we also use *ab initio* methods such as the Møller–Plesset second order perturbation theory (MP2)[61] to optimize the ground state of some specific compounds. Secondly, for the optimization of excited states structures and the calculation of vertical excitation energies (VEEs) and oscillator strengths, time-dependent density functional theory (TD-DFT) using the CAM-B3LYP functional with the 6-311++G(d,p) basis with GD3BJ dispersion is mainly employed. Unrelaxed energy scans along selected vibrational coordinates are also computed at this level. Binding energies are calculated when required by including the Boys and Bernardi counterpoise correction for removing the basis set superposition error (BSSE).[62] All these methods are implemented in Gaussian 09 computational package.[63]

It is important to note that some of the theoretical calculations presented in this thesis have been performed by other research groups in the context of established collaborations. In this regard, Prof. Lluís Blancafort from Universitat de Girona conducted the calculations for understanding the relaxation pathways of a set of isolated azaindole isomers in Chapter 3. Likewise, in Chapter 7, Prof. Diego Sampedro from Universidad de La Rioja modelled the main relaxation channels for a family of synthetic sunscreens. Further details regarding each specific problem will be given in Chapters 3-7.

2.6. References

1. Brun, A.; Georges, P.; Saux, G. L.; Salin, F., Single-shot characterization of ultrashort light pulses. *Journal of Physics D: Applied Physics* **1991,** *24* (8), 1225-1233.

2. O'Shea, P.; Kimmel, M.; Gu, X.; Trebino, R., Highly simplified device for ultrashort-pulse measurement. *Optics letters* **2001,** *26* (12), 932-934.

3. Boyd, R. W., *Nonlinear Optics, Third Edition*. Academic Press, Inc.: 2008.

4. Greenfield, S. R.; Wasielewski, M. R., Near-transform-limited visible and near-IR femtosecond pulses from optical parametric amplification using Type II ß-barium borate. *Optics Letters* **1995,** *20* (12), 1394-1396.

5. Enqvist, H., A Setup for Efficient Frequency Tripling of High-Power Femtosecond Lasers Pulses. *Lund Reports in Atomic Physics* **2004**.

6. Franken, P. A.; Hill, A. E.; Peters, C. W.; Weinreich, G., Generation of Optical Harmonics. *Physical Review Letters* **1961,** *7* (4), 118-119.

7. Antonov, V. S.; Knyazev, I. N.; Letokhov, V. S.; Matiuk, V. M.; Movshev, V. G.; Potapov, V. K., Stepwise laser photoionization of molecules in a mass spectrometer: a new method for probing and detection of polyatomic molecules. *Optics Letters* **1978,** *3* (2), 37-39.

8. Seel, M.; Domcke, W., Model studies on femtosecond time-resolved ionization spectroscopy of excited-state vibrational dynamics and vibronic coupling. *Chemical Physics* **1991,** *151* (1), 59-72.

9. Staniforth, M.; Stavros, V. G., Recent advances in experimental techniques to probe fast excited-state dynamics in biological molecules in the gas phase: dynamics in nucleotides, amino acids and beyond. *Proceedings of the Royal Society A: Mathematical, Physical and Engineering Sciences* **2013,** *469* (2159), 20130458.

10. Roberts, G. M.; Stavros, V. G., The role of $\pi\sigma^*$ states in the photochemistry of heteroaromatic biomolecules and their subunits: insights from gas-phase femtosecond spectroscopy. *Chemical Science* **2014,** *5* (5), 1698-1722.

11. Stavros, V. G.; Verlet, J. R., Gas-phase femtosecond particle spectroscopy: a bottom-up approach to nucleotide dynamics. *Annual Review of Physical Chemistry* **2016,** *67*, 211-232.

12. Wiley, W. C.; McLaren, I. H., Time-of-flight mass spectrometer with improved resolution. *Review of scientific instruments* **1955,** *26* (12), 1150-1157.

13. Estermann, I., Molecular beam technique. *Reviews of modern physics* **1946,** *18* (3), 300.

14. Levy, D. H., Laser spectroscopy of cold gas-phase molecules. *Annual Review of Physical Chemistry* **1980,** *31* (1), 197-225.

15. Pendlebury, J. M.; Smith, K. I., Molecular beams. *Contemporary Physics* **1987,** *28* (1), 3-32.

16. Baskin, J. S.; Zewail, A. H., Femtosecond Real-Time Probing of Reactions. 15. Time-Dependent Coherent Alignment. *The Journal of physical chemistry* **1994,** *98* (13), 3337-3351.

17. Imanbaew, D.; Gelin, M. F.; Riehn, C., Rotational and vibrational dynamics in the excited electronic state of deprotonated and protonated fluorescein studied by time-resolved photofragmentation in an ion trap. *Structural Dynamics* **2016,** *3* (4), 043211.

18. Pereira, M. A.; Share, P. E.; Sarisky, M. J.; Hochstrasser, R. M., Ultrafast rotational dynamics of electronically excited aniline molecules in solution from ultraviolet femtosecond fluorescence anisotropies.

The Journal of chemical physics **1991,** *94* (4), 2513-2522.

19. Hertel, I. V.; Radloff, W., Ultrafast dynamics in isolated molecules and molecular clusters. *Reports on Progress in Physics* **2006,** *69* (6), 1897-2003.

20. Demtröder, W., *Laser spectroscopy*. Springer: 1973; Vol. 5.

21. Zwier, T. S., Laser spectroscopy of jet-cooled biomolecules and their water-containing clusters: Water bridges and molecular conformation. *The Journal of Physical Chemistry A* **2001,** *105* (39), 8827-8839.

22. Shubert, V. A.; Zwier, T. S., IR- IR- UV Hole-Burning: Conformation Specific IR Spectra in the Face of UV Spectral Overlap. *The Journal of Physical Chemistry A* **2007,** *111* (51), 13283-13286.

23. Montero, R. l.; León, I.; Fernández, J. A.; Longarte, A., Femtosecond excited state dynamics of size selected neutral molecular clusters. *The journal of physical chemistry letters* **2016,** *7* (14), 2797-2802.

24. Berera, R.; van Grondelle, R.; Kennis, J. T. M., Ultrafast transient absorption spectroscopy: principles and application to photosynthetic systems. *Photosynthesis Research* **2009,** *101* (2), 105-118.

25. Bradler, M.; Baum, P.; Riedle, E., Femtosecond continuum generation in bulk laser host materials with sub-μJ pump pulses. *Applied Physics B* **2009,** *97* (3), 561.

26. Kovalenko, S. A.; Dobryakov, A. L.; Ruthmann, J.; Ernsting, N. P., Femtosecond spectroscopy of condensed phases with chirped supercontinuum probing. *Physical Review A* **1999,** *59* (3), 2369-2384.

27. Maciejewski, A.; Naskrecki, R.; Lorenc, M.; Ziolek, M.; Karolczak, J.; Kubicki, J.; Matysiak, M.; Szymanski, M., Transient absorption experimental set-up with femtosecond time resolution. Femto-and picosecond study of DCM molecule in cyclohexane and methanol solution. *Journal of Molecular Structure* **2000,** *555* (1-3), 1-13.

28. Megerle, U.; Pugliesi, I.; Schriever, C.; Sailer, C. F.; Riedle, E., Sub-50 fs broadband absorption spectroscopy with tunable excitation: putting the analysis of ultrafast molecular dynamics on solid ground. *Applied Physics B* **2009,** *96* (2-3), 215-231.

29. Abramczyk, H., *Introduction to laser spectroscopy*. Elsevier: 2005.

30. Johnson, P. J. M.; Prokhorenko, V. I.; Miller, R. J. D., Stable UV to IR supercontinuum generation in calcium fluoride with conserved circular polarization states. *Opt. Express* **2009,** *17* (24), 21488-21496.

31. Rulliere, C., *Femtosecond laser pulses*. Springer: 2005.

32. Dietzek, B.; Pascher, T.; Sundström, V.; Yartsev, A., Appearance of coherent artifact signals in femtosecond transient absorption spectroscopy in dependence on detector design. *Laser Physics Letters* **2007,** *4* (1), 38-43.

33. Kovalenko, S. A.; Ernsting, N. P.; Ruthmann, J., Femtosecond hole-burning spectroscopy of the dye DCM in solution: the transition from the locally excited to a charge-transfer state. *Chemical Physics Letters* **1996,** *258* (3), 445-454.

34. Raytchev, M.; Pandurski, E.; Buchvarov, I.; Modrakowski, C.; Fiebig, T., Bichromophoric

Interactions and Time-Dependent Excited State Mixing in Pyrene Derivatives. A Femtosecond Broad-Band Pump−Probe Study. *The Journal of Physical Chemistry A* **2003,** *107* (23), 4592-4600.

35. Beckwith, J. S.; Rumble, C. A.; Vauthey, E., Data analysis in transient electronic spectroscopy – an experimentalist's view. *International Reviews in Physical Chemistry* **2020,** *39* (2), 135-216.

36. Diels, J.-C.; Rudolph, W., *Ultrashort laser pulse phenomena*. Elsevier: 2006.

37. Ziolek, M.; Lorenc, M.; Naskrecki, R., Determination of the temporal response function in femtosecond pump-probe systems. *Applied Physics B* **2001,** *72* (7), 843-847.

38. Ziolek, M.; Naskrecki, R.; Lorenc, M.; Karolczak, J.; Kubicki, J.; Maciejewski, A., The influence of the excitation geometry on the temporal resolution in femtosecond pump–probe experiments. *Optics Communications* **2001,** *197* (4-6), 467-473.

39. Lorenc, M.; Ziolek, M.; Naskrecki, R.; Karolczak, J.; Kubicki, J.; Maciejewski, A., Artifacts in femtosecond transient absorption spectroscopy. *Applied Physics B* **2002,** *74* (1), 19-27.

40. Rasmusson, M.; Tarnovsky, A. N.; Åkesson, E.; Sundström, V., On the use of two-photon absorption for determination of femtosecond pump–probe cross-correlation functions. *Chemical physics letters* **2001,** *335* (3-4), 201-208.

41. Alfano, R. R.; Baldeck, P. L.; Ho, P. P.; Agrawal, G. P., Cross-phase modulation and induced focusing due to optical nonlinearities in optical fibers and bulk materials. *J. Opt. Soc. Am. B* **1989,** *6* (4), 824-829.

42. Lapini, A.; Vázquez, S. M.; Touceda, P. T.; Lima, M., Cross-phase modulation in visible-pump/mid-infrared-probe spectroscopy. *Journal of Molecular Structure* **2011,** *993* (1), 470-473.

43. Träger, F., *Springer handbook of lasers and optics*. Springer Science & Business Media: 2012.

44. Chosrowjan, H.; Taniguchi, S.; Tanaka, F., Ultrafast fluorescence upconversion technique and its applications to proteins. *The FEBS journal* **2015,** *282* (16), 3003-3015.

45. Kahlow, M. A.; Jarzęba, W. o.; DuBruil, T. P.; Barbara, P. F., Ultrafast emission spectroscopy in the ultraviolet by time-gated upconversion. *Review of scientific instruments* **1988,** *59* (7), 1098-1109.

46. Lakowicz, J. R., *Principles of fluorescence spectroscopy*. Springer science & business media: 2013.

47. Xu, J.; Knutson, J. R., Chapter 8 Ultrafast Fluorescence Spectroscopy via Upconversion: Applications to Biophysics. In *Methods in Enzymology*, Academic Press: 2008; Vol. 450, pp 159-183.

48. Soren Pedersen Ahmed, H. Z., Femtosecond real time probing of reactions XXII Kinetic description of probe absorption fluorescence depletion and mass spectrometry. *Molecular Physics* **1996,** *89* (5), 1455-1502.

49. Cannizzo, A.; Bräm, O.; Zgrablic, G.; Tortschanoff, A.; Oskouei, A. A.; van Mourik, F.; Chergui, M., Femtosecond fluorescence upconversion setup with broadband detection in the ultraviolet. *Optics Letters* **2007,** *32* (24), 3555-3557.

50. Gustavsson, T.; Sharonov, A.; Onidas, D.; Markovitsi, D., Adenine, deoxyadenosine and deoxyadenosine 5′-monophosphate studied by femtosecond fluorescence upconversion spectroscopy. *Chemical Physics Letters* **2002,** *356* (1), 49-54.

51. Ruckebusch, C.; Sliwa, M.; Pernot, P. d.; De Juan, A.; Tauler, R., Comprehensive data analysis of femtosecond transient absorption spectra: A review. *Journal of Photochemistry and Photobiology C: Photochemistry Reviews* **2012,** *13* (1), 1-27.

52. Van Stokkum, I. H. M.; Larsen, D. S.; Van Grondelle, R., Global and target analysis of time-resolved spectra. *Biochimica et Biophysica Acta (BBA)-Bioenergetics* **2004,** *1657* (2-3), 82-104.

53. van Wilderen, L. J. G. W.; Lincoln, C. N.; van Thor, J. J., Modelling Multi-Pulse Population Dynamics from Ultrafast Spectroscopy. *PLOS ONE* **2011,** *6* (3), e17373.

54. Yanai, T.; Tew, D. P.; Handy, N. C., A new hybrid exchange–correlation functional using the Coulomb-attenuating method (CAM-B3LYP). *Chemical Physics Letters* **2004,** *393* (1), 51-57.

55. Krishnan, R.; Binkley, J. S.; Seeger, R.; Pople, J. A., Self-consistent molecular orbital methods. XX. A basis set for correlated wave functions. *The Journal of Chemical Physics* **1980,** *72* (1), 650-654.

56. Frisch, M. J.; Pople, J. A.; Binkley, J. S., Self-consistent molecular orbital methods 25. Supplementary functions for Gaussian basis sets. *The Journal of Chemical Physics* **1984,** *80* (7), 3265-3269.

57. Grimme, S.; Antony, J.; Ehrlich, S.; Krieg, H., A consistent and accurate ab initio parametrization of density functional dispersion correction (DFT-D) for the 94 elements H-Pu. *The Journal of Chemical Physics* **2010,** *132* (15), 154104.

58. Grimme, S.; Ehrlich, S.; Goerigk, L., Effect of the damping function in dispersion corrected density functional theory. *Journal of Computational Chemistry* **2011,** *32* (7), 1456-1465.

59. Zhao, Y.; Truhlar, D. G., The M06 suite of density functionals for main group thermochemistry, thermochemical kinetics, noncovalent interactions, excited states, and transition elements: two new functionals and systematic testing of four M06-class functionals and 12 other functionals. *Theoretical Chemistry Accounts* **2008,** *120* (1), 215-241.

60. Adamo, C.; Barone, V., Toward reliable density functional methods without adjustable parameters: The PBE0 model. *The Journal of Chemical Physics* **1999,** *110* (13), 6158-6170.

61. Head-Gordon, M.; Pople, J. A.; Frisch, M. J., MP2 energy evaluation by direct methods. *Chemical Physics Letters* **1988,** *153* (6), 503-506.

62. Boys, S. F.; Bernardi, F., The calculation of small molecular interactions by the differences of separate total energies. Some procedures with reduced errors. *Molecular Physics* **1970,** *19* (4), 553-566.

63. Frisch, M.; Trucks, G.; Schlegel, H.; Scuseria, G.; Robb, M.; Cheeseman, J.; Scalmani, G.; Barone, V.; Mennucci, B.; Petersson, G.; Nakatsuji, H.; Caricato, M.; Li, X.; Hratchian, H. P.; Izmaylov, A. F.; Bloino, J.; Zheng, G.; Sonnenberg, J. L.; Hada, M.; Ehara, M.; Toyota, K.; Fukuda, R.; Hasegawa, J.; Ishida, M.; Nakajima, T.; Honda, Y.; Kitao, O.; Nakai, H.; Vreven, T.; Montgomery Jr., J. A.; Peralta, J. E.;

Ogliaro, F.; Bearpark, M. J.; Heyd, J. J.; Brothers, E. N.; Kudin, K. N.; Staroverov, V. N.; Kobayashi, R.; Normand, J.; Raghavachari, K.; Rendell, A. P.; Burant, J. C.; Iyengar, S. S.; Tomasi, J.; Cossi, M.; Rega, N.; Millam, J. M.; Klene, M.; Knox, J. E.; Cross, J. B.; Bakken, V.; Adamo, C.; Jaramillo, J.; Gomperts, R.; Stratmann, R. E.; Yazyev, O.; Austin, A. J.; Cammi, R.; Pomelli, C.; Ochterski, J. W.; Martin, R. L.; Morokuma, K.; Zakrzewski, V. G.; Voth, G. A.; Salvador, P.; Dannenberg, J. J.; Dapprich, S.; Daniels, A. D.; Farkas, O.; Foresman, J. B.; Ortiz, J. V.; Cioslowski, J.; Fox, D. J., Gaussian 09, rev. D. 01. *Gaussian Inc., Wallingford CT* **2009,** *19*, 227-238.

3. Photodynamics of Isolated Azaindoles

3.1. Introduction

The photophysics of azaindoles (AIs) is relevant in a biological context because of their chemical proximity to the DNA purine bases, adenine and guanine. They can be seen as a simplified version of adenine where only one instead of three indole carbon atoms are substituted by nitrogen (see the structures in Figure 3.1). In fact, these molecules have been considered as fundamental steps for a bottom-up approach to understand the relaxation pathways operative in DNA,[1] since one can discern the role of the different structural components, by individuating how the position of the pyridinic nitrogen atoms in the six-membered purine ring modulates the photophysics. AIs have been also proposed as blue fluorescent protein markers for *in vivo* imaging studies because they can replace tryptophan in peptides.[2-3] In spite of this intrinsic interest, the photophysics of the AI isomers, apart from 7-AI, have not received much attention up to now. 7-AI dimers[4-8] and water and alcohol clusters[6, 9-13] have been extensively studied as mimics of DNA base pairs and H-bonded networks, respectively. The isolated monomers have also been studied by theory and experiment,[7, 10, 14-18] but there are no time-resolved studies of the excited state dynamics. For the remaining isomers, only some studies in solution, which mainly focus on their aggregation properties, are available[2, 19-21] and no gas-phase studies on the photophysics have appeared.

The research presented in this chapter explores the relaxation mechanisms of a set of AI structural isomers (see Figure 3.1) in the isolated-phase tracked by TR-IY spectroscopy. The interpretation of the measured photodynamics has been grounded in MS-CASPT2//TD-DFT calculations of the excited state decay paths. For the set of isomers, the study permits us to postulate a common path involving a puckering mode of the pyridinic ring, which depending on the position of the nitrogen atom induces remarkably different excited state relaxation rates. Along this pathway, the nπ* state plays a key role by controlling the access to a CI with the ground state that mediates the IC process.

Additionally, we have studied how the photophysics of isolated AIs is altered by the addition of different solvents in order to establish the effect of the environment on the relevant $\pi\pi$* and nπ* states, in terms of polarity and specific interactions such as hydrogen bonding. These results will be provided in the next chapter.

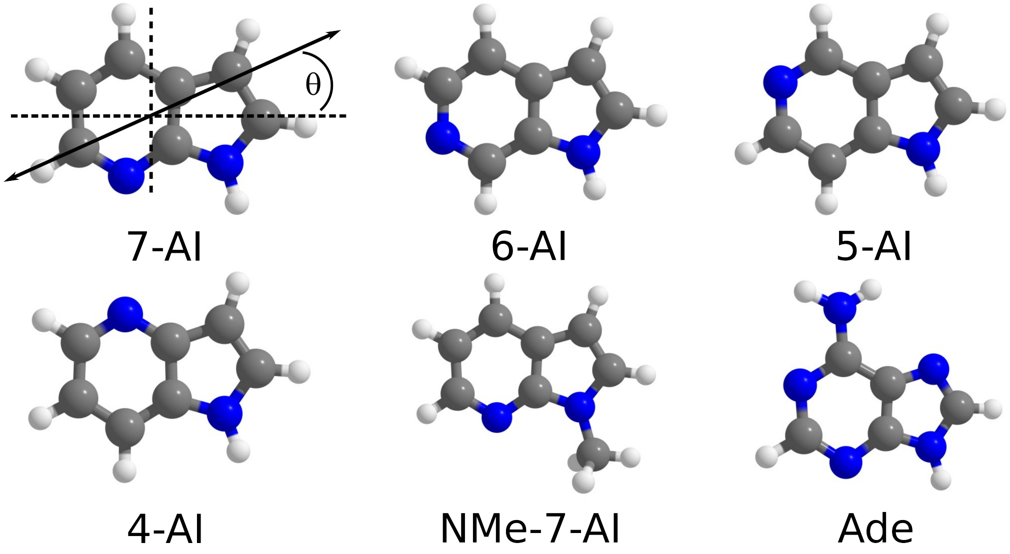

Figure 3.1. *Structures of AI derivatives considered in this work and adenine (Ade). The 7-AI structure shows the two axes of inertia (dashed lines) and the definition of the angle θ formed between the $\pi\pi^*$ transition dipole moment vector (double headed arrow) and the long axis.*

3.2. Experimental Methods

The experimental setup for the TR-IY experiments has been fully described in Chapter 2, section 2.3. 4-AI, 5-AI, and 6-AI (98%) were purchased from Alfa Aesar, while 7-AI (98%) and NMe-7-AI (95%) were acquired from Sigma-Aldrich and ABCR Chemie, respectively. All the samples were employed without further purification. The vapor pressure of the targeted samples, heated at temperatures that varied between 80 and 125 ºC, was mixed with 1.5-2 atm of Ar to form a supersonic expansion. After passing through a 0.8 mm skimmer, the molecules of interest were ionized by two-color pump-probe fs laser pulses. A fine control of the valve operation conditions and in particular, of the valve-laser synchronization, was mandatory to avoid the appearance of cluster fragments in the monomer mass channel (see the following section 3.2.1).

The generation of fs laser pulses was described in detail in section 2.1. Briefly, the commercial Coherent Mantis – Legend Elite oscillator-regenerative amplifier laser system yields a 1 kHz train of 35 fs pulses centered at 800 nm, with 3.5 mJ of energy per pulse. The excitation beam was tuned in the 305-250 nm range by the second harmonic of the SFG of the idler and signal of OPA2, and the 800 nm fundamental beam. The third harmonic of the fundamental at 267 nm was also used as pump beam in some measurements. For the probe, the fundamental 800 nm radiation was employed in most of the experiments. Alternatively, the second harmonic (400 nm) or 1305 nm pulses from OPA1 were also used. The pump and probe beams were focused in the ionization region by spherical mirrors, reaching intensities in the order of 10^9 and 10^{11}-10^{12} W cm^{-2}, respectively, below the threshold to produce any measurable ion in the absence of the probe. The magic angle configuration (54.7 º) was adopted for the relative polarization of the pump and probe beams. In order to derive the CC function, the 1+4' (1+5' for the 1305 nm probe) nonresonant ionization signal of ethylene was acquired simultaneously to the ion of interest. Depending on the pump-probe wavelengths, values between 70 and 90 fs were measured for the CC function.

3.2.1. Formation of 7-AI homoclusters

7-AI forms very stable homodimers, ((7-AI)$_2$ binding energy > 20 kcal mol^{-1}), which unfortunately can interfere in the detection of the isolated monomer, especially when ionization based detection schemes are employed. The formed dimers can fragment during the ionization and therefore they will be detected in the monomer mass channel. To avoid the formation of the dimers and/or minimize their contribution to the monomer mass channel signal, a fine-tuning of the experimental conditions is required, particularly those related to the expansion such as the stagnation pressure and the laser-valve timing. In order to illustrate the influence of these parameters, mass spectra and transients at the 7-AI monomer (118 Da) and (7-AI)$_2$ dimer (236 Da) mass channels were recorded at different laser-valve delays, following excitation and ionization at 289 and 800 nm, respectively, as shown in Figure 3.2. Previously, the optimum conditions of heating temperature and carrier gas (Ar) pressure were established at 125 ºC and 1.5 atm, in that order. Figure 3.2a$_i$ exhibit measurements recorded in the presence of dimers in the interrogated region of the expansion. Indeed, at 9.51 ms (490 μs) laser-valve delays the transient collected in the dimer channel (Figure 3.2a$_3$) shows the well-known dynamical signature that has been previously attributed to the dimer.[4, 8, 22-25] Additionally, the presence of a long-lived background suggests the formation of bigger clusters. These features are considerably weaker but still perceptible at 9.54 ms (460 μs) laser-valve delays, as shown in Figure 3.2b$_3$. Simultaneously, the monomer mass channels in Figure 3.2a$_2$ and 3.2b$_2$ show a rising component that can be attributed to the dynamics of fragmenting clusters. On the other hand, the data shown in Figure 3.2c$_i$ were recorded at laser-valve delays that minimize the formation of clusters. Under these conditions, the dimer channel does not show any meaningful signal, while the decays of the monomer channel can be safely assigned to the isolated 7-AI molecule.

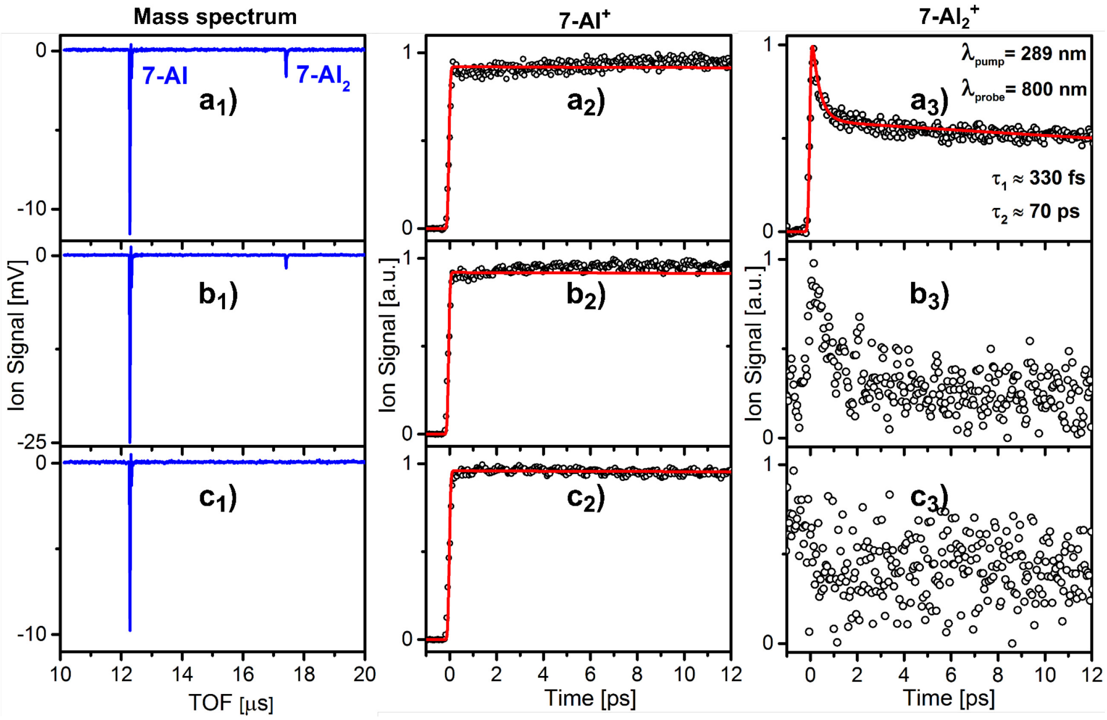

Figure 3.2. *Mass spectra (a_1, b_1 and c_1) and transients recorded at the 7-AI$^+$ (a_2, b_2 and c_2) and (7-AI)$_2^+$ (a_3, b_3 and c_3) mass channels at three different laser-valve delays: 9.51 (a_i), 9.54 (b_i) and 9.58 ms (c_i). The pump and probe wavelengths were 289 and 800 nm, respectively, for all the TR-IY measurements.*

3.3. Computational Methods

Quantum mechanical calculations were performed by Prof. Lluís Blancafort (Universitat de Girona) in order to describe the relaxation pathways of the different AI isomers in vacuum. The decay paths on the excited state potential energy surface were calculated combining time-dependent density functional theory (TD-DFT) and multi-state complete active space second order perturbation (MS-CASPT2) calculations, *i.e.* MS-CASPT2//TD-DFT. In this approach, the reaction paths are firstly optimized at the TD-DFT level, which is computationally efficient but does not account for multireference effects (static correlation). To account for these effects, the energies are refined with MS-CASPT2 single-point calculations along the TD-DFT path.

For the TD-DFT paths, the ππ* and nπ* minima were initially optimized, labelled ππ*-DFT and nπ*-DFT, the conical intersection (CI), and the transition structure (TS) connecting the CI with nπ*-DFT. The path from the Franck-Condon structure to ππ*-DFT was obtained with a linear interpolation in internal coordinates (LIIC). For 5-AI and

6-AI, $\pi\pi^*$-DFT is a first-order saddle point of C_s symmetry, and the path from $\pi\pi^*$-DFT to nπ^*-DFT is obtained with an intrinsic reaction coordinate (IRC) calculation.[26] For 7-AI, $\pi\pi^*$-DFT is a minimum, and the path to nπ^*-DFT is obtained with a LIIC. To complete the decay profile, in all cases the path from nπ^*-DFT to the CI was obtained with IRC calculations from the TS started in both directions. TD-DFT was preferred over CASSCF for the calculation of the paths because the $\pi\pi^*$ states with ^1L_a character were poorly described at the CASSCF level, resulting in a wrong order of the states in the Franck-Condon region.

In the MS-CASPT2//TD-DFT potential energy profiles (see Figure 3.3), the MS-CASPT2 minima did not coincide with the TD-DFT critical points because of the different vibronic $\pi\pi^*$/nπ^* interaction. This is due to the different gap between the $\pi\pi^*$ and nπ^* states at the two levels of theory. However the effect on the energetic description of the path is small because the surface is very shallow, and the MS-CASPT2 energy profiles retain the main features of the TD-DFT profiles. The MS-CASPT2 barriers were calculated as the difference between the lowest energy point before the TS, labelled S_1-Min, and that of the highest energy point along the path to the CI.

For the TD-DFT calculations, the CAM-B3LYP functional with the 6-311G(d,p) basis was used. The TD-DFT optimizations were carried out with Gaussian 16[27] package, and the CI optimizations at the TD-DFT level were conducted with a home implementation of the double-Newton-Raphson CI optimization algorithm[28] adapted to TD-DFT, using the nonadiabatic coupling vector for the projection.[29] In all cases the implementation of the full pseudo-eigenvalue TD-DFT equation[30] was employed, except for the CI optimizations, where the Tamm–Dancoff approximation was used to improve convergence.

For the MS-CASPT2 calculations, the ANO-L basis set with 4s3p2d contraction for C and N and 3s2p for H was employed. The complete active space self-consistent field calculations underlying MS-CASPT2 were carried out with an active space of 12 electrons in 10 orbitals (the nitrogen lone pair and the 9 π orbitals), state averaging over 8 states with equal weights. Such a number of states was necessary because of the poor CASSCF description of the states with ^1L_a character, which leads to substantial coupling of the lowest $\pi\pi^*$ states with the higher states in the MS-CASPT2 effective Hamiltonian. These calculations were conducted with Molcas 7.8.[31-32] For the MS-CASPT2 part we used an imaginary shift[33] of 0.1 a.u. and the ionization potential electron affinity correction[34] of 0.25 a.u., which is the default in Molcas 7.8.

3.4. Results and Discussion

The three lowest MS-CASPT2 vertical excitation energies (VEEs) of 4-AI, 5-AI, 6-AI and 7-AI are summarized in Table 3.1, together with the oscillator strength (*f*) and the direction of the transition dipole moment with respect to the long molecular axis (θ) (see Figure 3.1). For comparison, the data of adenine are also provided.[35] Moreover, Table 3.2 illustrates a comparison of the vertical excitations calculated for 7-AI with previous theoretical estimates, showing that the results for 7-AI are in qualitative agreement with previous CASPT2 studies.

For all isomers, there are three excited states near the excitation window of 300-267 nm: two bright ππ* transitions (oscillator strength 0.03-0.09) and an almost dark nπ* state (oscillator strength < 0.01). The lowest S_1 electronic state is a ππ* state, lying at 4.95 eV for 5-AI and 4.69 eV for the other isomers. The nπ* state is S_2 for 6-AI, and S_3 for 4-AI, 5-AI and 7-AI. It lies 0.15-0.64 eV above S_1. Finally, the higher-lying ππ* state lies between 4.77 and 5.05 eV. In the ππ* states, the transition dipole moment forms angles (θ) with absolute values of 0–73° with respect to the long axis of inertia, *i.e.* the ππ* states have intermediate character between ^1L_a and ^1L_b (the excitation polarization vectors are included as additional information in Figure 3.11). For comparison, in adenine the lowest S_1 state has the nπ* character.

Table 3.1. *MS-CASPT2(12,10)/ANO-L vertical excitations VEEs (in eV), oscillator strength f and angle θ (°) of the transition dipole moment with respect to the long axis of inertia for the four AI isomers and adenine.*

	4-AI			**5-AI**			**6-AI**			**7-AI[a]**			**Ade[b]**	
	***VEE* [eV]**	***f***	***θ* [°]**	***VEE* [eV]**	***f***	***θ* [°]**	***VEE* [eV]**	***f***	***θ* [°]**	***VEE* [eV]**	***f***	**[°]**	***VEE* [eV]**	***f***
S_1	4.69	0.099	0	4.95	0.028	-38	4.69	0.083	-73	4.69	0.043	45	4.85	0.006
S_2	4.83	0.065	52	5.06	0.050	-63	5.08	0.006	–	4.77	0.081	-26	5.09	0.004
S_3	4.94	0.007	–	5.10	0.003	–	5.14	0.064	-40	5.33	0.008	–	5.44	0.180

[a]See Table 3.2 for a comparison with previous theoretical data. [b]Reference 35. Oscillator strengths calculated at the CASPT2 level.

Table 3.2. *Comparison of vertical excitations of 7-AI calculated in this work with previous theoretical works.*

	S_1			**S_2**			**S_3**		
	***VEE* [eV]**	***f***	***θ* [°]**	***VEE* [eV]**	***f***	***θ* [°]**	***VEE* [eV]**	***f***	***θ* [°]**
MS-CASPT2/ ANO-L[a]	4.69	0.043	45	4.77	0.081	-26	5.33	0.008	–
EOM-CCSD/ aug-cc-pvtz[b]	4.85 (ππ*)	–	–	5.19 (ππ*)	–	–	5.40 (nπ*)	–	–
B2PLYP/ 6-311+g(2d,p)[c]	5.09	0.042	–	4.96	0.187	–	5.66	0.003	–
SACCI/cc-pvtz[d]	4.03	0.094	28	4.23	0.159	–	4.61	0.005	–
CASPT2/ANO[e]	4.22	0.043	27	4.49	0.072	-29	5.27	0.008	–
CASPT2/ 6-31g(d,p)[f]	4.43	0.049	30	4.95	0.069	-34	–	–	–

[a]This work. [b]Reference 15. [c]Reference 14; basis set includes Rydberg [2s,2p] diffuse functions on C,N atoms. [d]Reference 14; cc-pvdz for H; basis set on C,N atoms includes [2s,2p,2d] diffuse functions. [e]Reference 7. [f]Reference 16.

The MS-CASPT2//TD-DFT energy profiles for the excited state decay of the three AI isomers studied experimentally are presented in Figure 3.3a-c. The positions of the critical points are marked with asterisks: ππ*-DFT and nπ*-DFT are the TD-DFT optimized structures, whereas S_1-Min and S_1-TS are the lowest and highest energy points along the MS-CASPT2 path, which are used to calculate the MS-CASPT2 decay barriers. The MS-CASPT2 energy of the critical points is shown in Table 3.3, while the TD-DFT data are provided as supporting data in Table 3.5. Moreover, in section 3.6, Additional Information, the TD-DFT decay profiles are displayed in Figure 3.12, while the optimized structures are depicted in Figure 3.13.

Table 3.3. *MS-CASPT2(12,10)/ANO-L energies of critical points for 5AI-, 6-AI and 7-AI along the TD-CAM-B3LYP optimized decay paths.*

	E(S_1), MS-CASPT2[a] [eV]		
	5-AI	**6-AI**	**7-AI**
Franck-Condon	4.95 (0.028)	4.69 (0.083)	4.69 (0.043)
ππ*-DFT	4.52 (0.137)	4.29 (0.141)	4.26 (0.152)[b]
nπ*-DFT	4.38 (0.006)	4.27 (0.027)	4.34 (0.081)
S_1-Min[c]	4.25 (0.040)	4.27 (0.125)	4.19 (0.135)
TS[d]	4.38 (0.006)	4.34 (0.022)	4.60 (0.037)
S_1/S_0-CI[e]	3.92 ± 0.07 (-) [4.14 ± 0.08]	4.17 ± 0.13 (-) [4.22 ± 0.09]	4.15 ± 0.05 (-) [4.21 ± 0.29]

[a]Single-point energy on the TD-DFT optimized structures, oscillator strength in brackets. [b]MS-CASPT2 energy of second *ππ** minimum: 4.42, oscillator strength: 0.067. [c]Lowest-energy point in the Franck-Condon region at the MS-CASPT2 level. [d]Highest-energy point along the MS-CASPT2 path to the CI. [e]Average of S_1 and S_0 MS-CASPT2 energy ± half of the S_1-S_0 energy gap at the TD-DFT optimized CI; energy of higher-energy CIs provided in squares brackets.

The excited state paths lead from the Franck-Condon structure to the *ππ**-DFT, further to n*π**-DFT and from there to a CI with the ground state. The Franck-Condon region of the potential energy surface, *i.e.* the region where the molecule is planar or has only moderate puckering as opposed to the strongly puckered structures near the CI, shows strong vibronic coupling between the *ππ** and n*π** states. At the TD-DFT level, the *ππ** state optimized critical points for 5-AI and 6-AI are saddle points of C_s symmetry, and the lowest-energy structure in the Franck-Condon region is a minimum of C_1 symmetry with n*π** configuration. The minima along the MS-CASPT2 profile, S_1-Min, do not coincide with the TD-DFT minima because of the different vibronic *ππ**/n*π** interaction (see section 3.3, Computational Methods). For 5-AI, S_1-Min is a non-planar structure with mixed *ππ**/n*π** character, whereas for 6-AI it is a nearly planar structure with *ππ** character.

In contrast to 5-AI and 6-AI, for 7-AI there are three different TD-DFT critical points in the Franck-Condon region: two planar ones for the *ππ** states with relative energy of 4.26 and 4.42 eV, and a non-planar one for the n*π** state with relative MS-CASPT2 energy of 4.34 eV (see Table 3.3). We have considered the path involving the lowest *ππ** and the n*π** DFT critical points. At the MS-CASPT2 level, the lowest-energy structure in the Franck-Condon region, S_1-Min, lies along the LIIC between *ππ**-DFT and n*π**-DFT. It is non-planar and has predominant *ππ** character. The calculated transition dipole moment at S_1-Min has a negative angle of -30° with respect to the long inertial axis *a*, which is consistent with the experimental value of -14° measured for the 0–0 transition.[17] In fact, the S_1 state at S_1-Min correlates with S_2 at the vertical excitation geometry, which explains the discrepancies observed previously between the transition dipole moment direction calculated at that geometry for S_1 at different levels of theory,[14, 16, 36] and the experimentally determined one.[17] There is also good agreement between the calculated energy of the S_1-Min structures (4.52 for 5-AI; 4.29 for 6-AI; 4.19 for 7-AI) and the experimental onset of the absorption measured in this work (4.49, 4.08 and 4.29 eV, respectively; see also references 17 and 18 for 7-AI). Overall, the good agreement between experiment and theory validates our computational MS-CASPT2//TD-CAM-B3LYP approach.

The decay paths for the three molecules lead from the $n\pi^*$ minimum to a CI with the ground state where the nonradiative decay can occur. The $n\pi^*/S_0$ CIs (see the insets in Figure 3.3) are characterized by out-of-plane bending of one of the neighboring CH groups to the nitrogen atom (C_4, C_7 and C_6 in 5-AI, 6-AI and 7-AI, respectively). These structures are analogues of the lowest energy CI found in adenine,[37] labeled ^2E in some studies.[38] There are higher-energy CIs for the three molecules (see footnote of Table 3.3 and Figure 3.13), but we center on the paths to the ones with lowest energy. Although the paths are qualitatively similar for the three compounds, there are significant differences. The calculated barriers to access the CI are 0.13, 0.07 and 0.41 eV for 5-AI, 6-AI and 7-AI, respectively. In 6-AI, the highest-energy point along the path lies between $\pi\pi^*$-DFT and $n\pi^*$-DFT, and in 5-AI it is almost coincident with $n\pi^*$-DFT. This implies that the decay path from the $n\pi^*$-DFT region to the CI is barrierless for these molecules, and the bottleneck for decay to S_0 is effectively given by the barrier for $\pi\pi^*/n\pi^*$ interconversion. In 7-AI, however, S_1-TS lies half way between $n\pi^*$-DFT and the CI, and the barrier is significantly higher than for the other compounds. The differences in the potential energy surface translate into significant differences in the excited state lifetimes, as shown by the following time-resolved experiments.

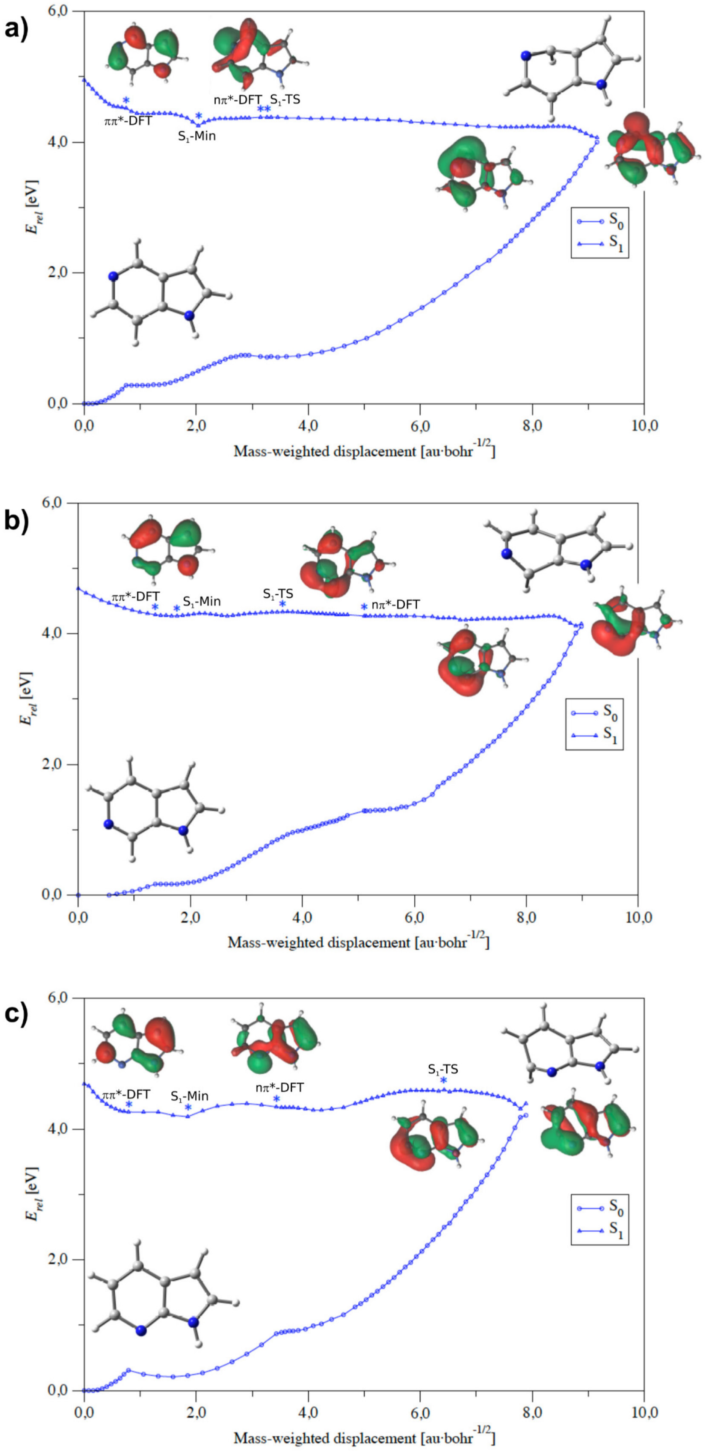

***Figure 3.3**. Excited state S_1 decay paths (MS-CASPT2/ANO-L energy profiles along TD-CAM-B3LYP/6-311G(d,p) optimized paths) for 5-AI (a), 6-AI (b) and 7-AI (c). The positions of the critical points are marked with asterisks (ππ*-DFT and nπ*-DFT are the TD-DFT minima; S_1-Min and S_1-TS are the lowest-and highest-energy points along the path at the MS-CASPT2 level). Insets: Ground state minima and CI structures, plots of the occupied orbitals involved in the excitation for representative structures along the path.*

The TR-IY experiments were recorded for the isolated 5-AI, 6-AI and 7-AI isomers after excitation with increasing energy, starting at the onset of absorption. Transients were collected at the AI$^+$ mass channel with 3- or 4-photon ionization at probe wavelength of 800 and 1305 nm, respectively. In each case, the region of the supersonic expansion to interrogate and the carrier gas pressure were optimized to avoid dimer or larger cluster formation (see section 3.2.1). Even though 4-AI was also studied spectroscopically, no meaningful ion signal was obtained in the attempted excitation region presumably due to failure to vaporize the sample.

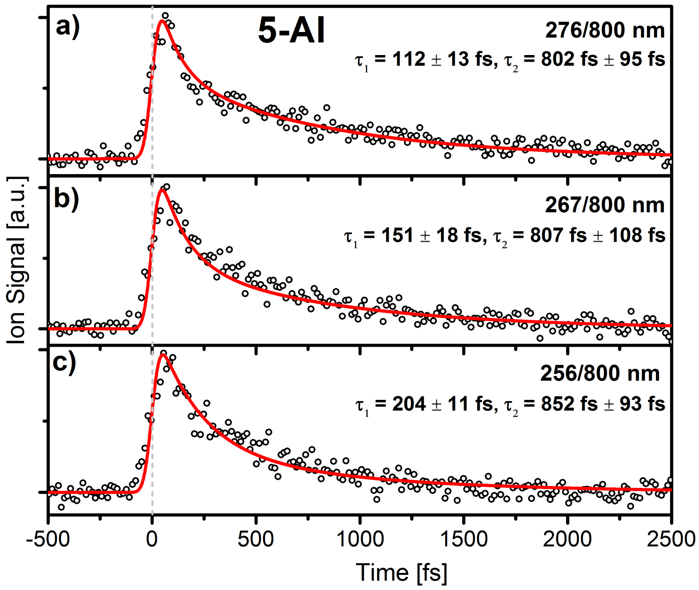

Figure 3.4. *5-AI$^+$ signals (circles) recorded at 276 (a), 267 (b) and 256 nm (c) excitation wavelength, using the 800 nm probe. The red line is the best fit obtained.*

The TR-IY measurements for 5-AI and 6-AI are shown in Figures 3.4a-c and 3.5a-d. Since no previous gas-phase absorption spectra are available for these molecules, the electronic absorption thresholds were determined by acquiring the 1+1' ionization signal at increasing pump energies, while using 800 nm radiation as probe. In this way, the thresholds were found to be about ~276 and ~304 nm for 5-AI and 6-AI, respectively. Therefore, the temporal evolution of 5-AI was tracked exciting at wavelengths from 276 nm to 256 nm, and that of 6-AI from 304 to 267 nm. Both isomers show fast time decays in the fs range. For 5-AI, a bi-exponential decay with lifetimes τ_1 ~100-200 fs and τ_2 ~800 fs was required to reproduce the recorded transients (Figure 3.4a-c).

On the other hand, the dynamics observed for 6-AI was even faster. The measurement after excitation at 304 nm (Figure 3.5a) reflects the CC function, as it corresponds to the nonresonant ionization of the molecule, which means that the onset of the absorption is not met yet. At shorter excitation wavelengths (Figure 3.5b-d) the collected data set were modelled by a single-exponential decay of ~100 fs, which reflects the relaxation of the prepared excited state to a location where the ionization probability drops to zero.

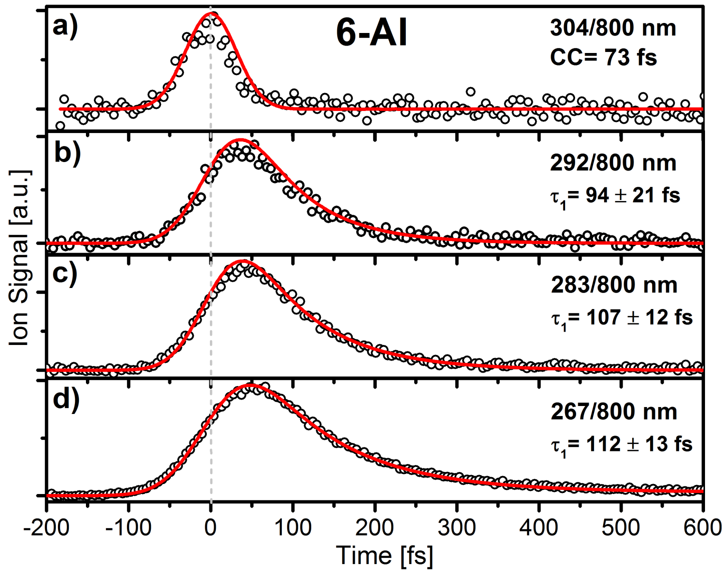

Figure 3.5. *6-AI$^+$ signals (circles) recorded at 304 (a), 292 (b), 283 (c) and 267 nm (d) excitation wavelengths, using the 800 nm probe. The red line is the best obtained fit.*

Trying to extend the ionization window to lower energies, and in particular to test the possibility of ionizing from triplet states, the role of changes in the ionization potential along the decay coordinate was assessed conducting experiments (1+2') with a higher ionization energy of 400 nm for 5-AI, as shown in Figure 3.6. These measurements yielded the same dynamics than with the 800 nm ionization pulse, which suggests that changes in the ionization potential do not play a significant role in the photodynamics, at least for 5-AI, and confirms that the decay of the ion signal reflects the relaxation to S_0.

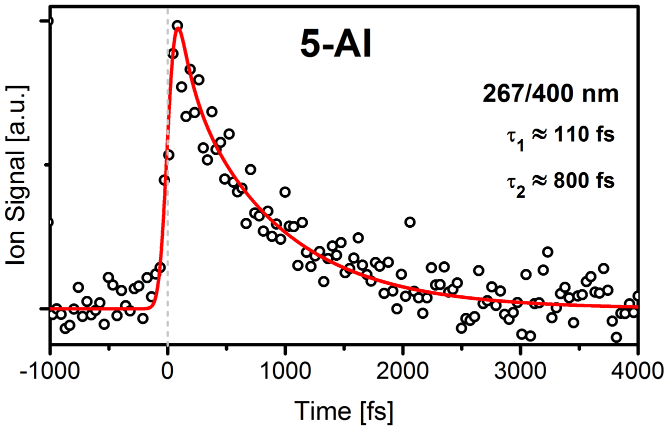

Figure 3.6. *5-AI$^+$ signal (circles) recorded at 267 nm excitation wavelength, using 400 nm radiation as probe.*

The results for 5-AI and 6-AI are consistent with the relaxation channels predicted in Figure 3.3a and b. For both isomers, ultrafast relaxation independent of the excitation energy is observed, which points to a common low barrier channel. In the case of 5-AI, the first component may describe the dynamics between the two close-lying ππ* states and the conversion to the nπ* state, and the second component corresponds to the decay to the ground state through the predicted CI. The shorter decay time seen for 6-AI, where only one component could be identified, is also consistent with the somewhat smaller barrier along the path to the CI compared to 5-AI (0.06 *vs.* 0.12 eV).

The transients of 7-AI were collected following excitation in the 289-250 nm range and are much slower than those found for 5-AI and 6-AI. Figure 3.7a-d summarizes the short time-scale (2.5 ps) decays collected at excitation energies in the 289-260 nm interval with the 1305 nm probe. The transient 3.7a recorded at 289 nm excitation, corresponding to the absorption origin at the L_b state fundamental band (34634 cm^{-1}), does not show any sign of ultrafast dynamics and therefore it can be modelled by the convolution of the CC function with a constant signal representing a decay in the ns range. At energies starting at about 760 cm^{-1} above the origin of L_b state (283 nm, Figure 3.7b), a τ_1 decay component of ~280 fs is noticeable. Additionally, an oscillatory pattern due to vibrational wavepacket activity is also observable in the signals. Very remarkably, these features were not observed in the experiments carried out with the 800 nm probe (see Figure 3.8a-e), which is due to the fact that multiphoton ionization with lower energy (1305 nm probe in this case) and therefore a higher number of photons is more sensitive towards relaxation processes connecting regions of similar energy.[39] The value of τ_1 remains almost constant (270-290 fs) when the excitation energy is increased (Figure 3.7b-d).

Long-term transients extending up to 63 ps were also recorded between 275 and 250 nm excitation wavelengths, while probing with 800 nm radiation. These TR-IY decays, shown in Figure 3.8f, permit to measure precisely the longer component (τ_2) observed in the short-scale transients, which shortens from 300 ps at 275 nm, up to 18 ps at 250 nm excitation.

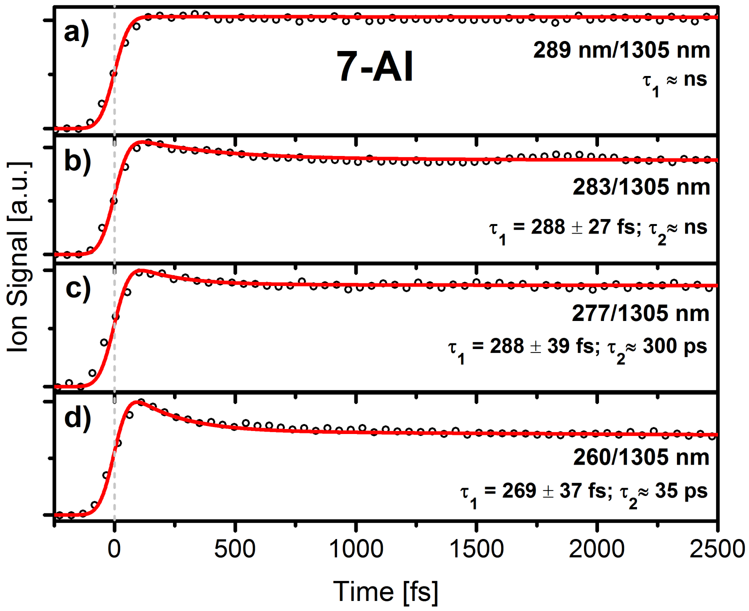

Figure 3.7. *7-AI$^+$ signals (circles) recorded at 289 (a), 283 (b), 277 (c) and 260 nm (d) excitation wavelengths, using the 1305 nm probe,*

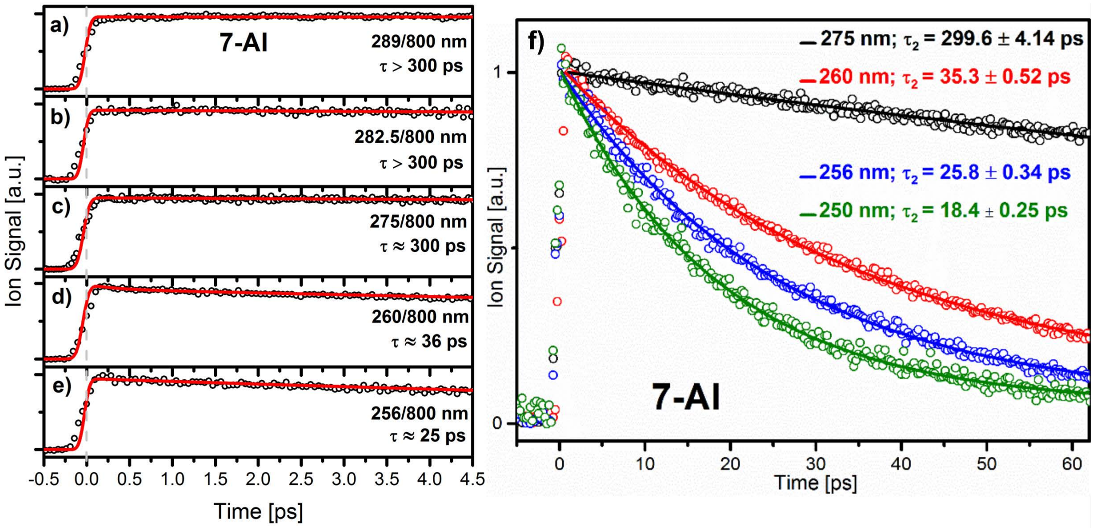

Figure 3.8. *Short- (a-e) and long-term (f) decays recorded for 7-AI$^+$ at 289–250 nm excitation with 800 nm probe. The dots are the experimental values, while the solid lines are the best obtained fit.*

Aiming to confirm the observed dynamics for 7-AI and to discard the intervention of (7-AI)$_2$ dimer or bigger homoclusters, similar measurements were conducted on NMe-7-AI. The methyl group on the pyridinic ring precludes the formation of clusters sustained by N-H···N hydrogen-bonds. Figure 3.9 shows a one-color resonance enhanced multi-photon ionization (REMPI) spectrum of jet-cooled NMe-7-AI recorded by a Nd:YAG pumped dye laser (Quantel TDL-90) in the region of the electronic origin (~33238 cm^{-1}).

The transients recorded after exciting at several vibronic bands across the spectrum and probing with 800 nm radiation are shown at short and long time-scales in Figure 3.10a-g. The methylated derivative perfectly matches the dynamical behavior found for the 7-AI, with a fast decay component (τ_1) between 400 and 200 fs and a slow one (τ_2) that shortens from hundreds to tens of ps as the excitation energy is increased. Moreover, these results also suggest that N–H dissociation[15] is not relevant with the current excitation energies.

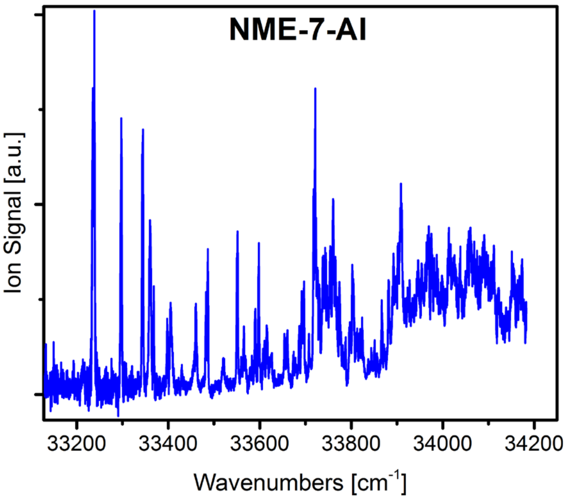

Figure 3.9. *One-color REMPI (1+1') spectrum of NMe-7-AI.*

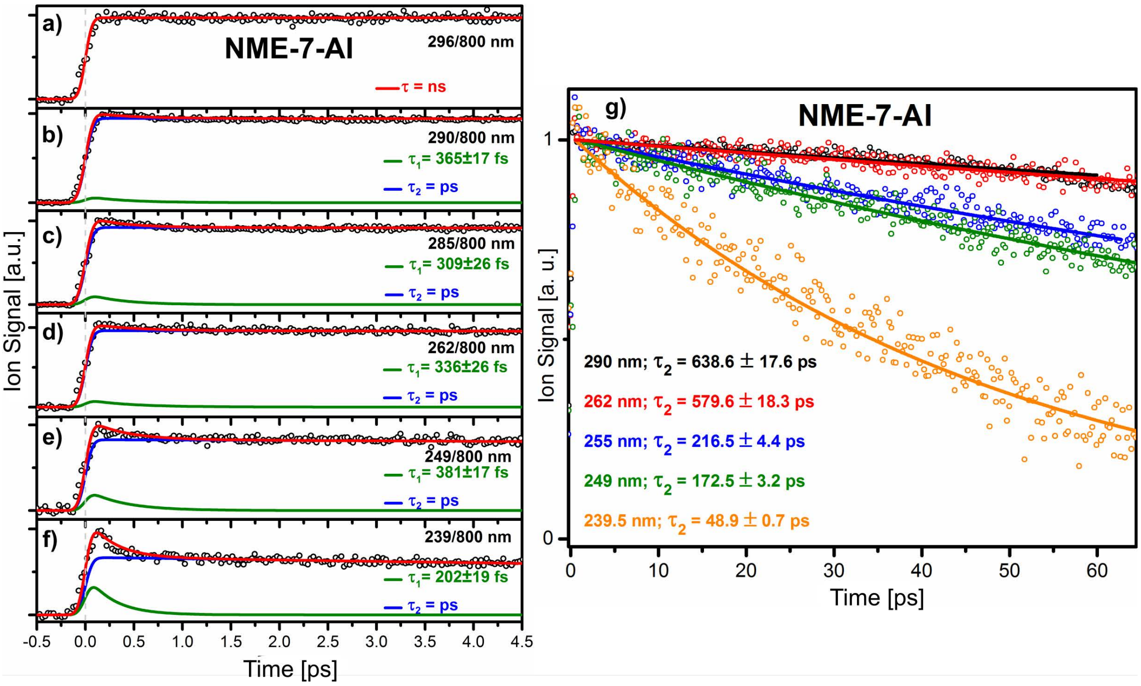

Figure 3.10. *Short-scale (a-f) and long-term (g) transients recorded at NMe-7-AI$^+$ mass channel after exciting at the indicated wavelengths and probing with 800 nm radiation. The dots are the experimental values, the red line the best obtained fit and the green and blue lines the indicated temporal components derived from the fit.*

The experimental results are consistent with the activated process predicted for 7-AI in Figure 3.3c, which has a calculated barrier of 0.41 eV. We suggest that the fast component is associated with interconversion between the two *ππ** states, which are separated by less than 0.1 eV at the Franck-Condon geometry. The $S_2 \rightarrow S_1$ IC is facilitated by an S_2/S_1 CI between the two *ππ** states located near the Franck-Condon geometry at 4.67 eV (see additional Figure 3.14). In turn, the long lifetime component is due to trapping of the *ππ** and n*π** state population before the CI is accessed.

In addition, for 7-AI we have also explored the possibility that the trapped S_1 population crosses over to the triplet state by ISC process. ISC requires small singlet/triplet gaps and high SOC, and Table 3.4 shows the singlet and triplet energies at the critical points that lie before the barrier to the CI. The S_1/T_1 energy gaps are too large for ISC to be efficient, since T_1 lies at least 0.6 eV below S_1 at the three structures. The S_1/T_2 gaps at *ππ**-DFT and S_1-Min are smaller, approximately 0.2 eV, however the SOC elements are small (< 1 cm^{-1}) because both S_1 and T_2 have *ππ** character. Finally, S_1/T_2 SOC is higher at n*π**-DFT, but the gap is again high, 0.5 eV. Although a more thorough investigation would be necessary to settle this issue unambiguously, these data suggest that ISC is not a favored process in 7-AI because there is no structure that satisfies both requirements of small energy gap near nπ^*-Min and large SOC near *ππ**-Min.

Table 3.4. *MS-CASPT2(12,10)/ANO-L singlet and triplet energies (in eV) and spin-orbit coupling elements (in* cm^{-1}*) at 7-AI critical points.*

	ππ*-DFT	**S_1-Min**	**nπ*-DFT**
S_1	4.26	4.19	4.34
T_1[a]	3.17 (< 0.1)	3.17 (0.6)	3.74 (8.6)
T_2[a]	4.50 (< 0.1)	4.37 (0.6)	4.83 (7.7)

[a]Spin-orbit coupling element in brackets.

3.5. Conclusions

Mechanistically, the main conclusion of the work presented in this chapter is that the excited state lifetime of the AIs depends on the energy of the n*π** state relative to the *ππ** states. It can be stated that the n*π** state functions as a gate state to access the n*π**/S_0 CI, as shown by our computed decay paths. This is further illustrated with the insets of Figure 3.3, which show the evolution of the occupied orbital involved in the excitation along the decay coordinate. At the CI, the orbital in question has substantial contribution from the nitrogen lone pair. Therefore, passage through the n*π** state is needed to access the CI, and the relative energy of this state determines the barrier. In 5-AI and 6-AI, the nπ* state (S_2) is close in energy to the ππ* states (0.11 and 0.39 eV higher than S_1 at the Franck-Condon geometry, respectively), which facilitates the access to the CI. In contrast, in 7-AI the nπ* state (S_3) is 0.64 eV higher than S_1 at the Franck-Condon geometry, which results in a higher barrier to reach the CI. The higher energy of the nπ* state in 7-AI can be attributed to the position of the NH pyrrole group relative to the pyridinic nitrogen atom. The NH nitrogen atom is more electronegative than the carbon ring atoms and helps to stabilize the pyridinic nitrogen lone pair, increasing the energy of the nπ* state. In 7-AI the two nitrogen atoms are separated by only two bonds, and the stabilization is stronger than in the other isomers where the separation is three or four bonds.

Based on our mechanistic picture, 4-AI should have a short excited state lifetime similar to 5-AI and 6-AI, because the relative position of the nπ* state in the vertical excitation spectrum is similar (0.14 eV higher than S_1 at the Franck-Condon geometry). This is consistent with steady-state fluorescence measurements in cyclohexane (see Figure 4.1b in the Chapter 4), which give almost no fluorescence for 4-AI, 5-AI and 6-AI and significant emission for 7-AI and NMe-7-AI. Turning our attention to adenine, it exhibits a bi-exponential decay profile similar to 5-AI but with a shorter τ_1 and a longer τ_2 lifetime (40 fs and 1.2 ps, respectively).[40] The main difference with respect to the AIs is that in adenine the nπ* state is S_1 at the Franck-Condon geometry at most levels of theory,[35, 37] and the lower energy of nπ* state appears to turn into a trapping state responsible of the τ_2 lifetime, as suggested by CASPT2 calculations.[41-42] This further shows how the energy of the nπ* state modulates the excited state lifetimes. Our results can also be compared with recent results on 2-aminopurine (2-AP), an isomer of adenine that is fluorescent in water. In 2-AP(H_2O)$_n$ clusters, selective hydration of the purine nitrogen atoms modulates the relative energy of the ππ* and nπ* states, and the excited state lifetimes increase as the nπ* energy raises.[43] This mechanistic picture is similar to the one that we provide for the AIs.

In summary, the work allows to rationalize the influence of the position of the nitrogen atoms in the six-membered ring on the relaxation channels operative in the studied molecules. In order to extend these ideas to biologically relevant relaxation processes, Chapter 4 studies the photodynamics of azaindoles in different solvents to explore the effect of solvation on the relevant ππ* and nπ* states.

3.6. Additional Information

3.6.1. Calculated Excitation Polarization

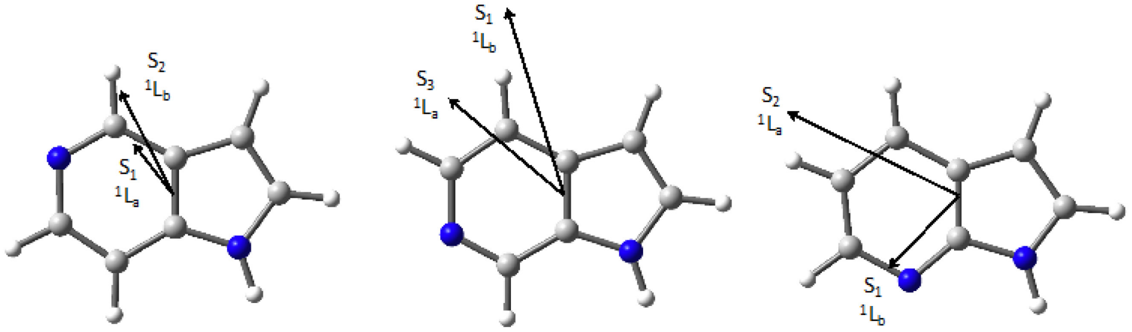

(a) 5-AI (b) 6-AI (c) 7-AI

Figure 3.11. *Calculated polarization at the Franck-Condon geometry for the lowest $\pi\pi^*$ states at the MS-CASPT2/ANO-L level of theory for (a) 5-AI, (b) 6-AI and (c) 7-AI. The states more aligned along the horizontal (long) axis are labeled ^1L_a, and those along the vertical (short) axis ^1L_b.*

3.6.2. TD-DFT Energies of Critical Points

Table 3.5. *TD CAM-B3LYP/6-311G(d,p) energies of critical points for the studied AIs.*

	5-AI		**6-AI**		**7-AI**	
	E_{S1} [eV][a,b]					
	TD-DFT	**MS-CASPT2**	**TD-DFT**	**MS-CASPT2**	**TD-DFT**	**MS-CASPT2**
Franck-Condon	5.25 (0.107)[c]	4.95 (0.028)	5.07 (0.080)	4.69 (0.083)	5.08 (0.084)	4.69 (0.043)
$\pi\pi^*$-Min	4.88 (0.130)	4.52 (0.137)	4.84 (0.117)	4.29 (0.141)	4.67 (0.124)[d]	4.26 (0.152)[b]
$n\pi^*$-Min	4.47 (0.003)	4.38 (0.006)	4.48 (0.014)	4.27 (0.027)	4.81 (0.049)	4.34 (0.081)
TS	4.64 (0.003)	4.38 (0.006)	4.57 (0.001)	4.34 (0.022)	4.91 (0.013)	4.60 (0.037)
S_1/S_0-CI[e]	4.55 (-)	3.92 (-)	4.61 (-)	4.17 (-)	4.60 (-)	4.15 (-)

[a] Oscillator strength in brackets. [b] Structures optimized at the TD-DFT level. [c] The lowest $\pi\pi^*$ state is S_2 at the TD-DFT level. Energy and oscillator strength of S_1: 5.16 (0.002). [d] Additional $\pi\pi^*$ minimum at 4.93 eV (oscillator strength 0.112). [e] CI optimized with the Tamm-Dancoff approximation. S_1/S_0 gaps at the full TDDFT level: 0.11 (5-AI), 0.14 (6-AI) and 0.11 eV (7-AI).

3.6.3. TD-DFT Energy Profiles of 5AI, 6-AI and 7-AI

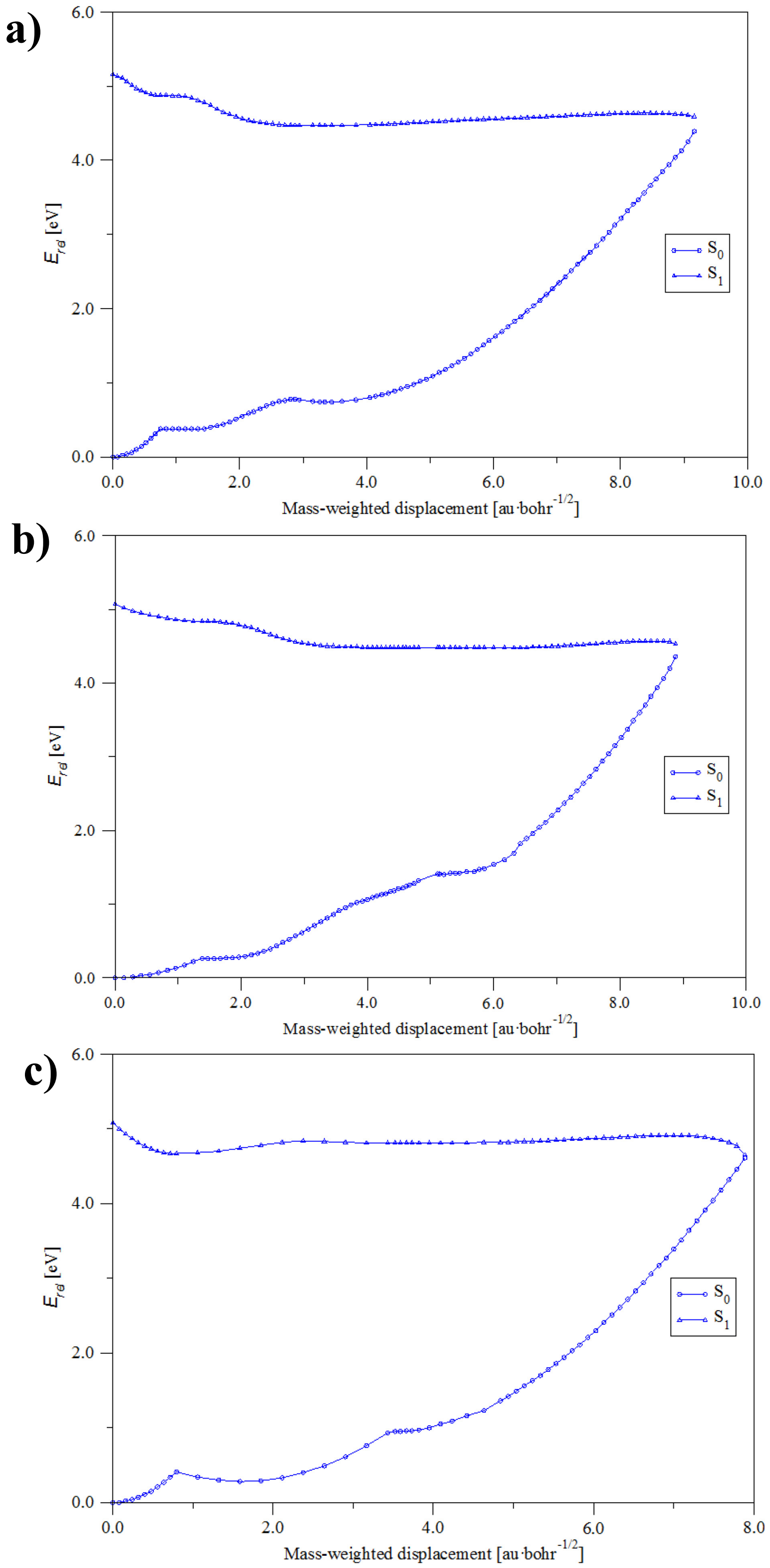

Figure 3.12. *TD-CAM-B3LYP/6-311G(d,p) decay pathways from the Franck-Condon geometry to the lowest-energy CI for 5-AI (a), 6-AI (b) and 7-AI (c).*

3.6.4. Calculated Structures for Critical Points along the Relaxation Pathways

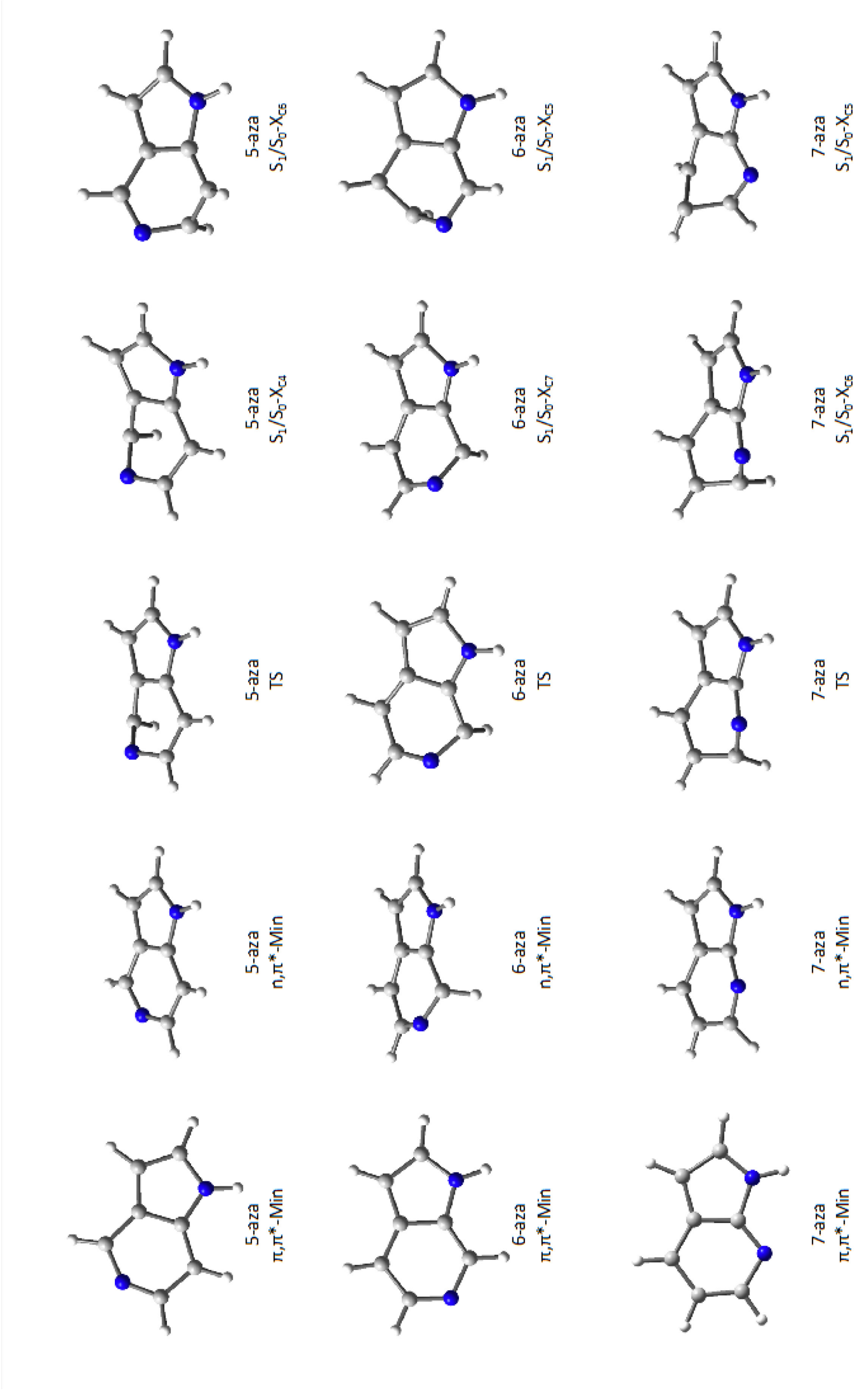

Figure 3.13. *TD-CAM-B3LYP/6-311G(d,p) optimized structures for the AIs studied theoretically.*

3.6.5. L_a/L_b Crossing for 7-AI

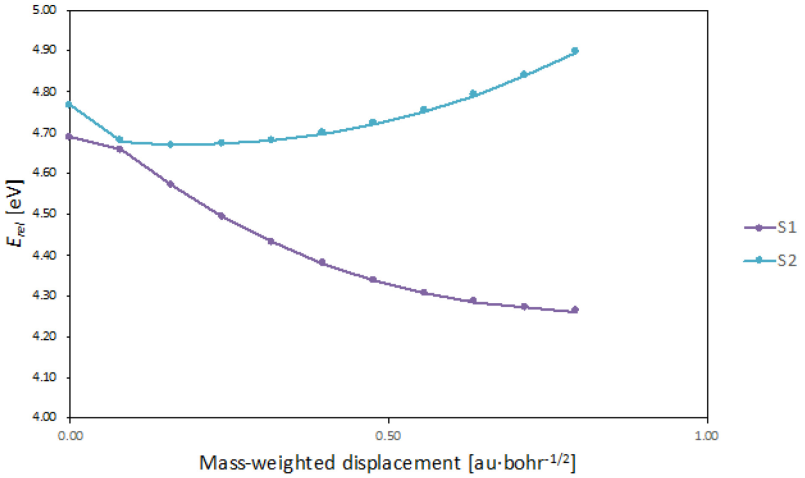

Figure 3.14. *MS-CASPT2/ANO-L energy profile of the S_1 and S_2 states along the linear interpolation in internal coordinates between the Franck-Condon structure and the lowest ππ* minimum for 7-AI, showing the L_a/L_b crossing.*

3.6.6. REMPI Spectrum of 7-AI

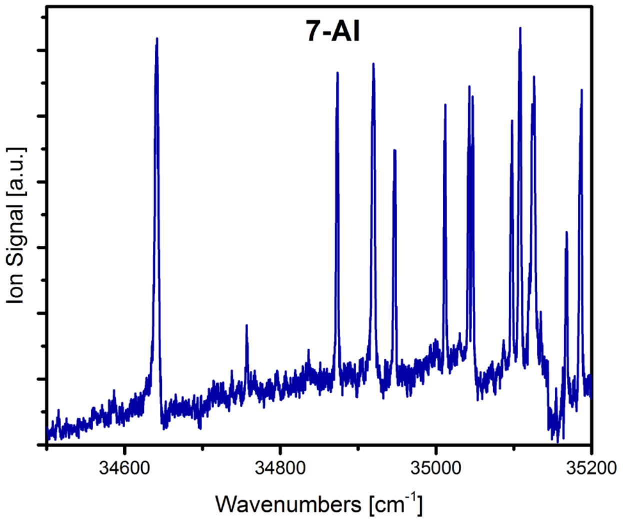

Figure 3.15. *One-color REMPI (1+1') spectrum of 7-AI.*

3.7. References

1. Marchetti, B.; Karsili, T. N. V.; Ashfold, M. N. R.; Domcke, W., A 'bottom up', ab initio computational approach to understanding fundamental photophysical processes in nitrogen containing heterocycles, DNA bases and base pairs. *Physical Chemistry Chemical Physics* **2016,** *18* (30), 20007-20027.

2. Merkel, L.; Hoesl, M. G.; Albrecht, M.; Schmidt, A.; Budisa, N., Blue Fluorescent Amino Acids as In Vivo Building Blocks for Proteins. *ChemBioChem* **2010,** *11* (3), 305-314.

3. Noichl, B. P.; Durkin, P. M.; Budisa, N., Toward intrinsically colored peptides: Synthesis and investigation of the spectral properties of methylated azatryptophans in tryptophan-cage mutants. *Peptide Science* **2015,** *104* (5), 585-600.

4. Douhal, A.; Kim, S. K.; Zewail, A. H., Femtosecond molecular dynamics of tautomerization in model base pairs. *Nature* **1995,** *378* (6554), 260-263.

5. Fuke, K.; Kaya, K., Dynamics of double-proton-transfer reaction in the excited-state model hydrogen-bonded base pairs. *The Journal of Physical Chemistry* **1989,** *93* (2), 614-621.

6. Nakajima, A.; Hirano, M.; Hasumi, R.; Kaya, K.; Watanabe, H.; Carter, C. C.; Williamson, J. M.; Miller, T. A., High-Resolution Laser-Induced Fluorescence Spectra of 7-Azaindole−Water Complexes and 7-Azaindole Dimer. *The Journal of Physical Chemistry A* **1997,** *101* (4), 392-398.

7. Serrano-Andrés, L.; Merchán, M.; Borin, A. C.; Stålring, J., Theoretical studies on the spectroscopy of the 7-azaindole monomer and dimer. *International Journal of Quantum Chemistry* **2001,** *84* (2), 181-191.

8. Crespo-Otero, R.; Kungwan, N.; Barbatti, M., Stepwise double excited-state proton transfer is not possible in 7-azaindole dimer. *Chemical Science* **2015,** *6* (10), 5762-5767.

9. Fang, H.; Mai, B. K.; Kim, Y., Excited-State Multiple Proton Transfer Depending on the Acidity and Basicity of Mediating Alcohols in 7-Azaindole–(ROH)2 (R=H, CH3) Complexes: A Theoretical Study. *Photochemistry and Photobiology* **2015,** *91* (2), 306-314.

10. Huang, Y.; Arnold, S.; Sulkes, M., Spectroscopy and Fluorescence Lifetimes of Jet-Cooled 7-Azaindole: Electronic States and Solvent Complex Geometry. *The Journal of Physical Chemistry* **1996,** *100* (12), 4734-4738.

11. Kerdpol, K.; Daengngern, R.; Kungwan, N., Excited-state proton-transfer reactions of 7-azaindole with water, ammonia and mixed water–ammonia: microsolvated dynamics simulation. *Molecular Simulation* **2015,** *41* (14), 1177-1186.

12. Pino, G. A.; Alata, I.; Dedonder, C.; Jouvet, C.; Sakota, K.; Sekiya, H., Photon induced isomerization in the first excited state of the 7-azaindole–(H2O)3cluster. *Physical Chemistry Chemical Physics* **2011,** *13* (13), 6325-6331.

13. Svartsov, Y. N.; Schmitt, M., Electronically excited states of water clusters of 7-azaindole: Structures, relative energies, and electronic nature of the excited states. *The Journal of Chemical Physics* **2008,** *128* (21), 214310.

14. Arulmozhiraja, S.; Coote, M. L.; Hasegawa, J.-y., Electronic spectra of azaindole and its excited state mixing: A symmetry-adapted cluster configuration interaction study. *The Journal of Chemical Physics* **2015,** *143* (20), 204304.

15. Young, J. W.; Pozun, Z. D.; Jordan, K. D.; Pratt, D. W., Excited Electronic State Mixing in 7-Azaindole. Quantitative Measurements Using the Stark Effect. *The Journal of Physical Chemistry B* **2013,** *117* (49), 15695-15700.

16. Brause, R.; Schmitt, M.; Krügler, D.; Kleinermanns, K., Determination of the excited state structure of 7-azaindole using a Franck-Condon analysis. *Molecular Physics* **2004,** *102* (14-15), 1615-1623.

17. Kang, C.; Yi, J. T.; Pratt, D. W., High resolution electronic spectra of 7-azaindole and its Ar atom van der Waals complex. *The Journal of Chemical Physics* **2005,** *123* (9), 094306.

18. Schmitt, M.; Ratzer, C.; Kleinermanns, K.; Leo Meerts, W., Determination of the structure of 7-azaindole in the electronic ground and excited state using high-resolution ultraviolet spectroscopy and an automated assignment based on a genetic algorithm. *Molecular Physics* **2004,** *102* (14-15), 1605-1614.

19. Cash, M. T.; Schreiner, P. R.; Phillips, R. S., Excited state tautomerization of azaindole. *Organic & Biomolecular Chemistry* **2005,** *3* (20), 3701-3706.

20. Tu, T.-H.; Chen, Y.-T.; Chen, Y.-A.; Wei, Y.-C.; Chen, Y.-H.; Chen, C.-L.; Shen, J.-Y.; Chen, Y.-H.; Ho, S.-Y.; Cheng, K.-Y.; Lee, S.-L.; Chen, C.-h.; Chou, P.-T., The Cyclic Hydrogen-Bonded 6-Azaindole Trimer and its Prominent Excited-State Triple-Proton-Transfer Reaction. *Angewandte Chemie International Edition* **2018,** *57* (18), 5020-5024.

21. Twine, S. M.; Murphy, L.; Phillips, R. S.; Callis, P.; Cash, M. T.; Szabo, A. G., The Photophysical Properties of 6-Azaindole. *The Journal of Physical Chemistry B* **2003,** *107* (2), 637-645.

22. Share, P.; Pereira, M.; Sarisky, M.; Repinec, S.; Hochstrasser, R. M., Dynamics of proton transfer in 7-azaindole. *Journal of Luminescence* **1991,** *48-49*, 204-208.

23. Takeuchi, S.; Tahara, T., Femtosecond Ultraviolet−Visible Fluorescence Study of the Excited-State Proton-Transfer Reaction of 7-Azaindole Dimer. *The Journal of Physical Chemistry A* **1998,** *102* (40), 7740-7753.

24. Fiebig, T.; Chachisvilis, M.; Manger, M.; Zewail, A. H.; Douhal, A.; Garcia-Ochoa, I.; de La Hoz Ayuso, A., Femtosecond Dynamics of Double Proton Transfer in a Model DNA Base Pair: 7-Azaindole Dimers in the Condensed Phase. *The Journal of Physical Chemistry A* **1999,** *103* (37), 7419-7431.

25. Hiroshi, S.; Kenji, S., Excited-State Double-Proton Transfer in the 7-Azaindole Dimer in the Gas Phase. Resolution of the Stepwise versus Concerted Mechanism Controversy and a New Paradigm. *Bulletin of the Chemical Society of Japan* **2006,** *79* (3), 373-385.

26. Gonzalez, C.; Schlegel, H. B., Reaction path following in mass-weighted internal coordinates. *Journal of Physical Chemistry* **1990,** *94* (14), 5523-5527.

27. Frisch, M. J.; Trucks, G. W.; Schlegel, H. B.; Scuseria, G. E.; Robb, M. A.; Cheeseman, J. R.; Scalmani, G.; Barone, V.; Petersson, G. A.; Nakatsuji, H.; Li, X.; Caricato, M.; Marenich, A. V.; Bloino, J.; Janesko, B. G.; Gomperts, R.; Mennucci, B.; Hratchian, H. P.; Ortiz, J. V.; Izmaylov, A. F.; Sonnenberg, J. L.; Williams; Ding, F.; Lipparini, F.; Egidi, F.; Goings, J.; Peng, B.; Petrone, A.; Henderson, T.; Ranasinghe, D.; Zakrzewski, V. G.; Gao, J.; Rega, N.; Zheng, G.; Liang, W.; Hada, M.; Ehara, M.; Toyota, K.; Fukuda, R.; Hasegawa, J.; Ishida, M.; Nakajima, T.; Honda, Y.; Kitao, O.; Nakai, H.; Vreven, T.; Throssell, K.; Montgomery Jr., J. A.; Peralta, J. E.; Ogliaro, F.; Bearpark, M. J.; Heyd, J. J.; Brothers, E. N.; Kudin, K. N.; Staroverov, V. N.; Keith, T. A.; Kobayashi, R.; Normand, J.; Raghavachari, K.; Rendell, A. P.; Burant, J. C.; Iyengar, S. S.; Tomasi, J.; Cossi, M.; Millam, J. M.; Klene, M.; Adamo, C.; Cammi,

R.; Ochterski, J. W.; Martin, R. L.; Morokuma, K.; Farkas, O.; Foresman, J. B.; Fox, D. J. *Gaussian 16 Rev. C.01*, Wallingford, CT, 2016.

28. Ruiz-Barragan, S.; Robb, M. A.; Blancafort, L., Conical Intersection Optimization Based on a Double Newton–Raphson Algorithm Using Composed Steps. *Journal of Chemical Theory and Computation* **2013,** *9* (3), 1433-1442.

29. Send, R.; Furche, F., First-order nonadiabatic couplings from time-dependent hybrid density functional response theory: Consistent formalism, implementation, and performance. *The Journal of Chemical Physics* **2010,** *132* (4), 044107.

30. Casida, M. E., Time-dependent density-functional theory for molecules and molecular solids. *Journal of Molecular Structure: THEOCHEM* **2009,** *914* (1), 3-18.

31. Aquilante, F.; De Vico, L.; Ferré, N.; Ghigo, G.; Malmqvist, P.-å.; Neogrády, P.; Pedersen, T. B.; Pitoňák, M.; Reiher, M.; Roos, B. O.; Serrano-Andrés, L.; Urban, M.; Veryazov, V.; Lindh, R., MOLCAS 7: The Next Generation. *Journal of Computational Chemistry* **2010,** *31* (1), 224-247.

32. Aquilante, F.; Pedersen, T.; Veryazov, V.; Lindh, R., Wiley Interdiscip. *Rev.: Comput. Mol. Sci* **2013,** *3* (2), 143-149.

33. Forsberg, N.; Malmqvist, P.-Å., Multiconfiguration perturbation theory with imaginary level shift. *Chemical Physics Letters* **1997,** *274* (1), 196-204.

34. Ghigo, G.; Roos, B. O.; Malmqvist, P.-Å., A modified definition of the zeroth-order Hamiltonian in multiconfigurational perturbation theory (CASPT2). *Chemical Physics Letters* **2004,** *396* (1), 142-149.

35. Conti, I.; Altoè, P.; Stenta, M.; Garavelli, M.; Orlandi, G., Adenine deactivation in DNA resolved at the CASPT2//CASSCF/AMBER level. *Physical Chemistry Chemical Physics* **2010,** *12* (19), 5016-5023.

36. Borin, A. C.; Serrano-Andrés, L., A theoretical study of the absorption spectra of indole and its analogs: indene, benzimidazole, and 7-azaindole. *Chemical Physics* **2000,** *262* (2), 253-265.

37. Improta, R.; Santoro, F.; Blancafort, L., Quantum Mechanical Studies on the Photophysics and the Photochemistry of Nucleic Acids and Nucleobases. *Chemical Reviews* **2016,** *116* (6), 3540-3593.

38. Barbatti, M.; Lischka, H., Nonadiabatic Deactivation of 9H-Adenine: A Comprehensive Picture Based on Mixed Quantum−Classical Dynamics. *Journal of the American Chemical Society* **2008,** *130* (21), 6831-6839.

39. Ovejas, V.; Fernández-Fernández, M.; Montero, R.; Longarte, A., On the ultrashort lifetime of electronically excited thiophenol. *Chemical Physics Letters* **2016,** *661*, 206-209.

40. Satzger, H.; Townsend, D.; Zgierski, M. Z.; Patchkovskii, S.; Ullrich, S.; Stolow, A., Primary processes underlying the photostability of isolated DNA bases: Adenine. *Proceedings of the National Academy of Sciences* **2006,** *103* (27), 10196-10201.

41. Blancafort, L., Excited-State Potential Energy Surface for the Photophysics of Adenine. *Journal of the American Chemical Society* **2006,** *128* (1), 210-219.

42. Serrano-Andrés, L.; Merchán, M.; Borin, A. C., Adenine and 2-aminopurine: Paradigms of modern theoretical photochemistry. *Proceedings of the National Academy of Sciences* **2006,** *103* (23), 8691-8696.

43. Lobsiger, S.; Blaser, S.; Sinha, R. K.; Frey, H.-M.; Leutwyler, S., Switching on the fluorescence of 2-aminopurine by site-selective microhydration. *Nature Chemistry* **2014,** *6* (11), 989-993.

4. PHOTODYNAMICS OF AZAINDOLES IN SOLUTION

4.1. Introduction

In the previous chapter, we concluded that the photodynamics of azaindoles (AIs) in the gas-phase is modulated by the position of the nitrogen atom in the six-membered ring, which alters the relative energy between the $\pi\pi^*$ and $n\pi^*$ excited states and therefore the accessibility to the CI that controls the relaxation pathway to the ground state. Aiming to provide a complete picture of the photophysics of these molecules, in this chapter we explore how the dynamical behavior of the AIs is affected when they are solved in different solvents. The study aims to establish the effect of the environment on the relevant $\pi\pi^*$ and $n\pi^*$ states, in terms of polarity and specific interactions such as hydrogen bonding.

In the light of the available literature, the photophysics of the 7-AI has attracted a greater deal of attention than the other structural isomers. Since the pioneering spectroscopic work of Taylor *et al.* revealing the excited state proton transfer (ESPT) reaction on 7-AI dimer,[1] this molecule has been considered a benchmark model for studying this process. Accordingly, several theoretical and experimental works on the photophysics of the 7-AI and its dimer have been conducted. In this sense, Douhal *et al.* reported the first time-resolved study with fs resolution for $(7\text{-AI})_2$ in the gas-phase, suggesting that the double proton transfer occurs on two steps: the first proton is transferred in hundreds of fs, while the second proton transfer takes place on the ps time-scale.[2] The exact nature of this mechanism, stepwise *vs.* concerted, has been the subject of a long lasting debate until recent years.[3-6]Additionally, the ESPT in clusters between 7-AI and water[7-10] or ammonia[11-12] has been also studied by several groups.

Regarding the works performed in the condensed-phase, Takeuchi *et al.*[13-14] and Zewail and co-workers[15-17] studied the photodynamics of 7-AI monomer and dimer in different solvents by employing FuC and TA techniques. Petrich and co-workers extensively studied the tautomerization of 7-AI and its methylated derivatives (NMe-7-AI and 1-Me-7-AI) in water[18-20] and linear alcohols,[20-21] observing that while in alcohols the tautomerization is promoted by a cyclic intermediate, in water the 7-AI tends to form H-bonds with two solvent molecules.

Although the above-described works explored the role of the specific interactions such as H-bonds, there is a lack of studies in polar aprotic solvents able to address the effect of polarity over the excited states. This is specially the case for the rest of AI isomers in solution, for which only some spectroscopic studies on 4-AI, 5-AI and 6-AI have been conducted.[22-26]

Regarding the more complex DNA bases, the role of the environment on their excited states, and how their photodynamics is altered with respect to the isolated-phase, has been a central issue.[27-34] In general, the canonical nucleobases tend to retain the photostability observed in their natural medium when they are placed in isolated conditions. For many pyrimidines[35-38] or purines[39-44], this property is based on ultrafast IC through a $\pi\pi^*/S_0$ CI accessed by out-of-plane deformations at the C_5 and C_2 atoms, respectively. However, the influence of the solvent is highly specific and it critically depends on the exact chemical nature of the considered solute/solvent system. Accordingly, a broad variety of effects have been described for different nucleobases and solvents. For instance, in some cases for which fragmentation is a main channel in isolation, in the condensed-phase, the excess energy provided by UV photoexcitation is transferred to the surrounding molecules by vibrational relaxation (IET), precluding the dissociation.[45] In other cases, the environment modulates severely the shape of excited state potentials, increasing the energy barriers to the CI responsible of the rapid deactivation and consequently the photostability of the molecule can be dramatically modified, allowing potentially harmful relaxation pathways.[31-32, 46]

The aim of this chapter is to decipher the main relaxation mechanisms of the AIs in solutions of different solvents. By comparing the results with those previously found in the gas-phase (see Chapter 3) we should be able to elucidate how polar aprotic and protic solvents affect the photodynamics of these molecules. The observations made for the AIs can contribute to understand these phenomena in more complex biological derivatives.

4.2. Experimental Methods

The time-resolved experiments were performed using the TA and FuC techniques, which have been extensively described in sections 2.4.2 and 2.4.4, respectively. The AI samples were dissolved in acetonitrile (ACN, 99.9%, Sigma-Aldrich), dichloromethane (DCM, 99.9%, Merk) and methanol (MeOH, 99.9%, Fischer Chemical) at different concentrations that varied from 6 to 33 mM.

The FuC measurements were conducted exciting the samples of interest at 267 and 300 nm (267 and 280 nm for 5-AI) produced in a third harmonic generation setup (2ω-3ω) and in the OPA2 (Coherent OPerA Solo), respectively. The excitation beam was focused onto a 0.3 mm optical path rotatory cuvette that contains the AIs solutions described above. The resulting emission was collected by an *f* = 60 mm lens and focused by a second one with *f* = 150 mm, onto a 0.2 mm thick BBO crystal, where it interacted with the fundamental 800 nm beam to generate the up-converted signal in the 230-255 nm interval, which corresponds to the 323-375 nm emission range. The up-converted light was then collimated and focused into the entrance of a photomultiplier coupled to a monochromator (CDP 220D), where the signal was integrated by a boxcar (CDP 2021A). The temporal overlap between the excitation and gate beams was controlled by a retroreflector mounted on a motorized delay stage that allows a maximum delay of ~2 ns with a precision of 1.5 fs. The relative polarization between the excitation and gate pulses was set at magic angle (54.7 º) by a Berek's waveplate. Temporal resolutions around 250 fs were reached for ACN and DCM solutions, while CC function values of about 300 fs were obtained for MeOH solutions.

The TA experiments were carried out on ACN and MeOH solutions at the same excitation conditions employed for FuC measurements. The samples were recirculating through a 0.2 mm optical path flow cell (Starna Scientific), in order to avoid the formation of photoproducts. The evolution of the prepared species was probed by a broadband continuum, covering from 340 to 750 nm. This WLC was produced by focusing (*f* = 100 mm fused silica lens) an ~1 μJ 800 nm fundamental beam on a 2 mm CaF_2 plate, which is mounted on a linear translation stage to periodically refresh the exposed area. The relative polarization of the pump-probe beams was set at magic angle configuration (54.7º) by a Berek's waveplate. The pump-probe delay was controlled by a linear translation stage (Thorlabs ODL220-FS) that permits a maximum delay of ~2.5 ns, after a second pass through the delay line. The instrumental response function was provided from the CAS derived from pure solvent measurements. Whereas for MeOH values between 120 and 190 fs were obtained, for ACN temporal resolutions around 250 fs were reached in the 340-750 nm probe range.

Additionally, steady-state absorption and fluorescence emission spectra of the AIs in cyclohexane (CH, 99.9%, Merk), ACN, DCM and MeOH were taken using a commercial UV/Vis spectrometer (Cintra 303 GBC Scientific Equipment Ltd.) and a spectrofluorimeter (FL920 Edinburgh Instruments), respectively.

4.3. Computational Methods

In order to explore the role of the solvent on the electronic structure of AI isomers and how it affects the relative energy of the different excited states with respect to the gas-phase, TD-DFT calculation were carried out with the Gaussian 09 package.[47] For that purpose, firstly the geometries of isolated AIs for S_0, S_1, S_2 and S_3 surfaces were optimized using the CAM-B3LYP functional and a 6-31++G(d,p) basis set. Then, vertical excitation energies and optimized geometries of S_0, S_1, S_2 and S_3 surfaces were predicted including bulk solvent effects by the polarizable continuum model (PCM) at the same PCM/(TD-)DFT level. The standard dielectric constants of 2.02 for CH, 35.89 for ACN, 8.93 for DCM and 32.62 for MeOH were employed in these calculations.

4.4. Results and Discussion

4.4.1. Theoretical Calculations

Table 4.1 shows the computed TD-DFT vertical excitations for all the AI isomers in the gas-phase and in different polar solvents such as ACN, DCM or MeOH. In general, the inclusion of polar solvents increases the vertical energy of the $n\pi^*$ excited state. For ACN and MeOH solutions, the $n\pi^*$ state is blueshifted about 0.3 eV for 4-AI, 5-AI and 6-AI, and around 0.1 eV for 7-AI, with respect to the gas-phase. Since DCM is a less polar solvent, the vertical energy of the $n\pi^*$ state increases ~0.25 eV for 4-AI, 5-AI and 6-AI, and ~0.07 eV for 7-AI. The energy of the $\pi\pi^*$ states is also affected by the polar solvents, being the $\pi\pi^*$ state with lager oscillator strength preferentially stabilized.

Additionally, the energies of the optimized geometries for the lowest singlet excited state (S_1-Min) for the AI isomers in ACN are summarized in Table 4.2, together with its vertical excitation. According to our calculations, in the isolated-phase S_1-Min is a structure with mixed $\pi\pi^*/n\pi^*$ character for 4-AI, 5-AI and 6-AI, while for 7-AI it exhibits $\pi\pi^*$ character. These predictions are in good agreement with the MS-CASPT2//TD-DFT calculations presented in the previous chapter, in which we stated that the S_1-Min is a non-planar structure for 5-AI and 6-AI, whereas for 7-AI is a planar $\pi\pi^*$ minimum. However, when the polar solvent is included the $n\pi^*$ state is strongly blueshifted and therefore S_1-Min is a structure with $\pi\pi^*$ character for 4-AI and 7-AI, while in 5-AI and 6-AI it still exhibits some mixed $\pi\pi^*/n\pi^*$ character.

Table 4.1. *Comparison of vertical excitations VEEs (in eV) for the first three singlet excited states of the AIs in the gas-phase and in different solvents computed at the TD-CAM-B3LYP/6-31++G(d,p) level.* [a]

		4-AI		**5-AI**		**6-AI**		**7-AI**	
		***VEE* [eV]**	***f***	***VEE* [eV]**	***f***	***VEE* [eV]**	***f***	***VEE* [eV]**	***f***
Gas Phase	**S_1**	4.96 (ππ*)	0.1622	5.13 (ππ*)	0.1063	4.99 (ππ*)	0.0855	4.99 (ππ*)	0.1353
	S_2	4.98 (nπ*)	0.0035	5.16 (nπ*)	0.0020	5.11 (nπ*)	0.0032	5.03 (ππ*)	0.0685
	S_3	5.05 (ππ*)	0.0059	5.34 (ππ*)	0.0030	5.34 (ππ*)	0.0632	5.34 (nπ*)	0.0042
ACN	**S_1**	4.68 (ππ*)	0.1077	4.81 (ππ*)	0.0827	4.76 (ππ*)	0.0854	4.67 (ππ*)	0.0819
	S_2	4.99 (ππ*)	0.0685	5.26 (ππ*)	0.0052	5.21 (ππ*)	0.0431	4.97 (ππ*)	0.1036
	S_3	5.29 (nπ*)	0.0035	5.53 (nπ*)	0.0023	5.44 (nπ*)	0.0033	5.46 (nπ*)	0.0041
DCM	**S_1**	4.67 (ππ*)	0.1082	4.83 (ππ*)	0.0846	4.78 (ππ*)	0.0858	4.66 (ππ*)	0.0827
	S_2	4.99 (ππ*)	0.0682	5.27 (ππ*)	0.0052	5.23 (ππ*)	0.0450	4.98 (ππ*)	0.1029
	S_3	5.29 (nπ*)	0.0035	5.43 (nπ*)	0.0022	5.35 (nπ*)	0.0033	5.41 (nπ*)	0.0040
MeOH	**S_1**	4.68 (ππ*)	0.1094	4.81 (ππ*)	0.0831	4.76 (ππ*)	0.0855	4.67 (ππ*)	0.0825
	S_2	4.99 (ππ*)	0.0679	5.26 (ππ*)	0.0052	5.22 (ππ*)	0.0433	4.97 (ππ*)	0.1035
	S_3	5.29 (nπ*)	0.0035	5.53 (nπ*)	0.0024	5.44 (nπ*)	0.0033	5.46 (nπ*)	0.0041

[a] Character of the excited states in brackets.

Table 4.2. *Comparison of vertical excitations and minimum energies of S_1 for the AIs in the gas-phase and ACN, computed at the TD CAM-B3LYP/6-31++G(d,p) level.*

		E(S_1) [eV][a]			
		4-AI	**5-AI**	**6-AI**	**7-AI**
Gas Phase	***VEE***	4.96 (0.1622) [ππ*]	5.13 (0.1063) [ππ*]	4.99 (0.0855) [ππ*]	4.99 (0.1353) [ππ*]
	S_1-Min	4.50 (0.0049) [nπ*]	4.47 (0.0067) [ππ*/nπ*]	4.44 (0.0049) [ππ*/nπ*]	4.59 (0.1369) [ππ*]
ACN	***VEE***	4.68 (0.1077) [ππ*]	4.81 (0.0827) [ππ*]	4.76 (0.0854) [ππ*]	4.67 (0.0819) [ππ*]
	S_1-Min	4.41 (0.3144) [ππ*]	4.51 (0.2355) [ππ*/nπ*]	4.52 (0.0662) [ππ*/nπ*]	4.36 (0.3107) [ππ*]

[a] Oscillator strengths in round brackets and character of the excited states in square brackets.

4.4.2. Steady-State Measurements

The relevant maxima of steady-state UV/Vis absorption and fluorescence spectra of dilute solutions (~$3\cdot10^{-5}$ M) of 4,5,6,7-AI and NMe-7-AI in CH, ACN, DCM and MeOH, together with the quantum yields relative to 7-AI are summarized in Table 4.3. The corresponding absorption and emission spectra are shown in Figures 4.1 and 4.2.

Table 4.3. *Steady-state UV/Vis absorption and emission spectral maxima, and relative fluorescence quantum yields (ϕ_{fl})^a of the studied AIs in different solvents.*

		CH	**ACN**	**DCM**	**MeOH**
4-AI	$\lambda_{max, abs}$ / nm	286	288	289	291
	$\lambda_{max, em}$ / nm	317	350	339	400
	Φ_{fl}	0.022	0.507	0.592	4.534
5-AI	$\lambda_{max, abs}$ / nm	259	264	263	266
	$\lambda_{max, em}$ / nm	311	379	335	403
	Φ_{fl}	0.043	0.022	0.001	19.676
6-AI	$\lambda_{max, abs}$ / nm	286/255	288/260	288/260	293/260
	$\lambda_{max, em}$ / nm	312	344	354	421
	Φ_{fl}	0.015	0.009	0.003	34.777
7-AI	$\lambda_{max, abs}$ / nm	286	287	288	290
	$\lambda_{max, em}$ / nm	311	350	339	364
	Φ_{fl}	1.0	1.0	1.0	1.0
NMe-7-AI	$\lambda_{max, abs}$ / nm	290	289	291	287
	$\lambda_{max, em}$ / nm	327	367	356	371
	Φ_{fl}	1.081	1.189	1.083	61.133

^{a}All the ϕ_{fl} reported are relative to 7-AI at 298 K.

Concerning the CH solutions, this non-polar solvent should not shift significantly the electronic states, since it is weakly perturbing and therefore the spectroscopy of the molecules should not differ from the gas-phase data. As it can be observed in Figure 4.1a, NMe-7-AI, 7-AI, 6-AI and 4-AI in CH exhibit an absorption band in the region from ~240 to ~315 nm. 7-AI, 6-AI and 4-AI exhibit a maximum at 286 nm, whereas for NMe-7-AI is located at 293 nm. Additionally, shoulders at the red side of the absorption band that correspond to the 0—0 transition are noticeable for NMe-7-AI (~310 nm), 7-AI (~293 nm), 6-AI (~293 nm) and 4-AI (~298 nm). Furthermore, 6-AI shows a second peak at 255 nm, which we attribute to the S_3 ($2\pi\pi^*$) state. These experimental observations are in good agreement with the gas-phase TD-DFT calculations (Table 4.1), which predicted a larger 0.35 eV energy gap between the $\pi\pi^*$ states for 6-AI, enabling the individual observation of the two $\pi\pi^*$ states absorption bands. The absorption spectrum of 5-AI in CH, in the 240-290 nm range, is clearly different from the rest of AI derivatives, exhibiting the absorption maximum at ~259 nm and the shoulder at ~283 nm. This is also in consonance with the gas-phase *ab initio* calculations that estimated the vertical excitation of S_1 ($1\pi\pi^*$) state for 5-AI at least 0.14 eV above the value of the rest isomers.

Regarding the steady-state emission spectra of AIs derivatives in CH (see Figure 4.1b), all the AI isomers show emission in the 290-395 nm range but the fluorescence intensity of 7-AI is two orders of magnitude larger than that registered for 6-AI, 5-AI and 4-AI. NMe-7-AI, also exhibits an intense redshifted fluorescence, from 305 to 410 nm. These results are in good agreement with the dynamics observed in the isolated-phase, where 7-AI and NMe-7-AI exhibit long excited state lifetimes. Consequently, based on our mechanistic picture for the AIs in the gas-phase, 4-AI in vacuum should have a short excited state lifetime similar to those reported for 6-AI and 5-AI.

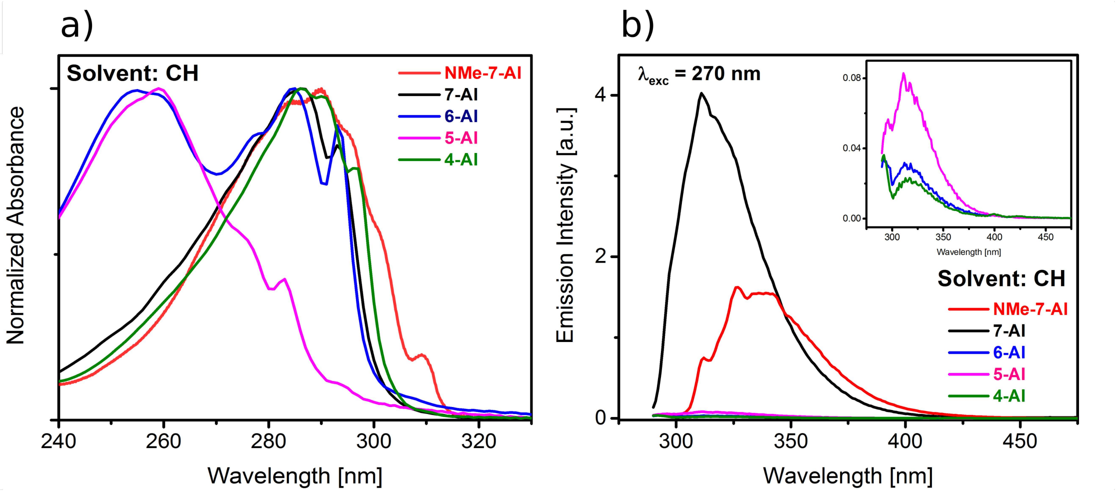

Figure 4.1. *Steady-state UV/Vis absorption (a) and fluorescence emission spectra (b) of AIs derivatives in cyclohexane.*

On the other hand, Figure 4.2a, c and e display the steady-state absorption spectra of AI derivatives in ACN, DCM and MeOH, in that order. In these polar solvents, the absorption spectra of the AIs are slightly redshifted and exhibit less resolved vibrational structure, but they do not show substantial differences with respect to those collected in CH (see Table 4.3). The redshifted shoulders are only noticeable in ACN and DCM solutions for 7-AI (~294 nm) and 6-AI (~296 nm). However, the steady-state fluorescence measurements in polar solvents profoundly differ from those observed in CH, as shown in Figure 4.2b, d and f.

For ACN (Figure 4.2b) and DCM solutions (Figure 4.2d), significant emission is observed for NMe-7-AI, 7-AI and 4-AI, whereas 6-AI and 5-AI give almost no fluorescence. Moreover, in contrast to ACN solutions, 6-AI in DCM exhibits more emission than 5-AI, even though both isomers give almost no fluorescence in comparison to the rest of AI derivatives. It is important to remark here that 4-AI in CH does not show a noticeable fluorescence, unlike ACN or DCM solutions. According to these results, the gas-phase long-lived 7-AI and NMe-7-AI exhibit strong fluorescence in all the studied solvents. Contrarily, the compounds showing ultrafast relaxation in the isolated-phase, 5-AI and 6-AI, are non-fluorescent in the polar aprotic solvents. On the other hand, 4-AI shows an intermediate behavior, switching on its fluorescence when solved in polar environments. These steady state observations correlate with the FuC measurements shown below and as we will further discuss, they can be rationalized in terms of the effect of the solvent polarity on the $n\pi^*$ state involved in the relaxation.

For MeOH solutions (Figure 4.2f), significant differences are observed with respect to the previously described polar aprotic solvents. Whereas NMe-7-AI gives a significant emission in the 325-495 nm range, with a maximum at ~371 nm, the 7-AI fluorescence is strongly quenched. The main reason of this observable is that in protic media 7-AI is capable of establishing H-bonds with solvent molecules, as it has been reported for water.[25] In comparison to 7-AI, 6-AI exhibits much higher fluorescence intensity and broadens its emission band, with a maximum peak at ~421 nm. Finally, 5-AI and 4-AI show a pronounced redshifted and more intense fluorescence compared to 7-AI, with the emission maxima at ~403 and ~400 nm, respectively. As we will discuss in more detail below, this behavior is fully conditioned by the appearance of tautomers that are formed by ESPT reaction through solvent molecules.

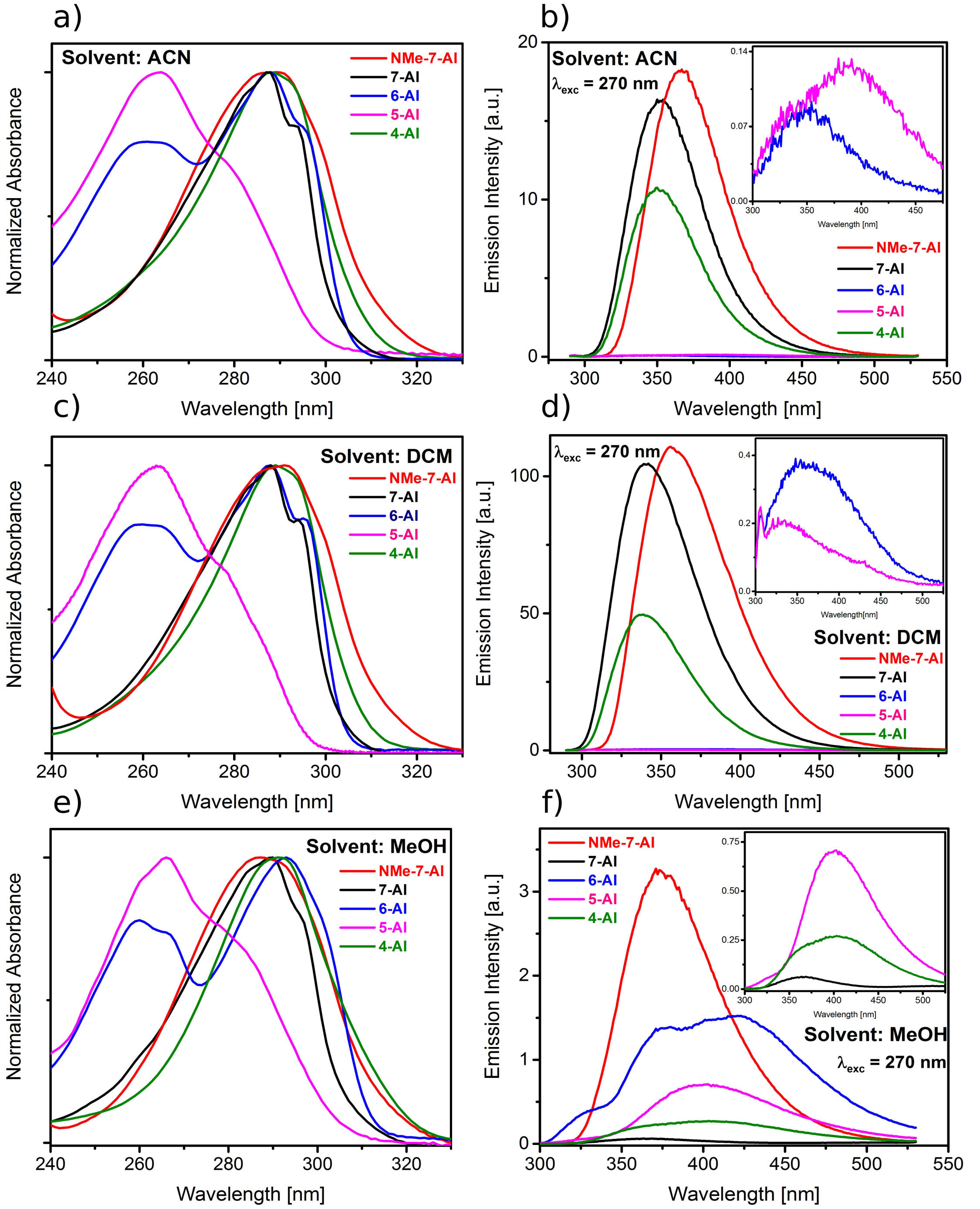

Figure 4.2. Steady-state UV/Vis absorption and fluorescence spectra of AI derivatives in acetonitrile (a-b), dichloromethane (c-d) and methanol (e-f).

Since solutions with higher concentrations (~6 mM) were required to conduct time-resolved experiments, the steady-state absorption and emission spectra of AI derivatives were studied increasing the concentration from 10^{-5} M up to 10^{-3} M. These measurements tried to explore the eventual formation of aggregates, in particular dimers and trimers that could interference with the detection of the targeted monomers. Figure 4.3 compares the concentration-dependent absorption and fluorescence spectra of 7-AI and 6-AI in CH and

ACN. For CH solutions, at high concentrations the absorption spectrum of 6-AI reveals a redshifted shoulder at about 305 nm, while 7-AI extends its absorption band to the red toward 320 nm. These observations indicate the formation of H-bonding aggregates in the non-polar solvent. Indeed, it is known that 6-AI and 7-AI tend to form trimers[26, 48] and dimers,[2-5, 13, 16, 49] respectively. The signatures of $(6\text{-AI})_3$ and $(7\text{-AI})_2$ were verified by collecting steady-state emission spectra (see Figure 4.3b), which reflect the emission maxima of the aggregates at ~482 nm. Unfortunately, for 4-AI and 5-AI, it was not possible to solve enough amount to reach the required concentrations and thus time-resolved experiments were not performed in this solvent. On the other hand, in the used polar solvents the AI derivatives do not show any significant dependence of their absorption or emission spectra on the concentration. Actually, polar solvents preclude the formation of self-aggregates because the solvent/solute interactions overpower those found in the self-aggregates,[25] making viable the study of monomers photodynamics by means of time-resolved techniques.

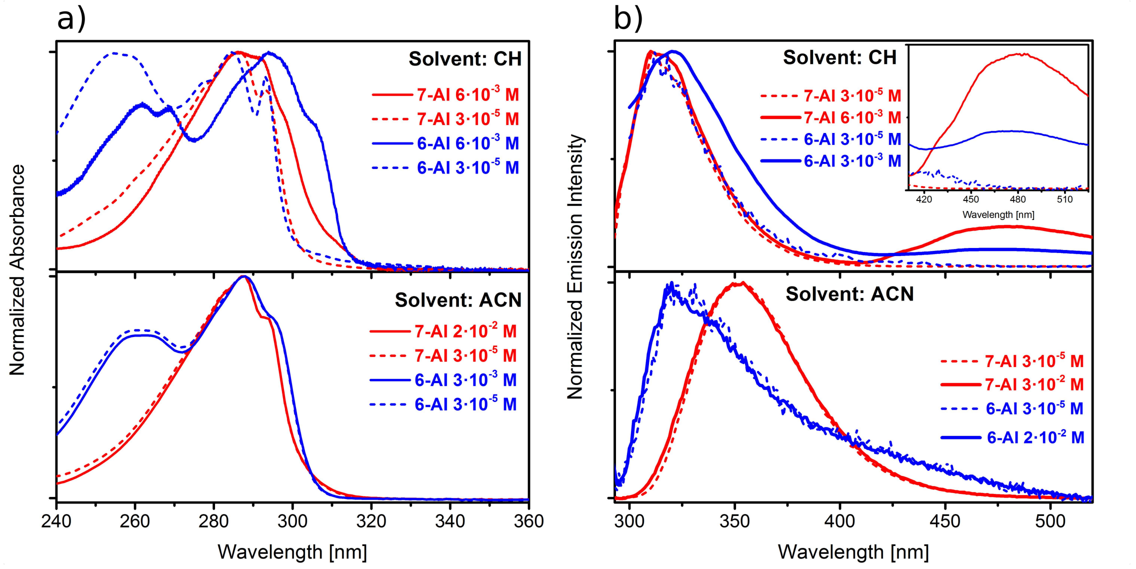

Figure 4.3. *Normalized steady-state absorption (a) and fluorescence (b) spectra of 7-AI and 6-AI isomers at different concentrations in cyclohexane (upper panel) and acetonitrile (lower panel).*

4.4.3. Time-Resolved Studies

The FuC transients of the AIs dissolved in ACN, DCM and MeOH were collected after excitation with 267 nm radiation, at a number of detection energies along the emission spectra. Furthermore, fluorescence decays were also recorded following photoexcitation with 300 nm (280 nm for 5-AI) for ACN solutions, although they did not provide additional information (included as supporting data in Figure 4.13). In order to facilitate the assignment of the extracted time constants, the solvation effect was checked by tracking the time-resolved emission of long-lived Coumarin 153 (C153) dissolved in each solvent. Additionally, to provide a more complete picture of the observed photodynamics, TA experiments on ACN solutions were conducted.

4.4.3.1. Acetonitrile Solutions

Figure 4.4 shows the FuC measurements conducted in ACN solutions at 338 (a_1-e_1), 355 (a_2-e_2) and 381 nm (a_3-e_3) emission wavelengths, following photoexcitation with 267 nm radiation. Although three time constants (τ_1, τ_2 and τ_3) were used to model all the fluorescence decays, in some transients cross-talking between the constants has been detected, revealing the multi-exponential character of some of the processes involved in the relaxation. The most remarkable observation is that the decays of 5-AI and 6-AI are much faster than those found for 4-AI, 7-AI and NMe-7-AI. This fact correlates with the steady-state fluorescence measurements, which showed that the emission is reduced several orders of magnitude for 5-AI and 6-AI. According to this, we will separate the description and analysis of the time-dependent data in two groups: fluorescent and non-fluorescent samples.

For the fluorescent 4-AI, 7-AI and NMe-7-AI, τ_1 shows values of hundreds of fs, while τ_2 and τ_3 reach values of few ps and ns, respectively (see Figures 4.4$a_{1\text{-}3}$, $d_{1\text{-}3}$ and $e_{1\text{-}3}$). The longest τ_3 accounts for the lifetime of the final emitting location of the excited state, while τ_1 and τ_2 are very likely related to vibrational relaxation processes. In fact, as the detection is shifted to the red, the τ_1 decay is less perceptible and even, in the case of 4-AI and 7-AI, becomes a rising signal (Figure 4.4a_3 and d_3). Such behavior is indicative of dynamic Stokes shift, which is a spectral redshift of the emission because of solvent reorganization during the excited state lifetime.[45, 50-51] It should be noted here that for NMe-7-AI, τ_1 remains as a decay component even at the longest detection wavelength (Figure 4.4e_3). We attribute this behavior to its redshifted steady-state emission spectrum, which would require moving the detection further to the red to observe the formation component.

Aiming to obtain the characteristic lifetimes related with the ACN solvation dynamics and to confirm the origin of τ_1 time component, FuC measurements were conducted for C153 in ACN, exciting at 400 nm and detecting at 493 and 561 nm emission wavelengths, as shown in Figure 4.5. C153 has been extensively used because it is considered an ideal model system to probe the solvation dynamics in several solvents due to its large dipole moment change, rigid structure, small nonradiative deactivation, invariant transition moment and large Stokes shift.[52-55] From this study, a multi-exponential behavior with two time constants (τ_0 and τ_1) was observed for the solvation dynamics. The emission transient detected in the blue region of the fluorescence spectrum of C153 in ACN (Figure 4.5a) shows a sub-ps decay (τ_0) and a ps decay component (τ_1), together with a constant decay component in the ns range (τ_2). The first two components correspond to the solvent response, while the longest one accounts for the S_1 state relaxation. These measurements match previous observations on the same system.[55] From this measurement, a fast response of about 1 ps can be expected for ACN solvation dynamics, which would confirm the origin of the τ_1 time component observed for the fluorescent AIs.

The origin of τ_2 is more obscure. Very remarkably, this lifetime appears as a formation component for all the fluorescent compounds. We tentatively ascribe this time component to a vibrational reorganization between the $\pi\pi^*$ states. Presumably, after 267 nm excitation a population equilibration scenario is possible between the $1\pi\pi^*$ and $2\pi\pi^*$ states.

Finally, the long τ_3 component indicates that the prepared excited state relaxes in the ps-ns time-scale toward a non-fluorescent location, which based on the complementary TA experiments (see Figure 4.7) should be the repopulation of the electronic ground state.

On the other hand, for the non-fluorescent 5-AI and 6-AI (Figure 4.4$b_{1\text{-}3}$ and $c_{1\text{-}3}$) τ_1 exhibits values of hundreds of fs, whereas τ_2 and τ_3 reach values of tens and hundreds of ps, respectively. In this case, the three lifetimes are observed as decay components at all the emission wavelengths, which does not permit to isolate the contribution of the solvation dynamics. By comparison with the dynamics described in the gas-phase, the full multi-exponential decay has to be attributed to the relaxation pathway that takes the molecule from the $\pi\pi^*$ locally excited state to the S_1/S_0 CI, and finally to the ground state. This path would involve vibrational relaxation and the coupling between the $\pi\pi^*$ and $n\pi^*$ states. Simultaneously, at the earlier times the solvent response has to be present too. Indeed, the fact that τ_1 slows as the emission wavelength is moved to the red could reflect this process.

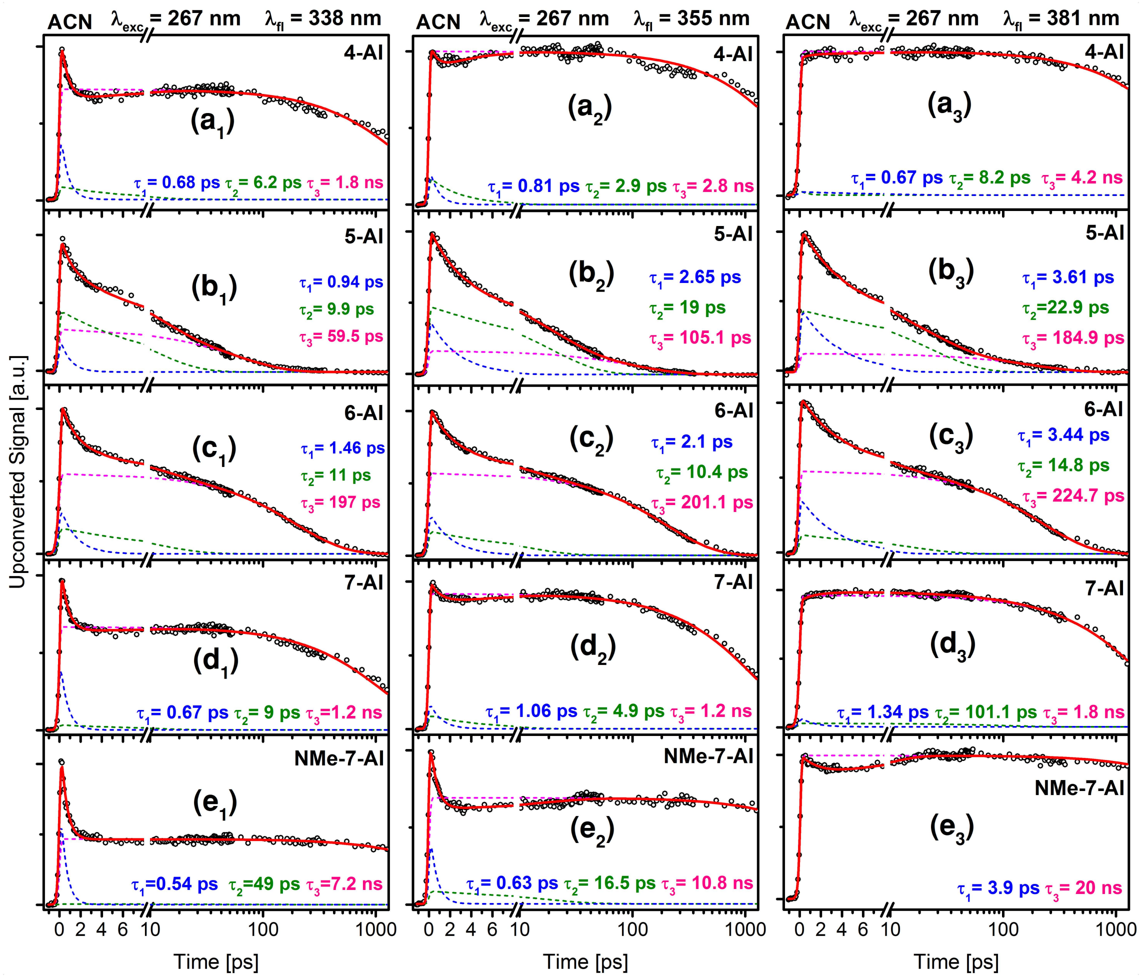

Figure 4.4. *Time-resolved fluorescence decays for acetonitrile solutions of AI derivatives, collected at 267 nm excitation and 338 (a₁-e₁), 355 (a₂-e₂) and 381 nm (a₃-e₃) emission wavelengths. The black dots represent the transient obtained, while the solid red line correspond to the exponential fit. Dash lines show the components of the fit.*

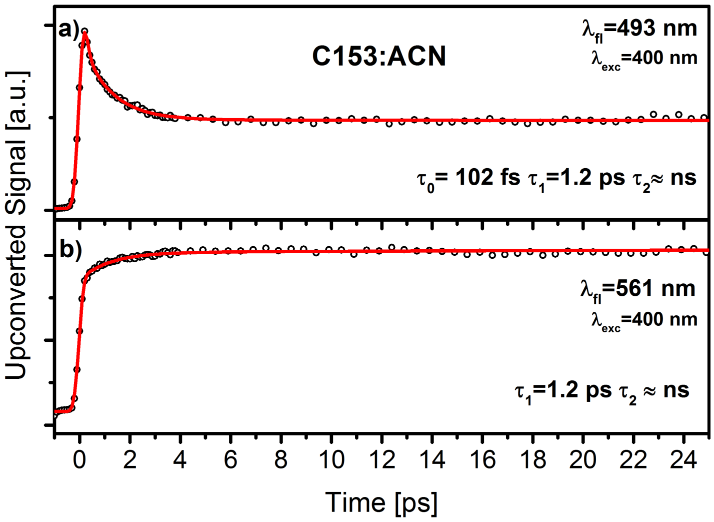

Figure 4.5. *Time-resolved fluorescence transients from C153 in ACN, collected at 493 (a) and 561 nm (b) emission wavelengths, after 400 nm excitation.*

Aiming to gain additional dynamical insights and to confirm the observations made in the FuC experiments, the relaxation mechanism of ACN solutions was further explored by means of TA spectroscopy. The measurements covered the 350-700 nm absorption range for several picoseconds after photoexcitation. The TA spectra of AI derivatives (see Figure 4.6) exhibit, along the full time window studied, an undistinguishable absorption signature that covered the whole probe range, which results from the overlap of the different spectral features. Consequently, no significant dynamical information about specific locations of the excited and ground state involved in the relaxation pathway was extracted from these measurements.

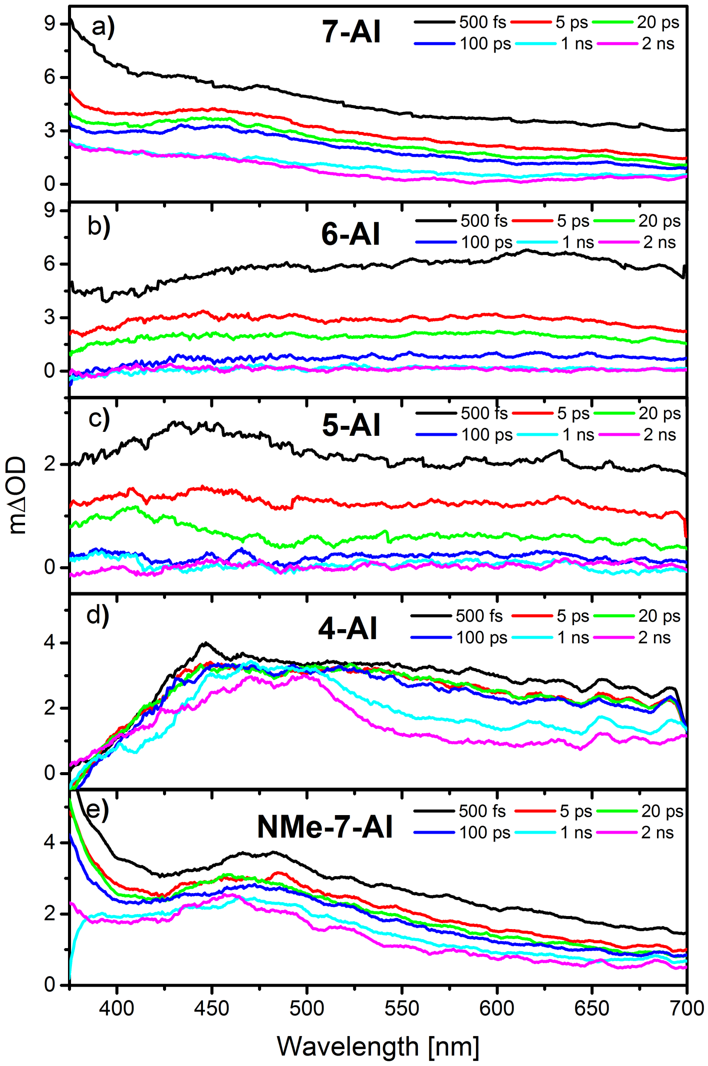

Figure 4.6. *TA spectra recorded at characteristic delay times after 267 nm excitation for 7-AI (a), 6-AI (b), 5-AI (c), 4-AI (d) and NMe-7-AI (e) in acetonitrile.*

Figure 4.7 displays the recorded TA decays for the AI derivatives at 500 (a_1-e_1) and 625 nm (a_2-e_2) probe wavelengths, following photoexcitation with 267 nm radiation. The excited state dynamics of the AIs decays with similar time components to those observed for the FuC experiments, which ensures that we are not observing an additional dynamical signature between dark states (for example triplet states) that we were not capable of noticing with the FuC technique. 5-AI and 6-AI (Figure 4.7b$_{1-2}$ and c$_{1-2}$) are able to relax to the ground state faster than 4-AI, 7-AI and NMe-7-AI (Figure 4.7a$_{1-2}$, d$_{1-2}$ and e$_{1-2}$). Moreover, the amplitudes of τ_1 and τ_2 for 5-AI and 6-AI are considerably larger than that for τ_3, whereas for the rest of AIs τ_3 exhibits the largest amplitude. It is noteworthy that, as it was observed in the fluorescence decays, the TA transients of 5-AI and 6-AI show slower values for τ_1 at longer probe wavelengths, which suggests that this time component describes the solvation dynamic, occurring at earlier times in parallel to other intramolecular relaxation processes.

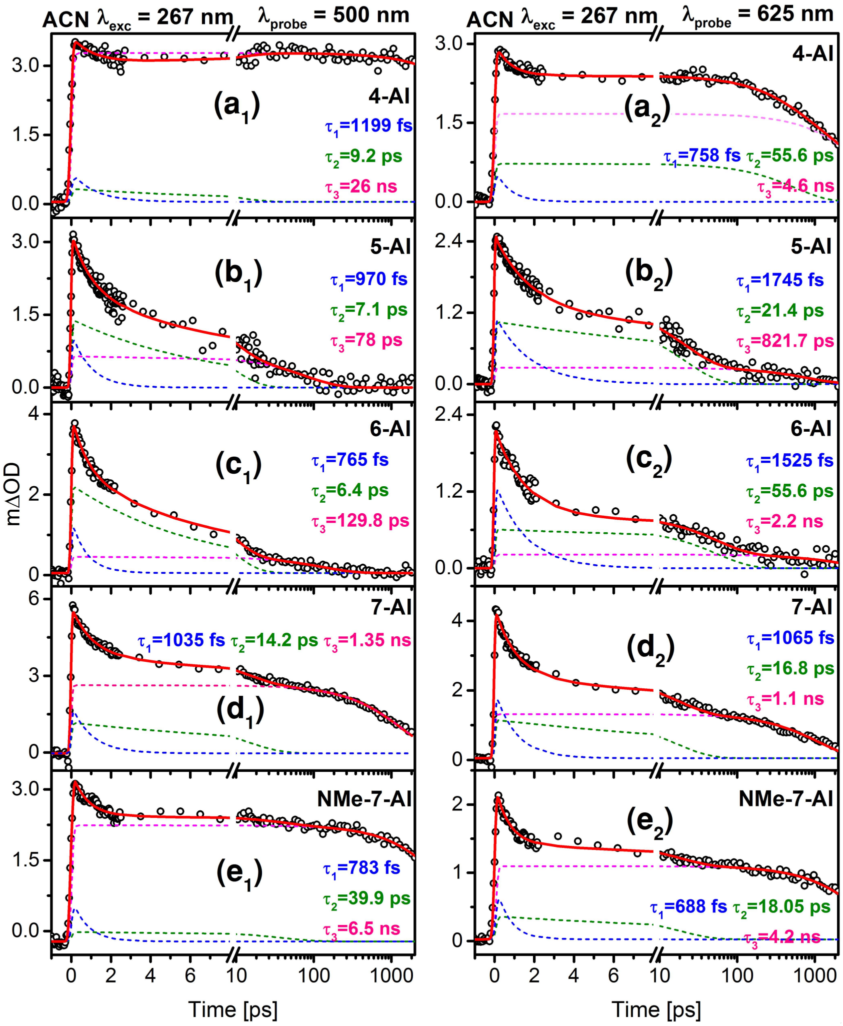

Figure 4.7. Transient absorption of the studied AIs in acetonitrile at 500 (a$_1$-e$_1$) and 625 nm (a$_2$-e$_2$) probe wavelengths, after 267 nm excitation.

By comparing the time-resolved studies conducted in ACN solutions with the previous results obtained in vacuum, the effect of this polar aprotic solvent on the photodynamics of AIs can be discussed. The PCM/TD-DFT calculations (see Tables 4.1 and 4.2) predicted a strong blueshift of the nπ* state for all the AI derivatives. Indeed, ACN changes the relative energy of the lowest excited states in the Franck-Condon region, altering the energy ordering of S_2 and S_3 for 4-AI, 5-AI and 6-AI. In this sense, we propose that the longer lifetimes observed for the non-fluorescent 5-AI and 6-AI molecules in ACN solutions, with respect to the isolated-phase, are due to the increase of barrier met on the route from the locally excited state to the nπ*/S_0 CI. Thus, the polarity of ACN modulates the topology of the involved potential energy surfaces and consequently the access to this CI.

Attending to the collected experimental results, the polarity of the environment changes more dramatically the photodynamics of 4-AI, from a behavior similar to 5-AI and 6-AI in non-polar media, to a relaxation that matches that found for the fluorescent 7-AI and NMe-7-AI. Accordingly, we propose that the relaxation mechanism for 4-AI in ACN is analogous to that described for 7-AI and NMe-7-AI, where the excitation/relaxation process involves only the ππ* excited states. The destabilization induced by the solvent would shift the nπ* surface to even higher energies than those found for 5-AI and 6-AI, blocking the access to it, and thus to the nπ*/S_0 relaxation channel.

As expected, for 7-AI and NMe-7-AI, the polarity of the solvent does not introduce significant changes in the operative relaxation channel, since the shift of the nπ* state is going to make the route *via* this state even less effective than in the isolated-phase.

4.4.3.2. Dichloromethane Solutions

To confirm the effects observed in ACN, time-resolved experiments were conducted in DCM, a less polar solvent than ACN ($P_{DCM} = 3.1 < P_{ACN} = 5.8$).[56-57] Figure 4.8 displays the collected FuC measurements at 338 (a_1-e_1), 355 (a_2-e_2) and 375 nm (a_3-e_3) emission wavelengths, after excitation with 267 nm. Additionally, the fluorescence decays of C153, which account for DCM solvation dynamics, are shown in Figure 4.9. The photodynamical behavior of the AIs confirms the trend found in ACN solutions: 5-AI and 6-AI exhibit faster relaxation times in the ps time-scale and absence of fluorescence, while 4-AI, 7-AI and NMe-7-AI show strong fluorescence and lifetimes in the ns scale.

In general, three time constants were used to model the experimental data, although in some cases single-exponential (Figure 4.8a_2 and e_3) or bi-exponential (Figure 4.8a_1 and d_2) fits were employed. The interpretation of these time constants is analogous to that offered for the transients collected in ACN.

Interestingly, the 5-AI and 6-AI transients show notable differences with respect to those collected in ACN. Although the multi-exponential lifetimes are similar in both solvents, the amplitude of τ_1 and τ_2 time constants is remarkably larger in DCM, yielding a faster average decay-time.[58] This result is in good terms with the solvent polarity effect. Since DCM is a weaker polar solvent than ACN, the nπ* state is less destabilized (see Table 4.1) and for this reason faster dynamics can be expected.

Nevertheless in the case of 4-AI, it seems that the polarity of DCM still shifts the nπ* state enough to avoid the access to this surface, exhibiting the same behavior than in the more polar ACN.

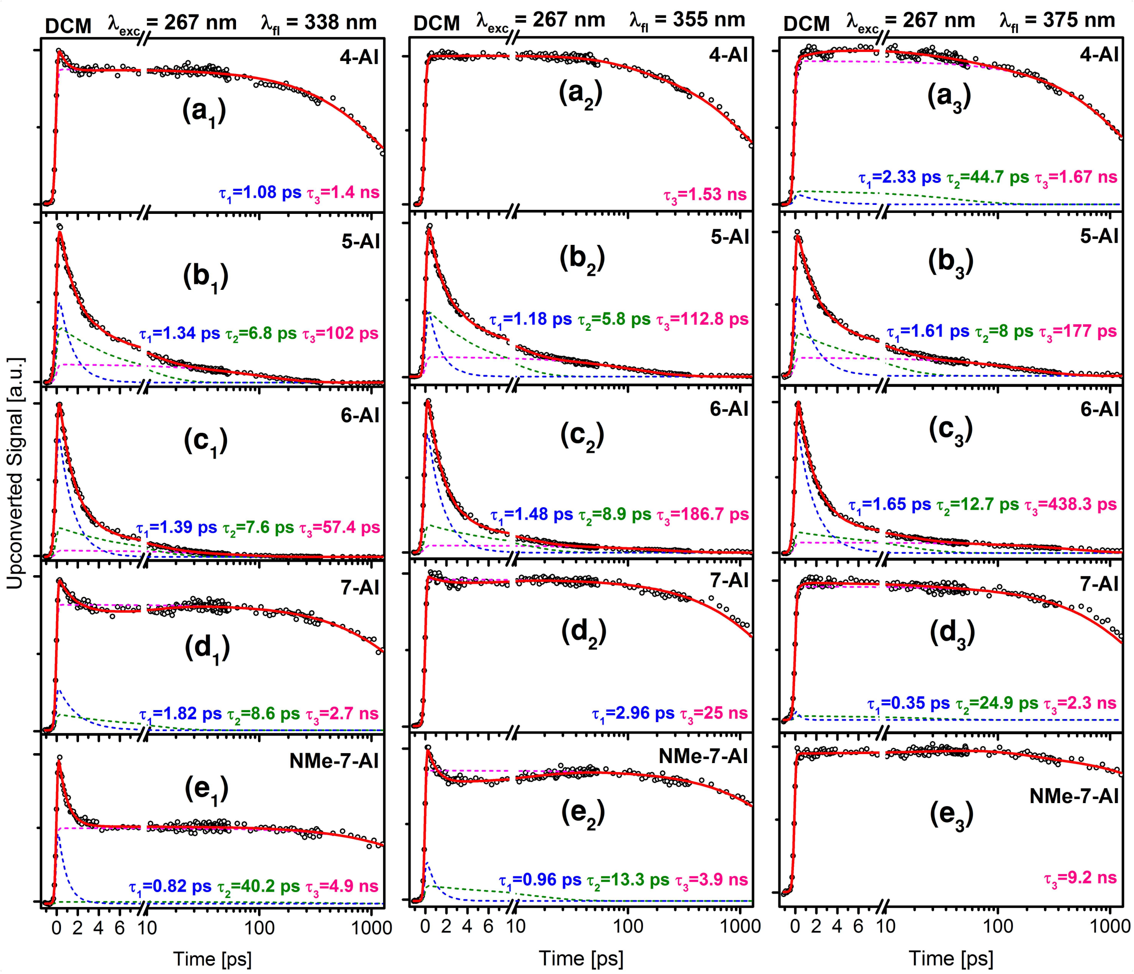

Figure 4.8. *Time-resolved fluorescence decays for dichloromethane solutions of AI derivatives, collected at 267 nm excitation and 338 (a_1-e_1), 355 (a_2-e_2) and 375 nm (a_3-e_3) emission wavelengths.*

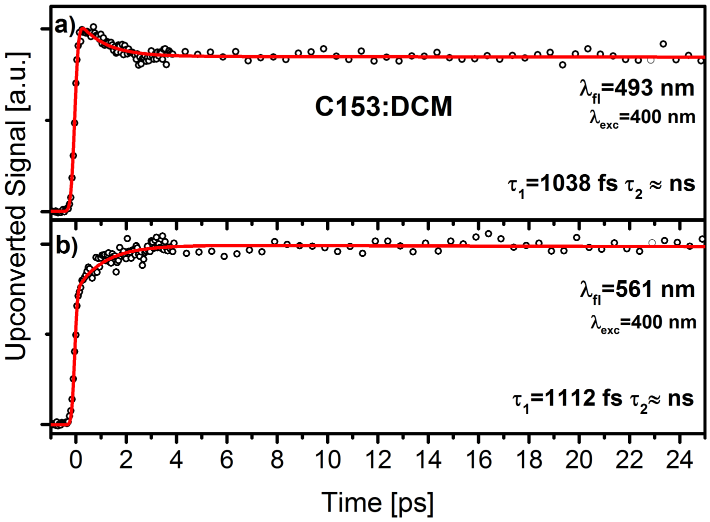

Figure 4.9. *Fluorescence decays of C153 in DCM, collected at 493 (a) and 561 nm (b) emission wavelengths, after 400 nm excitation.*

4.4.3.3. Methanol Solutions

The photodynamics of AI derivatives was also studied in protic media. Figure 4.10 shows the fluorescence decays collected in MeOH solutions at 323 (a_1-e_1), 355 (a_2-e_2) and 375 nm (a_3-e_3) emission wavelengths, following 267 nm excitation. These FuC measurements yielded a completely different photophysical behavior in comparison to that previously studied in polar aprotic solvents. As it can be observed, 7-AI is the isomer with the shortest lifetime. Furthermore, while 4-AI and 7-AI display faster decays than in ACN and DCM solutions, 5-AI and 6-AI exhibit a significantly slower excited state dynamics. Only NMe-7-AI shows transients similar to those registered in polar aprotic media. This behavior can be related to the anomalous florescence patterns found in the steady-state experiments (see Figure 4.2f). A detailed interpretation of the observed behavior requires of further investigation, since in this work we can only offer a rough preliminary picture.

For all the AIs, three time constants were employed to model the recorded transients. Generally, τ_1 is a decay of hundreds of fs for all the AIs at short detection wavelengths, but at 375 nm emission wavelength this lifetime becomes a rise for all the compounds, except for NMe-7-AI where it remains being a decay component (4.10e_3). On the other hand, τ_2 yields values of some picoseconds and its weight highly depends on the detection wavelength. These time constants can be associated to the solvent response, which as previous studies[53, 55, 59] and our own measurements in C153 (see Figure 4.11) show, is characterized in MeOH by a fast initial component of hundreds of fs and followed by a slower response in tens of ps.

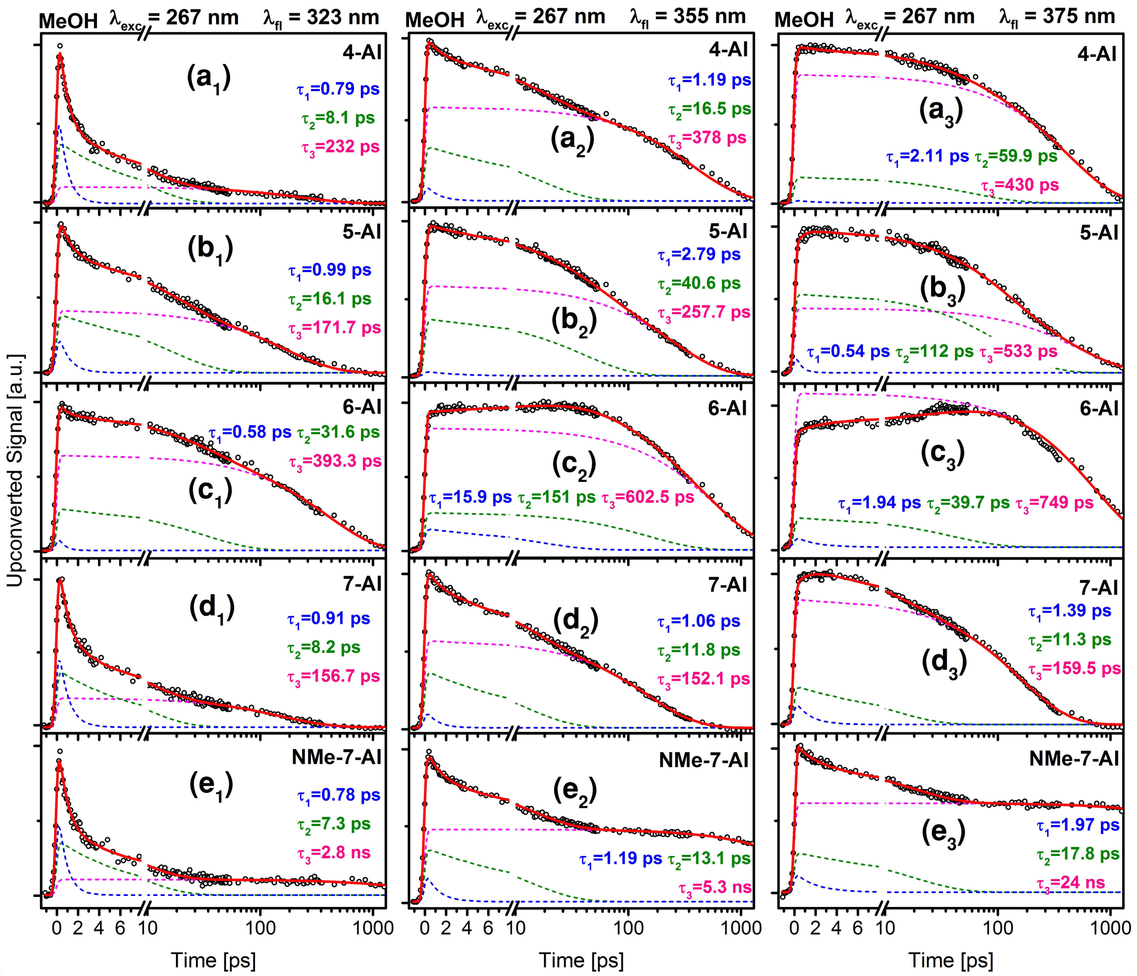

Figure 4.10. *Time-resolved fluorescence decays for methanol solutions of AI derivatives, collected at 267 nm excitation and 323 (a_1-e_1), 355 (a_2-e_2) and 375 nm (a_3-e_3) emission wavelengths.*

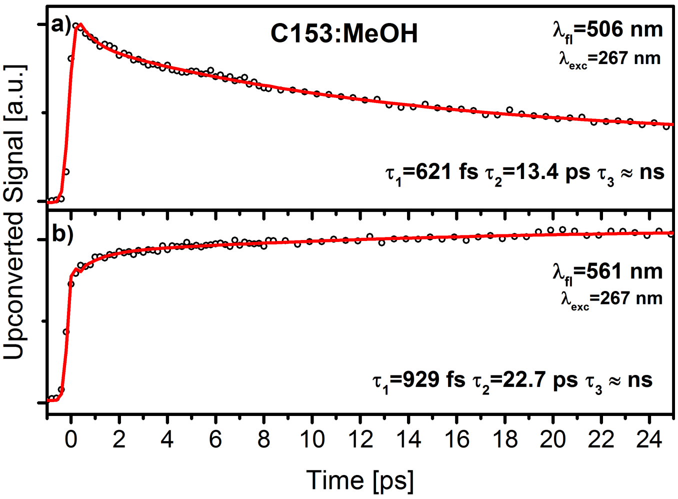

Figure 4.11. *Time-resolved fluorescence decays for MeOH solution of C153, collected at 506 (a) and 561 (b) nm emission wavelengths, after 267 nm excitation.*

The longer τ_3 lifetime can be conditioned by the appearence of ESPT processes that lead to the formation of tautomers. At least for 7-AI in water and methanol, it has been demonstrated the occurrence of this process that takes place in the ps time-scale.[18-21, 60] After photoexcitation, the donor nitrogen proton (-N-H) is transferred through a chain of solvent molecules to the proton acceptor (=N-H), yielding the corresponding tautomer (see Figure 4.12). The formed tautomer is characterized by a fluorescence band shifted to the red.[7]

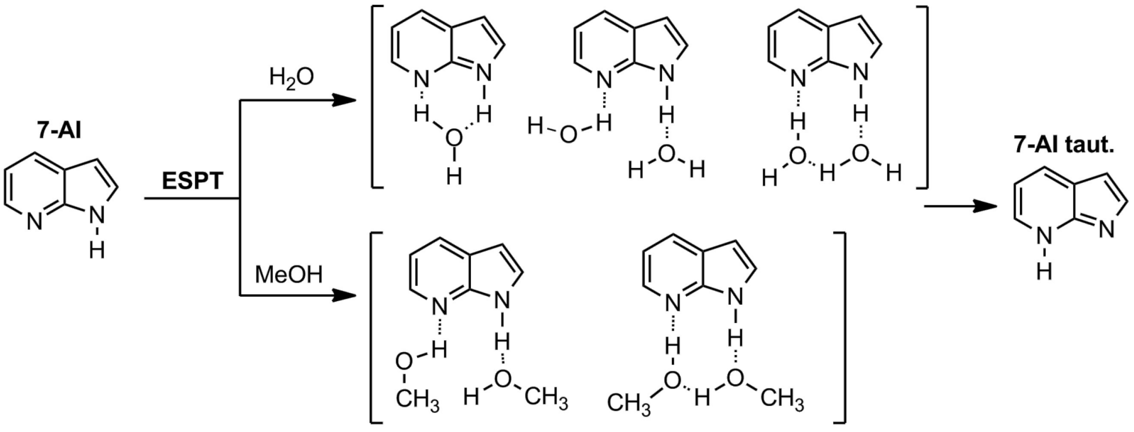

Figure 4.12. Schematic representation of ESPT process that yields the 7-AI tautomer. In water, the formation of cyclic intermediates has been reported,[25] however, the majority of 7-AI molecules in water or methanol establish H-bonds with two different solvent molecules.[61-62]

At least in the case of 7-AI, the measured ps lifetime seems to reflect this ESPT process. Nonetheless, additional measurements in the red portion of the spectrum should be conducted to confirm the formation of the tautomer.

For the other isomers (4-AI, 5-AI and 6-AI), the influence of this process is not so clear. ESPT has been reported in 6-AI trimers,[26] in methanol-water solutions of 6-AI and in basic water solutions of 4-AI and 5-AI, where the protonated forms are favored.[22-23, 25] Although, in principle, the occurrence of solvent assisted ESPT is feasible in the studied MeOH solutions, it has not been unambiguously characterized to date. Further studies are necessary to explore the influence of this channel in the observed dynamics.

However, an interesting observation regarding the eventual participation of ESPT in the observed dynamics for in 4-AI, 5-AI and 6-AI, is the behavior found in NMe-7-AI. Being the only studied compound that cannot present this channel, its steady-state fluorescence and dynamics in MeOH are very similar to those registered in the other studied polar solvents.

4.5. Conclusions

This chapter has presented the study of the excited state dynamics of AI derivatives in different solvents. For that purpose, firstly steady-state absorption and emission spectra of AIs in CH, ACN, DCM and MeOH were collected. The relaxation dynamics of the four AI isomers and NMe-7-AI was tracked in ACN, DCM and MeOH by FuC and TA measurements. Predictions on the vertical excitation energies in ACN, DCM and MeOH and on the excited state minima were obtained by PCM/TD-DFT calculations.

From the comparison of the calculations and the experimental data we can conclude, in correlation with the gas-phase results, that the lifetime of the studied AIs depends on the relative energy between the dark $n\pi^*$ and the bright $\pi\pi^*$ states, which is controlled by the polarity of the environment. As the calculations predict, the polarity of the solvent shifts the $n\pi^*$ surface to higher energies. This hampers the access to this surface and to the $n\pi^*/S_0$ CI, which according to the gas-phase studies, is the relaxation channel that controls the dynamics of the AIs.

4-AI is the compound that exhibited the most pronounced change in its photophysical properties, with the solvent polarity. It switches from a non-fluorescent behavior in the non-polar environment, similar to 5-AI and 6-AI, to exhibit strong fluorescence and ns relaxation lifetimes in the moderately polar DCM. This can be explained in terms of a strong destabilization of the $n\pi^*$ surface with respect to the initially excited $\pi\pi^*$ state, which blocks the channel mediated by the $n\pi^*/S_0$ CI. Thus, the relaxation pathway is analogous to that operative in 7-AI, which involves only the $\pi\pi^*$ states.

On the other hand, 5-AI and 6-AI show a less extreme behavior. The increasing polarity of DCM and ACN causes a progressive slowdown of the measured averaged fluorescence lifetime, but according to the extracted lifetimes, the access to the $n\pi^*$ surface seems still feasible.

Finally, the measurements conducted in MeOH showed, except for the methylated derivative NMe-7-AI, a different picture with respect to the photophysics observed in the polar aprotic media. In this case, the photodynamics seems to reflect ESPT reactions that lead to the formation of tautomers. Further studies able to detect the dynamical signature of the resulting reaction products would be required.

4.6. Additional Information

4.6.1. FuC Decays of the AIs with 300 nm Excitation

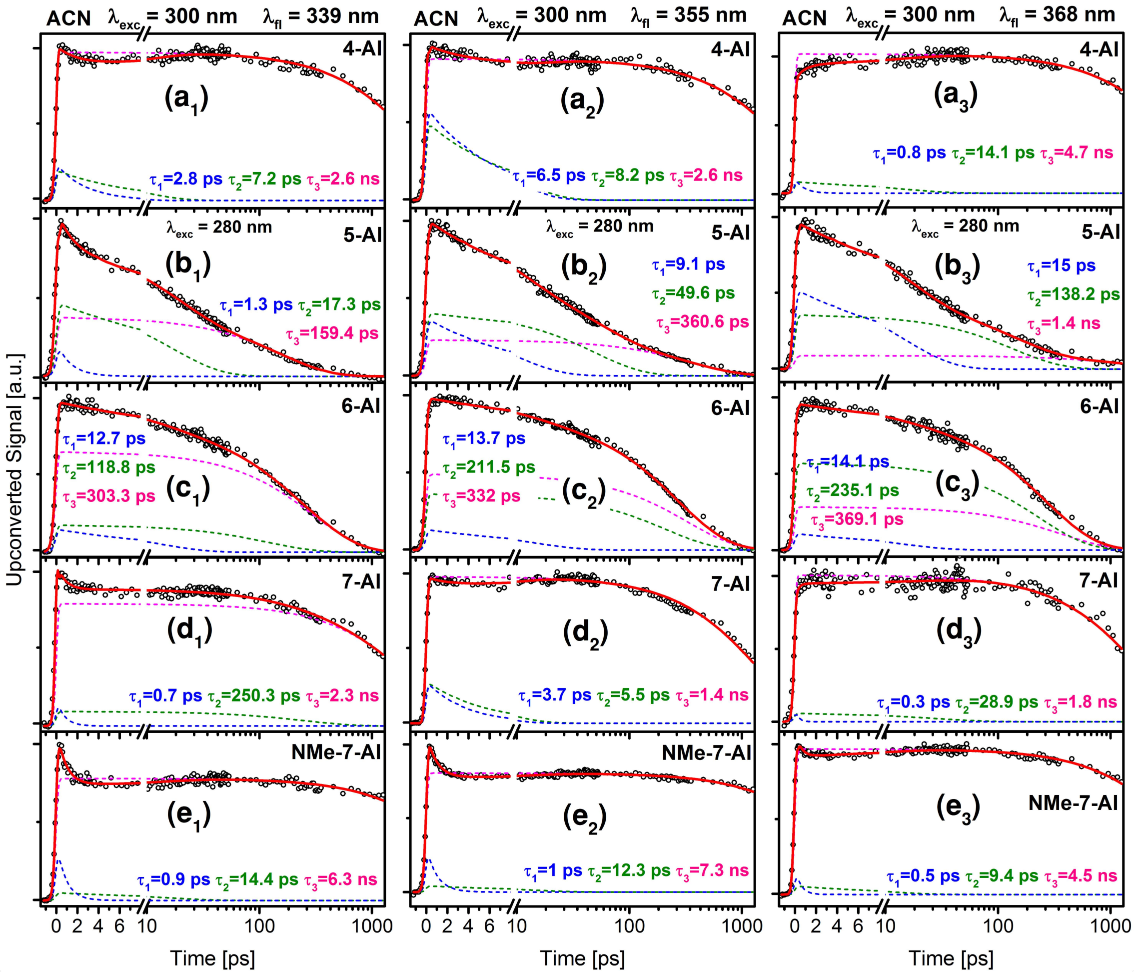

Figure 4.13. *Time-resolved fluorescence decays for acetonitrile solutions of AI derivatives collected at 338 (a_1-e_1), 355 (a_2-e_2) and 368 nm (a_3-e_3) emission wavelengths, after excitation with 300 nm (280 nm for 5-AI) radiation.*

4.7. References

1. Taylor, C. A.; El-Bayoumi, M. A.; Kasha, M., Excited-State Two-Proton Tautomerism in Hydrogen-bonded N-Heterocyclic Base Pairs. *Proceedings of the National Academy of Sciences* **1969,** *63* (2), 253.

2. Douhal, A.; Kim, S. K.; Zewail, A. H., Femtosecond molecular dynamics of tautomerization in model base pairs. *Nature* **1995,** *378* (6554), 260-263.

3. Catalán, J.; del Valle, J. C.; Kasha, M., Resolution of concerted versus sequential mechanisms in photo-induced double-proton transfer reaction in 7-azaindole H-bonded dimer. *Proceedings of the National Academy of Sciences* **1999,** *96* (15), 8338.

4. Hiroshi, S.; Kenji, S., Excited-State Double-Proton Transfer in the 7-Azaindole Dimer in the Gas Phase. Resolution of the Stepwise versus Concerted Mechanism Controversy and a New Paradigm. *Bulletin of the Chemical Society of Japan* **2006,** *79* (3), 373-385.

5. Crespo-Otero, R.; Kungwan, N.; Barbatti, M., Stepwise double excited-state proton transfer is not possible in 7-azaindole dimer. *Chemical Science* **2015,** *6* (10), 5762-5767.

6. Fuke, K.; Ishikawa, H., Dynamics of proton transfer reactions of model base pairs in the ground and excited states: Revisited. *Chemical Physics Letters* **2015,** *623*, 117-129.

7. Svartsov, Y. N.; Schmitt, M., Electronically excited states of water clusters of 7-azaindole: Structures, relative energies, and electronic nature of the excited states. *The Journal of Chemical Physics* **2008,** *128* (21), 214310.

8. Sakota, K.; Jouvet, C.; Dedonder, C.; Fujii, M.; Sekiya, H., Excited-State Triple-Proton Transfer in 7-Azaindole(H2O)2 and Reaction Path Studied by Electronic Spectroscopy in the Gas Phase and Quantum Chemical Calculations. *The Journal of Physical Chemistry A* **2010,** *114* (42), 11161-11166.

9. Pino, G. A.; Alata, I.; Dedonder, C.; Jouvet, C.; Sakota, K.; Sekiya, H., Photon induced isomerization in the first excited state of the 7-azaindole–(H2O)3cluster. *Physical Chemistry Chemical Physics* **2011,** *13* (13), 6325-6331.

10. Kungwan, N.; Kerdpol, K.; Daengngern, R.; Hannongbua, S.; Barbatti, M., Effects of the second hydration shell on excited-state multiple proton transfer: dynamics simulations of 7-azaindole: (H2O)1–5 clusters in the gas phase. In *Isaiah Shavitt: A Memorial Festschrift from Theoretical Chemistry Accounts*, Shepard, R.; Pitzer, R. M.; Dunning, T., Eds. Springer Berlin Heidelberg: Berlin, Heidelberg, 2016; pp 349-359.

11. Koizumi, Y.; Jouvet, C.; Norihiro, T.; Ishiuchi, S.-i.; Dedonder-Lardeux, C.; Fujii, M., Electronic spectra of 7-azaindole/ammonia clusters and their photochemical reactivity. *The Journal of Chemical Physics* **2008,** *129* (10), 104311.

12. Kerdpol, K.; Daengngern, R.; Kungwan, N., Excited-state proton-transfer reactions of 7-azaindole with water, ammonia and mixed water–ammonia: microsolvated dynamics simulation. *Molecular Simulation* **2015,** *41* (14), 1177-1186.

13. Takeuchi, S.; Tahara, T., Observation of dimer excited-state dynamics in the double proton transfer reaction of 7-azaindole by femtosecond fluorescence up-conversion. *Chemical Physics Letters* **1997,** *277* (4), 340-346.

14. Takeuchi, S.; Tahara, T., Femtosecond Ultraviolet−Visible Fluorescence Study of the Excited-State Proton-Transfer Reaction of 7-Azaindole Dimer. *The Journal of Physical Chemistry A* **1998,** *102* (40), 7740-7753.

15. Chachisvilis, M.; Fiebig, T.; Douhal, A.; Zewail, A. H., Femtosecond Dynamics of a Hydrogen-Bonded Model Base Pair in the Condensed Phase: Double Proton Transfer in 7-Azaindole. *The Journal of Physical Chemistry A* **1998,** *102* (4), 669-673.

16. Fiebig, T.; Chachisvilis, M.; Manger, M.; Zewail, A. H.; Douhal, A.; Garcia-Ochoa, I.; de La Hoz Ayuso, A., Femtosecond Dynamics of Double Proton Transfer in a Model DNA Base Pair: 7-Azaindole Dimers in the Condensed Phase. *The Journal of Physical Chemistry A* **1999,** *103* (37), 7419-7431.

17. Kwon, O.-H.; Zewail, A. H., Double proton transfer dynamics of model DNA base pairs in the condensed phase. *Proceedings of the National Academy of Sciences* **2007,** *104* (21), 8703.

18. Chen, Y.; Rich, R. L.; Gai, F.; Petrich, J. W., Fluorescent species of 7-azaindole and 7-azatryptophan in water. *The Journal of Physical Chemistry* **1993,** *97* (9), 1770-1780.

19. Gai, F.; Chen, Y.; Petrich, J. W., Nonradiative pathways of 7-azaindole in water. *Journal of the American Chemical Society* **1992,** *114* (22), 8343-8345.

20. Smirnov, A. V.; English, D. S.; Rich, R. L.; Lane, J.; Teyton, L.; Schwabacher, A. W.; Luo, S.; Thornburg, R. W.; Petrich, J. W., Photophysics and Biological Applications of 7-Azaindole and Its Analogs. *The Journal of Physical Chemistry B* **1997,** *101* (15), 2758-2769.

21. Rich, R. L.; Chen, Y.; Neven, D.; Negrerie, M.; Gai, F.; Petrich, J. W., Steady-state and time-resolved fluorescence anisotropy of 7-azaindole and its derivatives. *The Journal of Physical Chemistry* **1993,** *97* (9), 1781-1788.

22. Twine, S. M.; Murphy, L.; Phillips, R. S.; Callis, P.; Cash, M. T.; Szabo, A. G., The Photophysical Properties of 6-Azaindole. *The Journal of Physical Chemistry B* **2003,** *107* (2), 637-645.

23. Cash, M. T.; Schreiner, P. R.; Phillips, R. S., Excited state tautomerization of azaindole. *Organic & Biomolecular Chemistry* **2005,** *3* (20), 3701-3706.

24. Carnerero, J. M.; González-Benjumea, A.; Carmona, C.; Balón, M., Spectroscopic study of the ground and excited state prototropic equilibria of 4-azaindole. *Spectrochimica Acta Part A: Molecular and Biomolecular Spectroscopy* **2012,** *97*, 1072-1078.

25. Merkel, L.; Hoesl, M. G.; Albrecht, M.; Schmidt, A.; Budisa, N., Blue Fluorescent Amino Acids as In Vivo Building Blocks for Proteins. *ChemBioChem* **2010,** *11* (3), 305-314.

26. Tu, T.-H.; Chen, Y.-T.; Chen, Y.-A.; Wei, Y.-C.; Chen, Y.-H.; Chen, C.-L.; Shen, J.-Y.; Chen, Y.-H.; Ho, S.-Y.; Cheng, K.-Y.; Lee, S.-L.; Chen, C.-h.; Chou, P.-T., The Cyclic Hydrogen-Bonded 6-Azaindole Trimer and its Prominent Excited-State Triple-Proton-Transfer Reaction. *Angewandte Chemie International Edition* **2018,** *57* (18), 5020-5024.

27. Crespo-Hernández, C. E.; Cohen, B.; Hare, P. M.; Kohler, B., Ultrafast Excited-State Dynamics in Nucleic Acids. *Chemical Reviews* **2004,** *104* (4), 1977-2020.

28. Vries, M. S. d.; Hobza, P., Gas-Phase Spectroscopy of Biomolecular Building Blocks. *Annual Review of Physical Chemistry* **2007,** *58* (1), 585-612.

29. Gustavsson, T.; Improta, R.; Markovitsi, D., DNA/RNA: Building Blocks of Life Under UV Irradiation. *The Journal of Physical Chemistry Letters* **2010,** *1* (13), 2025-2030.

30. Kohler, B., Nonradiative Decay Mechanisms in DNA Model Systems. *The Journal of Physical Chemistry Letters* **2010,** *1* (13), 2047-2053.

31. Kleinermanns, K.; Nachtigallová, D.; de Vries, M. S., Excited state dynamics of DNA bases. *International Reviews in Physical Chemistry* **2013,** *32* (2), 308-342.

32. Barbatti, M.; Borin, A. C.; Ullrich, S., Photoinduced Phenomena in Nucleic Acids I: Nucleobases in the Gas Phase and in Solvents. Springer: Cham, 2015.

33. Boldissar, S.; de Vries, M. S., How nature covers its bases. *Physical Chemistry Chemical Physics* **2018,** *20* (15), 9701-9716.

34. Saija, F.; Cassone, G., *Prebiotic Photochemistry: From UreyMiller-like Experiments to Recent Findings*. Royal Society of Chemistry: 2021.

35. Kistler, K. A.; Matsika, S., Radiationless Decay Mechanism of Cytosine: An Ab Initio Study with Comparisons to the Fluorescent Analogue 5-Methyl-2-pyrimidinone. *The Journal of Physical Chemistry A* **2007,** *111* (14), 2650-2661.

36. Kistler, K. A.; Matsika, S., Cytosine in Context: A Theoretical Study of Substituent Effects on the Excitation Energies of 2-Pyrimidinone Derivatives. *The Journal of Physical Chemistry A* **2007,** *111* (35), 8708-8716.

37. Epifanovsky, E.; Kowalski, K.; Fan, P.-D.; Valiev, M.; Matsika, S.; Krylov, A. I., On the Electronically Excited States of Uracil. *The Journal of Physical Chemistry A* **2008,** *112* (40), 9983-9992.

38. Marchetti, B.; Karsili, T. N. V.; Ashfold, M. N. R.; Domcke, W., A ‘bottom up’, ab initio computational approach to understanding fundamental photophysical processes in nitrogen containing heterocycles, DNA bases and base pairs. *Physical Chemistry Chemical Physics* **2016,** *18* (30), 20007-20027.

39. Crespo-Hernández, C. E.; Martínez-Fernández, L.; Rauer, C.; Reichardt, C.; Mai, S.; Pollum, M.; Marquetand, P.; González, L.; Corral, I., Electronic and Structural Elements That Regulate the Excited-State Dynamics in Purine Nucleobase Derivatives. *Journal of the American Chemical Society* **2015,** *137* (13), 4368-4381.

40. Lobsiger, S.; Blaser, S.; Sinha, R. K.; Frey, H.-M.; Leutwyler, S., Switching on the fluorescence of 2-aminopurine by site-selective microhydration. *Nature Chemistry* **2014,** *6* (11), 989-993.

41. Barbatti, M.; Lischka, H., Nonadiabatic Deactivation of 9H-Adenine: A Comprehensive Picture Based on Mixed Quantum−Classical Dynamics. *Journal of the American Chemical Society* **2008,** *130* (21), 6831-6839.

42. Karunakaran, V.; Kleinermanns, K.; Improta, R.; Kovalenko, S. A., Photoinduced Dynamics of Guanosine Monophosphate in Water from Broad-Band Transient Absorption Spectroscopy and Quantum-Chemical Calculations. *Journal of the American Chemical Society* **2009,** *131* (16), 5839-5850.

43. Serrano-Andrés, L.; Merchán, M.; Borin, A. C., A Three-State Model for the Photophysics of Guanine. *Journal of the American Chemical Society* **2008,** *130* (8), 2473-2484.

44. Improta, R.; Santoro, F.; Blancafort, L., Quantum Mechanical Studies on the Photophysics and the Photochemistry of Nucleic Acids and Nucleobases. *Chemical Reviews* **2016,** *116* (6), 3540-3593.

45. Rosspeintner, A.; Lang, B.; Vauthey, E., Ultrafast Photochemistry in Liquids. *Annual Review of Physical Chemistry* **2013,** *64* (1), 247-271.

46. Beckstead, A. A.; Zhang, Y.; de Vries, M. S.; Kohler, B., Life in the light: nucleic acid photoproperties as a legacy of chemical evolution. *Physical Chemistry Chemical Physics* **2016,** *18* (35), 24228-24238.

47. Frisch, M.; Trucks, G.; Schlegel, H.; Scuseria, G.; Robb, M.; Cheeseman, J.; Scalmani, G.; Barone, V.; Mennucci, B.; Petersson, G.; Nakatsuji, H.; Caricato, M.; Li, X.; Hratchian, H. P.; Izmaylov, A. F.; Bloino, J.; Zheng, G.; Sonnenberg, J. L.; Hada, M.; Ehara, M.; Toyota, K.; Fukuda, R.; Hasegawa, J.; Ishida, M.; Nakajima, T.; Honda, Y.; Kitao, O.; Nakai, H.; Vreven, T.; Montgomery Jr., J. A.; Peralta, J. E.; Ogliaro, F.; Bearpark, M. J.; Heyd, J. J.; Brothers, E. N.; Kudin, K. N.; Staroverov, V. N.; Kobayashi, R.; Normand, J.; Raghavachari, K.; Rendell, A. P.; Burant, J. C.; Iyengar, S. S.; Tomasi, J.; Cossi, M.; Rega, N.; Millam, J. M.; Klene, M.; Knox, J. E.; Cross, J. B.; Bakken, V.; Adamo, C.; Jaramillo, J.; Gomperts, R.; Stratmann, R. E.; Yazyev, O.; Austin, A. J.; Cammi, R.; Pomelli, C.; Ochterski, J. W.; Martin, R. L.; Morokuma, K.; Zakrzewski, V. G.; Voth, G. A.; Salvador, P.; Dannenberg, J. J.; Dapprich, S.; Daniels, A. D.; Farkas, O.; Foresman, J. B.; Ortiz, J. V.; Cioslowski, J.; Fox, D. J., Gaussian 09, rev. D. 01. *Gaussian Inc., Wallingford CT* **2009,** *19*, 227-238.

48. Liu, Y.; He, Y.; Yang, Y.; Liu, Y., Theoretical study on the detailed excited state triple proton transfer mechanism of cyclic 6-Azaindole trimer. *Chemical Physics Letters* **2021,** *762*, 138137.

49. Kim, S. K.; Bernstein, E. R., 7-Azaindole and Its Clusters with Ar, CH, H, O, NH, and Alcohols: Molecular Geometry, Cluster Geometry, and Nature of the First Excited Singlet Electronic State. *The Journal of Physical Chemistry* **1990,** *94* (9), 3531-3539.

50. Jimenez, R.; Fleming, G. R.; Kumar, P. V.; Maroncelli, M., Femtosecond solvation dynamics of water. *Nature* **1994,** *369* (6480), 471-473.

51. Abbyad, P.; Childs, W.; Shi, X.; Boxer, S. G., Dynamic Stokes shift in green fluorescent protein variants. *Proceedings of the National Academy of Sciences* **2007,** *104* (51), 20189.

52. Rosenthal, S. J.; Xie, X.; Du, M.; Fleming, G. R., Femtosecond solvation dynamics in acetonitrile: Observation of the inertial contribution to the solvent response. *The Journal of Chemical Physics* **1991,** *95* (6), 4715-4718.

53. Horng, M. L.; Gardecki, J. A.; Papazyan, A.; Maroncelli, M., Subpicosecond Measurements of Polar Solvation Dynamics: Coumarin 153 Revisited. *The Journal of Physical Chemistry* **1995,** *99* (48), 17311-17337.

54. Karmakar, R.; Samanta, A., Solvation Dynamics of Coumarin-153 in a Room-Temperature Ionic Liquid. *The Journal of Physical Chemistry A* **2002,** *106* (18), 4447-4452.

55. Eom, I.; Joo, T., Polar solvation dynamics of coumarin 153 by ultrafast time-resolved fluorescence. *The Journal of Chemical Physics* **2009,** *131* (24), 244507.

56. Broekaert, J. A. C., Daniel C. Harris: Quantitative chemical analysis, 9th ed. *Analytical and Bioanalytical Chemistry* **2015,** *407* (30), 8943-8944.

57. Hill, S. J., Handbook of HPLC E. Katz, R. Eksteen, P. Schoenmakers and N. Miller (eds) Marcel Dekker, New York, 1998 xi + 1008 pages. US $225. ISBN 0-8247-9444-3. *Applied Organometallic Chemistry* **2000,** *14* (2), 130-131.

58. Lakowicz, J. R., *Principles of fluorescence spectroscopy*. Springer science & business media: 2013.

59. Sajadi, M.; Weinberger, M.; Wagenknecht, H.-A.; Ernsting, N. P., Polar solvation dynamics in water and methanol: search for molecularity. *Physical Chemistry Chemical Physics* **2011,** *13* (39), 17768-17774.

60. Chapman, C. F.; Maroncelli, M., Excited-state tautomerization of 7-azaindole in water. *The Journal of Physical Chemistry* **1992,** *96* (21), 8430-8441.

61. Fang, H.; Kim, Y., Excited-State Tautomerization in the 7-Azaindole-(H2O)n (n = 1 and 2) Complexes in the Gas Phase and in Solution: A Theoretical Study. *Journal of Chemical Theory and Computation* **2011,** *7* (3), 642-657.

62. Yi, J.; Fang, H., Theoretical investigation on the water-assisted excited-state proton transfer of 7-azaindole derivatives: substituent effect. *Journal of Molecular Modeling* **2017,** *23* (11), 312.

5. Excited State Dynamics of Pyrrole Clusters

5.1. Introduction

The importance of understanding the relaxation mechanisms that molecular aggregates undergo after electronic excitation in the environment provided by molecular clusters has been recognized since the pioneering works by A. H. Zewail, in the field of fs pump-probe methods.[1] Indeed, molecular cluster studies have been triggered fundamentally by the fact that these species can be seen as a controllable size model system able to fill the gap between the isolated gas-phase and the intrinsically complex condensed or solid-phases.[2-4] Hence, aiming to unravel the role of solvation on the photophysical and photochemical properties of relevant chromophoric molecules, numerous time-resolved studies have explored the photodynamics of solute(solvent)$_n$ neutral aggregates formed between biologically relevant aromatic chromophores (naphtol, pyrrole, indole, etc.) and protic solvents such as water or ammonia.[5]

The dynamics of electronically excited clusters containing multiple aromatic chromophore units, with the form (solute)$_n$, can be considered another well differentiated hot topic. These multi-chromophoric systems held by intermolecular forces offer an excellent opportunity to study the excitation and relaxation mechanisms at the supramolecular level. In this sense, electron and proton transfer processes, especially those involving electronic delocalization, which depending on the degree of coupling between the chromophores and the rate of the intramolecular deactivation can result in phenomena like coherent excitation delocalization and coherent/incoherent electron and electronic energy transfer. Consequently, several groups have conducted time-resolved studies on multi-chromophoric neutral aggregates, most of them involving DNA base pairs and their analogues.[5-11]

In order to gain meaningful dynamical information on the processes these species undergo after electronic photoexcitation, experimental methods capable of relating the recorded observables to specific size clusters are required. Owing to their simplicity and high sensitivity, the techniques based in the detection of mass-selected ions appear as the most extended methods. However, the methods that involve the ionization of a specific size cluster distribution formed in a cold molecular beam present in all cases, an important limitation that complicates the identification of the species responsible of the measured dynamics: fragmentation processes. Following photoexcitation, if the vibrational energy transferred to the excited state is enough to evaporate a molecule from the cluster, the dynamical signature of the IVR process driving the energy from the initially excited vibrational modes to those involved in the dissociation will be expressed in the parent cluster mass channel as a decay, and in the fragments channels as the complementary formation of lower mass species. Additionally, the fragmentation pattern can be even more complex, considering that the cluster fragmentation can also take place in the ion state after the interaction with the probe beam. In this case, part of the signal corresponding to a given cluster will be transferred to lower mass channels. Therefore, the information recorded in the mass channel of interest will include an indeterminate amount of larger clusters, making the interpretation of the temporal evolution of a particular specie into a hard task.

Aiming to overcome these difficulties, TR-ID spectroscopy has emerged as a valid spectroscopic method to track the dynamics of size-selected and conformer specific molecules,[11-12] from the overall dynamics recorded in a mass channel, by combining an IR ns laser tuned into a specific vibrational mode with the fs pump-probe signal corresponding to that particular cluster. In this chapter, we demonstrate the potential of this spectroscopic method by investigating the photodynamics of different multi-chromophoric aggregates containing pyrrole (Py) and N-methylpyrrole (NMPy) molecules. In fact, since the theoretical works conducted by Domcke and co-workers,[13-14] the role of the πσ* states in the electronic relaxation of photoexcited heteroaromatic molecules has attracted a great deal of attention due to their potential involvement in the relaxation channels of biomolecules and their chromophores.[15-18]

Pyrrole is a heterocyclic aromatic molecule with grand chemical and biological relevance because it acts as a building block in numerous large biomolecules such as amino acids or porphyrin derivatives (*e.g.* chlorophylls, chlorins or heme).[19] Furthermore, since its lowest S_1 excited state exhibits mixed Rydberg/valence 3s(N)/πσ* character at the Franck-Condon region, pyrrole has been extensively studied as a benchmark model for understanding the role of πσ* excited states on the photodynamics of heteroaromatic molecules.[20-29] Particularly relevant to the work presented in this chapter are the studies on the dimer conducted by Neville *et al.*[30] and Montero *et al.*,[11] observing the dynamical signature of $(Py)_2$ complex, which is considerably longer than the lifetimes recorded for the monomer and bigger size clusters, $(Py)_{n>2}$.

Additionally, we have explored how the photophysics of an isolated pyrrole molecule is altered by the addition of a water molecule in order to further our grasp of the environmental effects. In the light of the available literature, theoretical studies for the Py(H_2O) cluster predict electron transfer through the H-bond,[31-35] which inhibits the N-H photodissociation mediated by the πσ* state observed for the isolated Py.[36]

5.2. Experimental Methods

The generation of the laser pulses used within these experiments are described in detail in Chapter 2, alongside a detailed explanation of the TR-ID setup in section 2.3.4. Therefore, in this section information on the experimental variables specific to the work performed within this chapter is provided. Pyrrole (98%) and N-methylpyrrole (99%) were acquired from Sigma-Aldrich and used directly without further purification. The pyrrole-containing clusters were formed after expanding, through a pulsed valve (General Valve Series 9), an initial mixture of 4.5 atm of He and the vapor pressure of pyrrole, N-methylpyrrole and water at room temperature. Then, the stagnation pressure of He was carefully dropped below 2 atm by using a pressure-reducing regulator to avoid the formation of undesired clusters. The cluster size distribution was roughly controlled by adjusting the valve pulse duration and laser-valve delay.

The excitation fs pulses were tuned in the 240-253 nm range by the second harmonic of the sum frequency generation of the idler and signal of OPA2 (Coherent OPerA Solo), with the 800 nm fundamental beam. The fundamental output from the amplifier was used as the probe beam for all the experiments. A commercial OPO/OPA laser system (Laser Vision) with 10 cm^{-1} linewidth, pumped by a Nd:YAG (Continuum Surelite) was employed to produce the IR ns radiation in the 3200-3800 cm^{-1} interval.

The IR ns and the pump-probe fs beams were spatially overlapped on the ionization region, while the former was fired 100 ns in advance. The synchronization of these experiments was driven by the clock of the regenerative amplifier whose 1 kHz trigger output was divided in a delay generator (Stanford SR535) to reach a final 10 Hz sampling rate, which is the maximum repetition rate admitted by the IR ns source. The fs pump-probe beams, forming a small angle, were focused over the interaction region by spherical mirrors to reach intensities in the order of 10^{12} Wcm^{-2} for the probe, and around 10^9 W cm^{-2} for the pump, below the threshold to produce any measurable ion in the absence of the probe. The relative polarization of the fs pump-probe pulses was held at magic angle (54.7º). The well characterized 1+3’ ionization signal of the pyrrole monomer was employed to establish the zero delay time and to derive the CC function,[29] typically ~80 fs for the 240 nm pump. The IR-dip spectra were recorded at a particular ion mass channel by scanning the ns IR OPO while integrating the IR_{on} and IR_{off} ion signals resulting from the fs pump-probe pulses overlapped in time ($\Delta t = 0$). On the other hand, the TR-ID transients were collected by acquiring the IR_{on}-IR_{off} signal as a function of the fs pump-probe time delay, which was varied by translating a continuous displacement delay line (APE Scandelay 150), with the ns IR source fixed on a chosen vibration.

5.3. Computational Methods

Ab initio calculations were performed using Gaussian 09 computational package.[37] The geometry of pyrrole-containing clusters was optimized at the (TD-)CAM-B3LYP/6-311++G(d,p) level with Grimme's Dispersion, including Becke-Johnson damping (EmpiricalDispersion=GD3BJ) on the S_0, S_1 and D_0^+ surfaces. Furthermore, the vibrational frequencies, the vertical excitation energies, the oscillator strengths and the binding energies were also predicted. The binding energies were corrected calculating the BSSE by counterpoise procedure.[38]

5.4. Results

5.4.1. Computational Calculations

Figure 5.1 shows the optimized ground state structures of the studied pyrrole-containing clusters at the CAM-B3LYP/6-311G++(d,p) level. In the light of several theoretical[39-41] and experimental[30, 42-44] works, on the isolated-phase $(Py)_2$ adopts a T-shaped structure with C_s symmetry, in which the two pyrrole molecules are held by an N-H···π bond and form an angle of ~55.4°,[42] which is in agreement with the DFT calculations, as shown in Figure 5.1a. The Py unit with free N-H bond is labelled A, while the other molecule whose N-H bond interacts with the π cloud of A is labelled B.

Analogously, the Py(NMPy) cluster adopts a similar geometry, in which the N-H···π bond is formed because the Py unit acts as donor and interacts with the π cloud of NMPy molecule (see Figure 5.1b).[45] In contrast, due to the lack of H-bonds, the $(NMPy)_2$ aggregate exhibits a sandwich type configuration, where π-π stacking between the electronic clouds of the aromatic rings occurs, as shown in Figure 5.1c.

Table 5.1 summarizes the calculated three lowest vertical excitations for $(Py)_2$ dimer, Py(NMPy) cluster and $(NMPy)_2$ dimer at the DFT optimized S_0 geometries, together with the minimum energy at the optimized S_1 geometries and the binding energies at S_0 and S_1 surfaces. According to the *ab initio* calculations, the S_1 and S_2 electronic excited states of $(Py)_2$ have 3s character at the Franck-Condon region. The S_1 ($\pi_B 3s_A$) state has charge transfer (CT) character, with the dominant configuration corresponding to excitation from a π-orbital localized on monomer B to the 3s orbital localized on the N-atom of monomer A. In contrast, the S_2 ($\pi_A 3s_A$) state is dominated by a configuration corresponding to excitation from a π-orbital localized on monomer A to the 3s orbital localized on the same pyrrole unit. Similarly, the S_1 and S_2 ($\pi 3s_{NMPy}$) excited states of Py(NMPy) cluster have also 3s character at the Franck-Condon region, however the dominant configuration of these states is related to excitation from a delocalized π-orbital to the 3s orbital localized on the N-atom of NMPy unit. Finally, in the electronic structure of $(NMPy)_2$ homodimer, the S_1 and S_2 states present $\pi\sigma^*$ character. Since the two NMPy units are almost equivalent, the excited states reflect this symmetry and are therefore delocalized.

Regarding the binding energies, for the $(Py)_2$ complex in the ground state an energy of 26.21 kJ mol^{-1} (~0.272 eV) was predicted, which is higher to those reported in the works of Gómez-Zavaglia and Fausto[40] and Matsumoto *et al.*[43] where the binding energy was reported to be 12.47 and 9.18 kJ mol^{-1}, respectively. This energy difference can be attributed to the different computational levels used. Indeed, our calculations were performed at the CAM-B3LYP/6-311++G(d,p) level with GD3BJ dispersion, whereas Gómez-Zavaglia *et al.*[40] and Matsumoto *et al.*[43] employed the B3LYP functional with the 6-311++G(d,p) and the 6-311+G(d,p) basis sets, in that order. Since DFT calculations employing the B3LYP functional do not properly consider weak dispersion energies, it can be expected that calculations at the B3LYP level underestimate the value of the binding energies. For Py(NMPy) and $(NMPy)_2$ aggregates, the binding energies were predicted to be slightly higher in comparison to that of $(Py)_2$ dimer, concretely of 34.23 (~0.355) and 29.44 kJ mol^{-1} (~0.305 eV), respectively. Moreover, the binding energies for the S_1 surface were also obtained for the different clusters. In this case, the binding energy of the $(NMPy)_2$ complex (64.04 kJ mol^{-1} ≈ 0.66 eV) is stronger than those of $(Py)_2$ (48.38 kJ mol^{-1} ≈ 0.5 eV) and Py(NMPy) (35.48 kJ mol^{-1} ≈ 0.37 eV) clusters. Finally, our calculations predicted that the minimum energies at the optimized S_1 geometry lies about 0.58 eV (~4678 cm^{-1}) below the vertical excitation for $(Py)_2$ and Py(NMPy) clusters, while for $(NMPy)_2$ dimer lies 0.51 eV (~4113 cm^{-1}) below the vertical excitation.

Table 5.1. *Vertical excitations VEEs (in eV), oscillator strength f, minimum energy of optimized S_1 excited state (in eV) and binding energies (in kJ mol^{-1}) for $(Py)_2$, Py(NMPy) and $(NMPy)_2$ clusters.*

	State	Character	*VEE* [eV]	*f*	S_1-Min [eV]	Binding Energy [kJ mol^{-1}]
$(Py)_2$	S_1	$\pi_B \rightarrow 3s_A$	5.25	0.0022	4.66	-26.21 (S_0) -48.38 (S_1)
	S_2	$\pi_A \rightarrow 3s_A$	5.63	0.0057		
	S_3	$\pi_B \rightarrow \sigma^*$	5.77	0.0388		
Py(NMPy)	S_1	$\pi \rightarrow 3s_{NMPy}$	5.44	0.0001	4.86	-34.23 (S_0) -35.48(S_1)
	S_2	$\pi \rightarrow 3s_{NMPy}$	5.71	0.0090		
	S_3	$\pi \rightarrow \sigma^*$	5.86	0.0538		
$(NMPy)_2$	S_1	$\pi \rightarrow \sigma^*$	5.46	0.0024	4.95	-29.44 (S_0) -64.04 (S_1)
	S_2	$\pi \rightarrow \sigma^*$	5.59	0.0073		
	S_3	$\pi \rightarrow \sigma^*$	5.86	0.0635		

On the other hand, the structures of the clusters between pyrrole and water molecules have been reported by several works.[34-35, 46] On the basis of these works, two types of geometries have been investigated mostly for Py(H_2O) cluster, as shown in Figure 5.1d. The first complex is the so-called π-type structure, where the OH group of water molecule interacts with the π cloud of the pyrrole aromatic ring, forming an O-H ⋯ π bond. The second one is the σ-type structure, in which the pyrrole molecule acts as proton donor and the water molecule as acceptor, forming an N-H⋯O bond. In this sense, it has been reported that the σ-type structure is more stable than the π-type one according to their binding energies by ~6.4 kJ mol^{-1}.[46]

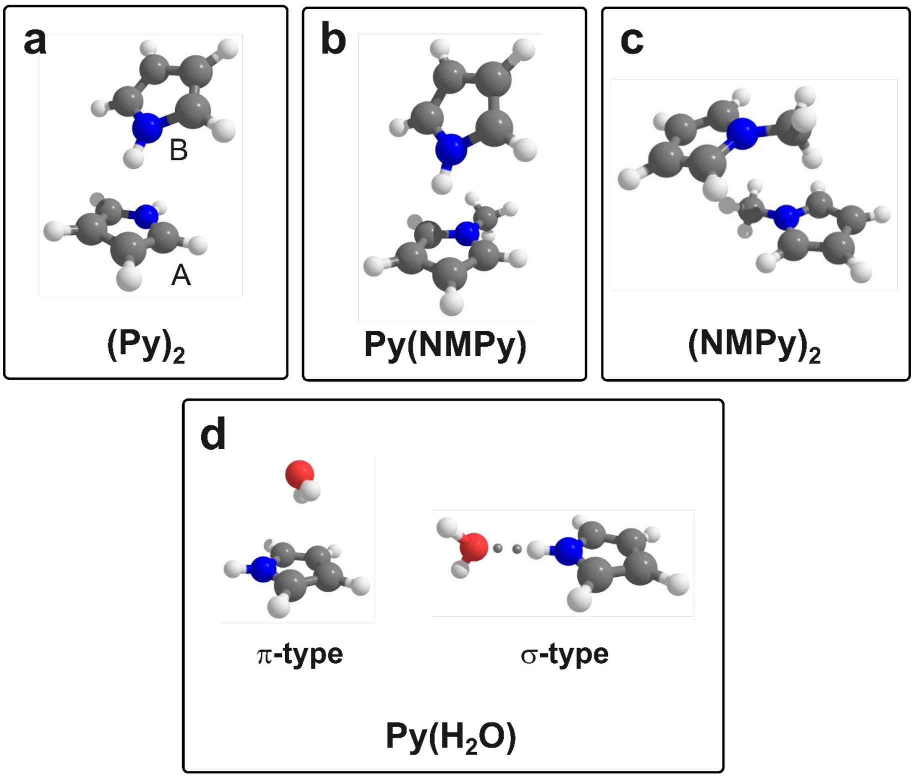

Figure 5.1. *Optimized ground state geometries for pyrrole dimer (a), Py(NMPy) (b), N-methylpyrrole dimer (c) and* $Py(H_2O)$ *clusters (d). The structures were computed at the CAM-B3LYP/6-311++G(d,p) level.*

Table 5.2 presents the vertical excitation energies of the three lowest excited states, together with the character and the oscillator strengths of the transitions, for the two main structures of $Py(H_2O)$ cluster. Additionally, the binding energy on the S_0 surface for the π- and σ-type structures are displayed. The calculations suggest that the relative energy between the more stable σ-type geometry and the π-type structure on the S_0 state is ~5.5 kJ mol^{-1}, which is slightly lower than the values reported by Nagy *et al.*[47] (6.4 kJ mol^{-1} at the MP2/6-31G(d) level), Kumar *et al.*[34] (10.1 kJ mol^{-1} at the B3LYP/6-311++G(d,p) level) and Matsumoto *et al.*[46] (6.49 kJ mol^{-1} at the MP2/6-31+G(d,p) level). This could be ascribed to the usage of the CAM-B3LYP functional instead of B3LYP or MP2 functionals. Furthermore, the binding energy on the S_1 potential for the σ-type $Py(H_2O)$ complex is predicted to be 71.02 kJ mol^{-1} (~0.736 eV). Finally, the minimum energy at the optimized S_1 geometry for the more stable σ-type structure is also shown, which lies at 4.41 eV, about 0.44 eV (~3549 cm^{-1}) below the vertical excitation.

Table 5.2. *Vertical excitations VEE (in eV), oscillator strength f, minimum energy of optimized S_1 excited state (in eV) and binding energies (in kJ mol^{-1}) for $Py(H_2O)$ cluster.*

	Type	State	Character	VEE [eV]	*f*	S_1-Min [eV]	Binding Energy [kJ mol^{-1}]
$Py(H_2O)$	***π***	S_1	$\pi_{Py} \rightarrow \sigma_w^*$	5.53	0.0002	–	-19.19 (S_0) – (S_1)
		S_2	$\pi_{Py} \rightarrow \sigma_{Py}^*$	6.21	0.0363		
		S_3	$\pi_{Py} \rightarrow \sigma_{Py}^*$	6.27	0.0262		
	σ	S_1	$\pi_{Py} \rightarrow \sigma_w^*$	4.84	0.0001	4.41	-24.68 (S_0) -71.02 (S_1)
		S_2	$\pi_{Py} \rightarrow \sigma_{Py}^*$	5.54	0.0000		
		S_3	$\pi_{Py} \rightarrow \sigma_{Py}^*$	5.69	0.0201		

The potential energy curves on the S_0 and S_1 states along the vector *R* connecting the pyrrole and water molecules were also computed, as shown in Figure 5.2. From the asymptotic values that S_0 and S_1 surfaces reach along the monomerization coordinate, the binding energies can be derived. For the S_0 state, a binding energy of ~0.295 eV (~28.46 kJ mol^{-1}) is observed, while for the S_1 state, a binding energy of ~0.78 eV (~75.26 kJ mol^{-1}) is extracted. Both values are in good agreement with those calculated by using the BSSE procedure.[38, 48] In addition, the maximum excitation is found at ~0.16 eV above the minimum energy of the S_1 potential (4.41 eV).

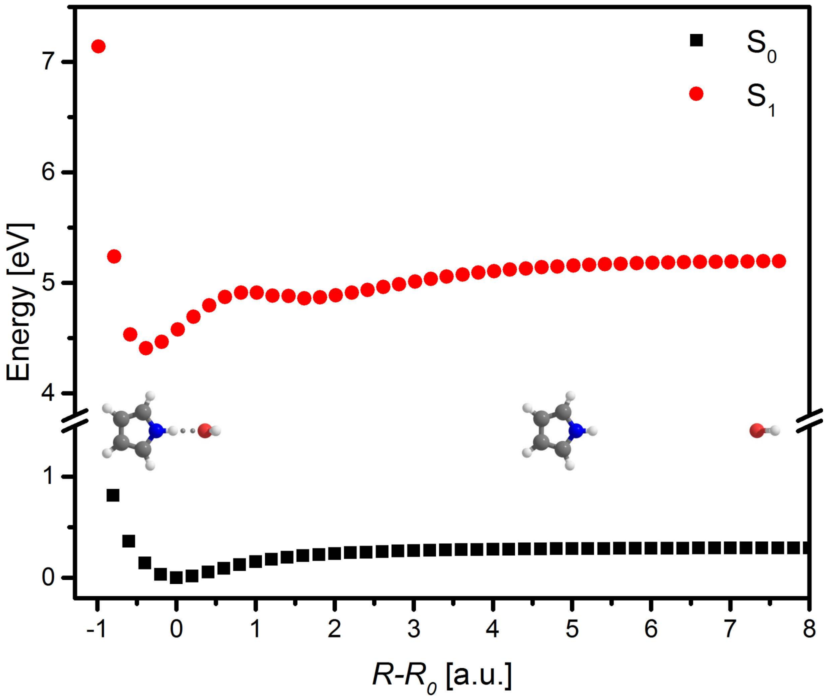

Figure 5.2. *Potential energy curves for the S_0 (black dots) and S_1 (red dots) states computed at the (TD-)DFT/CAM-B3LYP/6-311++G(d,p) level along the vector R connecting the pyrrole and water molecules.*

5.4.2. Time-Resolved Experiments

5.4.2.1. Pyrrole-N-methylpyrrole Cluster

Figure 5.3 shows a mass spectrum recorded at conditions that favor the formation of Py(NMPy) cluster, while the 240 nm pump and the 800 nm probe are overlapped in time. It is should be accounted that the higher detected mass channel corresponds to $(NMPy)_2^+$ and additionally $(Py)_2^+$ is formed. Aniline and p-toluidine traces from previous experiments are also noticeable.

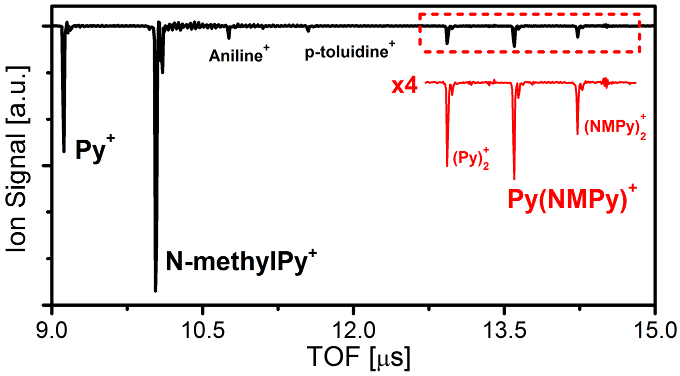

Figure 5.3. *Mass spectrum collected at expansion conditions that favored the formation of Py(NMPy) cluster, with the 240 nm pump and the 800 nm probe temporally overlapped.*

Aiming to analyze the composition of the supersonic expansion, IR-dip spectra at the $(Py)_2^+$ and $Py(NMPy)^+$ mass channels were collected by scanning the OPO laser from 3300 to 3550 cm^{-1}, as shown in Figure 5.4. The spectrum at pyrrole homodimer channel (Figure 5.4a) exhibits three prominent bands located at 3405, 3450 and 3522 cm^{-1}. By comparison with the IR-dip spectrum recorded by Montero *et al.*,[11] the N-H stretch absorptions centered at 3450 and 3522 cm^{-1} are attributed to the $(Py)_2$, whereas the band at 3405 cm^{-1} is mainly assigned to the trimer but contributions from bigger species are also probable. It is important to note that since the laser-valve conditions were set in order to favor the formation of pyrrole heteroclusters, the recorded IR-dip spectrum at $(Py)_2^+$ channel presented a worse signal-noise ratio in comparison to that collected by Montero *et al.*[11] On the other hand, the IR-dip spectrum collected at the $Py(NMPy)^+$ mass channel (Figure 5.4b) shows two bands at 3405 and 3438 cm^{-1}. The latter N-H stretch absorption can be attributed to the Py(NMPy) cluster due to the H-bond donor character of the pyrrole unit, which is well characterized in several studies.[11, 43-45] However, the feature at 3405 cm^{-1}, together with the structureless absorptions that extends up to 3350 cm^{-1}, would be the product of multiple clusters of unknown stoichiometry between the Py and NMPy units,[45] which indicates how this mass channel is affected by ionic fragmentation processes.

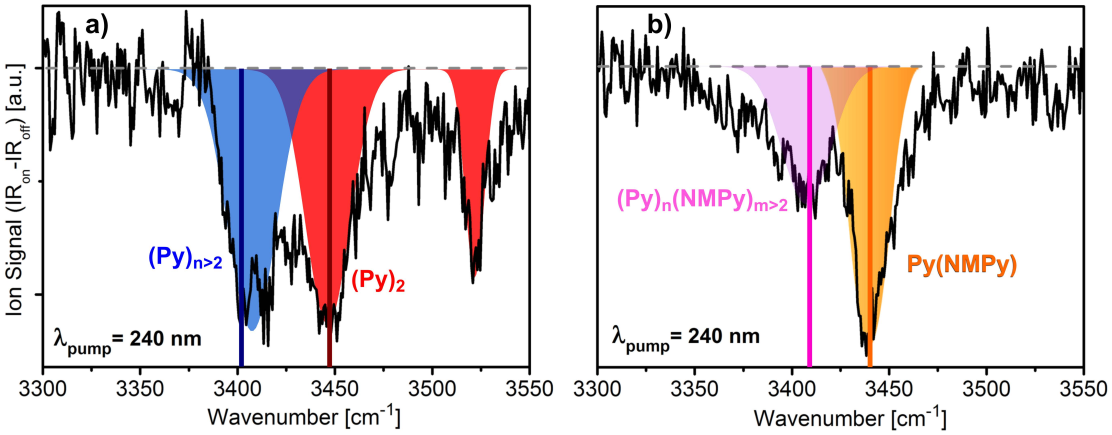

Figure 5.4. *IR-dip spectra recorded at the (Py)$_2^+$ (a) and Py(NMPy)$^+$(b) mass channels employing the 240 nm probe and the 800 nm probe. The laser-valve conditions were set to favor the formation of Py(NMPy) cluster. The red and blue colored peaks correspond to the (Py)$_2$ and Py)$_{n>2}$ species, respectively, while the orange and pink peaks indicate the Py(NMPy) and (Py)$_n$(NMPy)$_{n>2}$ clusters, in that order. The red and orange solid lines indicate the wavelength at which the dynamics of the (Py)$_2^+$ and Py(NMPy)$^+$ channels was tracked.*

In order to unravel the excited state dynamics of the Py-NMPy aggregates, TR-ID decays were collected at the (Py)$_2^+$ and Py(NMPy)$^+$ mass channels with the IR excitation fixed at 3440 cm^{-1}, as illustrated in Figure 5.5. The transient recorded at the (Py)$_2^+$ channel (Figure 5.5a) shows a nonresonant contribution at t = 0 (CC Gaussian function) and an additional decay component (τ_1) of 268 ± 14 fs, which reflects the relaxation of the (Py)$_2$ cluster and it is in agreement with the results reported by Montero *et al.*[11] Interestingly, the TR-ID decay at the Py(NMPy)$^+$ channel (Figure 5.5b) can also be modelled by a τ_1 = 220 ± 12 fs lifetime together with the CC function. Moreover, in both TR-ID transients τ_1 has negative sign, which reflects how after IR photoexcitation depopulation of the tracked specie occurs. Therefore, the τ_1 decay component extracted at the Py(NMPy)$^+$ mass channel reflects the excited state lifetime of the heterodimer.

In addition to the Py(NMPy) dimer, the photodynamics of the (NMPy)$_2$ complex was also studied. Figure 5.6 shows the transients recorded at the (NMPy)$_2^+$ mass channel, following 240 nm photoexcitation. Since this dimer does not present N-H bonds, no IR-dip excitation was employed while monitoring the ion signal. For this specie, the recorded dynamics is slower than those observed for $(Py)_2$ and Py(NMPy) clusters. Indeed, a bi-exponential decay with lifetimes τ_1 = 328 ± 36 fs and τ_2 = 3.3 ± 0.4 ps convoluted with the CC function was required to reproduce the registered transient.

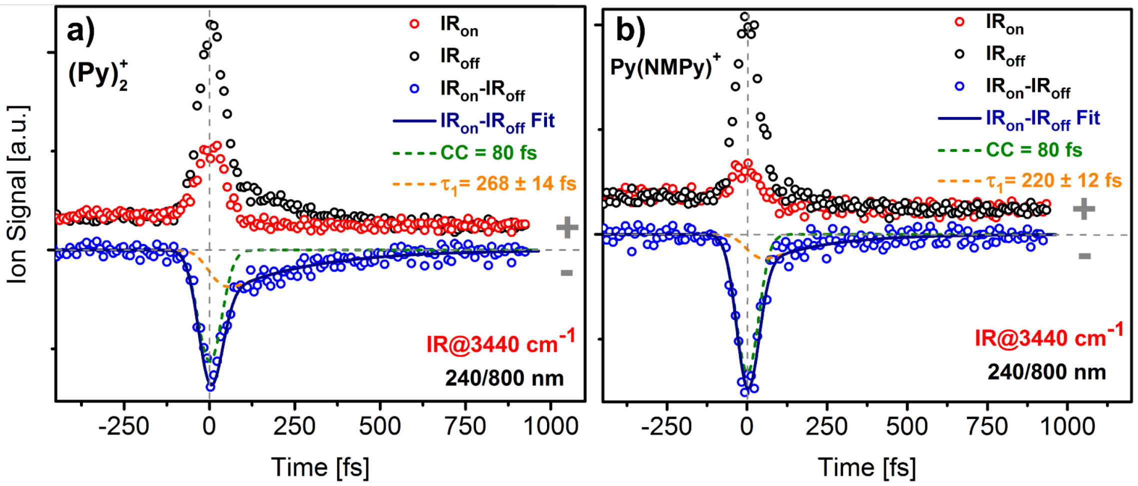

Figure 5.5. *TR-ID transients collected at the $(Py)_2^+$ (a) and $Py(NMPy)^+$ (b) mass channels, with the IR-dip laser tuned at 3440 cm^{-1}. The red and black dots represent the experimental data recorded with the IR laser on and off, respectively, by exciting with 240 nm and probing with 800 nm radiation. The blue dots and solid line correspond to the transient obtained by subtracting the IR_{on} and IR_{off} signals and its exponential fit. The green and orange dash lines represent the individual temporal components of the fit.*

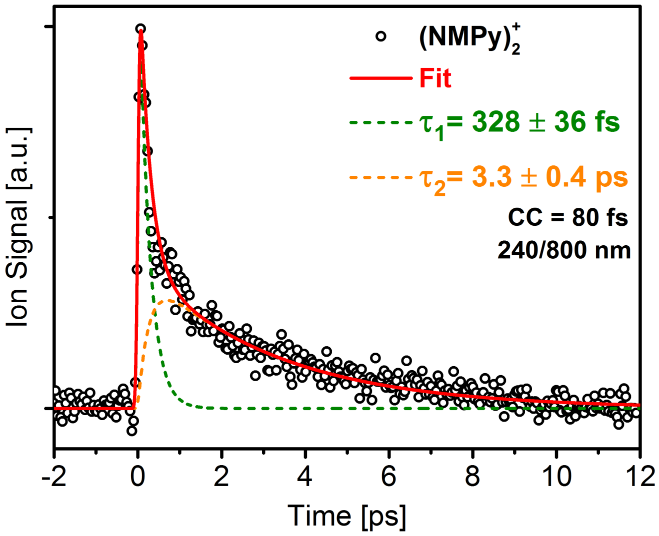

Figure 5.6. *Transient registered at the $(NMPy)_2^+$ mass channel with the excitation wavelength at 240 nm, using the 800 nm probe. The dots are the experimental data, while the red solid line is the exponential fitting function. The green and orange dash lines correspond to the individual time components of the fit.*

5.4.2.2. Pyrrole-Water Cluster

We also conducted experiments at conditions that favor the formation of Py(H_2O) cluster. Figure 5.7 shows the mass spectrum recorded at zero delay time between the 244 nm pump and the 800 nm probe. The higher detected mass corresponds to An^+ contamination from previous experiments and the Py^+ ion signal is out of scale.

The IR-dip spectrum at the Py(H_2O)$^+$ channel was collected by scanning the OPO laser from 3300 to 3800 cm^{-1}, as displayed in Figure 5.8. The spectrum shows three prominent bands centered at 3450, 3650 and 3748 cm^{-1}. By comparison with the IR spectra recorded by Matsumoto *et al.*,[46] whereas the feature at 3450 cm^{-1} can be assigned to the N-H stretch absorption, the bands at 3650 and 3748 cm^{-1} can be attributed to the symmetric and asymmetric O-H stretches, respectively.

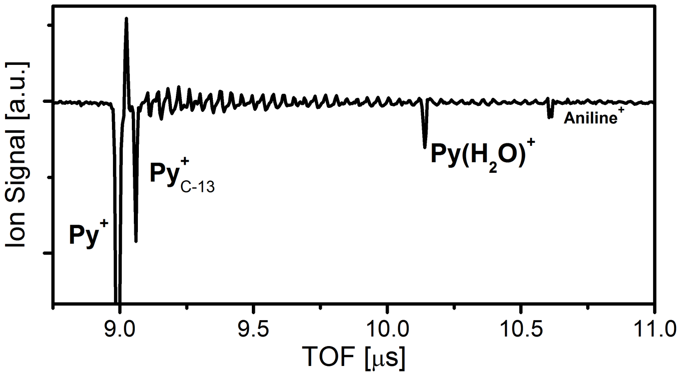

Figure 5.7. *Mass spectrum recorded at expansion conditions that favored the formation of Py(H_2O) cluster, with the 244 nm pump and the 800 nm probe temporally overlapped.*

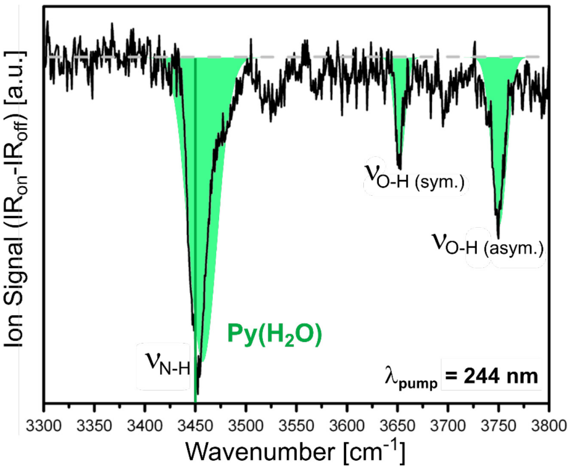

Figure 5.8. *IR-dip spectrum recorded at the Py(H_2O)$^+$ channel with the 244 nm pump and the 800 nm probe at zero delay time. The green colored peaks correspond to the prominent bands observed, whereas the green solid line indicate the wavelength at which the dynamics of the specie was tracked.*

The temporal evolution of the isolated Py(H_2O) aggregate was recorded with the IR excitation fixed at 3450 cm^{-1}. Figure 5.9 summarizes the TR-ID transients collected at 244 (a) and 253 nm (b) excitation wavelengths, while probing with 800 nm. Both transients can be modelled by a τ_1 ~165 fs decay, together with the CC function. This time component exhibits negative character that comes from the reduction of Py(H_2O) cluster signal after the fragmentation induced by the absorbed IR photon. Consequently, we ascribe the τ_1 lifetime to the relaxation of the Py(H_2O) cluster.

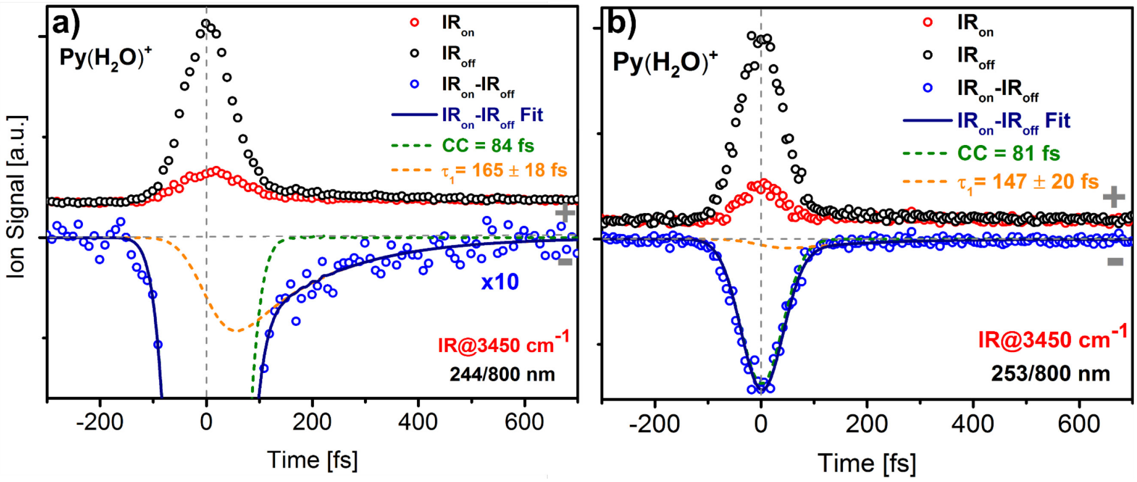

Figure 5.9. *TR-ID transients recorded at the Py(H_2O)$^+$ mass channel with the IR excitation fixed at 3450 cm^{-1}. The red and black dots represent the experimental data recorded with the IR laser on and off, respectively, at 244 (a) and 253 nm (b) excitation wavelengths, while probing with 800 nm radiation. The blue dots and solid line correspond to the transient obtained by subtracting the IR_{on} and IR_{off} signals and its exponential fit. The green and orange dash lines represent the individual temporal components of the fit.*

5.5. Discussion

5.5.1. Pyrrole-N-methylpyrrole Cluster

We start by discussing the recorded IR-dip spectrum and the extracted time constants for the Py(NMPy) cluster. The work conducted by Dauster *et al.*[44] studied the jet FTIR spectra of pyrrole self-aggregates and different heterodimers between pyrrole and H-bond acceptors such as benzene, 1,2,5-trimethylpyrrole or N-methylpyrrole. Furthermore, Matsumoto *et al.* studied the N-H stretching frequencies of pyrrole self-aggregates[43] and binary clusters between pyrrole and N-methylpyrrole[45] units by IR cavity ringdown spectroscopy. According to these studies, the Py(NMPy) heterodimer exhibits a band that is redshifted about 93 cm^{-1} respect to the N-H stretching of pyrrole monomer, concretely, is located at ~3438 cm^{-1}. This feature is perceptible in the IR-dip spectra of Figure 5.4b. Additionally, the broad absorption in the 3405-3350 cm^{-1} range can be attributed to the fragmentation of larger clusters containing the N-methylpyrrole unit. These clusters can be self-aggregates or heteroclusters of different stoichiometry between N-methylpyrrole and pyrrole molecules.[45]

Regarding the dynamical signatures observed for $(Py)_2$ and Py(NMPy) clusters, with the IR excitation fixed at 3440 cm^{-1}, we can assume that we are exclusively exciting these clusters since the N-H stretching of $(Py)_2$ is at 3450 cm^{-1}, while the N-H stretching of the heterodimer is located at 3438 cm^{-1}. The τ_1 ~268 fs decay observed at the $(Py)_2^+$ channel (Figure 5.5a) reflects the relaxation of the pyrrole homodimer. Additionally, the negative character that the CC function and the τ_1 component present means that the $(Py)_2$ signal is reduced after the absorption of IR photons, which is indicative of the depopulation of this specie and occurs due to a fragmentation process induced by the IR-dip laser. Indeed, the extracted lifetime and the sign of its individual time components is in agreement with that measured by Montero *et al.*,[11] ensuring that we were able to track selectively the dynamics of $(Py)_2$ cluster. Analogously, the TR-ID transient recorded at the $Py(NMPy)^+$ channel (Figure 5.5b) shows a similar dynamical behavior with a τ_1 ~220 fs decay. The time constants of the fit also show negative sign, meaning that the population of species exhibiting this lifetime are depleted after the absorption of IR photons, and consequently we assume that τ_1 indicates the relaxation process that Py(NMPy) cluster exclusively undergoes after photoexcitation.

According to the work conducted by Neville *et al.*,[30] the τ_1 ~268 fs lifetime extracted from the $(Py)_2^+$ channel can be attributed to the lifetime of the dimer CT complex, for which different relaxation pathways have been proposed. The *ab initio* calculations performed by Poterya *et al.*[41] suggested that H transfer between Py units is a possible mechanism. However, since the $(Py)_2$ cluster adopts a T-shaped structure, a geometry rearrangement is mandatory to allow the H transfer and this structure would be close from a $\pi\sigma^*/S_0$ CI. Therefore, IC to the ground state via $\pi\sigma^*/S_0$ and $\pi\pi^*/S_0$ CIs are more likely pathways. Furthermore, Neville *et al.* proposed various deactivation pathways like the N-H dissociation in the $S_1(\pi_B 3s_A)$ state, the slow separation to form a monomer pair or the formation of a co-planar excimer ion pair.[30]

From the recorded TR-ID transients for $(Py)_2$ and Py(NMPy) clusters (see Figure 5.5) and assuming that the electronic structure of Py(NMPy) is similar to that of $(Py)_2$, we can, in principle, infer that the N-H and C-N bond dissociation is an unlikely pathway for $(Py)_2$ and Py(NMPy), respectively. Indeed, the similarity observed on the collected decays, $\tau_1 = 268 \pm 14$ fs and $\tau_1 = 220 \pm 12$ fs for $(Py)_2$ and Py(NMPy), in that order, suggests that both aggregates relax through the same mechanism. Attending to our calculations and to previous studies available in the literature,[11, 30] the dominant relaxation pathway for these clusters may imply the neutral monomerization because of their weak binding energy in the S_1 (π3s) excited state (0.5 and 0.37 eV for $(Py)_2$ and Py(NMPy), respectively; see Table 5.1). In fact, following photoexcitation with the 240 nm pump both clusters have excess energy well above the binding energy of the S_1 (π3s) state. It should be mentioned here that Neville *et al.*[30] predicted, at the DFT/MRCI/aug-cc-pVDZ level, an energy barrier of ~0.1 eV along the monomerization coordinate for $(Py)_2$ dimer, which is small enough to enable the separation of pyrrole units to form a monomer pair. Despite the fact that our calculations suggest that this barrier is five times higher, since the system possesses excess energy enough to surmount it, the neutral monomerization of $(Py)_2$ complex can still be considered to take place.

Regarding $(NMPy)_2$ complex, the TR-IY measurement in Figure 5.6 yielded slower excited state decay time constants of $\tau_1 = 328 \pm 36$ fs and $\tau_2 = 3.3 \pm 0.4$ ps. This dynamical signature can be attributed to various relaxation pathways. The observed bi-exponential lifetime suggests a similar behavior to that reported for the NMPy monomer, in which after photoexcitation with wavelengths shorter than 243 nm, two alternative mechanisms become the major deactivation channels: IC to the ground state in tens of ps *via* $S_1(\pi\sigma^*)/S_0$ CI or, alternatively, ISC to the $T_1(^3\pi\pi^*)$ with a lifetime of few ns followed by C-N bond fission.[49-50] Furthermore, the bi-exponential decay observed for the dimer can be related to the multi-exponential decay character that the monomer exhibits because of IVR process. However, this dynamical behavior could also result from the fragmentation of bigger-size clusters due to the fact that the measurements were carried out without the size-selectivity provided by the IR excitation because the $(NMPy)_2$ aggregate does not present N-H bonds. Another possibility might be the neutral monomerization of the dimer, however the calculated binding energy for the $(NMPy)_2$ cluster in the S_1 excited state is stronger (0.66 eV; see Table 5.1) than those predicted for $(Py)_2$ and Py(NMPy) complexes. Consequently, according to our calculations, in principle the neutral dissociation of $(NMPy)_2$ dimer is an inhibited pathway.

5.5.2. Pyrrole-Water Cluster

From the IR spectra recorded by Matsumoto *et al.*[46] we can contrast that the band located at 3450 cm^{-1} corresponds to the N-H stretching absorption of Py(H_2O) cluster. Additionally, in this work the vibrational frequencies of the σ-type Py(H_2O) cluster were also calculated, predicting absorption bands at 3444, 3648 and 3783 cm^{-1}. Whereas the first band is the above-mentioned N-H stretch, the two remaining absorptions located at 3648 and 3783 cm^{-1} correspond to the symmetric and asymmetric O-H stretches of H_2O, respectively. This prediction is consistent with our assignment on Figure 5.8, even though experimentally the asymmetric O-H stretch is redshifted about 33 cm^{-1} with respect to the computational calculations.

Regarding the relaxation pattern exhibited by the Py(H_2O) cluster, with the IR source exciting the N-H stretch, the negative signs of the CC function and the τ_1 ~165 fs decay employed to model the TR-ID transients shown in Figure 5.9 indicate that after IR excitation, the population of Py(H_2O) cluster is reduced. In this sense, different research groups have conducted *ab initio* calculations in order to investigate the electron transfer process from the Py unit to water molecule.[32-34] According to the work of Sobolewski *et al.,*[32] the inclusion of a water molecule implies that the σ* electron cloud is transferred to the water molecule through the H-bond between the NH group of Py unit and the water molecule. This observation was further confirmed by the theoretical studies of Kumar *et al.*[34] and Frank and Damianos,[33] which estimate that the σ-type Py(H_2O) cluster undergoes charge transfer upon excitation and it is observable on a time-scale of ~100 fs. This lifetime might be indicative of the formation of a charge-transfer-to-solvent (CTTS) complex; however, the work of Kumar *et al.* suggests that the CTTS state is not stabilized until a cluster with at least three water molecules is formed.

Our theoretical calculations suggest that after vertical excitation, the Py(H_2O) cluster does not possesses sufficient excess energy above the binding energy of the S_1 ($\pi\sigma^*$) CT state (~0.73 eV) and therefore the neutral dissociation of the cluster could not be an active deactivation channel. Actually, since the maximum excitation energy for S_1 is found at ~0.16 eV above the minimum energy (~4.41 eV) and the vertical excitation of S_1 lies at 4.84 eV, cluster dissociation is not expected to occur. Although we cannot provide a conclusive explanation for the experimentally observed excited state dynamics in

Py(H_2O) complex, some hypothesis can be proposed:

(a) The τ_1 ~165 fs lifetime extracted from the TR-ID transients could reflect the loss of ionization cross section within the S_1 well. As shown in Figure 5.2, the CT character of the excited state gives rise to a very wide potential along the intermolecular distance. This would lead to large amplitude motion along the involved coordinate and, eventually, could produce a loss of Franck-Condon factors for the ionization, and consequently a decay of the signal.

(b) More complex mechanisms could take place after photoexcitation of pyrrole-water clusters. It has been shown that phenol aqueous solutions can lead to proton coupled electron transfer (PCET), *i.e*, a process in which the proton is released immediately after the electron transfer to the neighboring water molecules.[51] Although this hypothesis has to be properly checked on the basis of more elaborated *ab initio* calculations, the work of Frank and Damianos[33] seems to point to the thermodynamical viability of N-H bond dissociation in Py(H_2O) cluster.

5.6. Conclusions

The present work provides a new view on the excited state dynamics of pyrrole-containing clusters by means of TR-ID spectroscopy and TD-DFT calculations. The experimental measurements revealed that after photoexcitation with 240 nm radiation, the excited state dynamics of pyrrole dimer and pyrrole – N-methylpyrrole aggregate yielded a lifetime of about 268 and 220 fs, respectively, while for N-methylpyrrole dimer longer time constants of ~357 fs and ~3.6 ps were found. From the conducted *ab initio* calculations, we deduced that the dominant pathway for $(Py)_2$ and Py(NMPy) is the neutral dissociation of the clusters. Contrarily, the monomerization of the aggregate is not predicted to be the main relaxation channel for $(NMPy)_2$ dimer and therefore we attributed its longer lifetime to different plausible mechanisms such as IC to the ground state through $S_1(\pi\sigma^*)/S_0$ CI or ISC to the triplets and the subsequent dissociation of the C-N bond as invoked for N-methylpyrrole monomer.

In a similar way, our study in pyrrole-water aggregate revealed that following photoexcitation with 244 or 253 nm, the CT complex exhibits a lifetime of about 165 fs. According to the theoretical calculations, the neutral monomerization of the cluster is not a favored decay channel because of the high binding energy predicted for the S_1 state. For this reason, we tentatively proposed that the observed photodynamics can be the product of a more complex dissociative mechanism, involving electron transfer to the water molecule and N-H bond fission or, alternatively, the recorded decay could be produced due to an eventual loss of Franck-Condon factors.

5.7. References

1. Cheng, P.-Y.; Baskin, J. S.; Zewail, A. H., Dynamics of clusters: From elementary to biological structures. *Proceedings of the National Academy of Sciences* **2006,** *103* (28), 10570.

2. Hobza, P.; Zahradník, R.; Müller-Dethlefs, K., The world of non-covalent interactions: 2006. *Collection of Czechoslovak Chemical Communications* **2006,** *71* (4), 443-531.

3. Schermann, J.-P., *Spectroscopy and modeling of biomolecular building blocks*. Elsevier: 2007.

4. Hobza, P.; Müller-Dethlefs, K., *Non-covalent interactions: theory and experiment*. Royal Society of Chemistry: 2010.

5. Hertel, I. V.; Radloff, W., Ultrafast dynamics in isolated molecules and molecular clusters. *Reports on Progress in Physics* **2006,** *69* (6), 1897-2003.

6. Douhal, A.; Kim, S. K.; Zewail, A. H., Femtosecond molecular dynamics of tautomerization in model base pairs. *Nature* **1995,** *378* (6554), 260-263.

7. Farmanara, P.; Stert, V.; Radloff, W.; Hertel, I. V., Ultrafast Internal Conversion in Highly Excited Toluene Monomers and Dimers†. *The Journal of Physical Chemistry A* **2001,** *105* (23), 5613-5617.

8. Gador, N.; Samoylova, E.; Smith, V. R.; Stolow, A.; Rayner, D. M.; Radloff, W.; Hertel, I. V.; Schultz, T., Electronic Structure of Adenine and Thymine Base Pairs Studied by Femtosecond Electron−Ion Coincidence Spectroscopy. *The Journal of Physical Chemistry A* **2007,** *111* (46), 11743-11749.

9. Samoylova, E.; Radloff, W.; Ritze, H.-H.; Schultz, T., Observation of Proton Transfer in 2-Aminopyridine Dimer by Electron and Mass Spectroscopy. *The Journal of Physical Chemistry A* **2009,** *113* (29), 8195-8201.

10. Ai, Y.-J.; Zhang, F.; Cui, G.-L.; Luo, Y.; Fang, W.-H., Ultrafast deactivation processes in the 2-aminopyridine dimer and the adenine-thymine base pair: Similarities and differences. *The Journal of Chemical Physics* **2010,** *133* (6), 064302.

11. Montero, R.; León, I.; Fernández, J. A.; Longarte, A., Femtosecond Excited State Dynamics of Size Selected Neutral Molecular Clusters. *The Journal of Physical Chemistry Letters* **2016,** *7* (14), 2797-2802.

12. Nosenko, Y.; Kunitski, M.; Thummel, R. P.; Kyrychenko, A.; Herbich, J.; Waluk, J.; Riehn, C.; Brutschy, B., Detection and Structural Characterization of Clusters with Ultrashort-Lived Electronically Excited States: IR Absorption Detected by Femtosecond Multiphoton Ionization. *Journal of the American Chemical Society* **2006,** *128* (31), 10000-10001.

13. Sobolewski, A. L.; Domcke, W., Conical intersections induced by repulsive $1\pi\sigma^*$ states in planar

organic molecules: malonaldehyde, pyrrole and chlorobenzene as photochemical model systems. *Chemical Physics* **2000,** *259* (2), 181-191.

14. Sobolewski, A. L.; Domcke, W.; Dedonder-Lardeux, C.; Jouvet, C., Excited-state hydrogen detachment and hydrogen transfer driven by repulsive 1πσ* states: A new paradigm for nonradiative decay in aromatic biomolecules. *Physical Chemistry Chemical Physics* **2002,** *4* (7), 1093-1100.

15. Ashfold, M. N. R.; Cronin, B.; Devine, A. L.; Dixon, R. N.; Nix, M. G. D., The Role of πσ* Excited States in the Photodissociation of Heteroaromatic Molecules. *Science* **2006,** *312* (5780), 1637-1640.

16. Ashfold, M. N. R.; King, G. A.; Murdock, D.; Nix, M. G. D.; Oliver, T. A. A.; Sage, A. G., πσ* excited states in molecular photochemistry. *Physical Chemistry Chemical Physics* **2010,** *12* (6), 1218-1238.

17. Roberts, G. M.; Hadden, D. J.; Bergendahl, L. T.; Wenge, A. M.; Harris, S. J.; Karsili, T. N. V.; Ashfold, M. N. R.; Paterson, M. J.; Stavros, V. G., Exploring quantum phenomena and vibrational control in σ* mediated photochemistry. *Chemical Science* **2013,** *4* (3), 993-1001.

18. Roberts, G. M.; Stavros, V. G., The role of πσ* states in the photochemistry of heteroaromatic biomolecules and their subunits: insights from gas-phase femtosecond spectroscopy. *Chemical Science* **2014,** *5* (5), 1698-1722.

19. Battersby, A. R., Tetrapyrroles: the pigments of life. *Natural product reports* **2000,** *17* (6), 507-526.

20. Wei, J.; Riedel, J.; Kuczmann, A.; Renth, F.; Temps, F., Photodissociation dynamics of pyrrole: Evidence for mode specific dynamics from conical intersections. *Faraday Discussions* **2004,** *127* (0), 267-282.

21. Cronin, B.; Nix, M. G. D.; Qadiri, R. H.; Ashfold, M. N. R., High resolution photofragment translational spectroscopy studies of the near ultraviolet photolysis of pyrrole. *Physical Chemistry Chemical Physics* **2004,** *6* (21), 5031-5041.

22. Lippert, H.; Ritze, H.-H.; Hertel, I. V.; Radloff, W., Femtosecond Time-Resolved Hydrogen-Atom Elimination from Photoexcited Pyrrole Molecules. *ChemPhysChem* **2004,** *5* (9), 1423-1427.

23. Roberts, G. M.; Williams, C. A.; Yu, H.; Chatterley, A. S.; Young, J. D.; Ullrich, S.; Stavros, V. G., Probing ultrafast dynamics in photoexcited pyrrole: timescales for 1πσ* mediated H-atom elimination. *Faraday Discussions* **2013,** *163* (0), 95-116.

24. Sapunar, M.; Ponzi, A.; Chaiwongwattana, S.; Mališ, M.; Prlj, A.; Decleva, P.; Došlić, N., Timescales of N–H bond dissociation in pyrrole: a nonadiabatic dynamics study. *Physical Chemistry Chemical Physics* **2015,** *17* (29), 19012-19020.

25. Montero, R.; Ovejas, V.; Fernández-Fernández, M.; Conde, Á. P.; Longarte, A., Revisiting the relaxation dynamics of isolated pyrrole. *The Journal of Chemical Physics* **2014,** *141* (1), 014303.

26. Wu, G.; Neville, S. P.; Schalk, O.; Sekikawa, T.; Ashfold, M. N. R.; Worth, G. A.; Stolow, A., Excited state non-adiabatic dynamics of pyrrole: A time-resolved photoelectron spectroscopy and quantum

dynamics study. *The Journal of Chemical Physics* **2015,** *142* (7), 074302.

27. Kirkby, O. M.; Parkes, M. A.; Neville, S. P.; Worth, G. A.; Fielding, H. H., Non-radiative relaxation dynamics of pyrrole following excitation in the range 249.5–200nm. *Chemical Physics Letters* **2017,** *683*, 179-185.

28. Crane, S. W.; Zawadzki, M. M.; Thompson, J. O. F.; Kotsina, N.; Ghafur, O.; Townsend, D., Caveats in the interpretation of time-resolved photoionization measurements: A photoelectron imaging study of pyrrole. *The Journal of Chemical Physics* **2016,** *145* (23), 234304.

29. Lamas, I.; Longarte, A.; Peralta Conde, A.; Muga, G.; Townsend, D.; Montero, R., Dynamics of Pyrroles Excited to the 3s/πσ* State. *The Journal of Physical Chemistry A* **2019,** *123* (42), 8982-8993.

30. Neville, S. P.; Kirkby, O. M.; Kaltsoyannis, N.; Worth, G. A.; Fielding, H. H., Identification of a new electron-transfer relaxation pathway in photoexcited pyrrole dimers. *Nature Communications* **2016,** *7* (1), 11357.

31. Martoprawiro, M. A.; Bacskay, G. B., Quantum chemical studies of the pyrrole-water and pyridine-water complexes. *Molecular Physics* **1995,** *85* (3), 573-585.

32. Sobolewski, A. L.; Domcke, W., Photoejection of electrons from pyrrole into an aqueous environment: ab initio results on pyrrole-water clusters. *Chemical Physics Letters* **2000,** *321* (5), 479-484.

33. Frank, I.; Damianos, K., Excited state dynamics in pyrrole–water clusters: First-principles simulation. *Chemical Physics* **2008,** *343* (2), 347-352.

34. Kumar, A.; Kołaski, M.; Kim, K. S., Ground state structures and excited state dynamics of pyrrole-water complexes: Ab initio excited state molecular dynamics simulations. *The Journal of Chemical Physics* **2008,** *128* (3), 034304.

35. Gao, W.; Jiao, J.; Feng, H.; Xuan, X.; Chen, L., Natures of benzene-water and pyrrole-water interactions in the forms of σ and π types: theoretical studies from clusters to liquid mixture. *Journal of Molecular Modeling* **2013,** *19* (3), 1273-1283.

36. Johny, M.; Schouder, C. A.; Al-Refaie, A.; He, L.; Wiese, J.; Stapelfeldt, H.; Trippel, S.; Küpper, J., Molecular sunscreen: water protects pyrrole from radiation damage. *arXiv preprint arXiv:2010.00453* **2020**.

37. Frisch, M.; Trucks, G.; Schlegel, H.; Scuseria, G.; Robb, M.; Cheeseman, J.; Scalmani, G.; Barone, V.; Mennucci, B.; Petersson, G.; Nakatsuji, H.; Caricato, M.; Li, X.; Hratchian, H. P.; Izmaylov, A. F.; Bloino, J.; Zheng, G.; Sonnenberg, J. L.; Hada, M.; Ehara, M.; Toyota, K.; Fukuda, R.; Hasegawa, J.; Ishida, M.; Nakajima, T.; Honda, Y.; Kitao, O.; Nakai, H.; Vreven, T.; Montgomery Jr., J. A.; Peralta, J. E.; Ogliaro, F.; Bearpark, M. J.; Heyd, J. J.; Brothers, E. N.; Kudin, K. N.; Staroverov, V. N.; Kobayashi, R.; Normand, J.; Raghavachari, K.; Rendell, A. P.; Burant, J. C.; Iyengar, S. S.; Tomasi, J.; Cossi, M.; Rega, N.; Millam, J. M.; Klene, M.; Knox, J. E.; Cross, J. B.; Bakken, V.; Adamo, C.; Jaramillo, J.; Gomperts, R.; Stratmann, R. E.; Yazyev, O.; Austin, A. J.; Cammi, R.; Pomelli, C.; Ochterski, J. W.; Martin, R. L.; Morokuma, K.; Zakrzewski, V. G.; Voth, G. A.; Salvador, P.; Dannenberg, J. J.; Dapprich, S.; Daniels, A. D.; Farkas, O.; Foresman, J. B.; Ortiz, J. V.; Cioslowski, J.; Fox, D. J., Gaussian 09, rev. D. 01. *Gaussian*

Inc., Wallingford CT **2009,** *19*, 227-238.

38. Boys, S. F.; Bernardi, F., The calculation of small molecular interactions by the differences of separate total energies. Some procedures with reduced errors. *Molecular Physics* **1970,** *19* (4), 553-566.

39. Park, H.; Lee, S., Ab initio investigations of the pyrrole dimer: a direct observation of the π-facial hydrogen bond. *Chemical Physics Letters* **1999,** *301* (5), 487-492.

40. Gómez-Zavaglia, A.; Fausto, R., Self-Aggregation in Pyrrole: Matrix Isolation, Solid State Infrared Spectroscopy, and DFT Study. *The Journal of Physical Chemistry A* **2004,** *108* (34), 6953-6967.

41. Poterya, V.; Profant, V.; Fárník, M.; Slavíček, P.; Buck, U., Experimental and theoretical study of the pyrrole cluster photochemistry: Closing the πσ* dissociation pathway by complexation. *The Journal of Chemical Physics* **2007,** *127* (6), 064307.

42. Columberg, G.; Bauder, A., Pure rotational spectrum, quadrupole coupling constants and structure of the dimer of pyrrole. *The Journal of Chemical Physics* **1997,** *106* (2), 504-510.

43. Matsumoto, Y.; Honma, K., NH stretching vibrations of pyrrole clusters studied by infrared cavity ringdown spectroscopy. *The Journal of Chemical Physics* **2007,** *127* (18), 184310.

44. Dauster, I.; Rice, C. A.; Zielke, P.; Suhm, M. A., N–H···π interactions in pyrroles: systematic trends from the vibrational spectroscopy of clusters. *Physical Chemistry Chemical Physics* **2008,** *10* (19), 2827-2835.

45. Matsumoto, Y.; Murakami, S.; Honma, K., Fish-Bite structure by three-dimensional hydrogen-bond acceptor: IR spectroscopy of pyrrole and N-methylpyrrole binary clusters. *The Journal of Chemical Physics* **2012,** *137* (7), 074307.

46. Matsumoto, Y.; Honma, K., Hydrogen-bonded structures of pyrrole-solvent clusters: Infrared cavity ringdown spectroscopy and quantum chemical calculations. *The Journal of Chemical Physics* **2009,** *130* (5), 054311.

47. Nagy, P. I.; Durant, G.; Smith, D. A., Theoretical studies on hydration of pyrrole, imidazole, and protonated imidazole in the gas phase and aqueous solution. *Journal of the American Chemical Society* **1993,** *115* (7), 2912-2922.

48. Sherrill, C. D., Counterpoise correction and basis set superposition error. *School of Chemistry and Biochemistry, Georgia Institute of Technology* **2010**.

49. Blancafort, L.; Ovejas, V.; Montero, R.; Fernández-Fernández, M.; Longarte, A., Triplet Mediated C–N Dissociation versus Internal Conversion in Electronically Excited N-Methylpyrrole. *The Journal of Physical Chemistry Letters* **2016,** *7* (7), 1231-1237.

50. Woo, K. C.; Kim, S. K., Mode-specific excited-state dynamics of N-methylpyrrole. *Physical Chemistry Chemical Physics* **2019,** *21* (26), 14387-14393.

51. Oliver, T. A. A.; Zhang, Y.; Roy, A.; Ashfold, M. N. R.; Bradforth, S. E., Exploring Autoionization and Photoinduced Proton-Coupled Electron Transfer Pathways of Phenol in Aqueous Solution. *The Journal of Physical Chemistry Letters* **2015,** *6* (20), 4159-4164.

6. Photodynamics of Aniline Homoclusters

6.1. Introduction

On the way to understand more complex systems, and following the work performed on pyrrole-containing clusters, in the present chapter, we have comprehensively investigated the photodynamics of neutral aniline homoclusters, $(An)_n$. Since it is considered a model system to study aromatic amines, several experimental and theoretical works[1-11] have explored the electronic structure of aniline. More recently, as a part of an effort to unravel the photostable behavior in biologically relevant compounds, its relaxation mechanisms involving nonadiabatic couplings between valence and Rydberg states have been targeted by time and frequency domain experiments and calculations.[12-21] From these works, a detailed view of the photochemical and photophysical processes that aniline undergoes after photoexcitation, from its UV absorption onset (at ~294 nm), up to 200 nm, has been built. In this picture, the $^1\pi\sigma^*$ excited state, which results from the mixing of the $^1\pi3s(N)$ Rydberg and the $\pi\sigma^*$ (N-H) repulsive character excitation, plays a prominent role. This excited state is vertically located in the gas-phase at ~4.6 eV (269.51 nm) between the two optically bright S_1 and S_3 $^1\pi\pi^*$ states at 4.22 eV (293.86 nm) and 5.33 eV (232.61 nm), respectively.[8-9, 12, 19] The $^1\pi\sigma^* \leftarrow S_0$ transition is extremely weak, with an almost negligible oscillator strength ($f \approx 0.006$).[15, 20] However, it has been established that single photon excitation is the main way to form the $^1\pi\sigma^*$ state,[13, 20] although some population transfer between the S_1 $\pi\pi^*$ and the quasi-bonding 3s part of $^1\pi\sigma^*$ has also been postulated to occur through a $1^1\pi\pi^*/^1\pi\sigma^*$ CI.[12, 15, 21] Consequently, at excitation wavelengths shorter than 269.5 nm the evolution of the repulsive part of the $^1\pi\sigma^*$ state at extended N-H bond distances leads to H atom elimination, or alternatively to the ground state, through a $^1\pi\sigma^*/S_0$ CI.

Herein, we have tried to transfer some of the ideas gained about the photodynamics of an isolated aniline molecule to the photophysics/photochemistry of aniline homoclusters. Indeed, the isolated aniline aggregates seem to be an ideal environment to unravel the mechanisms of electron and proton transfer reactions induced by the presence of the $^1\pi\sigma^*$ states, which can occur between these non-covalently bonded units. These processes are particularly interesting because of their influence on more complex phenomena such as photosynthesis or the photostability of proteins and genetic material.[22-25]

Aniline homoclusters have been the subject of a number of spectroscopic studies that provide a solid ground for the current time-resolved research. The minimum energy structures of complexes with up to nine units have been deduced from IR spectroscopy and *ab initio* calculations.[26-30] Only in the case of the dimer, a single minimum energy geometry has been unambiguously established.[26-29] The electronic structure of aniline dimer has also been studied by UV spectroscopy and computational methods.[27, 30-31] Regarding the photophysics, the work by Poterya *et al.*[32] explored the photodissociation on the $^1\pi\sigma^*$ state, of cluster distributions by detecting the formed H fragments.

In this chapter, we have tracked the relaxation dynamics of neutral aniline dimers, $(An)_2$, and larger clusters, $(An)_{n>3}$, by employing TR-ID spectroscopy, which has allowed us to unambiguously extract the dynamical signature of $(An)_2$ from the rest of the formed aniline homoclusters. The results permit relating the dynamics induced by the $^1\pi\sigma^*$ state to the geometry and electronic structure of the cluster. Additionally, the collected data provide relevant information regarding the ionic fragmentation of the complexes that pave the ground for the selective study of bigger species held by non-covalent interactions.

6.2. Experimental Methods

As it was mentioned in the preceding chapter, the setup for TR-ID experiments has been thoroughly explained in Chapter 2, sections 2.3.3 and 2.3.4. Therefore, in this section details on the specifics concerning the experiments presented in this chapter are provided. Aniline (99%) was acquired from Sigma-Aldrich and used without further purification. The aniline homoclusters were formed in a supersonic expansion (General Valve Series 9) resulting of mixing 1.5 atm of He and the vapor pressure of aniline heated at 50 ºC. The cluster size distribution was roughly controlled by adjusting the valve pulse duration and laser-valve delay.

For these experiments, pump wavelengths in the 290-235 nm range were employed, which were generated from the second harmonic of the sum frequency mixing of either idler or signal output of OPA2 (Coherent OPerA Solo) with a portion of the 800 nm fundamental. The fundamental 800 nm radiation from the amplifier was used as the probe beam for all the experiments, whereas the IR ns radiation in the 3200-3700 cm^{-1} interval was produced from an OPO/OPA laser system (Laser Vision), with 10 cm^{-1} bandwidth, pumped by a Nd:YAG laser (Continuum Surelite) at 10 Hz.

The ns IR and fs pump-probe pulses were nearly collinearly introduced and spatially overlapped at the interaction region of the TOF spectrometer. The polarizations of the pump and probe pulses were set at magic angle (54.7º) relative to each other by means of a half-waveplate. Typically, the fs probe beam reached intensities in the order of 10^{11} Wcm^{-2}, while the pump was kept at 10^{9} Wcm^{-2}. The zero delay time and the Gaussian CC function was determined from the well characterized 1+3' ionization signal of pyrrole,[33] which was found to lie between 90 and 98 fs for the investigated excitation range. The TR-ID transients were recorded by integrating simultaneously the IR_{on} and IR_{off} signals, with the IR excitation fixed on a chosen vibration, as the pump-probe time delay was varied by adjusting the delay of the probe pulse with a continuous displacement delay line (APE Scandelay 150). Alternatively, the IR-dip spectra were collected at a particular mass channel by scanning the ns IR source, while integrating the IR_{on} and IR_{off} ion signals at zero pump-probe delay ($\Delta t = 0$). The synchronization of the fs and ns sources with the pulsed valve was controlled using a delay generator (Stanford SR535) in order to reach the maximum repetition rate admitted by the ns IR source, which is 10 Hz.

6.3. Results

6.3.1. Narrow Cluster Distribution

Figure 6.1 shows a series of mass spectra recorded at different laser-valve delays at zero delay time between the 267 nm pump and 800 nm probe. As has been reported in previous experiments of cluster ionized by fs pulses,[34-36] it is expected that the collected mass spectra are affected by fragmentation processes upon ionization. Consequently, controlling the cluster size distribution by adjusting the laser-valve delay is mandatory because even though the higher detected mass corresponds to $(An)_3^+$, bigger species are present in the interrogated region of the expansion. All the results presented in this section were conducted under conditions that favored the formation of smaller aggregates, which was achieve by probing the early times of the expansion.

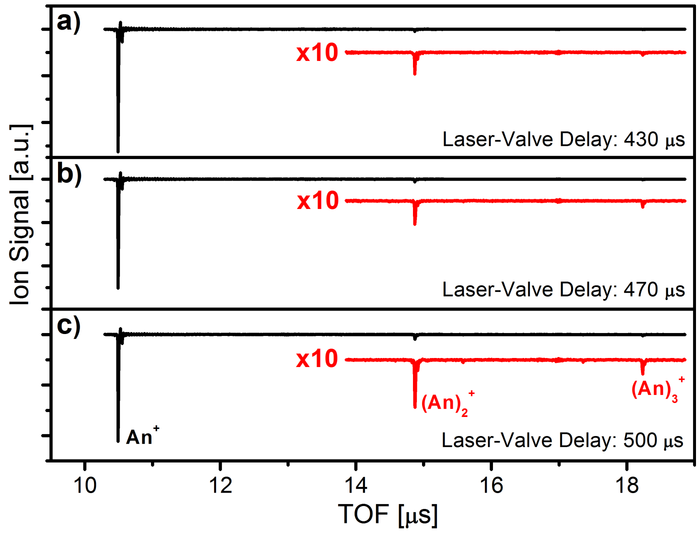

Figure 6.1. *Mass spectra recorded at different laser-valve delays with the 267 nm pump and the 800 nm probe temporally overlapped. The conditions that favored the formation of narrower cluster distributions were obtained at short delays.*

In order to elucidate the species contributing to the monomer, dimer and trimer mass channels, IR-dip spectra at different pump wavelengths were recorded. However, the $(An)_3^+$ trimer channel signal, under all the different attempted conditions, was too weak to obtain any meaningful spectrum. Figure 6.2 displays the recorded IR-dip spectra at the $(An)_2^+$ dimer mass channel, which was obtained, as explained above, by scanning the IR laser across 3200-3500 cm^{-1}, while registering the IR_{on}-IR_{off} signal. The two prominent bands centered at 3396 and 3470 cm^{-1} can be assigned to the symmetric and anti-symmetric N-H stretching, respectively, of a head-to-tail geometry of $(An)_2$.[26-29] It is noteworthy that the spectra, particularly when excitation at 264 nm was employed (Figure 6.2b), also exhibit a broad background, along with hints of other IR transitions. Attending to the IR spectra recorded by León *et al.*,[29] these features could be assigned to larger clusters. In fact, an intense multi-absorption in the 3300-3500 cm^{-1} is common to all the studied $(An)_{n=3-9}$ complexes.

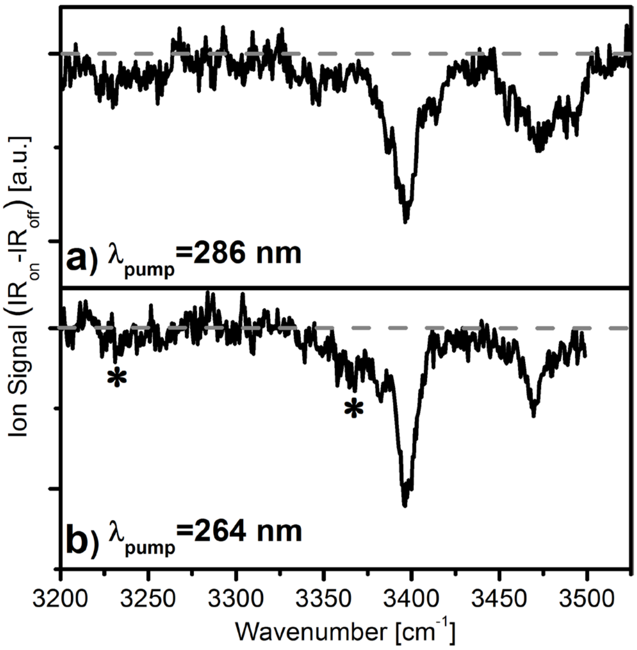

Figure 6.2. *IR-dip spectra collected at the* $(An)_2^+$ *mass channel. The fs pump (286 and 264 nm) and the 800 nm probe pulses were temporary overlapped* ($\Delta t = 0$)*. The asterisks indicate the position of features assigned to* $(An)_{n>2}$ *clusters.*

Once the composition of the beam was analyzed, the next step was to identify the excited state dynamics of the aniline clusters present in the beam. For this purpose, the IR excitation was fixed at the different transitions observed in the spectrum, while recording the temporal evolution of aniline monomer and dimer ion mass channels. The clusters were excited in the 290-235 nm range and probed with 800 nm radiation. Figure 6.3 summarizes the TR-ID transients recorded at the $(An)_2^+$ mass channel with the pump at 286 (a), 281 (b), 264 (c) and 235 nm (d) excitation wavelengths. In the transient 6.3a, recorded at 286 nm excitation, no dynamics other than a constant ionization signal is registered, whereas for transient 6.3b, at 281 nm, a picosecond rise component is noticeable. When excitation is moved to 264 nm (Figure 6.3c), the transient shows a CC Gaussian function (ω_{FWHM} = 98 fs), together with a long-lived background. However, at higher excitation energies such as 235 nm (Figure 6.3d) a single decay of 24 ± 7 fs is observed for the TR-ID transient. This change, as has been observed for the monomer, is associated with the excitation of a higher ππ* state. It is important to remark that the TR-ID measurements shown in Figure 6.3 have negative sign, which reflects the depopulation of $(An)_2$ channel after the IR photons are absorbed.

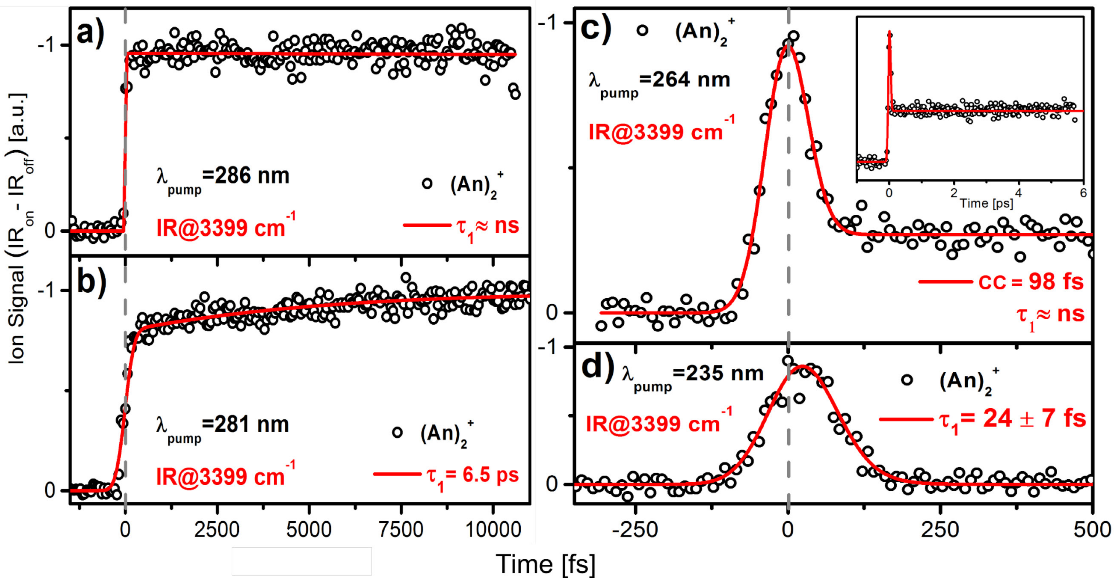

Figure 6.3. *TR-ID transients recorded at the* $(An)_2^+$ *mass channel after exciting at 286 (a), 281 (b), 264 (c) and 235 nm (d), and probing with 800 nm pulses. The IR ns laser was tuned at 3399* cm^{-1} *in all cases. The inset shows (c) at longer time delays. The dots correspond to the experimental data obtained by subtracting the* IR_{on} *and* IR_{off} *decays and the solid red lines are the exponential fits.*

6.3.2. Larger Clusters

Experiments at laser-valve delays that favor the interaction with bigger clusters than the dimer were also performed. In order to observe a complete picture of the photodynamics present at the dimer mass channel, a transient without IR-dip laser was recorded exciting with 264 nm and probing with 800 nm radiation, as shown in Figure 6.4. Under these conditions, an additional decay component (τ_1) of 140 ± 30 fs emerges, together with the CC Gaussian function and a long $\tau_2 > 10$ ps lifetime that accounts for the constant background. Consequently, the appearance of τ_1 can be related with the formation of $(An)_{n\geq 3}$ clusters, which are fragmented into dimers during the probe step.

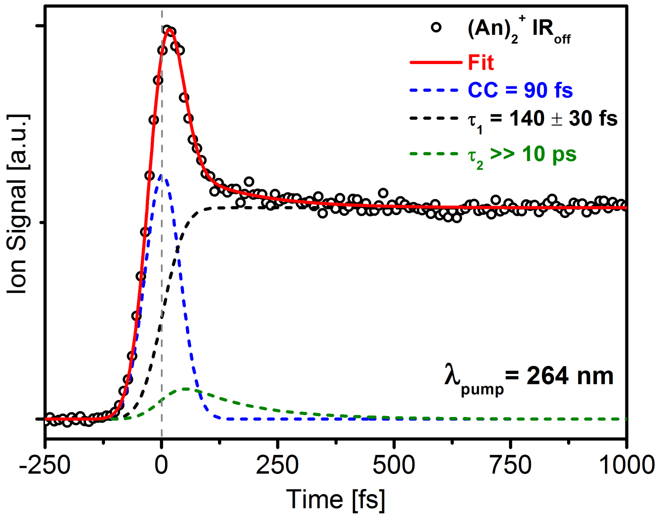

Figure 6.4. *Transient recorded at the (An)$_2^+$ mass channel, without IR-dip laser, at 264 nm excitation wavelength and using the 800 nm probe. The dots represent the experimental data and the red solid line corresponds to the exponential fit. The blue, green and black dash lines are the individual components of the fitting.*

Aiming to characterize the molecular beam when interaction with large aniline aggregates is favored, Figure 6.5 shows the IR-dip spectrum collected for the dimer mass channel at 264 nm excitation wavelength. The spectrum exhibits two prominent bands at 3396 and 3470 cm^{-1}, which closely resemble the features observed for narrow-distribution conditions and were assigned to the dimer. Nonetheless, as stated by León *et al.*,[29] these two bands are shared by trimers and bigger aniline homoclusters up to (An)$_9$. Additionally the IR-dip spectrum exhibits other unstructured absorptions in the proximity of the main sharp bands, with a particularly relevant shoulder at ~3360 cm^{-1} that is known to be a prominent band in aniline clusters up to five molecules. Therefore, it can be concluded that under these conditions clusters bigger than the dimer are being probed and fragmented into the dimer channel. However, due to the little selectivity of the IR spectrum, it is not possible to precisely identify the stoiquiometry of the contributing species. It is also important to note in Figure 6.5 that the IR-dip signal acquires positive or negative character, depending on the IR wavelength. The positive values correspond to the regions where the IR absorption causes the fragmentation of bigger clusters into dimers, producing an enhancement of the dimer ion signal, while the negative values correspond to dimer absorptions, which diminish the population of this specie.

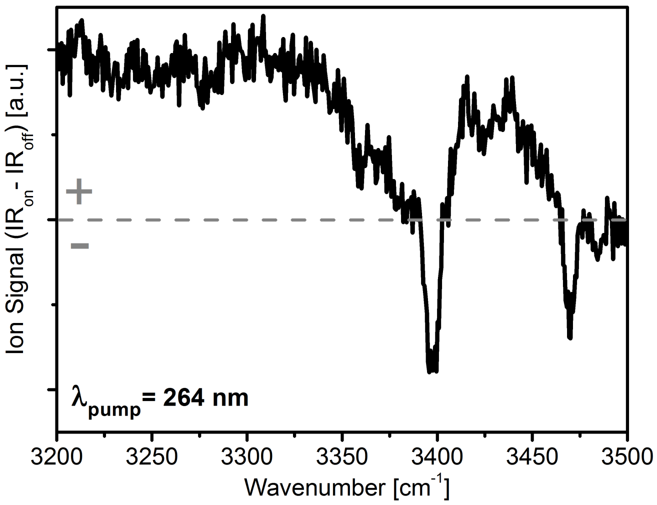

Figure 6.5. *IR-dip spectrum registered at the* $(An)_2^+$ *mass channel for large cluster distribution conditions. The 264 nm pump and the 800 nm probe were set at zero delay time (Δt = 0).*

Figure 6.6 shows the TR-ID decays collected, with the IR-dip laser tuned at 3399 (a) and 3360 cm^{-1} (b), in that order. As we observed, the former band is common to any $(An)_{n\geq2}$ cluster, while the latter is not present in $(An)_2$. Therefore, the comparison between both transients should allow us to isolate the dimer dynamics from the rest of homoclusters and establish the origin of τ_1. The TR-ID transients recorded are complex signals that comprise the effect that the IR photons have over the different temporal components of the decay, which are depicted with dashed lines. It can be noticed that when the IR laser is set at 3399 cm^{-1} the τ_1 and the CC function show a negative sign, while the τ_2 component is positive. However, when the IR excites the $(An)_{n>2}$ species (IR@3360 cm^{-1}) the τ_1 lifetime decreases, while the CC Gaussian and the τ_2 components, both with positive character, are enhanced. Indeed, a positive sign is indicative of dimers formation upon fragmentation of large aggregates, whereas a negative sign shows the depopulation of dimers after IR excitation. A comprehensive analysis of this behavior, in the context of the general photophysics of aniline clusters can be found in the following section.

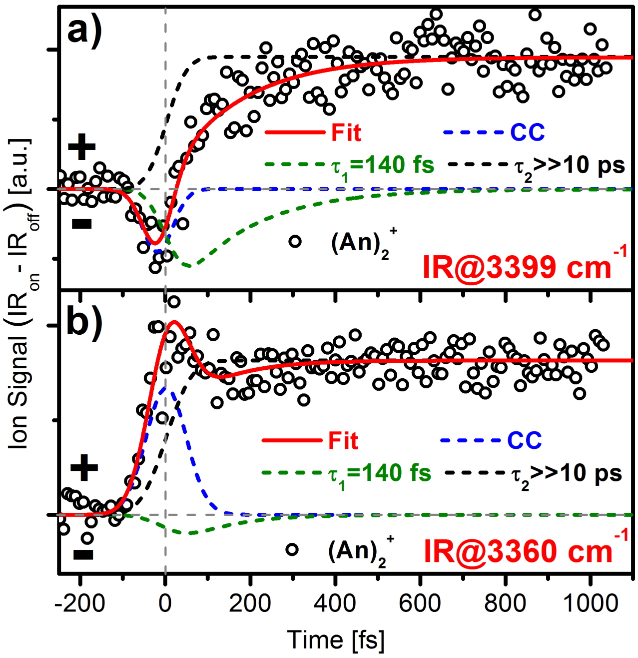

Figure 6.6. *TR-ID transients collected at the* $(An)_2^+$ *mass channel with the 264 nm pump and the 800 nm probe. The IR-dip laser was tuned at 3399 (a) and 3360* cm^{-1} *(b). The dots represent the experimental data obtained by subtracting the* IR_{on} *and* IR_{off} *signals and the red solid line corresponds to the exponential fit. The blue, green and black dash lines are the individual components of the fitting.*

6.4. Discussion

6.4.1. Aniline Dimer Photophysics

From the IR-dip spectra recorded at the $(An)_2^+$ mass channel under narrow cluster distribution conditions (see Figure 6.2) we can assume that the photodynamics of the dimer can be isolated from bigger species by fixing the IR excitation at 3399 cm^{-1}. Consequently, the TR-ID transients collected across the 286-235 nm excitation range reflect the relaxation processes this aggregate undergoes. Several experimental[26-27, 29-30] and theoretical works[28-29, 32] have stated that isolated $(An)_2$ adopts the symmetric head-to-tail arrangement, where the two anilines are equivalent and the NH_2 groups of each molecule interact with the π cloud of the other unit, as shown in Figure 6.7a. In this sandwich type configuration, due to the equivalence between the two NH_2 groups, the IR spectrum is composed of two transitions corresponding to the symmetric and anti-symmetric stretches, which is in agreement with the spectra presented in Figure 6.2.

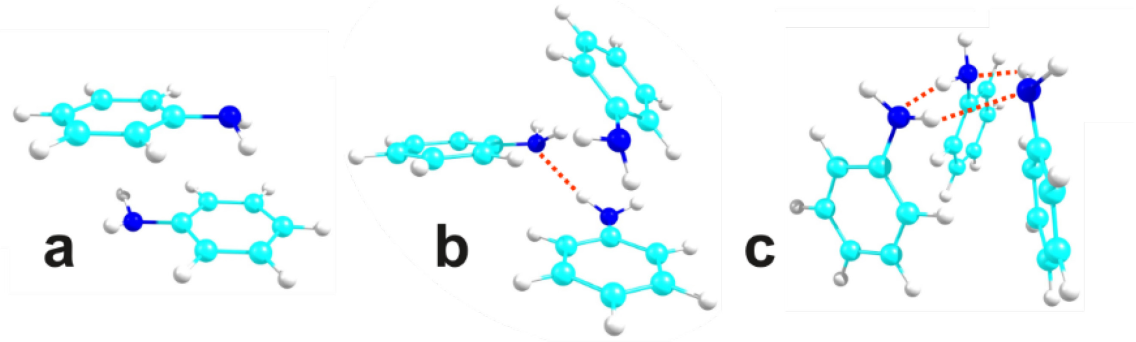

Figure 6.7. *Minimum energy geometries for aniline dimer (a) and trimers (b and c) computed at the M06-2X/6-311++G(d,p) level.*

Regarding the electronic structure of the $(An)_2$, according to calculations[31-32] and UV spectroscopy[30] the $\pi\pi^*$ character $S_1 \leftarrow S_0$ transition of the aniline monomer transforms into two $\pi\pi^*$ states that are delocalized between the two equivalent aniline units. The lower S_1 excited state of $(An)_2$ is symmetry forbidden, while the higher dipole-allowed S_2 excited state is responsible of the observed resonant two-photon ionization (R2PI) excitation spectrum, with origin at 33352 cm^{-1} (~4.13 eV).[30] The latter, characterized by a series of broad absorptions over a raising background, is the state populated in our pump-probe experiments through the 286-265 nm excitation interval. The corresponding decays show essentially a long-lived $\tau > 10$ ps background. When excitation wavelength is tuned at 264 nm (Figure 6.3c), the absorption of the S_2 state drops and a Gaussian that accounts for the non-resonant portion of the ionization is noticeable. However, in the light of calculations performed by Schemmel *et al.,*[31] the S_2 is predicted to be coupled to the lower dark S_1 through a CI that lies close to the Franck-Condon geometry and could be reached at low excitation energies. This coupling should induce the IC of the formed S_2, as postulated by Yeh *et al.*,[30] presumably at ultrafast rate. Nevertheless, no clear signs of such dynamics are observed in the dimer decays recorded across the S_2 absorption. Only at 281 nm (Figure 6.3b), the transients show some picoseconds raise in the ionization signal that could be related to this process, but no conclusive observations about it can be provided. A reason for the absence of a clear fingerprint of the S_2/S_1 coupling can be the small change in the ionization probability induced by the conversion process, which can be understood in view of the small energy gap predicted for the two involved states: 0.14 eV (vertical excitation).[31] In this situation, assuming a common ion state for both states, the little increment of the vibrational content associated to the conversion process might not be reflected in the probe dependent ionization efficiency. A similar lack of sensitivity for TR-IY experiments employing 800 nm multiphoton probes has been reported for the couplings between $\pi\pi^*$ states, presenting similar energy gaps in the cases of 1-aminonaphtalene,[37] indole[38] and tryptophan.[39]

The dimer signal is transformed into a 24 ± 7 fs ultrafast decay when the excitation is set at 235 nm (Figure 6.3d). Presumably at this wavelength another $\pi\pi$* state, which according to some calculations should be the bright S_4,[32] is reached, in close analogy to aniline monomer, in which the S_3 $\pi\pi$* state is also excited at this wavelength, giving rise to a τ ~21 fs decay that accounts for its ultrafast relaxation. For the monomer, several relaxation routes involving CIs with the S_2 ($\pi\sigma^*$), the S_1 ($\pi\pi^*$) and the ground state are accessible from S_3 ($\pi\pi^*$) according to the CASSCF calculations by Sala *et al.*[19] The same scenario can be invoked to explain the dimer decay at 235 nm.

However, the most revealing observation regarding the relaxation of the dimer in the explored excitation region is the lack, in opposition to the monomer behavior, of any dynamics assignable to the $\pi3s/\pi\sigma^*$ state. This statement relies, as it is further explained below, on the assumption that the τ~140 fs decay recorded at the dimer mass channel is originated by the fragmentation of bigger clusters. The absence of this relaxation channel can be correlated with the geometry predicted for the dimer and its associated electronic structure. In the symmetric head-to-tail arrangement, the hydrogen atoms of each NH_2 group interact with the π-cloud of the other aniline unit. For this conformation the N-H dissociation pathway is blocked and the σ^* is expected to rise in energy respect to the monomer. In fact, DFT calculations by Poterya *et al.* indicate that for the dimer the energy of the $\pi\sigma^*/S_0$ CI corresponding to the H atom dissociation is 1.4 eV higher than in the monomer.[32]

6.4.2. Photophysics of larger $(An)_{n\geq3}$ clusters

As we observed in the IR spectrum of Figure 6.2b even at laser-valve delays that maximize the formation of $(An)_2$, bigger clusters that fragment in the ion after the absorption of 800 nm probe photons are perceptible. In the light of the detailed IR spectra registered by León *et al.*,[29] the $(An)_{n\geq3}$ aggregates are characterized by a strong broad absorption centered at ~3360 cm^{-1} that accounts for the different types of N-H symmetric stretches. This feature is observable in the IR-dip spectrum performed under laser-valve conditions that favored the formation of $(An)_{n\geq3}$ clusters (see Figure 6.5). Furthermore, as the laser-valve delays are tuned to maximize the excitation of complexes with several aniline molecules, the IR spectrum of the dimer channel increasingly shows features characteristic of larger clusters until it turns into a non-resolved continuous absorption. However, even at such conditions the collected mass spectra only show a weak ion signal assignable to $(An)_3$. Therefore, we can deduce that in addition to modulating the observed ion distributions, fragmentation processes may also preclude the observation of certain intact species. This fact should be carefully considered in fs ionization experiments, when mass spectra are registered as proof of the eventual formation of aggregates.

Regarding the photophysics of $(An)_{n\geq3}$ clusters, firstly we should consider some fundamental ideas on the structure of these species. According to the work conducted by León *et al.*,[29] the aggregation geometries of aniline clusters are determined by the competition between subtle interactions: weak hydrogen bonds and dispersive forces. In this way, as many as four different structures are found to contribute to the trimer IR spectrum. The situation becomes more intricate as the number of aniline molecules increases. In fact, the IR spectra of aggregates larger than the pentamer already show a great similarity with that of liquid aniline at room temperature. As a consequence, the nature of the IR spectra and the poorly defined geometries of the complexes bigger than the dimer, together with the extensive fragmentation processes, do not allow us to extract the individual dynamics of the $(An)_{n\geq3}$ clusters. Nevertheless, from the analysis of Figure 6.6 TR-ID transients and by comparison with the well-defined dimer structure, some interesting facts can be established.

Based on the assignment of 3360 and 3399 cm^{-1} IR transitions, we can conclude that while the former exclusively excites $(An)_{n\geq3}$ clusters, the latter is also absorbed by $(An)_2$. For this reason, Figure 6.6a TR-ID measurement should be associated mainly, but not only, with $(An)_2$, whereas Figure 6.6b transient reflects the dynamics of the $(An)_{n\geq3}$ clusters. Figure 6.8 schematically shows that the subtraction of both set of data yields a transient that matches the decay obtained for $(An)_2$ at narrow cluster distribution conditions (see Figure 6.3c). Moreover, Figure 6.6b shows that for 3360 cm^{-1} excitation the total dimer signal (dots and red line) is positive at all delays, indicating that dimers (or species that fragment into dimers upon ionization) are created by fragmentation of bigger clusters that absorb the IR photons. Oppositely, the τ_1 ~140 fs component (green dash line) shows a negative character, meaning that the population of species exhibiting that lifetime is depleted after the IR is absorbed. This behavior can be understood in terms of the $(An)_{n\geq3}$ clusters that contribute to the dimer channel signal in the absence of IR, and whose population is reduced when the IR is absorbed. This result would confirm that the τ_1 ~140 fs lifetime is related exclusively to $(An)_{n\geq3}$ clusters.

On the other hand, when the IR is tuned at 3399 cm^{-1} (Figure 6.6a), all the complexes, including the dimer, are excited. Therefore, the population of species contributing to the dimer channel might be reduced, for example when the dimers are fragmented into monomers, or enhanced, as in the case of the newly formed dimers that result from the fragmentation of bigger clusters. Accordingly, the sign of CC function and the long background component (τ_2), which are shared by all complexes, is controlled by the balance between the species created/destroyed by the IR. In this situation, the number of contributors notably complicate the extraction of meaningful information. Regarding the τ ~140 fs component, its negative character can be again understood as explained above: it is present in the $(An)_{n\geq3}$ clusters but not in in the new dimers formed after the IR absorption. An interesting implication derived from this observation is that the dimers formed by IR fragmentation of bigger clusters retain the same structure as the ones originally formed in the expansion, or alternatively, they have enough time after the IR excitation to adopt the head-to-tail conformation.

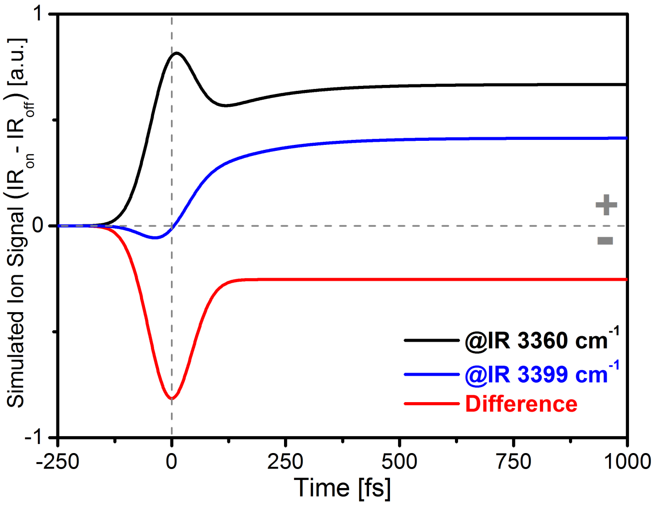

Figure 6.8. *The blue and black lines are the fits obtained from the TR-ID transients collected at the* $(An)_2^+$ *channel with the IR-dip laser tuned at 3399 and 3360 cm*$^{-1}$*, respectively. The red lines is the difference between both transients, which matches with the transient showed in Figure 6.3c.*

The present results can be contrasted with the N-H photodissociation studies by Poterya *et al.*[32] There, the formation of fast H fragments, attributed to the dissociation on the $\pi\sigma^*$ surface, is detected after exciting narrow distributions of aniline $(An)_{n\leq3}$ clusters at 243 nm. Although their measurements were carried out at excitation energies higher than those employed here, it is very likely that as it has been reported for the monomer, the $\pi\sigma^*$ state in the trimer is reached starting at lower energies.[19, 21] This being the case, we can correlate the appearance of H fragments with the current observation of the τ_1 ~140 fs lifetime, confirming the occurrence of $\pi\sigma^*$ type dynamics in the trimer structures.

The comparison of the dynamical behavior of dimers and trimers, in principle, would reinforce the simple idea of relating the availability of the H dissociation pathway to the involvement of the hydrogen atoms in H-bonds. In this picture, as the predicted minimum energy structures for the $(An)_{n\geq3}$ complexes present aniline units with N-H bonds not involved in intermolecular interactions, the $\pi\sigma^*$ repulsive surface should be energetically favored. This simplified view valid for the small clusters may not hold as the clusters scale up, or even less for the solution phase environment. In these more complex media, apart from the photodissocation channel, the $\pi\sigma^*$ states may get involved in other relaxation pathways as autoionization to form solvated electrons, or PCET process.[40-41]

Additionally, for these multi-chromophoric clusters the surrounding aniline units cannot be considered simple spectator solvent molecules, as they also can take part in the excitation. Regarding this aspect, the dimer represents a singular case, as the excitation is delocalized between both aniline subunits. On the contrary, owing to their geometries, the excitation of the $(An)_{n\geq3}$ clusters can probably be better understood as the sum of independent monomer units.

6.5. Conclusions

This study has explored the photodynamics of aniline aggregates by tracking the ultrafast relaxation of size selected neutral homoclusters. The targeted system has proved to be particularly challenging. Owing to the complex aggregation patterns of aniline, several conformational isomers of similar stability are present for the $(An)_{n\geq3}$ species, making it difficult to unravel their dynamical signature.[29] However, the applied methodology has enabled us to disentangle the particular relaxation of the dimer from that of the rest of the formed clusters. While for $(An)_{n\geq3}$ clusters dynamics along the repulsive $\pi\sigma^*$ state has been detected, the absence of this channel has been confirmed in dimers and related to their head-to-tail symmetric configuration. The study opens the door to understand the photophysical/photochemical behavior of specific aggregation states in light of the geometry adopted by the constituting monomer subunits.

6.6. References

1. Katsumi, K.; Hiroshi, T.; Saburo, N., The Vacuum Ultraviolet Absorption Spectra of Aniline and Some of Its N-Derivatives. *Bulletin of the Chemical Society of Japan* **1964,** *37* (9), 1336-1346.

2. Kimura, K.; Nagakura, S., Vacuum ultra-violet absorption spectra of various mono-substituted benzenes. *Molecular Physics* **1965,** *9* (2), 117-135.

3. Brand, J. C. D.; Williams, D. R.; Cook, T. J., Vibrational analysis of the first ultraviolet band system of aniline. *Journal of Molecular Spectroscopy* **1966,** *20* (4), 359-380.

4. Chernoff, D. A.; Rice, S. A., Single vibronic level fluoresence from aniline. *The Journal of Chemical Physics* **1979,** *70* (5), 2511-2520.

5. Mikami, N.; Hiraya, A.; Fujiwara, I.; Ito, M., The fluorescence excitation spectrum of aniline in a supersonic free jet: Double minimum potential for the inversion vibration in the excited state. *Chemical Physics Letters* **1980,** *74* (3), 531-535.

6. Gorse, A.-D.; Pesquer, M., A theoretical study of aniline and some derivatives in their ground states. *Journal of Molecular Structure: THEOCHEM* **1993,** *281* (1), 21-32.

7. Wang, Y.; Saebø, S.; Pittman Jr, C. U., The structure of aniline by ab initio studies. *Journal of Molecular Structure: THEOCHEM* **1993,** *281* (2-3), 91-98.

8. Ebata, T.; Minejima, C.; Mikami, N., A New Electronic State of Aniline Observed in the Transient IR Absorption Spectrum from S1 in a Supersonic Jet. *The Journal of Physical Chemistry A* **2002,** *106* (46), 11070-11074.

9. Honda, Y.; Hada, M.; Ehara, M.; Nakatsuji, H., Excited and ionized states of aniline: Symmetry adapted cluster configuration interaction theoretical study. *The Journal of Chemical Physics* **2002,** *117* (5), 2045-2052.

10. Drougas, E.; Philis, J. G.; Kosmas, A. M., Ab initio study of the structure of aniline in the S1 and S2 ππ* states. *Journal of Molecular Structure: THEOCHEM* **2006,** *758* (1), 17-20.

11. Rajasekhar, B. N.; Veeraiah, A.; Sunanda, K.; Jagatap, B. N., Excited states of aniline by photoabsorption spectroscopy in the 30 000–90 000 cm−1 region using synchrotron radiation. *The Journal of Chemical Physics* **2013,** *139* (6), 064303.

12. King, G. A.; Oliver, T. A. A.; Ashfold, M. N. R., Dynamical insights into π1σ∗ state mediated photodissociation of aniline. *The Journal of Chemical Physics* **2010,** *132* (21), 214307.

13. Montero, R.; Conde, Á. P.; Ovejas, V.; Martínez, R.; Castaño, F.; Longarte, A., Ultrafast dynamics of aniline in the 294-234 nm excitation range: The role of the πσ* state. *The Journal of Chemical Physics* **2011,** *135* (5), 054308.

14. Spesyvtsev, R.; Kirkby, O. M.; Vacher, M.; Fielding, H. H., Shedding new light on the role of the Rydberg state in the photochemistry of aniline. *Physical Chemistry Chemical Physics* **2012,** *14* (28), 9942-9947.

15. Roberts, G. M.; Williams, C. A.; Young, J. D.; Ullrich, S.; Paterson, M. J.; Stavros, V. G., Unraveling Ultrafast Dynamics in Photoexcited Aniline. *Journal of the American Chemical Society* **2012,** *134* (30), 12578-12589.

16. Spesyvtsev, R.; Kirkby, O. M.; Fielding, H. H., Ultrafast dynamics of aniline following 269–238 nm excitation and the role of the S2(π3s/πσ*) state. *Faraday Discussions* **2012,** *157* (0), 165-179.

17. Thompson, J. O. F.; Livingstone, R. A.; Townsend, D., Following the relaxation dynamics of photoexcited aniline in the 273-266 nm region using time-resolved photoelectron imaging. *The Journal of Chemical Physics* **2013,** *139* (3), 034316.

18. Wang, F.; Neville, S. P.; Wang, R.; Worth, G. A., Quantum Dynamics Study of Photoexcited Aniline. *The Journal of Physical Chemistry A* **2013,** *117* (32), 7298-7307.

19. Sala, M.; Kirkby, O. M.; Guérin, S.; Fielding, H. H., New insight into the potential energy landscape and relaxation pathways of photoexcited aniline from CASSCF and XMCQDPT2 electronic structure calculations. *Physical Chemistry Chemical Physics* **2014,** *16* (7), 3122-3133.

20. Thompson, J. O. F.; Saalbach, L.; Crane, S. W.; Paterson, M. J.; Townsend, D., Ultraviolet relaxation dynamics of aniline, N, N-dimethylaniline and 3,5-dimethylaniline at 250 nm. *The Journal of Chemical Physics* **2015,** *142* (11), 114309.

21. Kirkby, O. M.; Sala, M.; Balerdi, G.; de Nalda, R.; Bañares, L.; Guérin, S.; Fielding, H. H., Comparing the electronic relaxation dynamics of aniline and d7-aniline following excitation at 272–238 nm. *Physical Chemistry Chemical Physics* **2015,** *17* (25), 16270-16276.

22. Sobolewski, A. L.; Domcke, W., Computational Studies of the Photophysics of Hydrogen-Bonded Molecular Systems. *The Journal of Physical Chemistry A* **2007,** *111* (46), 11725-11735.

23. Neville, S. P.; Kirkby, O. M.; Kaltsoyannis, N.; Worth, G. A.; Fielding, H. H., Identification of a new electron-transfer relaxation pathway in photoexcited pyrrole dimers. *Nature Communications* **2016,** *7* (1), 11357.

24. Marchetti, B.; Karsili, T. N. V.; Ashfold, M. N. R.; Domcke, W., A ‘bottom up’, ab initio computational approach to understanding fundamental photophysical processes in nitrogen containing heterocycles, DNA bases and base pairs. *Physical Chemistry Chemical Physics* **2016,** *18* (30), 20007-20027.

25. Kim, N. J.; Chang, J.; Kim, H. M.; Kang, H.; Ahn, T. K.; Heo, J.; Kim, S. K., Femtosecond Decay Dynamics of Intact Adenine and Thymine Base Pairs in a Supersonic Jet. *ChemPhysChem* **2011,** *12* (10), 1935-1939.

26. Sugawara, K.-i.; Miyawaki, J.; Nakanaga, T.; Takeo, H.; Lembach, G.; Djafari, S.; Barth, H.-D.; Brutschy, B., Infrared Depletion Spectroscopy of the Aniline Dimer. *The Journal of Physical Chemistry* **1996,** *100* (43), 17145-17147.

27. Yamamoto, N.; Hino, K.; Mogi, K.; Ohashi, K.; Sakai, Y.; Sekiya, H., Hole-burning spectroscopy and ab initio calculations for the aniline dimer. *Chemical Physics Letters* **2001,** *342* (3), 417-424.

28. Schemmel, D.; Schütz, M., Molecular aniline clusters. I. The electronic ground state. *The Journal of Chemical Physics* **2010,** *132* (17), 174303.

29. León, I.; Usabiaga, I.; Arnaiz, P. F.; Lesarri, A.; Fernández, J. A., Frontispiece: Stepwise Nucleation of Aniline: Emergence of Spectroscopic Fingerprints of the Liquid Phase. *Chemistry – A European Journal* **2018,** *24* (41).

30. Yeh, J. H.; Shen, T. L.; Nocera, D. G.; Leroi, G. E.; Suzuka, I.; Ozawa, H.; Namuta, Y., Resonance Two-Photon Ionization Spectroscopy of the Aniline Dimer. *The Journal of Physical Chemistry* **1996,** *100* (11), 4385-4389.

31. Schemmel, D.; Schütz, M., Molecular aniline clusters. II. The low-lying electronic excited states. *The Journal of Chemical Physics* **2010,** *133* (13), 134307.

32. Poterya, V.; Nachtigallová, D.; Lengyel, J.; Fárník, M., Photodissociation of aniline N–H bonds in clusters of different nature. *Physical Chemistry Chemical Physics* **2015,** *17* (38), 25004-25013.

33. Lamas, I.; Longarte, A.; Peralta Conde, A.; Muga, G.; Townsend, D.; Montero, R., Dynamics of Pyrroles Excited to the 3s/πσ* State. *The Journal of Physical Chemistry A* **2019,** *123* (42), 8982-8993.

34. Hertel, I. V.; Radloff, W., Ultrafast dynamics in isolated molecules and molecular clusters. *Reports on Progress in Physics* **2006,** *69* (6), 1897-2003.

35. Montero, R.; León, I.; Fernández, J. A.; Longarte, A., Femtosecond Excited State Dynamics of Size Selected Neutral Molecular Clusters. *The Journal of Physical Chemistry Letters* **2016,** *7* (14), 2797-2802.

36. Peralta Conde, A.; Ovejas, V.; Montero, R.; Castaño, F.; Longarte, A., Influence of solvation on the indole photophysics: Ultrafast dynamics of indole–water clusters. *Chemical Physics Letters* **2012,** *530*, 25-30.

37. Montero, R.; Longarte, A.; Conde, Á. P.; Redondo, C.; Castaño, F.; González-Ramírez, I.; Giussani, A.; Serrano-Andrés, L.; Merchán, M., Photophysics of 1-Aminonaphthalene: A Theoretical and Time-Resolved Experimental Study. *The Journal of Physical Chemistry A* **2009,** *113* (48), 13509-13518.

38. Montero, R.; Conde, Á. P.; Ovejas, V.; Castaño, F.; Longarte, A., Ultrafast Photophysics of the Isolated Indole Molecule. *The Journal of Physical Chemistry A* **2012,** *116* (11), 2698-2703.

39. Ovejas, V.; Fernández-Fernández, M.; Montero, R.; Castaño, F.; Longarte, A., Ultrafast Nonradiative Relaxation Channels of Tryptophan. *The Journal of Physical Chemistry Letters* **2013,** *4* (11), 1928-1932.

40. Wohlgemuth, M.; Bonačić-Koutecký, V.; Mitrić, R., Time-dependent density functional theory excited state nonadiabatic dynamics combined with quantum mechanical/molecular mechanical approach: Photodynamics of indole in water. *The Journal of Chemical Physics* **2011,** *135* (5), 054105.

41. Szabla, R.; Šponer, J.; Góra, R. W., Electron-Driven Proton Transfer Along H2O Wires Enables Photorelaxation of πσ* States in Chromophore–Water Clusters. *The Journal of Physical Chemistry Letters* **2015,** *6* (8), 1467-1471.

7. Photodynamics of Synthetic Sunscreens

7.1. Introduction

UV radiation is considered a carcinogen since it is capable of causing DNA damage and other harmful effects in living organisms.[1-3] UV radiation is further sub-divided into three regions attending to its wavelength range: UV-A (400-315 nm), UV-B (315-280 nm) and UV-C (280-100 nm). Although most of the UV-C radiation is absorbed and scattered by the ozone layer, the amount of UV-A and UV-B radiation that reaches the Earth's surface is significant.[4-5] Therefore, the evolution of life on Earth has required the development of efficient photoprotection mechanisms, which in general rely on molecules able to strongly absorb and dissipate the excess of UV-A/UV-B radiation as heat, avoiding the occurrence of undesired photochemical processes.[6]

Moreover, it is widely accepted that a short excited state lifetime implies an enhanced photostability because nonradiative relaxation pathways, *e.g.* ultrafast IC, prevents molecules from photochemical reactions leading to the eventual formation of harmful photoproducts. Nonetheless, the photostability is ultimately linked to the molecular structure since subtle structural changes modify the topology of potential energy surfaces, thus altering the accessibility to the CIs that control the different deactivation pathways.[7] Consequently, the design of novel photoprotective compounds requires accurate models at the molecular level able to predict their spectroscopic and photodynamic properties.

Pursuing this goal, numerous studies have focused on understanding the spectroscopy[8-12] and the relaxation routes[13-21] of different natural sunscreens, whose photoprotection mechanisms could be replicated by synthetic UV absorbers.[18, 22-24] Among those species, mycosporine-like amino acids (MAAs), have emerged as very promising candidates. Previous studies on different MAAs and analogues have confirmed that these molecules show an excellent photostability under UV irradiation conditions.[21, 23, 25-26] Indeed, computational studies have also predicted a competitive photoprotection pathway after UV photoexcitation by the description of an ultrafast IC channel that efficiently leads to a hot ground state, which subsequently relaxes to the surroundings to recover the intact initial system.[13, 26] Lately, Woolley *et al.* have reported time-resolved experiments on two molecular models with core units similar to those of MAAs.[21] In one of the studied compounds, they determined the IC of the prepared excited state to the ground state in ~500 fs, followed by vibrational cooling in few picoseconds. However, the studied specie also exhibited a long-lived feature that was attributed to any remaining population trapped in a triplet state or to the formation of photoproducts in low-yield.[21]

Recently, Losantos *et al.* have introduced a new family of potential UV filters candidates inspired on natural MAAs that exhibited excellent properties as potential protectors against the deleterious effects of sunlight.[23] It should be noted here that the photoprotection mechanism of these compounds, the natural MAAs and related molecules like gadusol is completely different from those of commercial sunscreens, which usually implies a double bond isomerization (cinnamates),[10-11, 27-28] or an excited state proton transfer (avobenzone and oxybenzone).[29-33] Actually, the computational calculations carried out for the studied MAA motifs by Losantos *et al.* concluded that, following excitation, repopulation of the ground state occurs though a $S_1(\pi\pi^*)/S_0$ CI involving out-of-plane deformations.

The research presented in this chapter explores the photodynamics and the influence of key structural aspects on the relaxation mechanism of four promising compounds (see Figure 7.1) selected to fulfill the properties to be used as efficient sunscreens. The samples exhibit, from 1 to 4, absorption maxima at increasing wavelengths along the UV region, as shown in Figure 7.3, which makes of its combined application an efficient blocker of the solar radiation in the full UV-A/UV-B region. The collected computational and experimental results permit to propose a novel IC pathway that could be extended to other natural and new synthetic compounds.

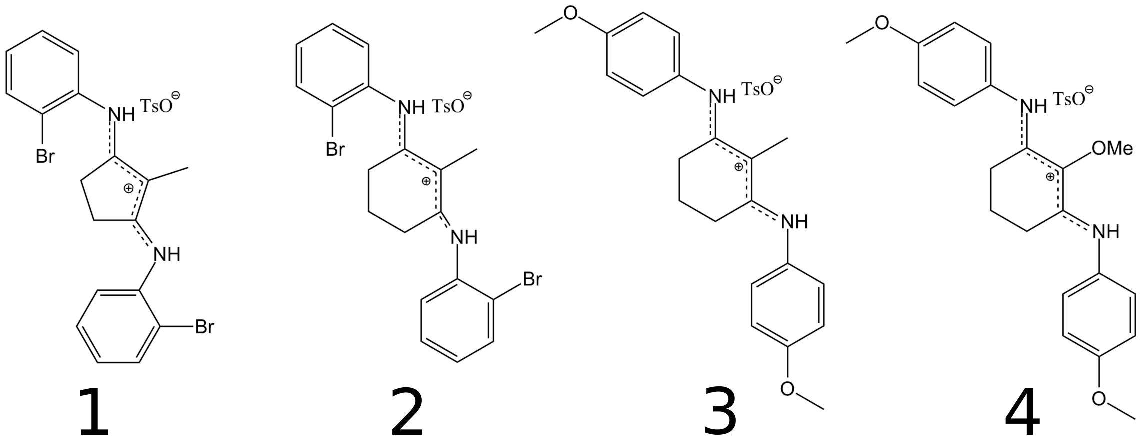

Figure 7.1. *Molecular structures of the mycosporine-like aminoacid (MAA) motifs studied in this chapter.*

7.2. Methods

7.2.1. Experimental Methodology

The studied MAAs samples 1-4 were synthesized by Prof. Sampedro's group (Universidad de La Rioja) according to the routes previously described.[23] The problem samples were dissolved in methanol (99.9%, Fischer Chemical) at concentrations from 7 to $8 \cdot 10^{-4}$ M for time-resolved experiments.

Steady-state UV/Vis absorption spectra of methanol solutions of the 1-4 compounds, at concentration adjusted to reach absorbance ≈ 0.5, were collected using a commercial UV/Vis spectrometer (Cintra 303 GBC Scientific Equipment Ltd.). Irradiation of the samples was performed through a Pyrex filtered 400 W medium-pressure Hg lamp, achieving an irradiation power of at least 5700 W m^{-2}, which is much higher than one sun (~1000 W m^{-2}).

The TA measurements were carried out exciting the methanol solutions of the samples of interest near the corresponding absorption maxima ─ λ_{pu} = 306 (1), 330 (2), 341 (3) and 353 nm (4) ─ by the pump laser pulses generated in OPA2 (Coherent OperA Solo). The WLC probe (λ_{pr} = 340 – 750 nm) was obtained through supercontinuum generation by focusing an ~1 μJ 800 nm fundamental beam on a 2 mm CaF_2 plate. The relative polarization of the pump and probe pulses was held at magic angle (54.7º) configuration. The sample solutions were introduced in a rotatory cell with a 0.3 mm path length to reach an absorbance around 0.7. The probe continuum transmitted through the sample was focused onto an optical fibre coupled to a spectrometer (Avantes AvaSpec-ULS2048XL) in order to collect the changes in the optical density (ΔOD). Additionally, the excitation narrowband signal was recorded to know the status of the excitation and to correct from intensity fluctuations. The pump-probe delay was varied by adjusting the probe beam pathway with a linear translation stage (Thorlabs ODL220-FS), which permitted a maximum delay of ~2 ns. The CC function and the zero-delay time at the different spectral wavelengths was derived from the CAS recorded from a pure methanol measurement.[34] Typically, values between 120 and 190 fs are obtained for the CC in the 350-650 nm probe range.

The FuC experiments were conducted on the same solutions employed for TA using a commercial kit (CDP FOG 100), which has been modified to allow the introduction of an external pump beam from the OPA2. The pump pulses were focused onto a rotatory cuvette of 0.3 mm optical path. The emission from the sample was mixed in a 0.2 mm thick BBO crystal with the 800 nm gate beam to generate the up-converted signal. The remaining excitation light was filtered using cut-off filters. The up-converted signal was detected by a photomultiplier coupled to a monochromator (CDP 220D), whose signal was integrated by a boxcar (CDP 2021A). The relative polarization between pump and gate pulses was set at magic angle (54.7º) configuration by a Berek's waveplate. Temporal resolutions of 100 fs were determined at the studied excitation and emission wavelengths by measuring the Raman response from pure methanol.

7.2.2. Computational Methods

In order to explore the main relaxation pathways and the photostability of the synthesized samples, Prof. Sampedro's group (Universidad de La Rioja) performed theoretical calculations.

The geometries of the critical points were computed using fully unconstrained *ab initio* quantum chemical computations in the framework of a CASPT2//CASSCF strategy.[35] This requires the reaction coordinate to be computed at the complete active space self-consistent field (CASSCF) level of theory and the corresponding energy profile to be re-evaluated at the complete active space perturbation theory to the second order (CASPT2) level of theory.

The CIs have been located at the CASSCF or CASPT2 level using the method implemented in Molcas 8.2.[36] This method also provides the components of the branching space.[37] The Gaussian 16[38] package was used for TD-DFT and MP2 computations. The energy of the CASSCF geometries was recalculated using the CASPT2 method implemented in Molcas 8.2 to take into account the effect of electron dynamic correlation. All CASPT2 results were obtained with state average with equal weights for each state. Both CASSCF and CASPT2 calculations were performed using the standard 6-31G* basis set. Two different active spaces were checked against the experimental data (14,13) and (6,5). In all cases, the chromophore considered included the π density (orbitals π and π* of bonds C=C, C=N and n N_{imine}).

Minimum energy paths (MEPs) where computed at the CASSCF level using the methodology present in Molcas 8.2. MEPs representing the steepest descendent minimum energy reaction path were built through a series of geometry optimizations, each requiring the minimization of the potential energy on a hyperspherical cross section of the potential energy surface centred on a given reference geometry and characterized by a predefined radius. The paths were computed using a value of 0.1 Da for the steps. Once the first lower energy optimized structure is converged, this is taken as the new hypersphere centre, and the procedure is iterated until the bottom of the energy surface is reached.

Bulk solvent effects on the UV-spectra were included using the polarizable continuum model (PCM)[39] implemented in Molcas 8.2. The molecule was considered as included in a cavity surrounded by an infinite medium with the dielectric constant corresponding to the specific solvent. The standard value of $\varepsilon = 32.63$ for methanol was used in these calculations.[39] The UV spectra were computed under non-equilibrium conditions, that is, only solvent electronic polarization is in equilibrium with excited-state electron density. Thus, only fast solvent degrees of freedom were considered. This kind of calculations is more adequate to compute vertical excitation energies, as those needed for the UV spectra. For the computed structures 3-4, the effect of the solvent in the photophysical properties seemed to be negligible. The same has been previously described for palythine[13] and the previously reported analogues.[23] Thus, the solvent was not included in the critical points calculations.

Thermal conversion was studied using MP2/6-31G* together with the polarizable continuum model (PCM) as implemented in Gaussian 16. The standard dielectric constant of 32.63 for methanol was used in these calculations. Additional details on the computational procedures are found in section 7.6.

7.3. Results

7.3.1. Computational Study

In an effort to understand the mechanism of photoprotection at the molecular level, the photochemical behavior of compound 3, chosen as a prototype model of the family,[23] was firstly explored by means of theoretical calculations. The absorption spectrum in methanol was computed using two different active spaces, namely (14,13) and (6,5), to ensure a good modelling of the system. In both cases, a $S_0 \rightarrow S_1$ strong absorption band (326 nm with $f = 1.1$ for (14,13) and 327 nm with $f = 0.83$ for (6,5)) with a clear $\pi\pi^*$ character was found. Thus, the UV spectrum seems not to be very influenced by the size of the active space. This was further checked by computing the relaxation path using both active spaces. In both cases, a high-energy CI point connecting the excited state S_1 with the ground state S_0 very similar to the one found in palythine,[40] gadusol[14] and the core structures for the designed sunscreens[23] was found (see additional Figure 7.11). The main geometrical feature of this S_1/S_0 CI is the out-of-plane distortion of the substituents on the cyclohexenimine ring that remain planar in the ground state minimum. However, a deeper exploration of the shape of the potential energy surface through a MEP calculation revealed that this CI point it is not directly accessible from the Franck-Condon region. Instead, a new deactivation channel was found consisting on an isomerization of one of the C=N bonds leading to a different S_1/S_0 CI point (see Figure 7.2). Moreover, the MEP corresponding to the sharp descent from the Franck-Condon region for 3 leads to a minimum on S_1, in which only one of the imine moieties is twisted out of the plane defined by the cyclohexenimine core. Decay to the ground state may take place from the associated S_1/S_0 CI point, which is less than 8 kcal mol^{-1} higher in energy than the S_1 minimum. Furthermore, no significant emission was observed experimentally at long time-scales in the UV/Vis range, indicating that the system, after surmounting this small energy barrier, can return to its electronic ground state.

Thus, the above data clearly show that the presence of the phenyl substituents critically alter the shape of the potential energy surface and the photoreactivity with respect to related compounds. A study based on the topology around the CI was performed (see additional Figure 7.11), where a very sloped and single-path CI was found. This analysis of the CI concluded that isomerization around one C=N in not efficient, yielding an aborted geometrical transformation of the imine moiety for molecule 3 (see section 7.6 for supporting information). In accordance, the possible generation of the *Z*-photosiomer was considered, however, no experimental evidences were found. Therefore, the computational data gathered for 3 suggests a different photoprotection mechanism that also implies a high photostability.

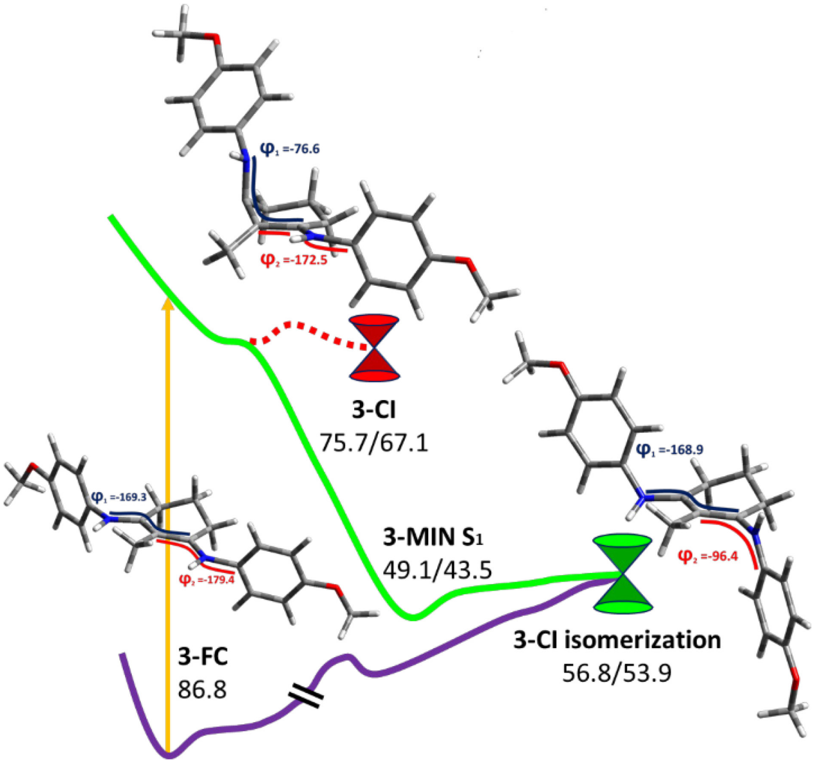

Figure 7.2. *Critical points along the MEP for compound 3. The MS-CASPT2 energies are reported in kcal mol^{-1} with respect to the electronic ground state minimum. Where two numbers are present, the first number corresponds to the S_1 energy, and the second number corresponds to the S_0 energy at the specified geometry.*

7.3.2. Experimental Study

Figure 7.3 shows the UV/Vis absorption spectra of 1-4 compounds in methanol, while the position of the maxima (λ_{exc}) can be found on Table 7.1.

The long-term photostability of the samples was also checked thoroughly by irradiation with a medium-pressure Hg lamp for more than 16h and ^{1}H-NMR analysis to ensure the lack of decomposition products. No signals attributable to other species were found by either NMR or UV. Particularly, the possible formation of *Z* photoisomer was examined by irradiating at -20ºC with monochromatic light (340 nm) or a 400 W Hg medium pressure lamp, monitoring the reaction by UV/Vis spectrometry. No trace of the photoisomer was found, in agreement with the aborted isomerization suggested by the calculations (see reference 23 for further details). However, the eventual formation of the photoisomer in short time-scales will be discussed in the following section.

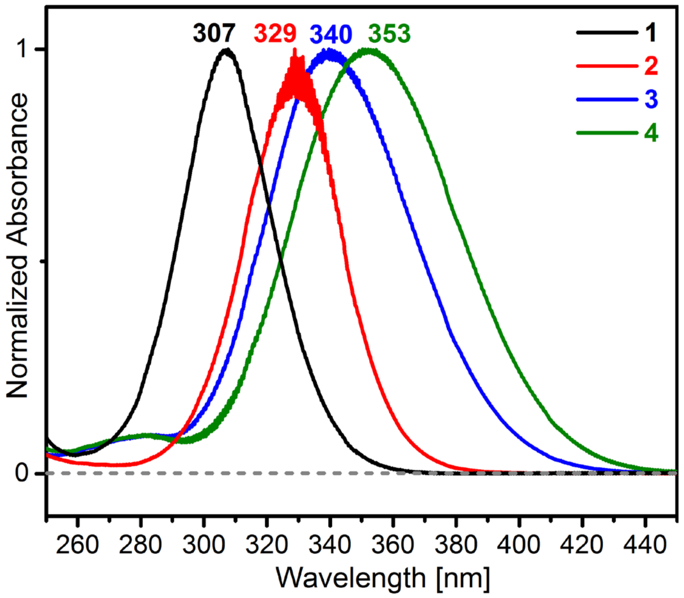

Figure 7.3. *Normalized steady-state UV/Vis absorption spectra of 7-8·10^{-4} M methanol solutions of the four studies molecules.*

The relaxation channels operating in molecules 1-4 were tracked by fs-FuC and TA measurements. Time-resolve fluorescence decays of the four studied compounds solved in methanol were collected after photoexcitation at the 306 (1), 330 (2), 341 (3) and 353 nm (4) wavelengths, respectively, at a number of detection energies along the emission spectra, without finding substantial differences in the transients. Figure 7.4 displays the time-resolved fluorescence decay curves, which were fitted by single exponentials and reflect the loss of the fluorescence across the detection range (400-600 nm) in similar lifetimes that vary between 150 and 650 fs for the four investigated molecules (see Table 7.1).

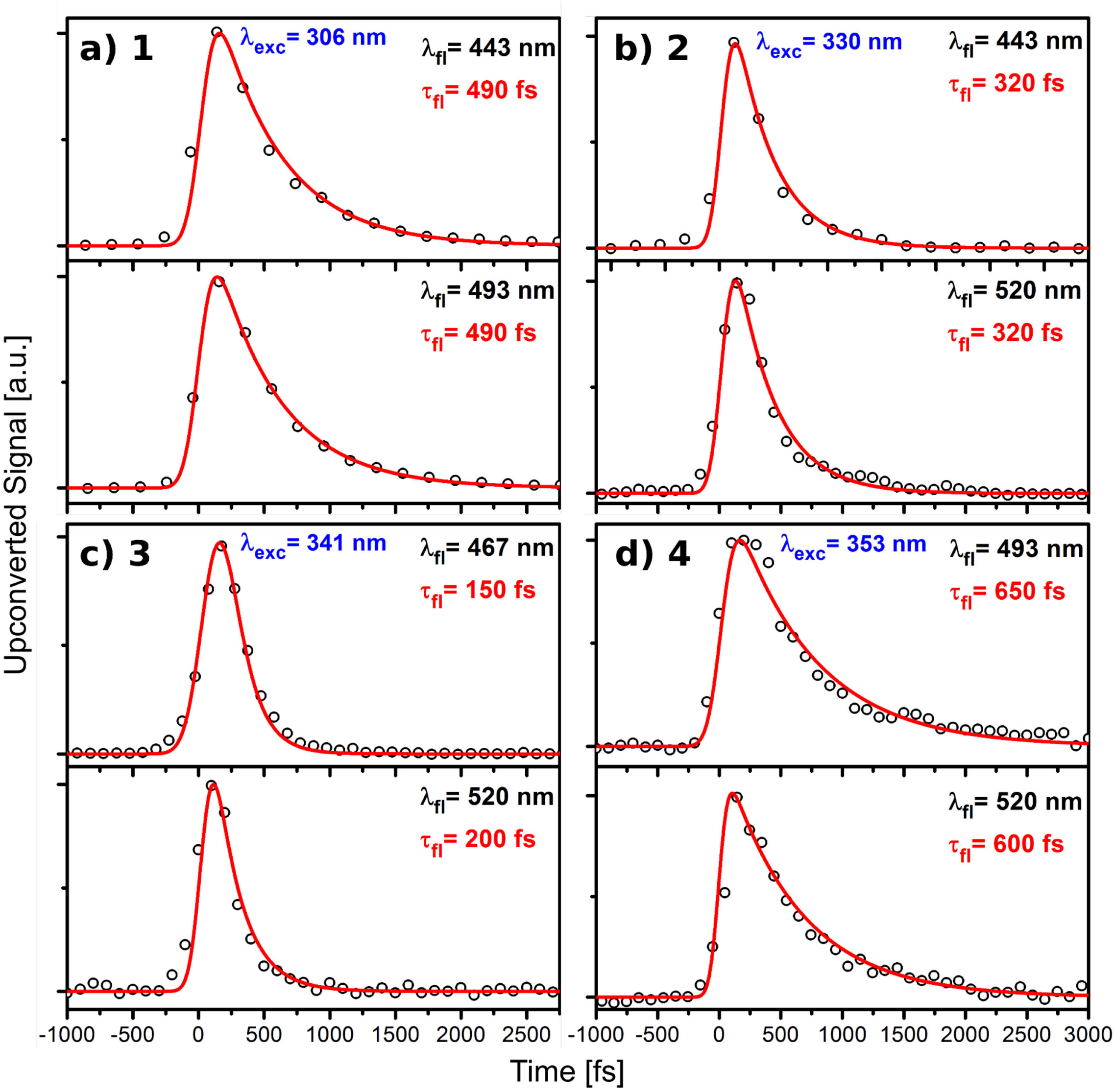

Figure 7.4. *Time-resolved fluorescence decays of 7-8·10^{-4} M methanol solution of molecules 1-4, collected at the indicated excitation and emission wavelengths. The black dots represent the experimental data obtained, whereas the solid red line corresponds to the best exponential fit.*

Further details on the photophysical behavior of the samples were gained by TA experiments showed in Figures 7.5 and 7.6. The measurements covered the 350-700 nm absorption range for several picoseconds after excitation. In all cases, the TA spectra display a broad absorption in the 450-550 nm range (extending further to the blue for compounds 1 and 2), whose red edge decays faster. It can also be noted, more clearly in molecules 1 and 2, that in this region the absorption is shifted from zero, indicating that is not formed directly from the initial excitation, but after a relaxation process instead. Although it will be discussed in detail in the following section, we can anticipate that the positive feature across the TA spectra can be attributed to the combination of two contributions: the absorption of the prepared excited state (ESA) and a band corresponding to a second location post relaxation of the prepared excited state.

The spectra of all samples (particularly weak in 4) also exhibit at their red edges a short living negative contribution to the TA signal. This feature is assigned to the stimulated emission (SE) of the prepared excited state, whose lifetime should correlate with those measured in the time-resolved fluorescence experiments. Additionally, a negative TA signal that corresponds to the bleach of the initially cold ground state (GSB) is observed at the blue edge (~350 nm) for molecule 4, which is the compound absorbing at the lowest energy.

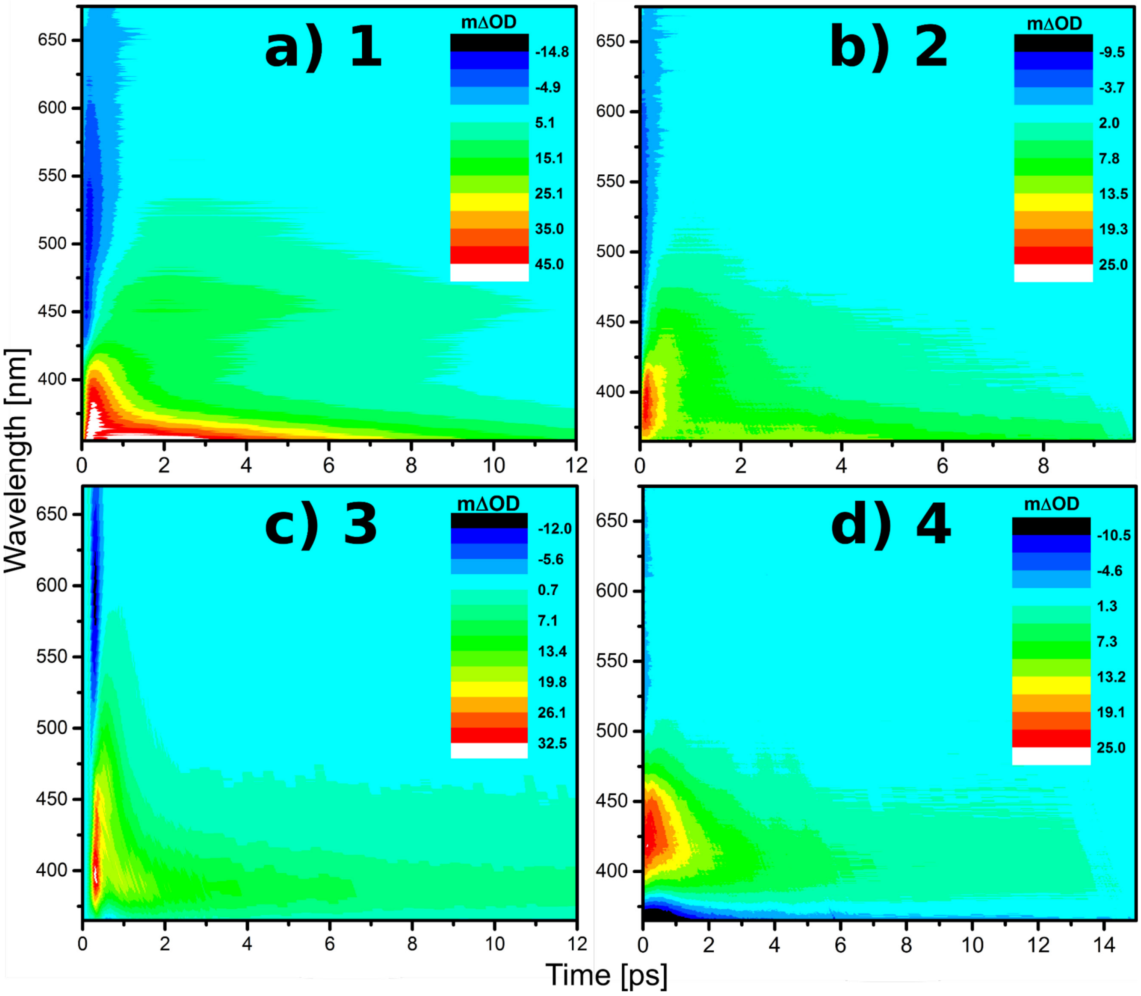

Figure 7.5. *TA spectra of 7-8·10^{-4} M methanol solution of 1-4 compounds photoexcited at 306 (a), 330 (b), 341 (c) and 353 nm (d).*

In order to describe the temporal evolution of the four samples TA spectra, a global fit function, resulting of the convolution of a Gaussian with three exponentials, τ_1, τ_2 and τ_3 (τ_0, τ_1 and τ_2 for compound 1), was employed. The temporal evolutions of absorption spectra for each molecule are illustrated by their respective decay associated spectra (DAS) in Figure 7.6, while the extracted time constants are displayed in Table 7.1. In these plots, each trace shows the spectral distribution of the pre-exponential factor (a_0, a_1, a_2 or a_3) associated to a particular temporal constant retrieved from the global fitting. A detailed discussion on the assignment of the measured τ lifetimes and the meaning of the DAS regions can be found below.

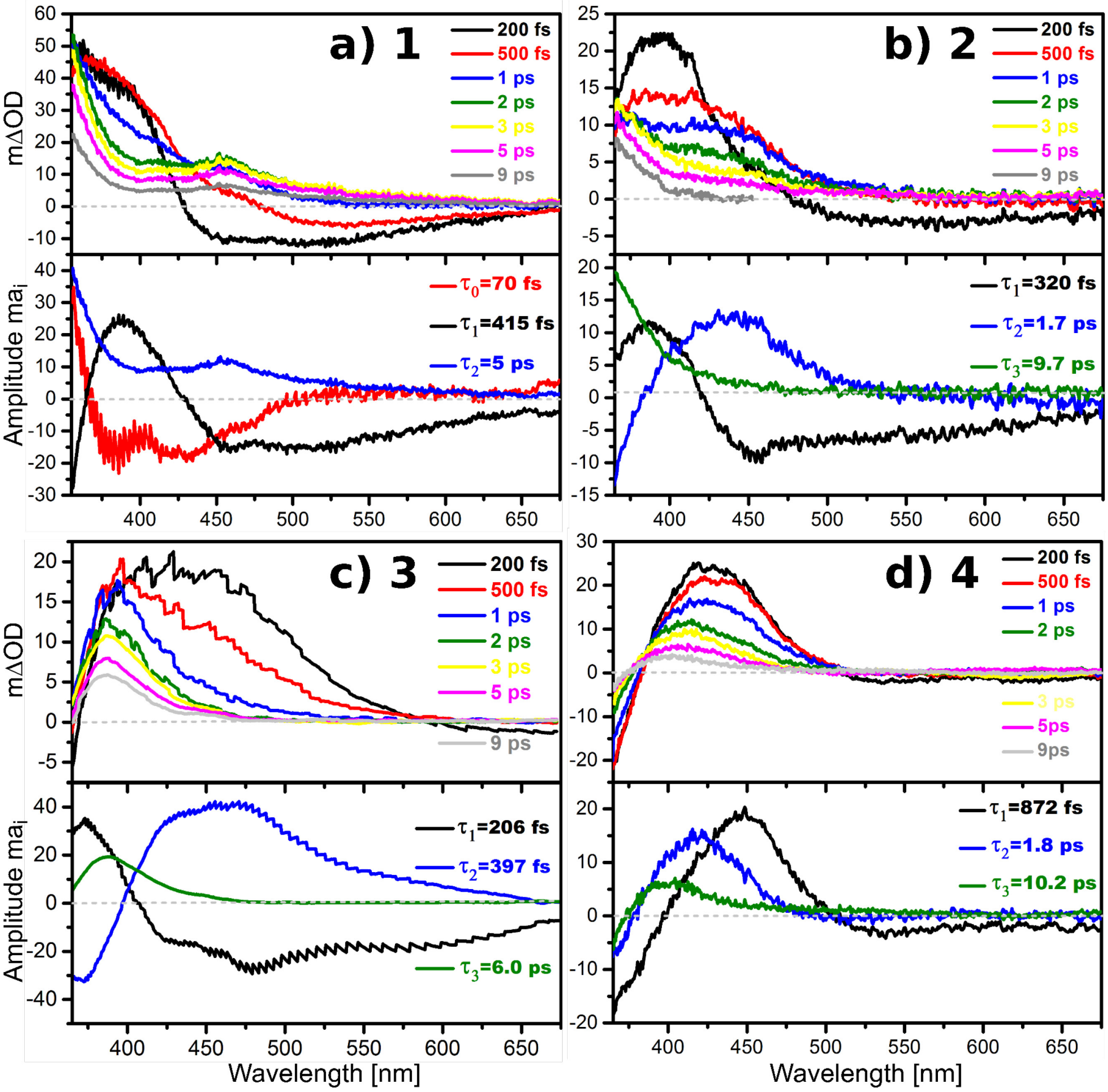

Figure 7.6. *Spectra at selected time delays (upper panels) and DAS (lower panels) for the lifetimes derived from the fitting of the TA spectra showed in Figure 7.5 for 1-4 compounds.*

Table 7.1. *Summary of the lifetimes resulting from the exponential fit of fluorescence up-conversion (FuC) and the global fit of transient absorption (TA) measurements for 1-4 compounds in methanol.*

Compound	**FuC**	**TA**
1 $\lambda_{exc} = 306$ nm	$\lambda_{fl} = 443$ nm → $\tau_{fl} = 490 \pm 25$ fs $\lambda_{fl} = 493$ nm → $\tau_{fl} = 490 \pm 25$ fs	$\tau_0 = 70 \pm 21$ fs $\tau_1 = 415 \pm 43$ fs $\tau_2 = 5.0 \pm 0.22$ ps
2 $\lambda_{exc} = 330$ nm	$\lambda_{fl} = 443$ nm → $\tau_{fl} = 320 \pm 16$ fs $\lambda_{fl} = 520$ nm → $\tau_{fl} = 320 \pm 16$ fs	$\tau_1 = 320 \pm 110$ fs $\tau_2 = 1.7 \pm 0.48$ ps $\tau_3 = 9.7 \pm 1.04$ ps
3 $\lambda_{exc} = 341$ nm	$\lambda_{fl} = 467$ nm → $\tau_{fl} = 150 \pm 15$ fs $\lambda_{fl} = 520$ nm → $\tau_{fl} = 200 \pm 15$ fs	$\tau_1 = 206 \pm 65$ fs $\tau_2 = 397 \pm 190$ fs $\tau_3 = 6.0 \pm 0.40$ ps
4 $\lambda_{exc} = 353$ nm	$\lambda_{fl} = 493$ nm → $\tau_{fl} = 650 \pm 32$ fs $\lambda_{fl} = 520$ nm → $\tau_{fl} = 600 \pm 30$ fs	$\tau_1 = 872 \pm 201$ fs $\tau_2 = 1.8 \pm 0.15$ ps $\tau_3 = 10.2 \pm 0.22$ ps

7.4. Discussion

We begin by discussing the TA spectra for the four studied compounds. Each molecule show absorption maxima centred across the UV-A/UV-B region (Table 7.1, Figure 7.3), and their combined absorption produces an efficient blocker of the solar UV radiation. According to the computed spectra, the observed band can be assigned to the $\pi\pi^*$ character $S_0 \rightarrow S_1$ transition (see section 7.6, Additional Information), placing other excited states at considerably higher energies (S_2 is *ca.* 60 kcal mol^{-1} above S_1 for sample 3). Considering that no changes in the absorption spectra are observed after long-term exposition to UV radiation and femtosecond excitation pulses, we can assume that only the S_1 and S_0 states of the targeted samples, other than the C=N *Z*-photoisomer that will be discussed below, are involved in the excitation and the explored relaxation window.

The FuC data indicate unambiguously that the initially formed excited state relaxes in all cases in few hundreds of femtoseconds toward a non-fluorescent location, which based on the computational study and the TA data should be the ground state of molecule. The emission is observed for some of the samples at wavelengths as long as 600 nm, the limit of the experimental setup to detect the fluorescence free from the interference of the gate beam second harmonic. Correspondingly, the SE emission contribution can be noticed in the TA measurements at wavelengths longer than 675 nm. This bathochromic shift of the emission reveals a large geometrical change along the excited state relaxation pathway. This is compatible with the isomerization coordinate predicted by calculations, further supporting the TA data.

Focusing on the TA measurements, it should be noted here that the small spectral discrimination of the extracted time constants notably complicates the analysis. However, the correlation with the computational and fluorescence data can help to interpret the derived time constants. In principle, although the four studied samples exhibit singularities that would be discussed in detail; a general relaxation scheme can be invoked to explain the observed dynamical behavior. We suggest that the τ_1 constant, which correlates with the measured fluorescence lifetimes, reflects the relaxation of the initially prepared S_1 $\pi\pi^*$ state, whereby population to the vibrationally hot electronic ground state is achieved. In the case of 1, an additional very short τ_0 component is required to model the early times of the relaxation. This τ_0 originates in the initially excited state and seems to accounts for the initial S_1 state population evolution out of the Franck-Condon region. The τ_0 DAS lifetime is positive only for the shortest wavelengths, acquiring negative values in the ~370-490 nm interval. The τ_1 lifetime is present through the full studied range, where at least three distinctive spectral regions according to the signs of the τ_1 DAS and the TA signal, can be observed:

(a) The lowest energy portion of the spectra that extends up to the detection limit at 650 nm, where τ_1 is the only temporal constant present. In this region both, the τ_1 DAS and the TA signal have a negative character, indicating the presence of an emission. Owing to its τ_1 lifetime, it can be assigned to the prepared state SE. As already mentioned above, the SE presumably extends even to longer wavelengths beyond the detection limit. We note also that in the case of samples 1 and 4 this contribution is considerably weaker.

(b) For molecules 1-3, there is a region of positive TA signal in the ~425-550 nm range, where the τ_1 DAS stays negative while the τ_2 DAS shows a positive value. The signs indicate that this portion of the spectrum is formed with τ_1 and subsequently decays with τ_2. The fact that 4 does not exhibit this region, but a positive τ_1 instead, is explained below.

(c) Peaking around 385 nm, the τ_1 DAS of 1-3 show a positive feature attributed to the S_1

excited state absorption (ESA). For 1, this band overlaps with a negative τ_0 feature that accounts for the formation of this S_1 location. It is also worth to note in 4 the τ_1 positive band is red-shifted, with a maximum at ~450 nm. This causes an extensive overlap with the hot ground state absorption and also permits to observe the GSB negative contribution at the highest energies of the spectra.

To assign the τ lifetimes retrieved from the fitting, the TA measurements can be correlated with the fluorescence and the computational results. The τ_1 component, which matches the FuC decays, is found in the red edge of the spectra and describes the disappearance of the SE signal. Accordingly, we can assign it to the IC of the prepared S_1 state to form a hot ground state. The components τ_2 and τ_3 can be assigned to the vibrational cooling that takes place in the ground state formed during the first hundreds of femtoseconds. The fact that these components are not present in the red portion of the spectra attributed to the SE reinforces their assignation to ground state processes For the four studied compounds, the DAS of τ_2 shows a positive value in the ~385-500 nm region that switches to negative (molecules 2-4) at the blue edge of the spectrum. This behavior could be explained as the red to blue shift of the ground state spectrum cooling. Accordingly, the longer τ_3 component, which appears at the blue portion of the TAS, characterizes the relaxation of colder sections of the electronic ground state. During the modelling process, we have detected a considerable cross-talking between the values of the τ_2 and τ_3 constants, which can be justified by the nature of the cooling process. In the case of compound 1, the longer τ_3 component is not required to model the ground state cooling, which is probably related to the fact that the formed vibrationally hot ground state is shifted to higher energies respect to the other molecules. In general, the four studied compounds share a very similar photophysical pattern and the proposed interpretation of the dynamical processes can be applied to all of them. The differences found in the fluorescence and TA data among the four studied molecules can be basically explained in terms of the $S_0 \rightarrow S_1$ excitation energies and the relative energies of the $S_0 \rightarrow S_1$ and $S_1 \rightarrow S_n$ transitions.

Ii is worth to note that owing mainly to the little spectral discrimination found between the τ time components, we may conceive at least one alternative interpretation compatible with the FuC and TA data. In close analogy to the τ_0 and τ_1 lifetimes found in molecule 1, both τ_1 and τ_2 could be associated to the S_1 excited state. In this view, τ_1 would account for the S_1 prepared population moving along the relaxation coordinate, while τ_2 would be associated to the IC from a relaxed location on S_1 state to the vibrationally hot S_0. The fluorescence from this relaxed location should be shifted to lower energies, out of the fluorescence and absorption detection regions, which could explain the fact that only τ_1 is found in the fluorescence and SE signals. The remaining τ_3 would be related with the vibrational cooling on the hot ground state formed after the IC. However, this second assignment does not alter substantially the photophysical properties of the studied molecules other than them having a slightly longer-living S_1 excited state.

The carried out computational aids to establish the operative relaxation pathway by pointing at the coordinate that may promote the S_1/S_0 nonadiabatic coupling. According to it, the inclusion of the two phenyl substituents favours the C=N isomerization channel *vs.* the out-of-plane ring deformation path, which is the calculated MEP for the simplified methyl-substituted model. The former path should be accompanied, on the way to the corresponding CI, by a considerably larger S_1 stabilization (~1.6 eV for molecule 3, as shown in Figure 7.2), than that estimated along the out-of-plane coordinate. Additionally, the proposed channel could lead, after returning back to the ground state, to the permanent formation of the slightly less stable *Z*-isomer. In our opinion, the fluorescence and TA data are fully compatible with the photoisomerization reaction path. However, neither spectral features nor long-term dynamical constants that could be associated with the formation of the photoisomer were detected. As it was briefly mentioned, owing to the low isomerization barrier calculated in the ground state (with respect to the excitation energy), the process could not yield a detectable permanent population of the slightly less stable Z-isomer. Additionally, the similar predicted absorption spectrum could preclude its selective detection by the employed spectroscopic methods. The current results should be compared with the recent work by Woolley *et al.*[21] on a simpler MAA-based compounds. They found a similar S_1/S_0 IC relaxation channel, but in contrast with the results herein presented, a small population remain trapped in the S_1 for longer time-scales. However, according to our computational predictions, the presence of the aliphatic substituents in the molecule studied by Woolley *et al.* should favor the pyramidalization over the photoisomerization as the driving relaxation coordinate. In this scenario, although we cannot unambiguously identify from the experimental data the path leading to the observed S_1/S_0 IC, we tentatively propose the photoisomerization coordinate as the motion behind the photophysical properties of the studied compounds. Future studies on specifically designed derivatives should permit to further explore the dependence of the dynamics on the chemical structure of these species.

7.5. Conclusions

This chapter has presented the spectroscopic study of a set of compounds, which based in the natural properties of MAAs have been rationally designed by Prof. Sampedro's group to act as efficient solar photoprotectors at different absorption wavelengths across the UV-A/UV-B region. The photophysical and photochemical behavior of each molecule has been experimentally explored by fs-TA and FuC techniques, finding in all cases an analogous relaxation channel that involves the IC of the prepared excited state in hundreds of fs. The experimental observations have been rationalized by CASPT2//CASSCF quantum computations, which have revealed a novel relaxation channel that could drive the S_1/S_0 coupling when phenyl rings are included as iminic substituents. The calculated MEPs indicate that for the latter species the steepest pathway out of the Franck-Condon region implies the photoisomerization around one of the C=N bonds, being accessible along this route a S_1/S_0 CI located slightly above the S_1 minimum. This route differs from the pyramidalization pathway found for the previously studied palatine and related compounds.[13-14]

In summary, the demonstrated photoprotective behavior, together with the high absorption efficiency and excellent photostability showed by the synthesized molecules opens the door for their potential application in photoprotection and guides the design of new molecules with specific properties.

7.6. Additional Information

7.6.1. General information of the studied synthetic sunscreens

1 ($C_{25}H_{24}Br_2N_2O_3S$): *(E)*-2-bromo-N-(3-((2-bromophenyl)amino)-2-methylcyclopent-2-en-1-ylidene)benzenaminium 4-methylbenzenesulfonate.

Molecular weight: 592.35

^{1}H-NMR (400 MHz, MeOD) δ ppm 7.8-7.7 (m, 2H), 7.7-7.7 (m, 2H), 7.5 (s, 4H), 7.4-7.3 (m, 2H), 7.2 (d, J = 7.8 Hz, 2H), 2.6 (bs, 4H), 2.4 (s, 3H), 2.1 (bs, 3H).

^{13}C-NMR (75 MHz, MeOD) δ ppm 182.4, 143.4, 141.7, 137.7, 135.1, 134.7, 131.9, 131.7, 131.4, 130.4, 130.2, 129.8, 126.9, 125.7, 122.6, 117.9, 107.4, 29.1, 21.3, 7.3.

UV/Vis (ACN): λ = 306 nm (ε = 33600 $M^{-1}cm^{-1}$)

MP: 205 ºC (descomposition)

2 ($C_{26}H_{26}Br_2N_2O_3S$): *(E)*-2-bromo-N-(3-((2-bromophenyl)amino)-2-methylcyclohex-2-en-1-ylidene)benzenaminium 4-methylbenzenesulfonate

Molecular weight: 606.37

^{1}H-NMR (400 MHz, MeOD) δ ppm 7.82 (d, J = 7.9 Hz, 2H), 7.70 (d, J = 8.1 Hz, 2H), 7.57-7.37 (m, 8H), 7.23 (d, J = 7.8 Hz, 2H), 2.40 (t, J = 6.6 Hz, 4H), 2.37 (s, 3H), 2.15 (s, 3H), 1.88-1.75 (m, 2H).

^{13}C-NMR (75 MHz, MeOD) δ ppm 173.5, 143.6, 141.6, 137.6, 134.8, 131.8, 130.8, 130.2, 129.8, 127.0, 123.4, 101.4, 28.5, 21.3, 21.1, 9.6.

UV/Vis (ACN): λ = 330 nm (ε = 27610 $M^{-1}cm^{-1}$)

MP: 210 ºC (descomposition)

3 ($C_{28}H_{32}N_2O_5S$): *(E)*-4-methoxy-N-(3-((4-methoxyphenyl)amino)-2-methylcyclohex-2-en-1-ylidene)benzenaminium 4-methylbenzenesulfonate

Molecular weight: 508.63

^{1}H-NMR (400 MHz, MeOD) δ ppm 7.69 (d, J = 8.0 Hz, 2H), 7.21 (d, J = 8.8 Hz, 6H), 7.02 (d, J = 8.8 Hz, 4H), 3.83 (s, 6H), 2.52(t, J = 5.8 Hz, 4H), 2.36 (s, 3H), 2.07 (s, 3H), 1.87-1.67 (m, 2H).

^{13}C-NMR (100 MHz, MeOD) δ ppm 172.1, 160.9, 143.7, 141.6, 131.1, 129.8, 128.9, 127.0, 115.7, 100.4, 56.1, 28.7, 21.6, 21.3, 9.5.

UV/Vis (ACN): λ = 341 nm (ε = 32410 $M^{-1}cm^{-1}$)

MP: 270 ºC (descomposition)

4 ($C_{28}H_{32}N_2O_6S$): *(E)*-4-methoxy-N-(2-methoxy-3-((4-methoxyphenyl)amino)cyclohex-2-en-1-ylidene)benzenaminium 4-methylbenzenesulfonate.

Molecular weight: 524.46

^{1}H-NMR (400 MHz, MeOD) δ ppm 7.70 (d, J = 8.0 Hz, 2H), 7.28-7.15 (m, 6H), 7.03 (d, J = 8.6 Hz, 4H), 3.83 (s, 6H), 3.78 (s, 3H), 2.62 (t, J = 5.8 Hz, 4H), 2.36 (s, 3H), 1.89-1.73 (m, 2H).

^{13}C-NMR (100 MHz, MeOD) δ ppm 164.8, 160.8, 143.7, 141.6, 130.4, 129.8, 129.2, 128.4, 127.0, 115.7, 60.2, 56.1, 27.4, 21.5, 21.3.

UV/Vis (ACN): λ = 353 nm (ε = 31120 $M^{-1}cm^{-1}$)

MP: 210 ºC (descomposition)

7.6.2. Active space selection

Two different active spaces were checked to model compound **3** (14,13) and (6,5). The core chromophore was considered to be formed by the π density (orbitals π and π* of bonds C=C, C=N and π N_{imine}) and, in the extended active space, four π and π* orbitals of the phenyl rings, as seen below. The selected active orbitals for the selected (14,13) active space are shown in Figure 7.7. In case of using a (6,5) as active space, the orbitals present are 1, 2, 5, 8 and 13, excluding all the phenyl orbitals. In both cases the involved transition is a π - π* between orbitals 5 and 8.

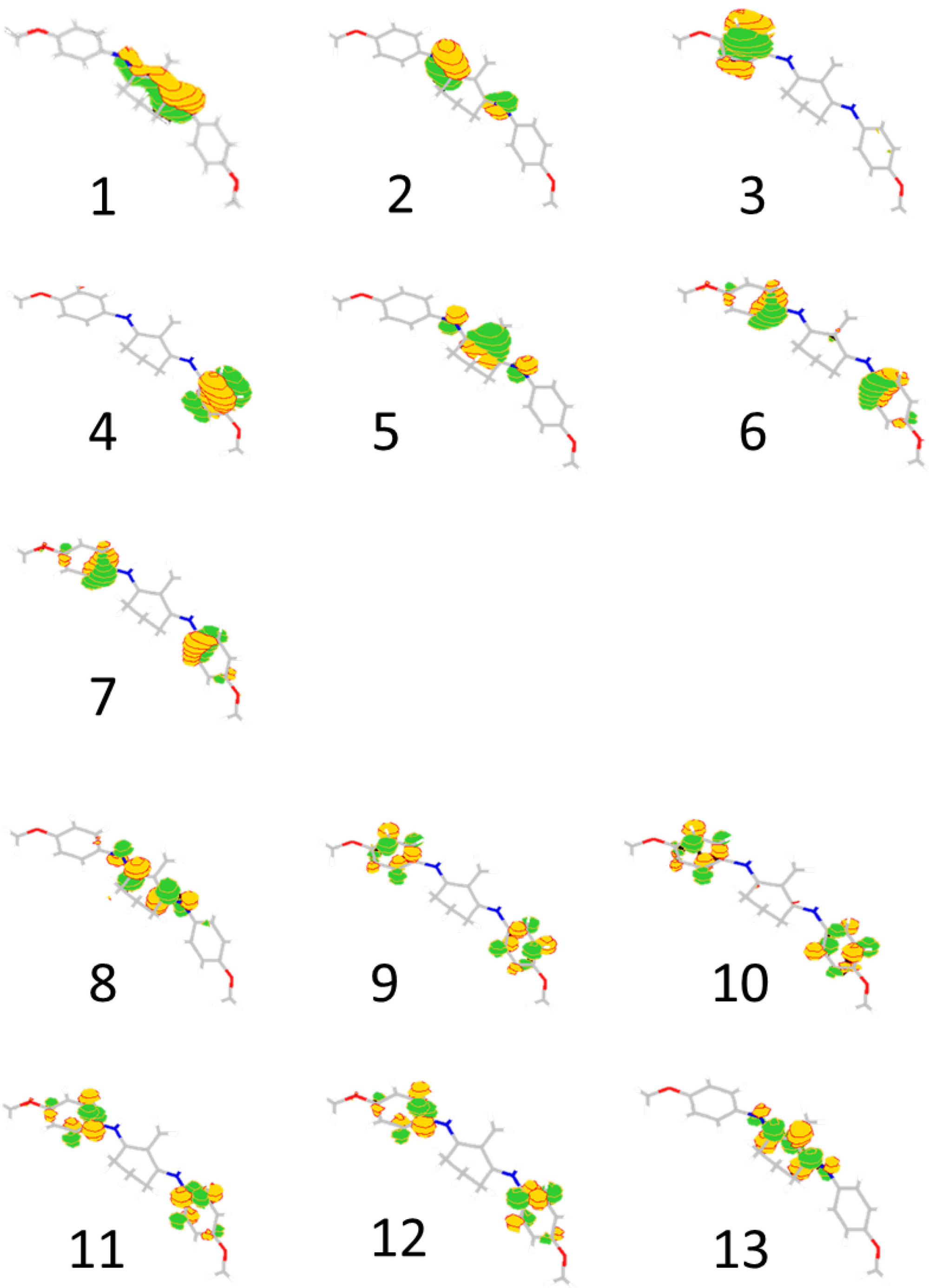

***Figure** 7.7. Orbitals involved in the (14,13) active space of **3**.*

Absorption spectra were computed for both active spaces (14,13) and (6,5) to check for differences. In both cases, a transition between S_0-S_1 was observed at 326nm and 327nm, respectively. The oscillator strength values changed from $f = 1.1066305$ to $f = 0.82943528$ due to lack of the phenyl ring contribution in the smaller active space. To ensure the ability of the (6,5) active space to reproduce the potential energy surface, the MEP was also computed for both active spaces.

7.6.3. Minimum Energy Pathways

The MEP was computed for both active spaces obtaining the same energetic profile as shown in Figure 7.8. A different, new deactivation channel consisting of the imine isomerization competing with the out-of-plane movement of the substituents of the cycle was found.[13]

The new deactivation path involving a C=N isomerization leads to the formation of a minimum in the potential energy surface followed by a CI only 8 kcal mol^{-1} higher in energy. This barrier is low enough to allow for a fast deactivation to the ground state in agreement with the experimental data.

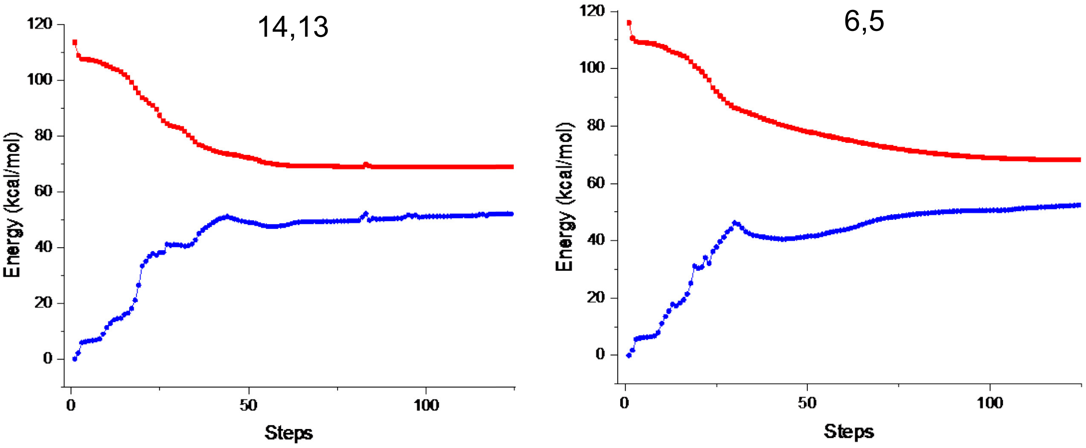

Figure 7.8. Comparison of MEP (CASSCF) with both active spaces.

In order to ensure this differential effect of the aryl moieties on the shape of the potential energy surface, we also computed the MEP for the simplified compound **A** in which the phenyl substituents are changed by methyl groups (**A** has not been synthesized and it was studied only computationally, see Figures 7.9 and 7.10). As the more relevant feature, it should be noted that the shape of the potential energy surface clearly resembles that of palythine and related compound inclunding the movement of substituents out of the plane of the cycle. In contrast, the minimum in the excited state related to the photoisomerization of a C=N bond is *ca.* 10 kcal/mol higher in energy and no CI of isomerization was found.

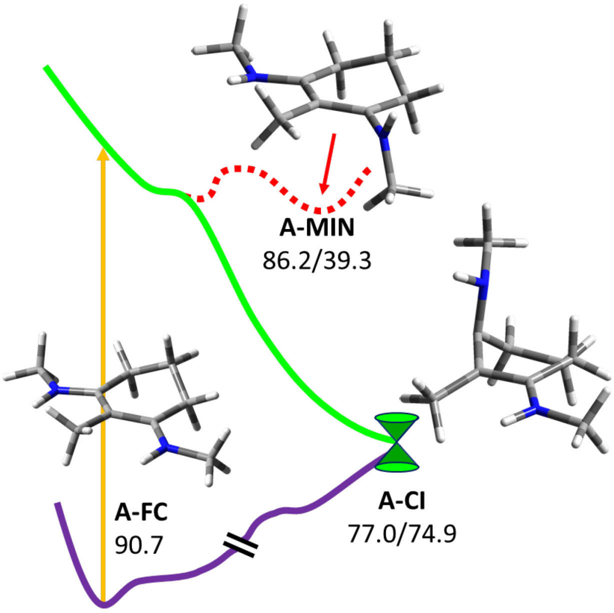

Figure 7.9. *Critical points along the potential energy surface for **A** (CASPT2 energies relative to S_0).*

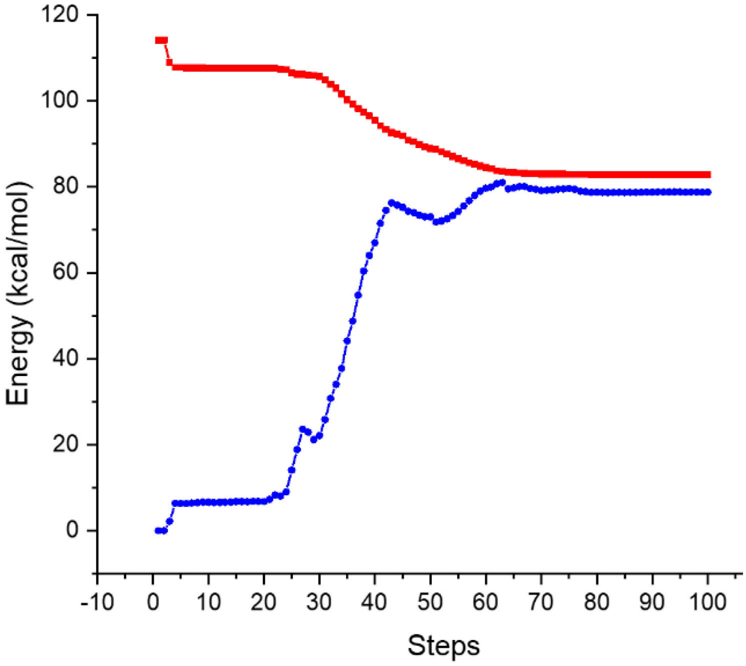

Figure 7.10. *MEP (CASSCF) connecting Franck-Condon region to the CI (right).*

7.6.4. Isomerization: CI and Thermal Reversion

The topology around the CI is a key factor to understand any deactivation mechanism. In this case, we found according to Molcas descriptors,[3] a highly sloped funnel leading to the formation of a single product. This means a CI that promotes an aborted geometrical transformation with stating material recovery and not the appearance of photoproducts.

Thus, a low (if any) isomerization quantum yield for the photoisomerization is expected.

The shape of the potential energy surface around the CI was explored by applying geometrical distortions along the *x* and *y* vectors, as shown in Figure 7.11. These vectors are a mathematical transformation of the classical descriptors (gradient difference and derivative coupling vector). The gradient difference and derivative coupling vectors are also shown in Figure 7.11. Specifically, the movement related with the derivative coupling vector corresponds with an aborted isomerization.

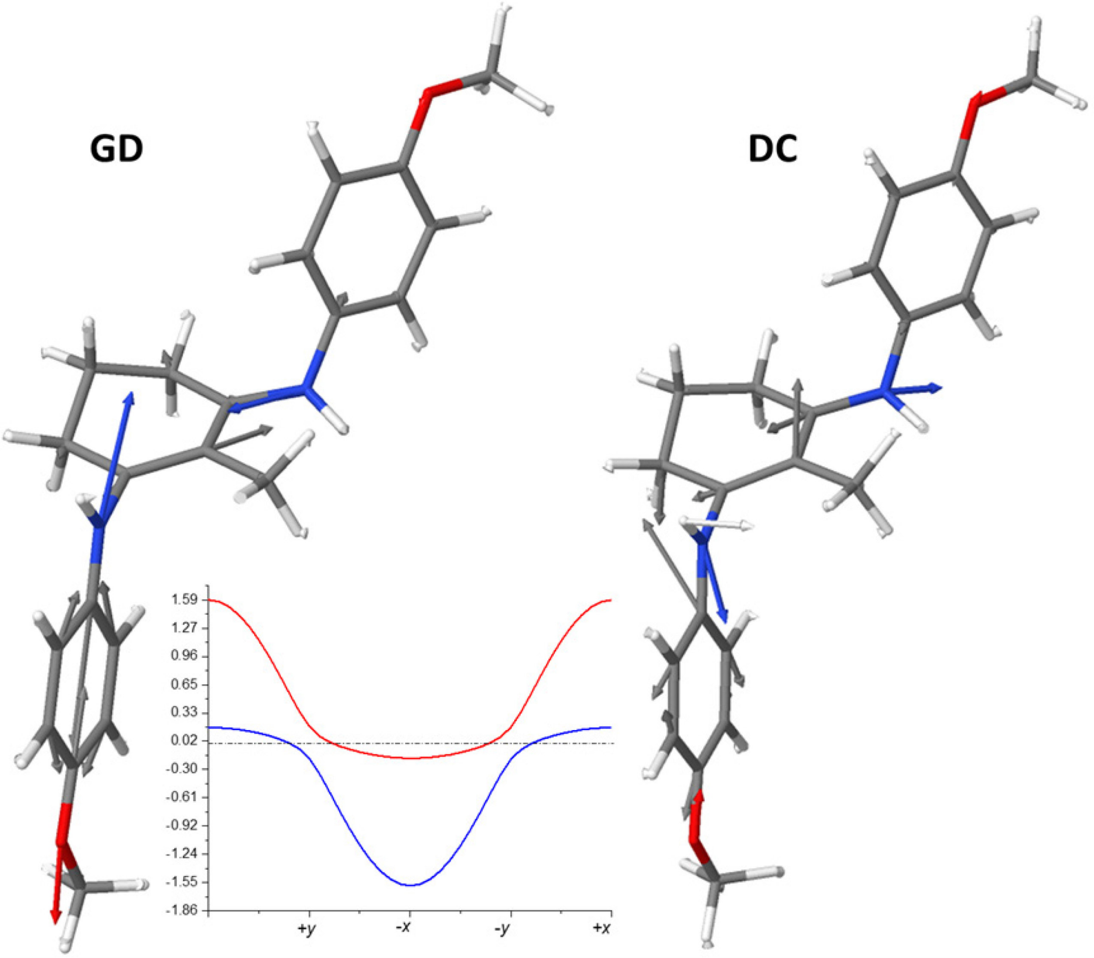

Figure 7.11. *Potential energy surface topology around the CI and S_1 (red) and S_0 (blue) energy difference (kcal/mol). CI isomerization vectors gradient difference (left) and derivative coupling (right).*

Even with a sloped CI topology, the formation of the *Z*-isomer could still be possible. In fact, this feature has been also observed in natural MAAs as a complementary mechanism of photoprotection. In addition, both the starting isomer and the photoisomer contribute to the photoprotection as they absorb in a similar region of the spectrum (see computed absorption in Figure 7.12). To explore the relative stability and UV capabilities of the *Z*-isomer, we computed both isomers at the MP2 level including methanol as solvent to reproduce the experimental data (Figure 7.11).

The *Z*-photoisomer can be thermally converted to the starting *E*-isomer through a transition state characterized by computing the intrinsic reaction coordinate. The obtained TS connects both isomers through a low energy barrier (13.7 kcal mol^{-1}, see Figure 7.12). This process should be fast enough to avoid the accumulation of the photoisomer at room temperature.

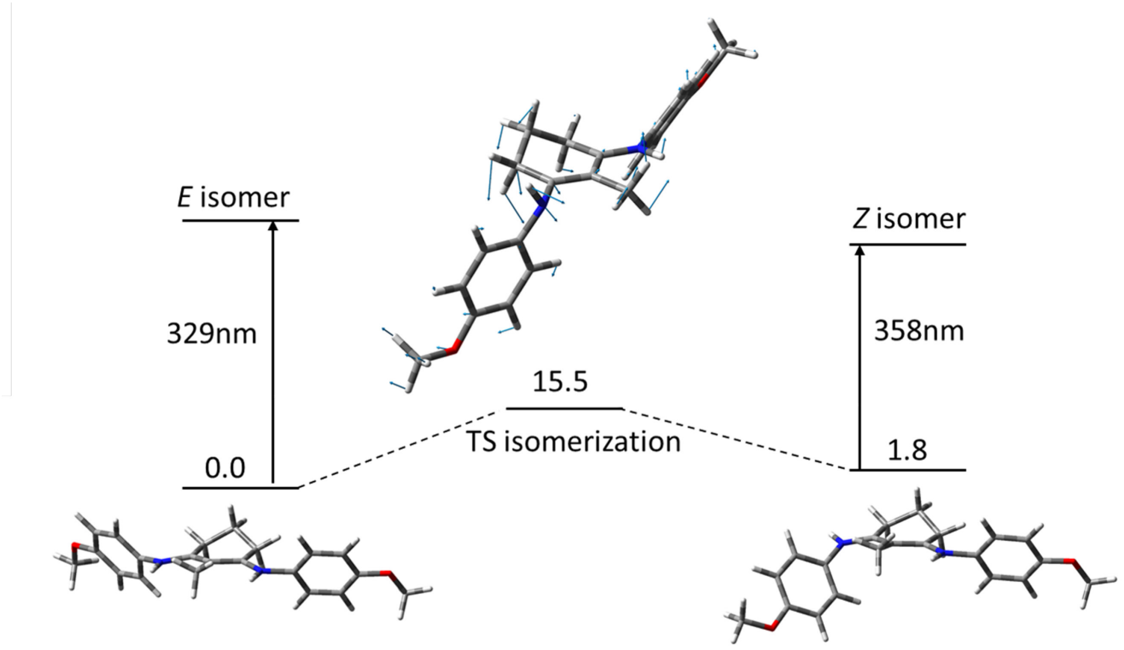

Figure 7.12. *Schematic isomerization path and TS with displacement vectors. Energies in kcal mol^{-1} and absorption wavelengths in nm.*

7.7. References

1. McAuliffe, D. J.; Blank, I. H., Effects of UVA (320–400 nm) on the Barrier Characteristics of the Skin. *Journal of Investigative Dermatology* **1991,** *96* (5), 758-762.

2. Gallagher, R. P.; Lee, T. K., Adverse effects of ultraviolet radiation: A brief review. *Progress in Biophysics and Molecular Biology* **2006,** *92* (1), 119-131.

3. Narayanan, D. L.; Saladi, R. N.; Fox, J. L., Review: Ultraviolet radiation and skin cancer. *International Journal of Dermatology* **2010,** *49* (9), 978-986.

4. Frederick, J. E.; Snell, H. E.; Haywood, E. K., Solar Ultraviolet Radiation at the Earth's surface. *Photochemistry and Photobiology* **1989,** *50* (4), 443-450.

5. Matsumi, Y.; Kawasaki, M., Photolysis of Atmospheric Ozone in the Ultraviolet Region. *Chemical*

Reviews **2003,** *103* (12), 4767-4782.

6. Bens, G., Sunscreens. In *Sunlight, Vitamin D and Skin Cancer*, Reichrath, J., Ed. Springer New York: New York, NY, 2008; pp 137-161.

7. Otterstedt, J. E. A., Photostability and molecular structure. *The Journal of Chemical Physics* **1973,** *58* (12), 5716-5725.

8. M. Bandaranayake, W., Mycosporines: are they nature's sunscreens? *Natural Product Reports* **1998,** *15* (2), 159-172.

9. Tan, E. M. M.; Hilbers, M.; Buma, W. J., Excited-State Dynamics of Isolated and Microsolvated Cinnamate-Based UV-B Sunscreens. *The Journal of Physical Chemistry Letters* **2014,** *5* (14), 2464-2468.

10. Dean, J. C.; Kusaka, R.; Walsh, P. S.; Allais, F.; Zwier, T. S., Plant Sunscreens in the UV-B: Ultraviolet Spectroscopy of Jet-Cooled Sinapoyl Malate, Sinapic Acid, and Sinapate Ester Derivatives. *Journal of the American Chemical Society* **2014,** *136* (42), 14780-14795.

11. Miyazaki, Y.; Inokuchi, Y.; Akai, N.; Ebata, T., Direct spectroscopic evidence of photoisomerization in para-methoxy methylcinnamate revealed by low-temperature matrix-isolation FTIR spectroscopy. *The Journal of Physical Chemistry Letters* **2015,** *6* (7), 1134-1139.

12. Domingos, S. R.; Schnell, M., Wet Sunscreens in the Gas Phase: Structures of Isolated and Microsolvated Oxybenzone. *The Journal of Physical Chemistry Letters* **2018,** *9* (17), 4963-4968.

13. Sampedro, D., Computational exploration of natural sunscreens. *Physical Chemistry Chemical Physics* **2011,** *13* (13), 5584-5586.

14. Losantos, R.; Churio, M. S.; Sampedro, D., Computational exploration of the photoprotective potential of gadusol. *ChemistryOpen* **2015,** *4* (2), 155-160.

15. Baker, L. A.; Horbury, M. D.; Greenough, S. E.; Coulter, P. M.; Karsili, T. N. V.; Roberts, G. M.; Orr-Ewing, A. J.; Ashfold, M. N. R.; Stavros, V. G., Probing the Ultrafast Energy Dissipation Mechanism of the Sunscreen Oxybenzone after UVA Irradiation. *The Journal of Physical Chemistry Letters* **2015,** *6* (8), 1363-1368.

16. Baker, L. A.; Greenough, S. E.; Stavros, V. G., A Perspective on the Ultrafast Photochemistry of Solution-Phase Sunscreen Molecules. *The Journal of Physical Chemistry Letters* **2016,** *7* (22), 4655-4665.

17. Baker, L. A.; Horbury, M. D.; Greenough, S. E.; Allais, F.; Walsh, P. S.; Habershon, S.; Stavros, V. G., Ultrafast Photoprotecting Sunscreens in Natural Plants. *The Journal of Physical Chemistry Letters* **2016,** *7* (1), 56-61.

18. Baker, L. A.; Marchetti, B.; Karsili, T. N.; Stavros, V. G.; Ashfold, M. N., Photoprotection: extending lessons learned from studying natural sunscreens to the design of artificial sunscreen constituents. *Chemical Society Reviews* **2017,** *46* (12), 3770-3791.

19. Baker, L. A.; Clark, S. L.; Habershon, S.; Stavros, V. G., Ultrafast Transient Absorption Spectroscopy of the Sunscreen Constituent Ethylhexyl Triazone. *The Journal of Physical Chemistry Letters* **2017,** *8* (10), 2113-2118.

20. Luo, J.; Liu, Y.; Yang, S.; Flourat, A. L.; Allais, F.; Han, K., Ultrafast Barrierless Photoisomerization and Strong Ultraviolet Absorption of Photoproducts in Plant Sunscreens. *The Journal of Physical Chemistry Letters* **2017,** *8* (5), 1025-1030.

21. Woolley, J. M.; Staniforth, M.; Horbury, M. D.; Richings, G. W.; Wills, M.; Stavros, V. G., Unravelling the Photoprotection Properties of Mycosporine Amino Acid Motifs. *The Journal of Physical Chemistry Letters* **2018,** *9* (11), 3043-3048.

22. Rodrigues, N. D. N.; Staniforth, M.; Stavros, V. G., Photophysics of sunscreen molecules in the gas phase: a stepwise approach towards understanding and developing next-generation sunscreens. *Proceedings of the Royal Society A: Mathematical, Physical and Engineering Sciences* **2016,** *472* (2195), 20160677.

23. Losantos, R.; Funes-Ardoiz, I.; Aguilera, J.; Herrera-Ceballos, E.; García-Iriepa, C.; Campos, P. J.; Sampedro, D., Rational design and synthesis of efficient sunscreens to boost the solar protection factor. *Angewandte Chemie* **2017,** *129* (10), 2676-2679.

24. Abiola, T. T.; Whittock, A. L.; Stavros, V. G., Unravelling the Photoprotective Mechanisms of Nature-Inspired Ultraviolet Filters Using Ultrafast Spectroscopy. *Molecules* **2020,** *25* (17), 3945.

25. Conde, F. R.; Churio, M. S.; Previtali, C. M., Experimental study of the excited-state properties and photostability of the mycosporine-like amino acid palythine in aqueous solution. *Photochemical & Photobiological Sciences* **2007,** *6* (6), 669-674.

26. Losantos, R.; Sampedro, D.; Churio, M. S., Photochemistry and photophysics of mycosporine-like amino acids and gadusols, nature's ultraviolet screens. *Pure and Applied Chemistry* **2015,** *87* (9-10), 979-996.

27. Miyazaki, Y.; Yamamoto, K.; Aoki, J.; Ikeda, T.; Inokuchi, Y.; Ehara, M.; Ebata, T., Experimental and theoretical study on the excited-state dynamics of ortho-, meta-, and para-methoxy methylcinnamate. *J Chem Phys* **2014,** *141* (24), 244313.

28. Chang, X.-P.; Li, C.-X.; Xie, B.-B.; Cui, G., Photoprotection Mechanism of p-Methoxy Methylcinnamate: A CASPT2 Study. *The Journal of Physical Chemistry A* **2015,** *119* (47), 11488-11497.

29. Karsili, T. N. V.; Marchetti, B.; Ashfold, M. N. R.; Domcke, W., Ab Initio Study of Potential Ultrafast Internal Conversion Routes in Oxybenzone, Caffeic Acid, and Ferulic Acid: Implications for Sunscreens. *The Journal of Physical Chemistry A* **2014,** *118* (51), 11999-12010.

30. Dunkelberger, A. D.; Kieda, R. D.; Marsh, B. M.; Crim, F. F., Picosecond Dynamics of Avobenzone in Solution. *The Journal of Physical Chemistry A* **2015,** *119* (24), 6155-6161.

31. Baker, L. A.; Horbury, M. D.; Greenough, S. E.; Ashfold, M. N.; Stavros, V. G., Broadband ultrafast photoprotection by oxybenzone across the UVB and UVC spectral regions. *Photochemical & Photobiological Sciences* **2015,** *14* (10), 1814-1820.

32. Li, C.-X.; Guo, W.-W.; Xie, B.-B.; Cui, G., Photodynamics of oxybenzone sunscreen: Nonadiabatic dynamics simulations. *The Journal of chemical physics* **2016,** *145* (7), 074308.

33. Baker, L. A.; Grosvenor, L. C.; Ashfold, M. N.; Stavros, V. G., Ultrafast photophysical studies of a multicomponent sunscreen: Oxybenzone–titanium dioxide mixtures. *Chemical Physics Letters* **2016,** *664*, 39-43.

34. Dietzek, B.; Pascher, T.; Sundström, V.; Yartsev, A., Appearance of coherent artifact signals in femtosecond transient absorption spectroscopy in dependence on detector design. *Laser Physics Letters* **2007,** *4* (1), 38-43.

35. Olivucci, M., *Computational photochemistry*. Elsevier: 2005.

36. Aquilante, F.; Autschbach, J.; Carlson, R. K.; Chibotaru, L. F.; Delcey, M. G.; De Vico, L.; Fdez. Galván, I.; Ferré, N.; Frutos, L. M.; Gagliardi, L., Molcas 8: New capabilities for multiconfigurational quantum chemical calculations across the periodic table. *Journal of computational chemistry* **2016,** *37* (5), 506-541.

37. Fdez. Galván, I.; Delcey, M. G.; Pedersen, T. B.; Aquilante, F.; Lindh, R., Analytical State-Average Complete-Active-Space Self-Consistent Field Nonadiabatic Coupling Vectors: Implementation with Density-Fitted Two-Electron Integrals and Application to Conical Intersections. *Journal of Chemical Theory and Computation* **2016,** *12* (8), 3636-3653.

38. Frisch, M. J.; Trucks, G. W.; Schlegel, H. B.; Scuseria, G. E.; Robb, M. A.; Cheeseman, J. R.; Scalmani, G.; Barone, V.; Petersson, G. A.; Nakatsuji, H.; Li, X.; Caricato, M.; Marenich, A. V.; Bloino, J.; Janesko, B. G.; Gomperts, R.; Mennucci, B.; Hratchian, H. P.; Ortiz, J. V.; Izmaylov, A. F.; Sonnenberg, J. L.; Williams; Ding, F.; Lipparini, F.; Egidi, F.; Goings, J.; Peng, B.; Petrone, A.; Henderson, T.; Ranasinghe, D.; Zakrzewski, V. G.; Gao, J.; Rega, N.; Zheng, G.; Liang, W.; Hada, M.; Ehara, M.; Toyota, K.; Fukuda, R.; Hasegawa, J.; Ishida, M.; Nakajima, T.; Honda, Y.; Kitao, O.; Nakai, H.; Vreven, T.; Throssell, K.; Montgomery Jr., J. A.; Peralta, J. E.; Ogliaro, F.; Bearpark, M. J.; Heyd, J. J.; Brothers, E. N.; Kudin, K. N.; Staroverov, V. N.; Keith, T. A.; Kobayashi, R.; Normand, J.; Raghavachari, K.; Rendell, A. P.; Burant, J. C.; Iyengar, S. S.; Tomasi, J.; Cossi, M.; Millam, J. M.; Klene, M.; Adamo, C.; Cammi, R.; Ochterski, J. W.; Martin, R. L.; Morokuma, K.; Farkas, O.; Foresman, J. B.; Fox, D. J. *Gaussian 16 Rev. C.01*, Wallingford, CT, 2016.

39. Tomasi, J.; Mennucci, B.; Cammi, R., Quantum mechanical continuum solvation models. *Chemical reviews* **2005,** *105* (8), 2999-3094.

40. Sampedro, D., In Photochemistry: UV/VIS Spectroscopy, Photochemical Reactions, and Photosynthesis; Maes, KJ; Willems, JM, Eds. Nova Science Publishers: Hauppauge, New York: 2011.

8. Conclusion and Outlook

8.1. Summary

In this thesis, the photodynamics of molecular systems with different aromatic chromophores has been investigated employing femtosecond time-resolved spectroscopic techniques. Although each individual research has its own purpose, the overall theme of this thesis resides in understanding the mechanisms that drive the photostable behavior of biologically relevant species. In this sense, the bottom-up approach has been demonstrated to be an essential tool to shed light on the excited state dynamics of large and complex biomolecules. Studying these systems by systematically increasing their structural and environmental complexity has permitted us to enhance our knowledge on the understanding of the relaxation pathways available for model systems of biological molecules and specially to decipher the modulations introduced by structural changes and/or intermolecular interactions on their photochemistry.

Additionally, the experiments presented throughout the present thesis have shown the potential, versatility and complementarity of fs pump-probe methods to unravel the ultrafast dynamical behavior of molecular systems in either vacuum or solution. The isolated-phase studies were conducted by means of TR-IY or TR-ID spectroscopies, whereas for the condensed-phase experiments TA and FuC techniques were mainly used.

The first chapter of this thesis provided a general overview of the basis of femtochemistry. Fundamental concepts for understanding molecular dynamics and time-resolved experiments were described. Furthermore, a brief introduction to the photostability of life related molecules and photoprotection concept, which are the backbone of this thesis, was given.

An outline of the different experimental setups and computational methods employed in the following chapters was given in Chapter 2. Firstly, a brief description of the generation of the pump and probe pulses was given, starting from the laser system and followed by nonlinear optical processes required to modify the wavelength of the fundamental beam. Then, the spectroscopic techniques utilized for experiments in the isolated- and condensed-phases and the specific details of each setup were thoroughly described in sections 2.3 and 2.4, respectively. Finally, the methods for data modelling and computational calculations were explained.

Chapter 3 presented the first ever time-resolved ionization study of a set of azaindole structural isomers (4-AI, 5-AI, 6-AI and 7-AI). This work demonstrated the influence of the position of the nitrogen atom in the pyridinic ring on the photodynamics of isolated AIs. The relaxation of the molecules in the gas-phase at the low energy portion of their spectra was tracked by TR-IY spectroscopy, while the decay paths were predicted with MS-CASPT2//TD-DFT calculations. Although the ultrashort measured lifetimes for 5-AI and 6-AI were in contrast to the long-lived excited state found for 7-AI, the calculations described a common relaxation pathway. We postulated that the initially excited $\pi\pi^*$ state decays to the ground state *via* a CI accessed through an $n\pi^*$ state, which functions as a gate state. Thus, this study revealed how the position of the N atom in the six-membered ring determines the barrier for the coupling between the $\pi\pi^*$ and $n\pi^*$ states and therefore the rate of the nonradiative relaxation to the ground state. It should be noted here that in parallel to our time-resolved experiments, Noble *et al.* published a study of the photofragmentation of 7-AI, 6-AI and 5-AI, in which they further confirm the shorter excited state lifetimes for 5-AI and 6-AI.[1]

In Chapter 4, the complexity of the system was increased by studying the photodynamics of AIs in different solvents through steady-state and time-resolved measurements. From the conducted experiments we concluded that the excited state lifetime of these molecules in solution depends critically on the polarity of the medium, which is capable of altering dramatically the relative energy between the $\pi\pi^*$ and $n\pi^*$ states and therefore favor or inhibit the access to the relaxation channel mediated by the $n\pi^*/S_0$ CI. The solvent polarity effect was especially perceptible for 4-AI isomer, which modified its photophysical behavior from being a non-fluorescent compound in non-polar media to exhibit average lifetimes of few ns in polar aprotic solvents. Thus, we concluded that, similarly to 5-AI and 6-AI, the relaxation pathway of 4-AI in cyclohexane is mediated by the $n\pi^*/S_0$ CI, whereas in acetonitrile and dichloromethane the mechanism is analogous to that of 7-AI, involving only the $\pi\pi^*$ states. Regarding 5-AI and 6-AI isomers, in the studied polar aprotic solvents showed average lifetimes in the ps time-scale, which became slower when the polarity of the solvent was increased. Taking into account these measurements and the TD-DFT calculation, we stated that the $n\pi^*/S_0$ channel seem to be still active for these isomers. Finally, in polar protic media we observed that the dynamical behavior of the AIs was completely different due to the possible formation of tautomers through ESPT processes.

Chapter 5 demonstrated the validity of the TR-ID method not only to obtain the IR spectrum, but also to unravel the photodynamical behavior of size-selected molecular clusters. The measurements carried out for pyrrole-containing clusters yielded a ~268 and ~220 fs lifetime for pyrrole dimer and pyrrole – N-methylpyrrole complex, respectively, which according to the performed *ab initio* calculations reflected the neutral dissociation of the clusters, after photoexcitation with 240 nm. However, for the N-methylpyrrole dimer a bi-exponential dynamical behavior with time components of ~357 fs and ~3.6 ps was observed. The computational calculations predicted that for this aggregate, the neutral dissociation could not be the main relaxation channel and consequently we attributed its photodynamics to different possible routes that were previously observed for the N-methylpyrrole monomer. Additionally, we also conducted TR-ID measurements for the pyrrole-water cluster, from which we extracted a lifetime of ~165 fs. According to the TD-DFT calculations, in this charge transfer complex the neutral dissociation of the cluster is also an inhibited pathway. For this reason, we hypothesized that the observed lifetime could reflect a more complex dissociative mechanism involving a PCET reaction.

Chapter 6 explored the photodynamics of neutral aniline homoclusters formed in a supersonic expansion. Investigations were performed exciting in the 290 – 235 nm region together with an IR ns excitation and an 800 nm ionizing probe by TR-ID spectroscopy. The TR-ID measurements enabled the isolation of the dynamics of aniline dimer from that originated in bigger species of the generated distribution. Interestingly, and differently from the monomer and $(An)_{n \geq 3}$ clusters, the dimer did not present a signature attributable to the N-H bond fission driven by the dissociative $^1\pi\sigma^*$ state. This fact can be explained in terms of the symmetric head-to-tail structure adopted by the dimer, in which each molecule established two N-H$\cdots\pi$ interactions, leading to the destabilization of the H dissociation channel. The observations from this study have permitted relating the photophysics to the interactions established by the aniline units and confirming previous observations and theoretical predictions on the structure of aniline aggregates.

In Chapter 7, the photoprotective capabilities of four synthetic sunscreens inspired on the natural mycosporine-like aminoacids (MAAs) were discussed. Their photodynamics was investigated by TA spectroscopy and FuC technique, while the minimum energy relaxation pathways were modeled by CASSCF/CASPT2 methods. The synergy between time-resolved experiments and computational predictions provided a comprehensive picture of the CIs that govern the photophysics in these compounds. Following UV excitation to the S_1 ($\pi\pi^*$) state, the initially prepared population undergoes relaxation along a C=N isomerization channel on $\tau_1 = 200 - 800$ fs ($\tau_0 = 70$ fs for sample 1). Then, relaxation to the ground state occurs through S_1/S_0 CI on a time-scale around $\tau_2 = 0.4 - 1.8$ ps ($\tau_1 = 415$ fs for 1), while $\tau_3 = 6 - 10.2$ ps ($\tau_2 = 5$ ps for 1) accounts for the vibrational cooling of the hot ground state. Therefore, we postulated that the presence of the two phenyl substituents on the studied samples favored the C=N isomerization channel in detriment of the out-of-plane ring deformation predicted for simpler MAA-based sunscreens with aliphatic substituents.[2] This work demonstrated the excellent properties as sunscreens of the studied compounds and provided novel mechanistic insights for the rational design of new species with improved properties.

Finally, this Chapter looks into the research work our research group is expected to develop in the foreseeable future.

8.2. Future Work

There are numerous possibilities for future experiments that may be conducted in order to address open questions in the systems studied in this thesis. In this section, a brief outlook on the potential avenues for future research is given.

8.2.1. Photophysics of Azaindoles

The work presented in Chapters 3 and 4 provided a detailed picture of the photodynamics of AIs in vacuum and solution, respectively. However, there are still several questions that can be explored. Firstly, since the performed calculation suggested that the decay pathways for the isolated AIs involved an out-of-plane deformation of one of the neighboring CH groups to the pyridinic N atom (C_5, C_4, C_7 and C_6 in 4-AI, 5-AI, 6-AI and 7-AI, in that order), selective replacement of the H atom of these sites by a methyl or amino group is expected to offer additional dynamical insight. Indeed, the inclusion of different substituents could be a good strategy to alter the barrier for the $n\pi^*/S_0$ CI, which would lead to changes in the photophysical properties of these molecules, and therefore provide us valuable information about alternative relaxation channels.

On the other hand, the effect of hydrogen bonding solvents on the photodynamics of the AIs is another topic where further time-resolved studies and computational calculations are required. Our future TA measurements will be particularly oriented towards the observation of proton/electron transfer processes induced by the solvent media, especially in aqueous solution. In this sense, an alternative to solution-phase experiments could be to elucidate the role of the environment by studying the dynamical signature of micro-solvated clusters, with the form AI(solvent)$_n$, by means of TR-ID spectroscopy. Figure 8.1 shows the preliminary TR-IY transients collected for 6-AI(H_2O)$_n$ clusters, following 267 nm excitation. These measurements reveal that significantly slower decays are observed with respect to the gas-phase, even with the inclusion of a single water molecule, revealing the strong destabilization of the nπ* state in H-bonding media. Nevertheless, further experiments including the IR ns excitation, along with computational calculations are required not only to unravel the main deactivation channels of the AIs solvated by a number of water molecules, but also to record the IR spectra of these molecular aggregates.

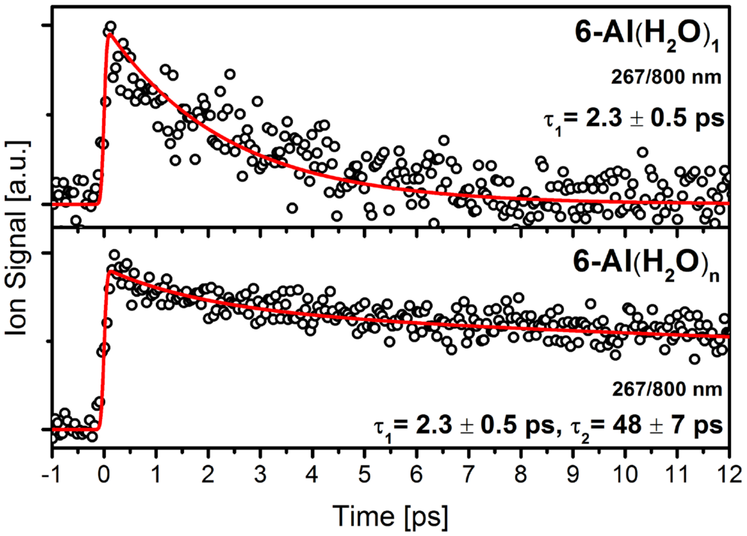

Figure 8.1. *TR-IY transients collected for 6-AI(H_2O)$_n$ clusters after excitation with 267 nm, while probing with 800 nm.*

8.2.2. Photodynamics of Aniline in Solution

The work on aniline homoclusters presented in this thesis, together with previous experiments conducted on aniline monomer[3] provided us a detailed picture of the photodynamics of this molecule in the gas-phase. However, for a more in depth understanding of the photophysical and photochemical behavior of aniline, the study of this molecule in the condensed-phase is mandatory. Currently, we are tracking the photodynamics of aniline and some of its derivatives in different solvents such as cyclohexane, methanol or water.

In the light of the available literature, the photodynamical behavior of aniline in aqueous solution is significantly altered with respect to the gas-phase. The works carried out by Saito *et al.*[4-5] reported the formation of solvated electrons and a long-lived S_1 excited state whose lifetime is about 930 ps, while in ethanol, acetonitrile or cyclohexane this lifetime is ~3-4 ns. According to these works, water essentially increases the rate of the IC respect to the gas-phase and non-polar environments. Furthermore, the study conducted by Poterya *et al.*[6] revealed that the N-H bond dissociation promoted through the $\pi\sigma^*$ state is an inaccessible pathway for aniline embedded on the surface of large water clusters. Indeed, the steady-state UV absorption and fluorescence spectra of aniline in aqueous and non-polar media have been reported by Saito *et al.*[4] and Tobita *et al.*,[7] respectively. In those spectra, in principle there is not any insight of the $\pi\sigma^*$ state. More recently, Suzuki and co-workers[8] further confirmed the long-lived character of S_1 excited state lifetime for aniline in water by employing extreme UV time-resolved photoelectron spectroscopy.

Our preliminary TA experiments and TD-DFT calculations seems to show that, as it has been predicted for pyrrole molecule,[9-10] the $\pi\sigma^*$ state plays also a crucial role as CTTS state in the UV ionization of aniline in aqueous solutions. This hypothesis will be tested on the basis of more elaborated *ab initio* calculations and further TA measurements in a recently developed pre-pump–pump–probe scheme in order to obtain a rigorous identification of the different spectral features appearing in the TA spectra.

8.2.3. Potential Sunscreens

The work on the MAA-based sunscreening agents synthesized by Prof. Sampedro highlighted a new relaxation mechanism for these kind of compounds, which was based on the C=N isomerization. There is much current research on the role of different substituents on the dynamical behavior of these molecules. Consequently, the relaxation channels of molecules with potential applications as sunscreens, in particular those derived from MAAs, will be investigated in solution and, when possible, in the gas-phase. We expect that future research in collaboration with Prof. Sampedro permits to elucidate the mechanisms behind the photostability of these molecular systems in order to guide the design of a novel generation of photoprotective compounds.

8.3. References

1. Noble, J. A.; Marceca, E.; Dedonder, C.; Phasayavan, W.; Féraud, G.; Inceesungvorn, B.; Jouvet, C., Influence of the N atom position on the excited state photodynamics of protonated azaindole. *Physical Chemistry Chemical Physics* **2020,** *22* (46), 27280-27289.

2. Woolley, J. M.; Staniforth, M.; Horbury, M. D.; Richings, G. W.; Wills, M.; Stavros, V. G., Unravelling the Photoprotection Properties of Mycosporine Amino Acid Motifs. *The Journal of Physical Chemistry Letters* **2018,** *9* (11), 3043-3048.

3. Montero, R.; Conde, Á. P.; Ovejas, V.; Martínez, R.; Castaño, F.; Longarte, A., Ultrafast dynamics of aniline in the 294-234 nm excitation range: The role of the πσ* state. *The Journal of Chemical Physics* **2011,** *135* (5), 054308.

4. Saito, F.; Tobita, S.; Shizuka, H., Photoionization of aniline in aqueous solution and its photolysis in cyclohexane. *Journal of the Chemical Society, Faraday Transactions* **1996,** *92* (21), 4177-4185.

5. Saito, F.; Tobita, S.; Shizuka, H., Photoionization mechanism of aniline derivatives in aqueous solution studied by laser flash photolysis. *Journal of Photochemistry and Photobiology A: Chemistry* **1997,** *106* (1), 119-126.

6. Poterya, V.; Nachtigallová, D.; Lengyel, J.; Fárník, M., Photodissociation of aniline N–H bonds in clusters of different nature. *Physical Chemistry Chemical Physics* **2015,** *17* (38), 25004-25013.

7. Tobita, S.; Ida, K.; Shiobara, S., Water-induced fluorescence quenching of aniline and its derivatives in aqueous solution. *Research on Chemical Intermediates* **2001,** *27* (1), 205-218.

8. West, C. W.; Nishitani, J.; Higashimura, C.; Suzuki, T., Extreme ultraviolet time-resolved photoelectron spectroscopy of aqueous aniline solution: enhanced surface concentration and pump-induced space charge effect. *Molecular Physics* **2021,** *119* (1-2), e1748240.

9. Sobolewski, A. L.; Domcke, W., Photoejection of electrons from pyrrole into an aqueous environment: ab initio results on pyrrole-water clusters. *Chemical Physics Letters* **2000,** *321* (5), 479-484.

10. Kumar, A.; Kołaski, M.; Kim, K. S., Ground state structures and excited state dynamics of pyrrole-water complexes: Ab initio excited state molecular dynamics simulations. *The Journal of Chemical Physics* **2008,** *128* (3), 034304.